

ENHANCED IONIC CONDUCTIVITY OF CERIA-BASED COMPOUNDS
FOR THE ELECTROLYTE APPLICATION IN SOFCS

By

SHOBIT OMAR

A DISSERTATION PRESENTED TO THE GRADUATE SCHOOL
OF THE UNIVERSITY OF FLORIDA IN PARTIAL FULFILLMENT
OF THE REQUIREMENTS FOR THE DEGREE OF
DOCTOR OF PHILOSOPHY

UNIVERSITY OF FLORIDA

2008

© 2008 Shobit Omar

To my loving family

ACKNOWLEDGMENTS

First of all, I would like to acknowledge my advisor, Dr. Juan C. Nino, for his support and guidance. His faith in me helped me through the tough times in my research and was a constant source of inspiration. His virtues of critical assessment and raising the bar for achievement helped me expand my potential. I would like to thank Dr. Eric D. Wachsman for his invaluable suggestions and fruitful discussions. I would also like to thank my other committee members (Dr. Wolfgang Sigmund, Dr. Simon R. Phillpot and Dr. Mark Orazem) for their time, guidance and constructive comments. Further, I like to thank Dr. Jacob L. Jones for the XRD discussions and Dr. Scott Perry for coming as a substitute in my PhD defense and for providing feedback about my research.

I would also like to convey my heartfelt thanks to Dr. Juan Nino's former and current group members: Samantha Yates, Lu Cai, Wei Qiu, Peng Xu, Mohammed Elshennawy, Satyajit Phadke, Laurel Wucherer, Marta Giachino, Kevin Tierney, Donald Moore, Louis Perez, Jillian Saxon and David Paredes for providing me excellent research environment and being helpful. I gratefully acknowledge all the fuel cell group members (Dr. Eric Wachsman's group) especially Doh Won Jung, Sean Bishop, Dr. Tak-keun Oh, Dr. Heesung Yoon, and Dr. Keith Duncan for the helpful materials science discussion. Special thanks go to Jin Soo Ahn for being a wonderful colleague and a friend. I had really enjoyed working with him for the last one year.

I also wish to acknowledge all my friends at the University of Florida (UF) with whom I had a wonderful time in Gainesville. Sankara Sarma Tatiparti, Rakesh Kumar Behera, Mahesh Tanniru, Krishna Prakash Ganesan (Machaa), Abhijit Pramanick,

Pankaj Nerikar, and Priyank Shukla, all of them had provided me a great company here in UF.

Also, I like to thank my elder brother Ritesh Omar who spent numerous sleepless night worrying about my welfare. My sister in law Smita Omar whose encouraging words had kept my enthusiasm up during the final stages of my Ph.D. work. And, last but not least, I express my sincere gratitude to my mother Rekha Omar and father Rajendra Omar for always supporting my decisions. Their love and belief in me has shaped me into who I am today. I cannot imagine myself having any of my success without my family's strong support behind me.

TABLE OF CONTENTS

	<u>page</u>
ACKNOWLEDGMENTS	4
LIST OF TABLES	9
LIST OF FIGURES	10
ABSTRACT	15
CHAPTER	
1 INTRODUCTION	17
1.1 Statement of Problem and Motivation	17
1.2 Scientific Approach	19
1.3 Organization of the Dissertation	22
2 BACKGROUND	24
2.1 Solid State Electrochemistry	24
2.2 Fuel Cells	24
2.3 Introduction to Solid Oxide Fuel Cells	26
2.4 Solid Oxide Electrolyte	29
2.4.1 Ceria Based Materials	31
2.4.2 Ionic Conductivity	34
2.4.2.1 Temperature dependence	35
2.4.2.2 Oxygen partial pressure dependence	37
2.4.2.3 Dopant concentration dependence	39
2.5 Association of Defects	40
2.6 Impedance Spectroscopy	41
3 MATERIALS AND EXPERIMENTAL PROCEDURES	46
3.1 Materials Selection	46
3.2 Experimental Procedures	46
3.2.1 Powder Processing	48
3.2.1.1 Conventional solid state route	49
3.2.1.2 Co-precipitation route	52
3.2.2 Forming	55
3.2.3 Solid State Sintering	56
3.2.3.1 Conventional sintering	56
3.2.3.2 Microwave sintering	57
3.2.4 Sample Preparation for Characterization	58
3.2.4.1 Ionic conductivity	58
3.2.4.2 X-ray diffraction	58

3.2.4.3 Scanning electron microscopy	58
3.2.4.4 Transmission electron microscopy	59
3.2.5 Impedance Spectroscopy Experimental Setup	60
4 IONIC CONDUCTIVITY AND DOPING STRATEGIES FOR IONIC CONDUCTIVITY ENHANCEMENT	62
4.1 Ionic Conductivity	62
4.2 Co-doping Strategies	65
4.2.1 Critical Dopant Ionic Radius	65
4.2.1.1 Theory	66
4.2.1.2 Materials selection	67
3.2.1.3 Results and discussion	68
4.2.1.4 Summary and conclusion	74
4.2.2 Density Functional Theory Calculation	74
4.2.2.1 Theory	75
4.2.2.2 Materials selection	78
4.2.2.3 Results and discussion	79
4.2.2.4 Summary and conclusion	95
4.3 Processing Effects on Ionic Conductivity	96
5 STRUCTURE-PROPERTY RELATIONSHIPS IN DOPED CERIA MATERIALS AT HIGH TEMPERTATURES	99
5.1 Introduction	99
5.2 Crystal Structure of Trivalent Acceptor Doped Ceria at High Temperature	106
5.2.1 High Temperature X-Ray Diffraction	106
5.2.2 Lattice Strain	108
5.2.2.1 Thermal strain	108
5.2.2.2 Chemical strain	114
5.3 Ionic Conductivity of Trivalent Acceptor Doped Ceria at High Temperatures ..	122
5.3.1 Activation Energy	128
5.3.2 Pre-Exponential Coefficient	133
5.4 Revisiting Critical Dopant Ionic Radius	136
5.5 Summary and Conclusions	140
6 PROCESSING EFFECTS ON THE IONIC CONDUCTIVITY	143
6.1 Introduction	143
6.2 Experimental Procedures	148
6.3 Results and Discussion	150
6.3.1 Microstructure	150
6.3.2 Ionic Conductivity	154
6.4 Summary and Conclusions	158

7	BUTTON CELL PERFORMANCE TESTING.....	160
7.1	Introduction	160
7.2	Experimental Procedure	160
7.3	Results and Discussion.....	166
7.3.1	Particle Size	166
7.3.2	Microstructural Analysis.....	168
7.3.3	Impedance Analysis	169
7.3.4	Power Density	171
7.4	Summary and Conclusion.....	173
8	SUMMARY AND FUTURE WORK	175
8.1	Summary	175
8.2	Future Work	180
8.2.1	Doping Strategy.....	180
8.2.2	Ionic Conductivity	181
8.2.3	Processing.....	182
8.2.4	Performance Testing.....	183
A	DEFECT CHEMISTRY AND THERMODYNAMIC IN POINT DEFECTS.....	185
B	IONIC CONDUCTIVITY AND DEFECT COMPLEXES	187
B.1	Oxygen Ion Conductivity.....	187
B.2	Defect Complexes	188
B.2.1	Dimers.....	189
B.2.2	Trimers.....	190
C	HIGH TEMPERATURE XRD PATTERNS OF CERIA COMPOUNDS.....	192
D	EXTRAPOLATION METHOD TO CALCULATE LATTICE PARAMETER	195
	LIST OF REFERENCES	197
	BIOGRAPHICAL SKETCH.....	207

LIST OF TABLES

<u>Table</u>	<u>page</u>
2-1	Typical characteristics of various Fuel cells..... 25
2-2	$P_{O_2}^*$ of doped ceria systems..... 38
4-1	Comparison of the ΔH and $\log \sigma_o$ for $Gd_{0.10}Ce_{0.90}O_{2-\delta}$, $Sm_{0.05}Nd_{0.05}Ce_{0.90}O_{2-\delta}$ and $Sm_{0.075}Nd_{0.075}Ce_{0.85}O_{2-\delta}$ measured below $550^\circ C$. Further, σ of these oxide materials at $550^\circ C$ is also reported. 91
5-1	Activation energies for ZrO_2 and CeO_2 systems doped with Ca^{2+} 100
5-2	Fitted (331) XRD peak profile parameters for $Gd_{0.10}Ce_{0.90}O_{2-\delta}$ at $400^\circ C$, measured while the furnace is heating up and cooling down. 105
5-3	Thermal expansion coefficient constants for different doped ceria systems..... 110
5-4	Thermal expansion coefficient constants for $Sm_{x/2}Nd_{x/2}Ce_{1-x}O_{2-\delta}$ 113
5-5	Relationship between lattice parameter and dopant ionic radius for $D_{0.10}Ce_{0.90}O_{2-\delta}$ at different temperatures. 117
5-6	Relationship between lattice parameter and dopant content (x) for $Sm_{x/2}Nd_{x/2}Ce_{1-x}O_{2-\delta}$ system at higher temperatures..... 120
5-7	Critical dopant ionic radius for trivalent acceptor dopant cation for host ceria, for different temperatures. 138
6-1	Abbreviation of samples synthesized using different techniques..... 150
6-2	Comparison of the grain ionic conductivity of $Sm_{0.075}Nd_{0.075}Ce_{0.85}O_{2-\delta}$ and $Gd_{0.10}Ce_{0.90}O_{2-\delta}$ at $600^\circ C$ 157
7-1	Comparison between the total ASR obtained from I-V characteristic and impedance measurement. 171

LIST OF FIGURES

<u>Figure</u>	<u>page</u>
1-1 Schematic of a solid oxide fuel cell.....	18
1-2 Ionic conductivity of fluorite structure oxides.	20
2-1 Cubic fluorite structure of ceria.....	32
2-2 Oxygen vacancy jump in doped ceria system.....	33
2-3 Ionic conductivity as a function of dopant concentration in doped zirconia systems.	39
2-4 Oxygen vacancy trapped in the tetrahedral site.....	40
2-5 Typical impedance response for a given relaxation process..	42
2-6 Typical impedance spectrum of an electroded polycrystalline ceramic material. The equivalent circuit to fit the spectrum is also shown.	44
3-1 Flow chart for the powder synthesis using conventional solid state reaction and different characterization techniques.	47
3-2 XRD patterns of $\text{Lu}_{0.10}\text{Ce}_{0.90}\text{O}_{2-\delta}$ calcined at different temperatures for 10 h.	50
3-3 XRD patterns of different doped ceria systems calcined at 1450°C for 10 h.	51
3-4 Particle size distribution of $\text{Sm}_{0.075}\text{Nd}_{0.075}\text{Ce}_{0.85}\text{O}_{2-\delta}$ synthesized using solid oxide route.....	52
3-5 XRD pattern of $\text{Sm}_{0.075}\text{Nd}_{0.075}\text{Ce}_{0.85}\text{O}_{2-\delta}$ synthesized using co-precipitation technique.....	54
3-6 Particle size distribution of $\text{Sm}_{0.075}\text{Nd}_{0.075}\text{Ce}_{0.85}\text{O}_{2-\delta}$ synthesized using co-precipitation technique.....	55
3-7 Sample placed in the thermal pod for microwave sintering.	57
3-8 AC impedance spectroscopy experimental setup.....	60
4-1 Grain ionic (GI) conductivity comparison of $\text{D}_{0.10}\text{Ce}_{0.90}\text{O}_{2-\delta}$ at 400°C.....	67
4-2 XRD profiles of $\text{Lu}_x\text{Nd}_y\text{Ce}_{1-x-y}\text{O}_{2-\delta}$ and $\text{Gd}_{0.056}\text{Y}_{0.044}\text{Ce}_{0.90}\text{O}_{2-\delta}$ taken at room temperature.	69
4-3 XRD profiles of $\text{D}_{0.10}\text{Ce}_{0.90}\text{O}_{2-\delta}$ taken at room temperature.....	70

4-4	Elastic strain as a function of dopant concentration for $\text{Sm}_{x/2}\text{Nd}_{x/2}\text{Ce}_{1-x}\text{O}_{2-\delta}$ and $\text{Nd}_x\text{Ce}_{1-x}\text{O}_{2-\delta}$.	71
4-5	Arrhenius plot for the bulk ionic conductivity of $\text{Gd}_{0.10}\text{Ce}_{0.90}\text{O}_{2-\delta}$, $\text{Lu}_{0.10}\text{Ce}_{0.90}\text{O}_{2-\delta}$, and $\text{Lu}_{0.054}\text{Nd}_{0.046}\text{Ce}_{0.90}\text{O}_{2-\delta}$ systems in air.	73
4-6	Total interaction energy between dopant cation and oxygen vacancy sitting in nearest neighbor (NN) and next to nearest neighbor (NNN) site (of dopant cations) for different trivalent cations	76
4-7	Cubic fluorite structure of doped ceria, where oxygen vacancy reside in nearest neighbor (NN) site A) and next to nearest neighbor (NNN) site B) of dopant cation.	77
4-8	Scanning electron micrograph of the surface of $\text{Sm}_{0.05}\text{Nd}_{0.05}\text{Ce}_{0.90}\text{O}_{2-\delta}$ sintered pellet.	79
4-9	XRD patterns of $\text{Sm}_{x/2}\text{Nd}_{x/2}\text{Ce}_{1-x}\text{O}_{2-\delta}$ measured at room temperature.	80
4-10	Shift in (111) and (200) XRD peaks position of $\text{Sm}_{x/2}\text{Nd}_{x/2}\text{Ce}_{1-x}\text{O}_{2-\delta}$ with increase in dopant concentration (x).	81
4-11	Lattice parameter as a function of dopant concentration (mol%) for $\text{Sm}_{x/2}\text{Nd}_{x/2}\text{Ce}_{1-x}\text{O}_{2-\delta}$ and $\text{Nd}_x\text{Ce}_{1-x}\text{O}_{2-\delta}$.	82
4-12	Typical impedance spectrum of a polycrystalline $\text{Sm}_{0.075}\text{Nd}_{0.075}\text{Ce}_{0.85}\text{O}_{2-\delta}$ ceramic measured in air at 300°C.	84
4-13	Arrhenius plots for the grain ionic conductivity of $\text{Sm}_{x/2}\text{Nd}_{x/2}\text{Ce}_{1-x}\text{O}_{2-\delta}$	85
4-14	Log σ_0 as a function of activation energy measured below 475°C for $\text{Sm}_{x/2}\text{Nd}_{x/2}\text{Ce}_{1-x}\text{O}_{2-\delta}$.	86
4-15	Grain ionic conductivity as a function of x, dopant concentration (mol%) in $\text{Sm}_{x/2}\text{Nd}_{x/2}\text{Ce}_{1-x}\text{O}_{2-\delta}$ and $\text{Gd}_x\text{Ce}_{1-x}\text{O}_{2-\delta}$.	88
4-16	Arrhenius plot for the grain ionic conductivity of $\text{Gd}_{0.10}\text{Ce}_{0.90}\text{O}_{2-\delta}$, $\text{Sm}_{0.075}\text{Nd}_{0.075}\text{Ce}_{0.85}\text{O}_{2-\delta}$ and $\text{Sm}_{0.05}\text{Nd}_{0.05}\text{Ce}_{0.90}\text{O}_{2-\delta}$.	89
4-17	Grain ionic conductivity of $\text{Sm}_{x/2}\text{Nd}_{x/2}\text{Ce}_{1-x}\text{O}_{2-\delta}$ as a function of x, dopant concentration (mol%).	92
4-18	Activation energy for oxygen ion diffusion in $\text{Sm}_{x/2}\text{Nd}_{x/2}\text{Ce}_{1-x}\text{O}_{2-\delta}$ measured below 475°C and above 475°C, as a function of x.	93
4-19	Grain ionic conductivity comparison of doped ceria systems at 600°C between our work and literature.	97

5-1	The (331) peak in XRD profiles of $\text{Gd}_{0.10}\text{Ce}_{0.90}\text{O}_{2-\delta}$ measured at 400°C in different ramping conditions.....	105
5-2	XRD profiles of measured $\text{Sm}_{0.10}\text{Ce}_{0.90}\text{O}_{2-\delta}$ at different temperature in air.	106
5-3	XRD profiles of measured $\text{Lu}_{0.10}\text{Ce}_{0.90}\text{O}_{2-\delta}$ at different temperature in air.....	107
5-4	Thermal expansion of $\text{D}_{0.10}\text{Ce}_{0.90}\text{O}_{2-\delta}$ ceramic systems (where $\text{D}^{3+} = \text{Lu}^{3+}, \text{Yb}^{3+}, \text{Er}^{3+}, \text{Dy}^{3+}, \text{Gd}^{3+}, \text{Sm}^{3+}, \text{Sm}^{3+}/\text{Nd}^{3+}, \text{Nd}^{3+}$) in air.....	109
5-5	Thermal expansion coefficient (at 600°C) as a function of dopant ionic radius for $\text{D}_{0.10}\text{Ce}_{0.90}\text{O}_{2-\delta}$ systems.	111
5-6	Thermal expansion of $\text{Sm}_{x/2}\text{Nd}_{x/2}\text{Ce}_{1-x}\text{O}_{2-\delta}$ ceramic systems (where $x = 0.01, 0.03, 0.05, 0.08, 0.10, 0.12, 0.15,$ and 0.20) in air.....	112
5-7	Thermal expansion coefficient (α) at 600°C for $\text{Sm}_{x/2}\text{Nd}_{x/2}\text{Ce}_{1-x}\text{O}_{2-\delta}$ as a function of dopant concentration.....	114
5-8	Lattice expansion of $\text{D}_{0.10}\text{Ce}_{0.90}\text{O}_{2-\delta}$ systems as a function of dopant ionic radius.....	116
5-9	Lattice expansion in $\text{Sm}_{x/2}\text{Nd}_{x/2}\text{Ce}_{1-x}\text{O}_{2-\delta}$ system as a function of dopant concentration at different temperatures.....	119
5-10	Vegard's slope as a function of temperature for $\text{Sm}_{x/2}\text{Nd}_{x/2}\text{Ce}_{1-x}\text{O}_{2-\delta}$ system. .	120
5-11	Grain ionic conductivity comparison of different doped ceria materials (with 10 mol% dopant content).....	125
5-12	Grain ionic conductivity as a function of dopant concentration and temperature.	127
5-13	Normalized grain ionic conductivity as a function of dopant concentration and temperature.	128
5-14	Activation energy for oxygen vacancy diffusion in doped ceria systems with 10 mol% dopant.....	130
5-15	Migration and Association enthalpies for oxygen vacancy diffusion determined from the Arrhenius plot of doped ceria systems.....	131
5-16	Pre-exponential coefficient in the Arrhenius ionic conductivity plot of $\text{D}_{0.10}\text{Ce}_{0.90}\text{O}_{2-\delta}$ systems.....	134
5-17	Lattice parameter mismatch between $\text{D}_{0.10}\text{Ce}_{0.90}\text{O}_{2-\delta}$ and pure ceria, as a function of dopant cation ionic radius at 500°C. The grain ionic conductivity of $\text{D}_{0.10}\text{Ce}_{0.90}\text{O}_{2-\delta}$ at 500°C is also shown.....	139

6-1	A) Continuous layer of an siliceous phase in the grain boundary of $Gd_{0.10}Ce_{0.90}O_{2-\delta}$ B) Glassy phase formed at the three-grain junction in $Sm_{0.05}Nd_{0.05}Ce_{0.90}O_{2-\delta}$.	145
6-2	Comparison of the temperature – time profile in conventional solid state sintering and microwave sintering.	149
6-3	SEM images of Conventional sintering + Solid oxide route, and Microwave sintering + Co-precipitation technique.	151
6-4	TEM images of the microwave sintered $Sm_{0.075}Nd_{0.075}Ce_{0.85}O_{2-\delta}$ sample.	151
6-5	Grain boundary in the polycrystalline ceramic synthesized using microwave sintering and conventional solid state sintering.	152
6-6	Electron dispersive X-ray spectrum of Sm_{CoSo} sample.	153
6-7	Impedance spectrum of Sm_{MiCo} and Sm_{CoSo} samples at 350°C, in air.	154
6-8	Arrhenius plot for the ionic conductivity of $Sm_{0.075}Nd_{0.075}Ce_{0.85}O_{2-\delta}$ and $Gd_{0.10}Ce_{0.90}O_{2-\delta}$ materials.	156
7-1	Schematic of anode-supported prototype solid oxide fuel cell.	161
7-2	Green tape of NiO-GDC and the circular punched tape.	162
7-3	Flow chart for the fabrication of anode-supported prototype SOFC.	164
7-4	Experimental setup for the I-V characteristics measurement of the test SOFC sample.	165
7-5	Particle size distribution of $Sm_{0.075}Nd_{0.075}Ce_{0.85}O_{2-\delta}$ synthesized using co-precipitation technique and $La_{0.6}Sr_{0.4}Co_{0.2}Fe_{0.8}O_{3-\delta}$.	167
7-6	FE-SEM images of cross-section view of electrodes and electrolyte, and surface of the electrolyte.	169
7-7	Impedance spectrum of the SOFC cell measured at different temperatures.	169
7-8	Area specific resistance at different temperatures.	170
7-9	The I-V characteristics of the prototype SOFC sample with $Sm_{0.075}Nd_{0.075}Ce_{0.85}O_{2-\delta}$ electrolyte at various temperatures	172
C-1	XRD profiles of pure ceria collected at high temperatures.	192
C-2	XRD profiles of $Yb_{0.10}Ce_{0.90}O_{2-\delta}$ collected at high temperatures.	192
C-3	XRD profiles of $Y_{0.10}Ce_{0.90}O_{2-\delta}$ collected at high temperatures.	193

C-4	XRD profiles of $\text{Dy}_{0.10}\text{Ce}_{0.90}\text{O}_{2-\delta}$ collected at high temperatures.	193
C-5	XRD profiles of $\text{Gd}_{0.10}\text{Ce}_{0.90}\text{O}_{2-\delta}$ collected at high temperatures.	194
C-6	XRD profiles of $\text{Sm}_{0.10}\text{Ce}_{0.90}\text{O}_{2-\delta}$ collected at high temperatures.	194
D-1	Plot of calculated lattice parameter, a with respect to $\cos^2\theta$ for pure ceria at different temperatures.	196

Abstract of Dissertation Presented to the Graduate School
of the University of Florida in Partial Fulfillment of the
Requirements for the Degree of Doctor of Philosophy

ENHANCED IONIC CONDUCTIVITY IN CERIA-BASED COMPOUNDS FOR THE
ELECTROLYTE APPLICATION IN SOFCs

By

Shobit Omar

August 2008

Chair: Juan C. Nino

Major: Materials Science and Engineering

Higher ionically conductive solid oxide electrolytes operating at intermediate temperatures (400 to 700°C) are critical for the application of portable power generation device based on solid oxide fuel cells (SOFCs). Doped ceria materials show promise due to their higher ionic conductivity, and good thermodynamic stability in the intermediate temperature range. Among the doped ceria electrolytes, $\text{Gd}_{0.10}\text{Ce}_{0.90}\text{O}_{2-\delta}$ (GDC) is widely accepted to exhibit the highest ionic conductivity. To further enhance the ionic conductivity in ceria in this work, novel co-doping strategies are tested. Co-doping based on Sm^{3+} and Nd^{3+} as dopant cations resulted in an increase in the ionic conductivity. It is shown that at 550°C, the ionic conductivity of $\text{Sm}_{0.075}\text{Nd}_{0.075}\text{Ce}_{0.85}\text{O}_{2-\delta}$ is observed to be 30 % higher than that of GDC.

From the literature, it is known that the ionic conductivity depends upon the processing variables. Thus, to have a clear understanding of the ionic conductivity trend as a function of dopant type, a consistent set of ionic conductivity data is developed for different doped ceria materials synthesized under similar processing conditions. It was observed that for single dopants, Nd^{3+} is the best dopant cation for host ceria.

The critical dopant ionic radius (r_c) was determined for trivalent doped ceria system at high temperatures. The elastic strain and the ionic conductivity of doped ceria systems measured at 500°C, show that the elastic strain – ionic conductivity relationship based on r_c concept is not a successful strategy in doped ceria.

Further, the effect of processing condition on $\text{Sm}_{0.075}\text{Nd}_{0.075}\text{Ce}_{0.85}\text{O}_{2-\delta}$ materials is tested. Co-doped ceria is synthesized using different processing routes. It is observed that the grain ionic conductivity of $\text{Sm}_{0.075}\text{Nd}_{0.075}\text{Ce}_{0.85}\text{O}_{2-\delta}$ synthesized using co-precipitation technique and microwave sintering is around 45 % higher than that of GDC at 550°C. Finally, the performance of the anode-supported prototype SOFC using $\text{Sm}_{0.075}\text{Nd}_{0.075}\text{Ce}_{0.85}\text{O}_{2-\delta}$ as an electrolyte is analyzed at intermediate temperatures. An exceptionally high power density of 1.38 W/cm² is obtained at 650°C, using 90 cm³/minute of dry air and wet hydrogen in cathode and anode sides, respectively. The power density of a tested cell shows that the $\text{Sm}_{0.075}\text{Nd}_{0.075}\text{Ce}_{0.85}\text{O}_{2-\delta}$ ceramic electrolyte can successfully generate higher performance in SOFCs working in the intermediate temperature range.

CHAPTER 1 INTRODUCTION

1.1 Statement of Problem and Motivation

The continuous increase in demand for fuels, limited oil resources and increasing global warming requires for the use of renewable sources of energy.^{1,2} These renewable sources include solar, biomass, hydropower, geothermal, and wind energy.³ Research on the use of these sources mainly focuses on the development of new technologies (e.g., fuel cells, batteries, solar cells, windmills etc.) that can efficiently create cleaner sustainable energy. Among them, fuel cell technology shows significant promise.⁴ Development and commercialization of this technology would be a major step forward towards the goal of sustainable energy production. Among various fuel cells, solid oxide fuel cell (SOFC) is considered by many to be the most desirable fuel cell for generating electricity from hydrocarbon fuels.⁵ This is because they are highly efficient, environmentally friendly, corrosion resistant, and have the potential to operate directly on existing transportation fuels ranging from gasoline to jet fuels.⁶

Figure 1-1 shows the main components of SOFC, i.e., cathode, electrolyte and anode. The operation of the device will be described in detail in chapter 2. Although SOFC offers a lot of promise in energy-conversion system, the current technology, based on a stabilized ZrO_2 electrolyte, must operate in the region of 1000°C to avoid unacceptable high ohmic losses.⁷ The high operating temperature requires the use of selected materials to withstand such extreme conditions. If the operating temperature can be lowered to $400\text{-}700^\circ\text{C}$, which is termed the intermediate temperature (IT) range, it will open up the possibility for a wide range of materials in SOFC. It will not only improve the reliability (i.e., hours of operation) of the device, but also lower the cost and

time it takes to heat up to the operating temperature. A main goal of the Department of Energy is to accelerate the development of SOFCs and get them commercialized as quickly as possible making them affordable option for power generation. Extensive research has been performed through the Solid State Energy Conversion Alliance (SECA) program which include an industrial team, a core technology program team, and federal government experts.⁸ The main target of this program is to place SOFCs into market by 2010 at a cost of nearly \$400/kW. These fuel cells will be 3-10 kW in size, adaptable for various applications.⁸

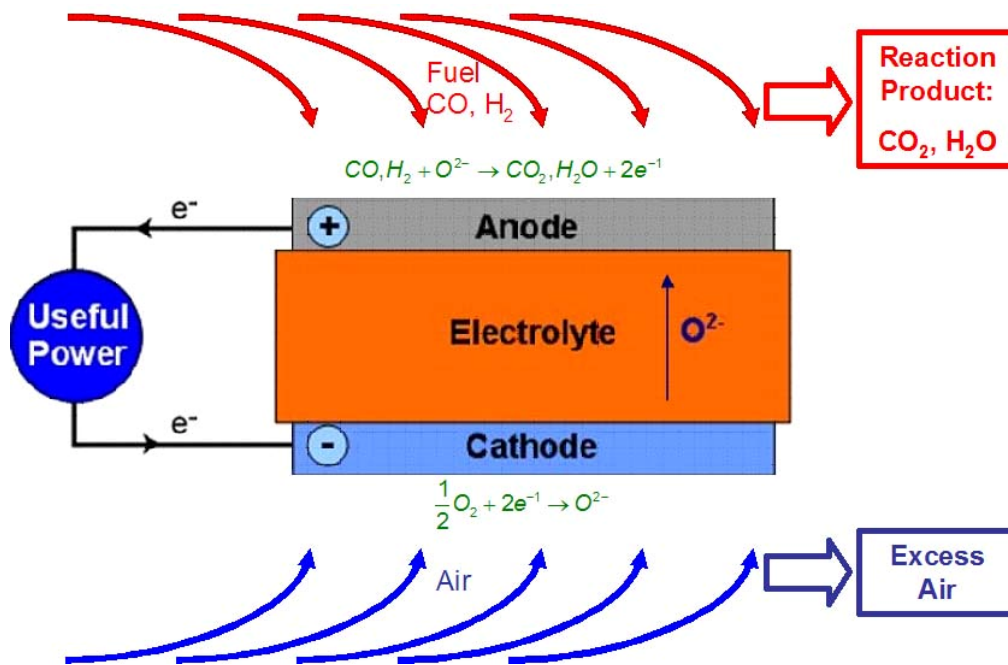


Figure 1-1. Schematic of a solid oxide fuel cell.

However, with the current state-of-the-art SOFC materials, lowering the operating temperature increases the ohmic losses and electrode polarizations. This has a detrimental effect on the performance and efficiency of the device. Thus, there is a need to develop materials for all the components of SOFCs that show improved properties in the IT range. In the present work, research is focused on developing solid

oxide electrolyte materials with enhanced ionic conductivity for the IT application of SOFCs.

1.2 Scientific Approach

A summary of the ionic conductivity of oxide materials are shown in Figure 1-2.⁹ All these ionically conductive materials exhibit the cubic fluorite crystal structure. Among the oxygen ion conductors, bismuth oxide based materials show the highest ionic conductivity in IT range. However, these materials undergo an order–disorder transition at around 600°C, which limits their application as solid oxide electrolytes. Although doped zirconia materials are stable at intermediate temperatures, their ionic conductivity is comparatively lower than other candidate materials. In recent years, SOFC electrolyte research primarily has focused on doped ceria.¹⁰⁻¹² Doped ceria materials exhibit higher ionic conductivity than doped zirconia, and show better thermodynamic stability than doped Bi₂O₃ in the IT range. Among doped ceria materials, Gd-doped ceria exhibits the highest ionic conductivity.¹³ The main objective of this dissertation is to identify dopants and doping strategies that can further enhance the ionic conductivity of ceria.

Numerous works have been performed in understanding the effect of different acceptor dopants on the ionic conductivity in ceria.^{10,14} Since processing variables affect the ionic conductivity, a wide range of ionic conductivity data is reported for a given composition in doped ceria.^{7,15} Thus, a clear understanding of the ionic conductivity trend as a function of dopant type is still lacking.

To overcome this, a consistent set of ionic conductivity data will be developed for different doped ceria materials synthesized under similar processing conditions. The

comparison of this consistent data will allow selecting the potential acceptor dopants that can enhance the ionic conductivity in ceria.

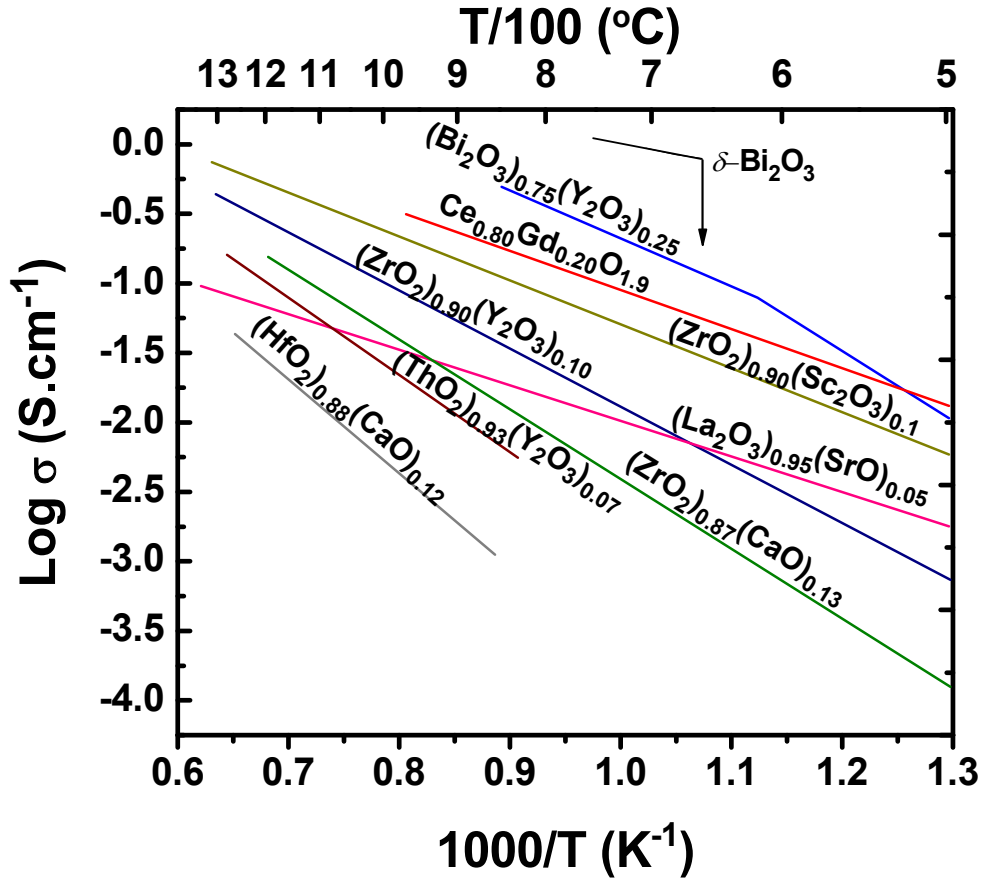


Figure 1-2. Ionic conductivity of fluorite structure oxides.⁹

In the literature, co-doping in ceria is well established to increase the ionic conductivity.¹⁶ However, in the previous work, no systematic rationales behind selecting acceptor dopants were provided.¹⁷⁻²⁰ Experiment will be conducted to test the novel co-doping strategies for a series of acceptor dopants, which will be selected based on their ionic radius. After identifying the co-dopants, the effect of dopant concentration on the ionic conductivity will be examined.

The structure (elastic strain) – property (ionic conductivity) relationship in the literature for doped ceria shows Gd^{3+} as the ideal dopant since it creates the minimum elastic lattice strain.^{21,22} It is difficult to compare both aspects as the ionic conductivity is measured at intermediate temperatures, and the elastic strain is determined at room temperature. Therefore, to perform a fair comparison between structure and property, for all the doped ceria materials, both the ionic conductivity and elastic strain will be measured at high temperatures.

After identifying the dopants and optimizing the dopant concentration, the effect of different processing variables on the ionic conductivity will be performed. The higher ionic conductivity material will be synthesized using varying processing routes, to obtain different ceramic microstructures. The effect of fast firing using microwave sintering on the ionic conductivity of novel ceramic material will be studied.

Finally, the potential of the novel co-doped ceria as an electrolyte will be tested in a real SOFC environment. Anode-supported SOFC prototypes based on the novel electrolyte will be fabricated. The power density measurement of the SOFC samples will be performed using current-voltage characteristics at intermediate temperatures.

Different characterization techniques will be utilized to achieve all the above objectives. The ionic conductivity measurement will be performed using ac-impedance spectroscopy technique inside the quartz reactor at high temperatures, in air. High temperature X-ray diffraction will be used to characterize the crystal structure parameters of doped ceria materials. Microstructural analysis will be performed using scanning electron microscopy and transmission electron microscopy.

1.3 Organization of the Dissertation

Chapter 2 presents a brief introduction on the solid state electrochemistry, solid oxide fuel cells, solid oxide electrolytes, and the main requirements for the material to be used as an electrolyte in SOFC environment. This general crystallography of fluorite structure, ionic conduction in doped fluorite oxides, and the ionic conductivity dependence on temperature, dopant concentration, and the oxygen partial pressure are also covered. In addition, a brief overview of impedance spectroscopy technique is also presented. In Chapter 3, materials selection, details of the experimental procedures and the various characterization techniques used are covered.

Chapter 4 discusses the doping strategies that are tested on ceria, in order to enhance the ionic conductivity of the materials. This chapter presents the ionic conductivity results of novel ceramic electrolyte materials, and their comparison to $\text{Gd}_{0.10}\text{Ce}_{0.90}\text{O}_{2-\delta}$ electrolyte.

In Chapter 5, a consistent set of ionic conductivity data at intermediate temperatures, for different doped ceria systems synthesized under similar experimental conditions, is presented. In addition, crystal lattice elastic strain for different doped ceria systems at higher temperatures, and its comparison with the ionic conductivity at the corresponding temperature are described. Further, the relation between critical dopant ionic radius and the ionic conductivity of doped ceria system is revisited. After understanding the structure and property in doped ceria systems, the effects of processing on the ionic conductivity are also covered in Chapter 6. Different processing routes are used to synthesize phase pure samples of our novel ceramic electrolyte. The effects of processing variables on the microstructure, and ionic conductivity are described in this chapter.

Chapter 7 presents in detail the experimental setup and the fabrication of anode-supported prototype of SOFC. Further, power density results of SOFC device using the novel ceramic electrolyte are discussed. Chapter 8 presents the summary of the dissertation and the areas for future work in doped ceria materials. At the end of the thesis, four appendices present the basic information about the defect chemistry, and thermodynamic of point defects (Appendix A), ionic conductivity and defect complexes (Appendix B), X-ray diffraction profile for various doped ceria materials collected at different temperatures in air (Appendix C), and extrapolation method to estimate lattice parameter of cubic structure material (Appendix D).

CHAPTER 2 BACKGROUND

2.1 Solid State Electrochemistry

Electrochemistry is the branch of chemistry that covers all the phenomena in which a chemical change is the result of electrical force and, vice versa, where an electric force is generated as a result of chemical processes. When associated with the chemistry and physics of solid state compounds, it is called solid state electrochemistry. Solid state electrochemistry involves the study of thermodynamics, kinetics and mechanism of electrochemical reactions in solid state materials. It is a well established field which finds lot of applications in various fields. Electrochemical gas sensors, fuel cells, batteries, and electrochromic devices are few areas where the knowledge of solid state electrochemistry is exploited.²³ Further, it can be divided into two main subjects, ionics and electrodics. In ionics, the emphasis is on the properties of electrolyte materials, while electrodics involves understanding electrode reactions. Both subjects require fundamental understanding of structural and defect chemistry, diffusion and transport in solids, conductivity and electrochemical reactions, and adsorption and reactions on solid surfaces.²⁴ The basic information about the defect chemistry, thermodynamic barriers, and diffusion processes in solid materials are provided in Appendix A and elsewhere.²⁴

2.2 Fuel Cells

The concept of generating electrical power from a simple electrochemical cell was first demonstrated by Sir William R. Grove in 1839.²⁵ At that time, the electrochemical device was known as Grove cell instead of fuel cell. The Grove cell provided nearly double the voltage of the Daniell cell which was the major device in the early years of

batteries. It was believed that a power generation using hydrogen as a fuel could replace coal, the primary source of energy at that time. The term fuel cell wasn't used until 1889, when scientists Ludwig Mond and Charles Langer attempted to build the first practical device using hydrogen to produce electricity. In 1959, Bacon was able to assemble a stack of 40 fuel cells which exhibited a useful power density.²⁶ Bacon's cell, which was modified by Pratt and Whitney, became the onboard power system for the Apollo space vehicle that enabled astronauts to land on the moon in 1969. Today, scientists and technologists all over the world are working to advance the fuel cell technologies for use in everyday appliances, such as computers and cell phones as well as to power homes, office buildings, and even vehicles.

Table 2-1. Typical characteristics of various Fuel cells.⁶

Type of Fuel Cell	Typical Electrolyte	Charge Carrier	Operating Temperatures (°C)	Efficiency (%)
SOFC	Y Stabilized ZrO ₂ ,	O ²⁻	1000	60-70
	Gd Doped CeO ₂ ,		600-800	
	Er Stabilized Bi ₂ O ₃		600	
PEMFC	Perfluorosulfonic Acid	H ⁺	50-100	35-40
AFC	KOH (aqueous)	OH ⁻	70-100	60
MCFC	Li ₂ CO ₃ -K ₂ CO ₃ (molten)	CO ₃ ²⁻	650	50-60
PAFC	H ₃ PO ₄	H ⁺	200	40-45

A fuel cell can be described as an electrochemical conversion device that uses oxygen and hydrogen or hydrocarbons to generate electricity with the only byproducts being water and heat (shown in Figure 1-1). Like a simple battery it consists of an electrolyte sandwiched between two electrodes (a porous anode and cathode).⁵ However, while a battery only stores electricity, a fuel cell produces electricity and does

not need recharging. Theoretically, as long as fuels (i.e., hydrogen or hydrocarbons, and oxygen) are supplied, it will continuously generate electricity.

Fuel cells are generally classified by the type of electrolytes incorporated within the fuel cell: e.g., alkaline fuel cell (AFC), polymer electrolyte membrane fuel cell (PEMFC), phosphoric acid fuel cell (PAFC), molten carbonate fuel cell (MCFC) and solid oxide fuel cell (SOFC).²⁷ For PEMFCs and PAFCs, protons move through the electrolyte towards the cathode where they combine with oxygen and electrons, to produce water and heat. For AFCs, MCFCs and SOFCs, negative ions diffuse through the electrolyte toward the anode to oxidize the hydrogen fuel to produce water and electrons. The electrons move through the anode to the external circuit and back to the cathode, providing a source of useful electrical energy in an external circuit. The general characteristics of these fuel cells are given in Table 2-1.⁶ Further useful technological information and their current application status is published in a variety of books, review papers, and websites.²⁸⁻³¹

Fuel cells offer the promise of higher efficiency in energy conversion and electric power generation for many different applications. However, as main incentive for investing in the fuel cell research and development is the substantially reduced environmental impacts if the long-term energy scenario based on renewable energy source, i.e., hydrogen can be realized.

2.3 Introduction to Solid Oxide Fuel Cells

As the name implies, SOFCs uses an ion conducting solid-oxide or ceramic as an electrolyte. The first ceramic solid-oxide electrolyte was discovered by Nernst in 1899.^{5,32} The first successful operation of a ceramic fuel cell at 1000°C was demonstrated by Baur and Preis in 1937.³³ Since that time, SOFC technology has

made excellent technical progress. Fuel cells based on the state of the art yttria stabilized zirconia electrolyte, have been operated for thousand of hours showing excellent performance. In the last few decades, SOFC research and development received significant attention which shows the widening interest in this technology.

Among various types of fuel cell technologies, SOFC is considered to be one of the most desirable fuel cell for generating electricity from hydrocarbon fuels. This is because of their ability to use currently available fossil fuels, thus reducing production cost. SOFCs have so far been operated on methane, propane, butane, fermentation gas, gasified biomass and paint fumes with minimal fuel processing.⁵ Other fuel cell technologies require pure hydrogen as their fuel. This makes them highly fuel flexible and far superior to other technologies such as PEMFC, MCFC. In addition, SOFCs have the highest efficiencies of all fuel cells and, potentially, a long life expectancy.³⁴ The typical efficiency when used separately is around 40-60%. However, this figure can reach 70 % when the hot exhaust of the cell is used in a hybrid combination with gas turbines. Further, the high operating temperature of SOFCs (~1000°C) eliminates the need for expensive Pt catalysts, which is the case for PEMFC or other low temperature fuel cells. Thus, they do not get poisoned by carbon monoxide. In addition, their high operating temperature allows direct use of natural gas, thus eliminating the need for an expensive, external reformer. Furthermore, because SOFC is a two phase gas/solid system, many of the problems associated with liquid electrolytes such as corrosion, flooding, electrolyte distribution, and maintaining a stable triple phase boundary region are eliminated. They are attractive as an energy source because they are clean, reliable and environmentally friendly. Emission of pollutants from fuel cells (such as

CO, NO_x, SO_x) are several orders of magnitude lower than those produced by conventional combustion engines. Finally, the vibration-free operation of SOFCs eliminates the noise associated with conventional power generation systems. For these reasons, SOFCs may be considered to be “The Future of Power Generation”.

Figure 1-1 shows a schematic of a typical SOFC. The dense solid oxide electrolyte is sandwiched between two porous electrodes (anode and cathode). Each component serves several functions in the cell, and meets certain requirements (such as conductivity, chemical and structural stability, compatibility, and mechanical properties) for a particular condition.³⁵ The operation of SOFCs involves oxidation of the fuel at the anode, and reduction of the oxidant at the cathode. Air flows along the cathode side. When an oxygen molecule contacts the cathode/electrolyte interface, it splits into two oxygen ions. These oxygen ions diffuse into the electrolyte material and migrate to the other side of the cell where they encounter the anode. The oxygen ions encounter the fuel at the anode/electrolyte interface and react, producing water, carbon dioxide, heat, and most importantly electrons. These electrons transport through the anode to the external circuit and back to the cathode, providing a source of useful electrical energy in the form of direct current in an external circuit. The open circuit voltage (E°) is given by the Nernst equation,

$$E^{\circ} = \frac{RT}{4F} \ln \left(\frac{pO_2(\text{cathode})}{pO_2(\text{anode})} \right) \quad (2-1)$$

where R , T , F and the pO_2 's are the universal gas constant, absolute temperature, Faraday's constant, and the oxygen partial pressures, respectively. Under cell operating conditions, i.e., when a current passes through it, the cell voltage (E) is given by,

$$E = E^{\circ} - IR - \eta_A - \eta_C \quad (2-2)$$

where I is the current passing through the cell, R is the resistance of the cell, and η_A and η_C are the voltage losses due to the polarization associated with anode and cathode, respectively. For a high power density SOFC, the resistive losses and the electrode polarizations need to be minimized. The amount of power produced by a fuel cell depends upon several factors, such as fuel cell type, cell size, the temperature at which it operates, and the pressure at which the gases are supplied to the cell.³⁶ Still, a single fuel cell produces enough electricity for only the smallest applications. Therefore, in order to generate sufficient voltage, individual fuel cells are typically connected in stacks and electrically connected in series through interconnects. A typical fuel cell stack may consist of hundreds of fuel cells.

2.4 Solid Oxide Electrolyte

In 1899, W. Nernst³² suggested that ZrO_2 is a solid conductor for oxygen ions. However, the explanation for the conduction mechanism in this material was first given by C. Wagner³⁷. Doping of ZrO_2 with different acceptor metal cations results in oxygen vacancies which are the charge carriers in this material. The acceptor doped ZrO_2 is typically used as a solid oxide electrolyte in sensors for measuring oxygen partial pressures and in fuel cells and electrolyzers. In order to reduce the ohmic losses, these devices are typically used at higher temperatures ($\sim 1000^{\circ}C$). Thus, the main requirements for good solid oxide electrolytes are mainly fixed by the high operating temperature which dictates constraints of different types,

1. High ionic conductivity ($> 0.1 \text{ S.cm}^{-1}$ at $1000^{\circ}C$).
2. Low electronic transference number ($< 10^{-3}$).

3. Large electrolytic domain.
4. Chemically stable under extreme conditions i.e., low reducing atmosphere (10^{-22} atmosphere) and high temperatures (1000°C).
5. Good phase stability and a good match of thermal expansion coefficient with other cell components.
6. High mechanical strength i.e., fracture toughness (> 400 MPa).

In an effort to lower the operating temperature of SOFCs, numerous research groups have focused on developing materials with higher ionic conductivity than doped ZrO_2 . Higher ionically conductive electrolytes are not only important for SOFC applications but also play a vital role in chemical processing, oxygen and hydrogen generators, electrochemical gas sensors, and combustion control. High oxygen diffusivity has been observed in oxides which exhibit large tolerance for atomic disorder. Several investigations have focused on cubic fluorite structured oxides due to their relatively open structure. The most successful oxide electrolytes have been those based on group IVB oxides (i.e., ZrO_2 , HfO_2 , CeO_2 or ThO_2) with additions of either an alkaline earth oxides (e.g. CaO or SrO), Sc_2O_3 , Y_2O_3 or a rare earth oxides.³⁸ Optimization of these materials has led to 8 mol% yttria-stabilized zirconia (YSZ) as the favored electrolyte for solid oxide fuel cells (SOFCs) application.³⁹ Although YSZ is purely an ionic conductor even at reducing atmospheres, its high operational temperature restricts its usage to multi-MW SOFC systems (e.g.: electrical generation plants). For smaller SOFC stacks (3-5 kW), ionic conductive materials are required that can operate in intermediate temperature (IT) range i.e. $400\text{-}700^{\circ}\text{C}$ without compromising the internal resistance of the cell. Studies of new electrolytes led to the

discovery of other materials e.g., δ - Bi_2O_3 and doped CeO_2 . A summary of the ionic conductivity of different fluorite structured oxides is shown in Figure 1-2. It can be seen that δ - Bi_2O_3 and yttria-stabilized Bi_2O_3 exhibit the highest ionic conductivity among all oxygen ion conducting materials in IT range. The exceptional conductivity is due to the unique intrinsic defect fluorite structure of this material. Because of the stoichiometry of the material, 25% of the oxygen sites are vacant. Therefore, there are an excess number of equipotential sites implying a random distribution of oxygen ions at high temperatures. This results in high oxygen ion mobility. However, Bi_2O_3 based materials possess a number of disadvantages, including thermodynamic instability in reducing atmospheres, volatilization of Bi_2O_3 at moderate temperatures, a high corrosive activity and low mechanical strength.^{40,41} Hence, the applicability of these oxides in electrochemical cell is considerably limited. In the last few decades, ceria based electrolytes have attracted much attention as an alternative of YSZ in SOFCs. As shown in Figure 1-2, the ionic conductivity of gadolinium doped ceria is about one order of magnitude higher than that of YSZ. In addition, they exhibit good thermal stability which makes them superior to yttria-stabilized Bi_2O_3 .

2.4.1 Ceria Based Materials

In recent years ceria-based materials have attracted considerable attention especially in the application like solid oxide electrolytes and environmental catalysis.^{9,42} In the automotive industry, ceria is used in catalytic converter inside the engine.⁴³ It acts as a buffer, absorbing or releasing oxygen, depending on the condition of the engine. It can effectively reduce harmful emissions like NO_x to pure nitrogen and convert harmful carbon monoxide to the less harmful carbon dioxide.^{44,45} Further, it exhibits high absorption for ultraviolet rays and it is transparent to visible light which

makes it a prospective material to replace ZnO and TiO₂ in sunscreen applications.⁴⁶ In the present work, doped ceria materials in the role of solid electrolytes for the intermediate temperature SOFCs will be discussed in detail.

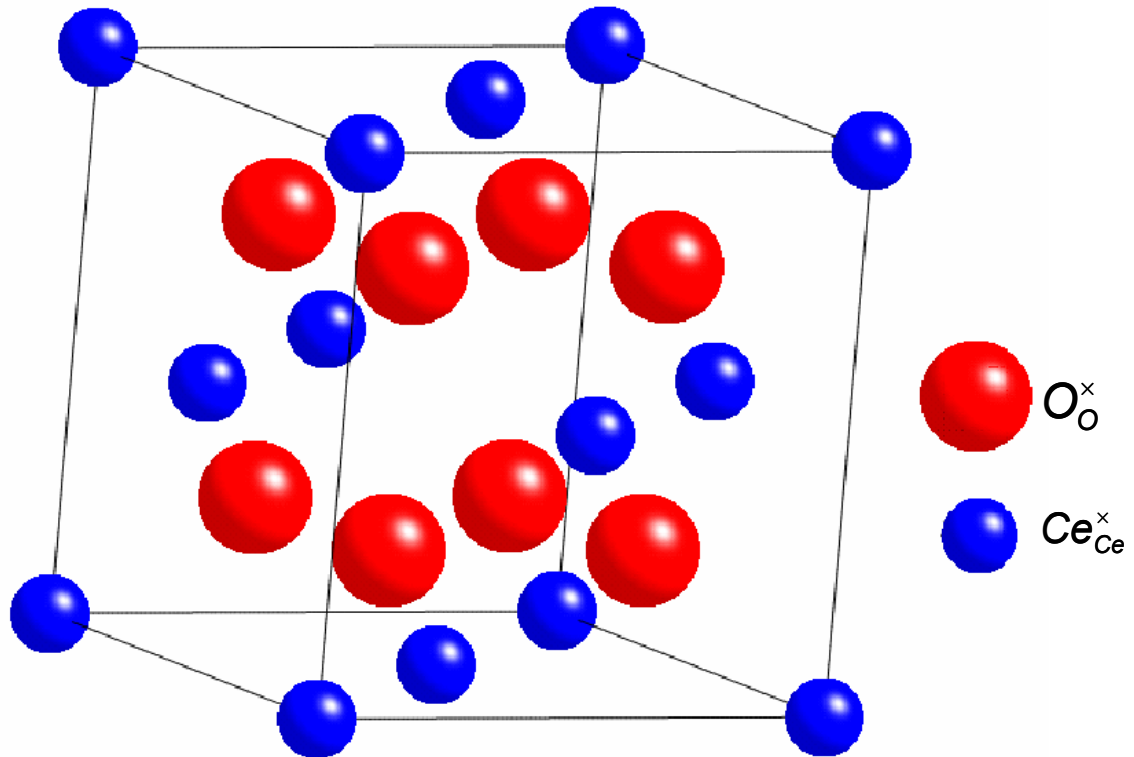


Figure 2-1. Cubic fluorite structure of ceria.

Pure stoichiometric ceria possesses the cubic fluorite structure which is stable from room temperature to the melting point. Figure 2-1 shows the cubic fluorite structure of ceria where Ce⁴⁺ and O²⁻ ions are located at 4a and 8c Wyckoff positions, respectively. The space group associated with this structure is Fm $\bar{3}m$ and the number of molecules of CeO₂ present in the unit cell is four ($Z = 4$). The standard lattice parameter of pure ceria at room temperature is 5.4114 Å.⁴⁷ According to the radius ratio scheme proposed by Pauling, coordination number is related to cation-anion radius

ratio (r_c/r_a). For the cation positioned at the center of the anion cube, r_c/r_a value should be higher than 0.732.²⁴ In stoichiometric ceria, the Ce^{4+} cation establishes eight-fold coordination with O^{2-} anions, while the O^{2-} resides in the tetrahedral position. However, the theoretical r_c/r_a ratio in ceria is 0.702.⁴⁸ This value is below the critical r_c/r_a which is a prerequisite for eight fold coordination. Thus, CeO_2 does not follow radius ratio scheme which is well suited for other known structures.

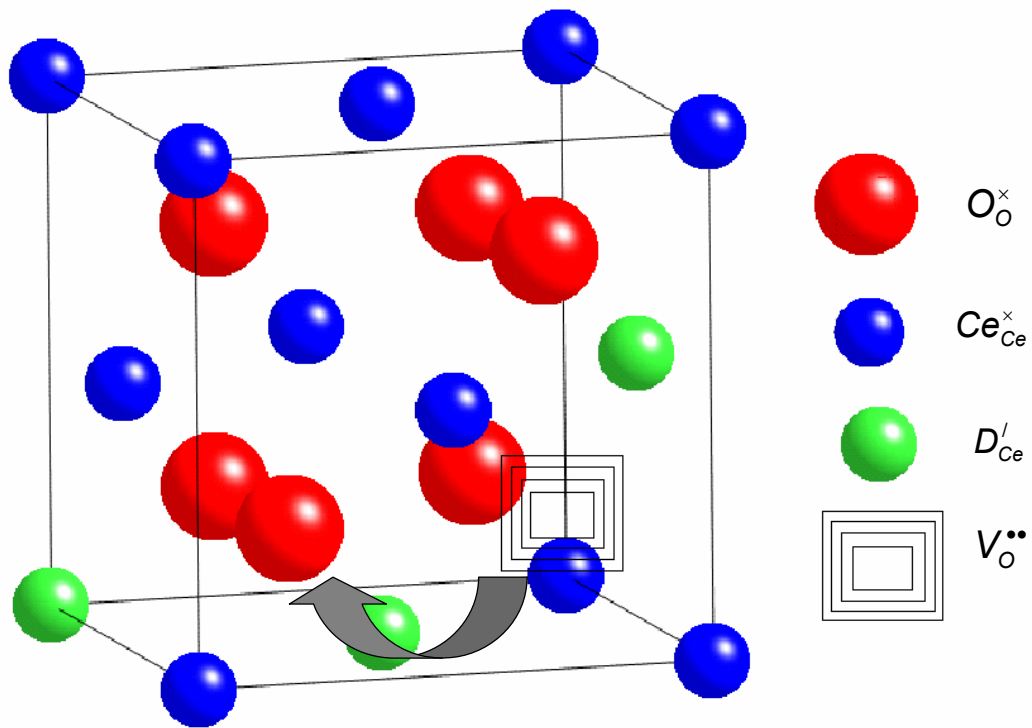
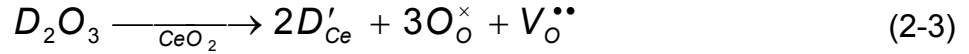


Figure 2-2. Oxygen vacancy jump in doped ceria system.

Ionic conduction in oxide fluorites takes place via an oxygen vacancy diffusion mechanism. At high oxygen partial pressures, cubic fluorite structure of undoped ceria do not possess any oxygen vacancies. Thus, pure ceria is not a good ionic conductor. These oxygen vacancies are incorporated into the ceria structure during the substitution

of Ce^{4+} by an acceptor dopant cation in the lattice, which can be represented by the following defect equation using Kröger-Vink notation.



Most of the oxygen ions tend to vibrate in the region of their tetrahedral sites and migrate from one regular tetrahedral site to the other. This migration process is called discrete hopping. Normally, oxygen ions will not occupy the octahedral sites of Ce^{4+} ions in the face centered cubic lattice since these are the interstitial sites.

Figure 2-2 shows the diffusion of oxygen vacancy from one tetrahedral site to another in doped ceria.

2.4.2 Ionic Conductivity

Ionic conductivity (σ_i) in the case of a pure oxygen ion conductor is given by,

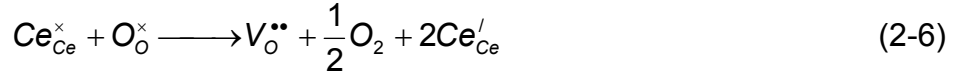
$$\sigma_i = [V_O^{\bullet\bullet}] N_o q_i \mu_i \quad (2-4)$$

where N_o is the number of oxygen sites per unit volume, $[V_O^{\bullet\bullet}]$ is the mole fraction of mobile oxygen vacancy present in the oxygen sublattice, and q_i and μ_i are the charge and mobility of oxygen ion, respectively. When electrons or electron holes are localized on ions in the lattice, as in CeO_{2-x} or $Fe_{1-x}O$, the semiconductivity arises from electrons or electron holes moving from one ion to another, which is called hopping-type semiconductivity.²³ Thus, the total conductivity (σ_t) of a solid is the sum of the contributions due to ions (σ_i), electron (σ_e), and hole (σ_h) as follows,

$$\sigma_t = \sigma_i + \sigma_e + \sigma_h \quad (2-5)$$

The electron and hole conductivities of the solid oxide electrolyte must be kept as low as possible to prevent losses from leakage currents. In order to force the electrons liberated from the fuel into the external circuit, where they can do useful work, there

must be a huge resistance to prevent them from going through the electrolyte. At high temperatures (>1000°C) and under reducing atmospheres, ceria shows a tendency to transform from Ce(IV) to Ce(III).



This results in the increase in the n-type conductivity which promotes the formation of electron hopping paths inside the electrolyte material and deteriorates the overall performance of the cell. The ionic conductivity contribution to the total conductivity can be described in terms of the ionic transference number t_i which is defined as,

$$t_{ion} = \frac{\sigma_{ion}}{\sigma_{ion} + \sigma_{elec}} \quad (2-7)$$

As mentioned earlier, one of the main requirements for a good electrolyte is a high ionic transference number especially in extreme conditions. Lower ionic transference not only degrades the associated cell efficiency but also expands the materials (due to the formation of additional oxygen vacancies) both of which have a deleterious effect on the mechanical properties.⁴⁹ The yttria stabilized zirconia, is pure ionic conductor at high temperatures (1000°C) and oxygen partial pressure (< 10⁻²² atmosphere) with an ionic transference number of 1.

2.4.2.1 Temperature dependence

Ionic conduction in the oxygen ion conductors is a thermally activated process. The temperature dependence of electrical conductivity of doped fluorite oxides can be expressed as,

$$\sigma T = \sigma_0 \exp\left(-\frac{E_A}{kT}\right) \quad (2-8)$$

where σ_0 is a pre-exponential constant, T is the absolute temperature, and E_A is the activation energy for electrical conduction. Equation (2-9) is a detailed form of an Arrhenius relationship.

$$\sigma T = \frac{q_v^2}{k} [V_{O^{**}}] N_o a^2 v_o \exp\left(\frac{\Delta S_m}{k}\right) \exp\left(-\frac{\Delta H_m}{kT}\right) \quad (2-9)$$

Here N_o is the number of oxygen sites per unit volume, $[V_{O^{**}}]$ is the fraction of free mobile oxygen vacancy present in the oxygen sublattice, q_v is the charge oxygen vacancy, a is the ion jump distance, v_o is an appropriate lattice vibration, and ΔS_m and ΔH_m is the entropy and the enthalpy change during oxygen ion diffusion, respectively. For a complete derivation of this equation, refer to Appendix B. Equation (2-9) provides the clear view of the relationship between the conductivity and temperature. It is important to note that $[V_{O^{**}}]$ in equation (2-9) is the concentration of free mobile oxygen vacancies. In a distorted cubic structure of doped ceria system, oxygen vacancies tend to interact with acceptor dopant cations. These interactions result in the localization of oxygen vacancies near the dopant cations. The association of point defects will be discussed in more detail in a later section of this chapter. With the increase in thermal energy (temperature), the localized oxygen vacancies try to free themselves from dopant cations which results in the increase of mobile oxygen vacancy concentration. Thus, the pre-exponential constant (σ_0) in equation (2-9) depends upon the concentration of free oxygen vacancies which itself is a complex function of temperature. Hence, the ionic conductivity of doped fluorite oxides cannot be expressed by a single exponential equation.

2.4.2.2 Oxygen partial pressure dependence

The rate of electrochemical reaction depends upon the driving force for the process to occur.²⁴ The driving force is a measure of how far the system is from the equilibrium state. In the case of SOFCs, the driving force is the oxygen partial pressure difference between the cathode and anode sides. The higher the partial pressure difference, the larger the power density that can be obtained from the cell. Thus, extreme opposite condition in both electrodes (i.e., high reducing atmosphere in anode side and high oxidizing condition in cathode side) is necessary to obtain reasonable power from the single cell. Normal atmospheric pressure of air is usually maintained in the cathode side of SOFC. Oxide ceramics are usually stable in such conditions but problem can arise at low oxygen partial pressure. Doped ceria tends to partially reduce from Ce(IV) to Ce(III) in the reducing condition ($< 10^{-15}$ atmospheres) at the anode side of the cell. For a material to be use as an electrolyte in SOFCs, it must have a high ionic transference number. The ionic transference number starts decreasing under reducing atmosphere and generates conduction electrons by the following defect reaction,



Applying the law of mass action to the above reaction, the electron concentration at equilibrium can be written as,

$$n = \frac{K(T)^{1/2}}{[\text{V}_\text{O}^{\bullet\bullet}]^{1/2} p\text{O}_2^{1/4}} \quad (2-11)$$

where $K(T)$ is a equilibrium constant which depends solely on the temperature. The $[\text{V}_\text{O}^{\bullet\bullet}]$ can be assumed to be unchanged due to the reduction of doped ceria in which a

large number of oxygen vacancies is already generated via doping. Thus, the ionic conductivity is independent of oxygen partial pressure and the equation can be written as,

$$n = \frac{K(T)^{1/2}}{pO_2^{1/4}} \quad (2-12)$$

The ionic transference number (t_{O_2}) which is described as,

$$t_{O_2} = \frac{\sigma_i}{\sigma_i + \sigma_e} = \frac{1}{1 + \left(\frac{\sigma_e}{\sigma_i}\right)} \quad (2-13)$$

As conductivity primarily depends upon the concentration of charge carrier, t_{O_2} can be written as,

$$t_{O_2} = \left[1 + \left(\frac{P_{O_2}}{P_{O_2}^*} \right)^{-1/4} \right]^{-1} \quad (2-14)$$

where $P_{O_2}^*$ is the parameter associated with $K(T)$. From equation (2-14), it can be seen that $P_{O_2}^*$ at a given temperature corresponds to the oxygen partial pressure at which t_{O_2} equals to 0.5.

Table 2-2. $P_{O_2}^*$ of doped ceria systems.⁵⁰

Composition	$P_{O_2}^*$ (atmosphere)			
	500°C	700°C	850°C	1000°C
$Ce_{0.9}Ca_{0.1}O_{1.9}$	10^{-20}	10^{-13}	10^{-9}	-
$Ce_{0.905}Ca_{0.095}O_{1.95}$	10^{-26}	10^{-17}	10^{-13}	10^{-10}
$Ce_{0.9}Gd_{0.1}O_{1.95}$	-	1.2×10^{-19}	1.7×10^{-15}	-
$Ce_{0.5}Gd_{0.5}O_{1.75}$	-	1.5×10^{-16}	6.5×10^{-14}	-

Table 2-2 shows the value of $P_{O_2}^*$ for ceria based solid solutions at different temperatures. At 700°C, $Gd_{0.10}Ce_{0.90}O_{1.95}$ shows the $P_{O_2}^*$ value of 10^{-19} atmospheres. With the increase in temperature, this value increases to 10^{-15} atmospheres. Thus, it is essential to develop electrolytes which not only contain higher dopant concentration, but also exhibit higher ionic conductivity, so that they can operate in the lower IT range.

2.4.2.3 Dopant concentration dependence

The effect of dopant concentration on ionic conductivity is illustrated in Figure 2-3, where total ionic conductivities of doped zirconia systems are plotted as a function of dopant content.⁵¹

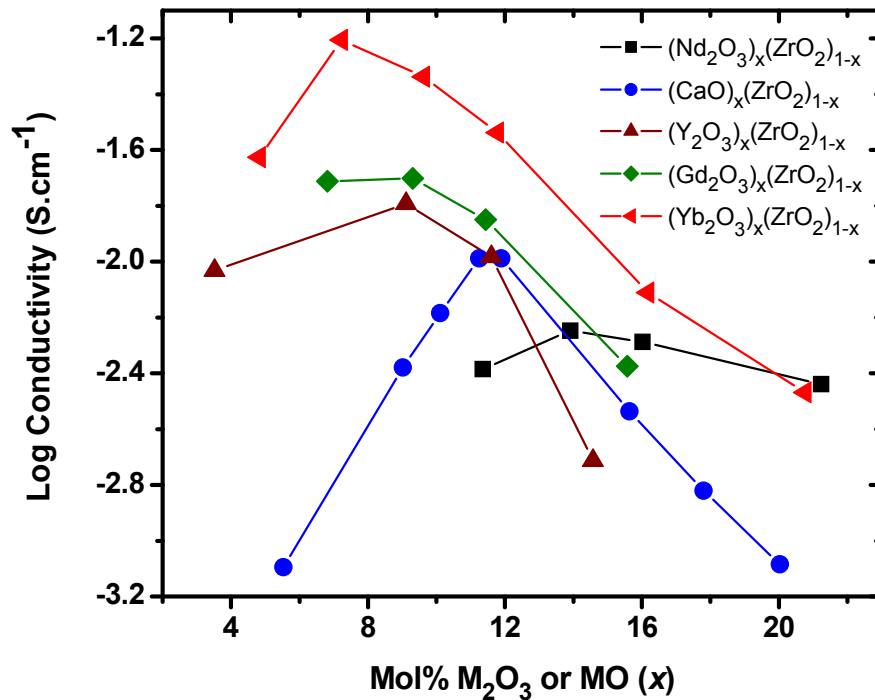


Figure 2-3. Ionic conductivity as a function of dopant concentration in doped zirconia systems.⁵¹

In the dilute regime, the ionic conductivity as a function of dopant cation is consistent with the Arrhenius relationship in equation (2-9). It increases with the

increase in the number of charge carriers i.e., oxygen vacancies. However, it is experimentally observed that the ionic conductivity reaches a maximum at certain dopant concentration, and then decreases. This is the general behavior observed in all the other fluorite oxide systems. Further, the observed peak positions are not the same for different dopant cations. It has been argued that the observed decrease in conductivity is associated with dopant cation and oxygen vacancy interactions; this will be discussed in the subsequent section.^{9,52}

2.5 Association of Defects

Whenever charged defects (D'_A) are incorporated into the crystal structure, there must be defects with opposite charges to preserve charge neutrality. These defects are prone to strongly associate with each other due to electrostatic attraction between the oppositely charged defects. Also, there is a possibility for elastic interaction to relieve the local stresses associated with both defects.⁵² The end result is the formation of local defect structures such as $(D'_A - V_O^{\bullet\bullet} - D'_A)$ and $(D'_A - V_O^{\bullet\bullet})^*$, which effectively reduces the number of mobile oxygen ions, thus leading to a substantial drop in the ionic conductivity of the electrolyte at higher dopant content (as shown in Figure 2-3).

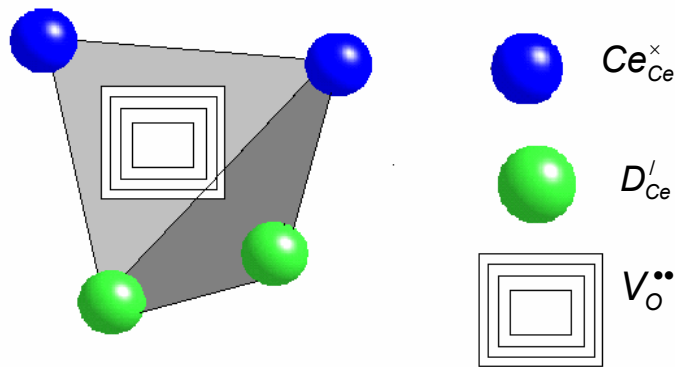


Figure 2-4. Oxygen vacancy trapped in the tetrahedral site.

Figure 2-4 shows the situation in which an oxygen vacancy is trapped in a tetrahedral site which is surrounded by oppositely charged dopant cations and neutral host cations. The binding energy between these defects is mainly due to the coulombic attraction of the defects caused by the effective charges in the lattice. However, it also includes terms due to the relaxation of the lattice around the defect which depend on the effective charge, polarizability and ionic radius of the dopant cation. Thus, in the lower intermediate temperature range, total activation energy (ΔH) is the sum of migration enthalpy (ΔH_m) and association enthalpy (ΔH_a).^{9,53} With the increase in temperature, the thermal vibrations of the local defect structures become more important. The stage comes when the thermal energy overcomes the binding energy of these local defect structures and most of the oxygen vacancies are set free to diffuse from one site to another. Above this temperature, oxygen vacancies require only ΔH_m to cross the energy barrier.

2.6 Impedance Spectroscopy

Alternating current (ac) electrochemical impedance spectroscopy (EIS) is a valuable technique for the characterization of various electrochemical processes.^{54,55} EIS has increased the understanding of the limiting processes for different materials as well as effects of processing and microstructure of materials in tests applying electrode pellets, and other electrochemical devices. It measures voltage (or current) as a current (or voltage) is applied on the test sample over a wide range of frequencies. Impedance at a given frequency (ω) is determined using Ohm's law i.e., the ratio between ac voltage and ac current. Since the output impedance is a complex number, therefore at any given frequency, it contains real (Z') and imaginary (Z'') components. The complex impedance data is typically represented as a "Nyquist" plot, where the real impedance

and negative imaginary impedance is plotted in the x and y coordinates, respectively. The sign convention for the imaginary impedance is typically used in the plot as the capacitive behavior often dominates the processes in ceramic materials. With the choice of sign convention, most of the processes of interest for SOFCs occur in the first quadrant of the complex impedance plot. The frequency range examined is typically from 0.01 to 10^7 Hz. The upper limit on the test frequency is determined by the limitation of the instrument, while the lower limit is usually determined by the time it takes for data acquisition. However, these limitations are of not much concern as the most of the phenomenon lie in the measurable frequency range. The response of the cell is usually modeled in terms of equivalent circuits, i.e., a group of electrical circuit elements (resistors, capacitors, inductors) that are connected in a way that would give the same impedance response as the cell.

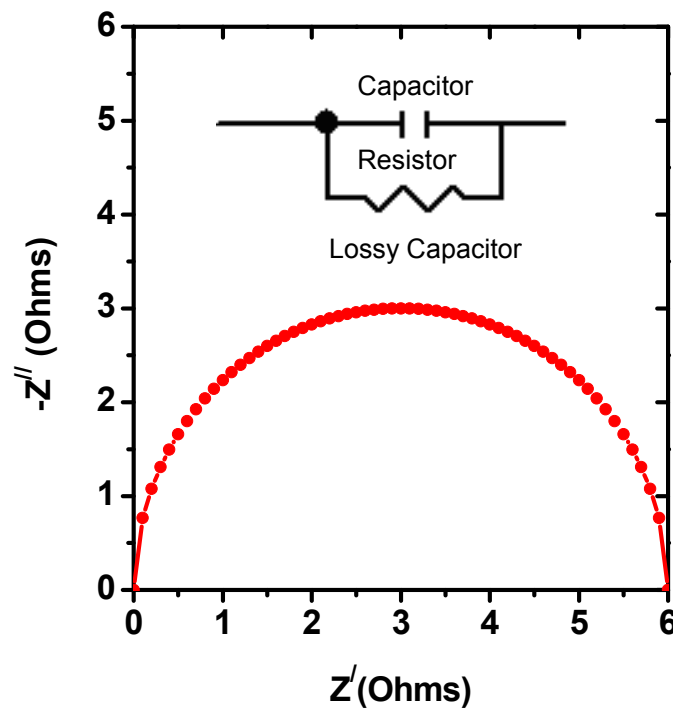


Figure 2-5. Typical impedance response for a given relaxation process. A parallel resistor-capacitor element is also shown which represents a “lossy capacitor”.

One of the main advantages of using EIS is that it assists in identifying the relaxation time associated with the processes occurring at the atomic and microstructural level. Each distinct process has its own real and imaginary impedances, with a characteristic relaxation frequency. A typical impedance response for a given relaxation process, and its equivalent circuit is shown in Figure 2-5. A parallel RC element represents a “lossy capacitor” with a typical relaxation time which corresponds to the process. Such behavior could be characteristic, for example, of a double-layer capacitance (due to charge separation between electrode and electrolyte) in parallel with a resistance to charge transfer or a polarization resistance. Thus a semi-circle in a complex impedance plot is a representation of a relaxation process with a distinct “time constant”. The peak of the semicircle will occur at the characteristic frequency, ω_0 .

The Nyquist plot of the electrochemical cell may contain more than one semi-circle, which is indicative of various relaxation processes occurring in the cell. Often the time constant for two processes lie very close to each other. In this case, semi-circles must be de-convoluted in order to determine each individual contribution. A typical complex impedance response of an electroded polycrystalline ceramic is shown in Figure 2-6. In the figure, three main features can be observed: incomplete depressed arc at high frequency and two distinct arcs at low frequency. The high frequency arc was identified as the grain polarization while the remaining two arcs at low frequencies correspond to grain boundary and electrode polarization processes. In the ideal case, the center of the semi-circle should lie on the x-axis. However, it is usually the case, that the center of the semi-circle is depressed below the x-axis. The equivalent circuit for such response is similar to that shown in Figure 2-5; however, in place of capacitor a

constant phase element (CPE) is required to model the experimental data. A constant phase element is equivalent to a distribution of capacitors in parallel whose phase angle is somewhat less than 90° . Further, a depressed semi-circle in the complex impedance plot has been described in several ways. For example, the depressed semicircle in the intra-grain polarization can be attributed to the microstructural inhomogeneities within the sample. In addition, the depressed electrode polarization semi-circle in solid electrode is explained by the surface roughness of the electrode.

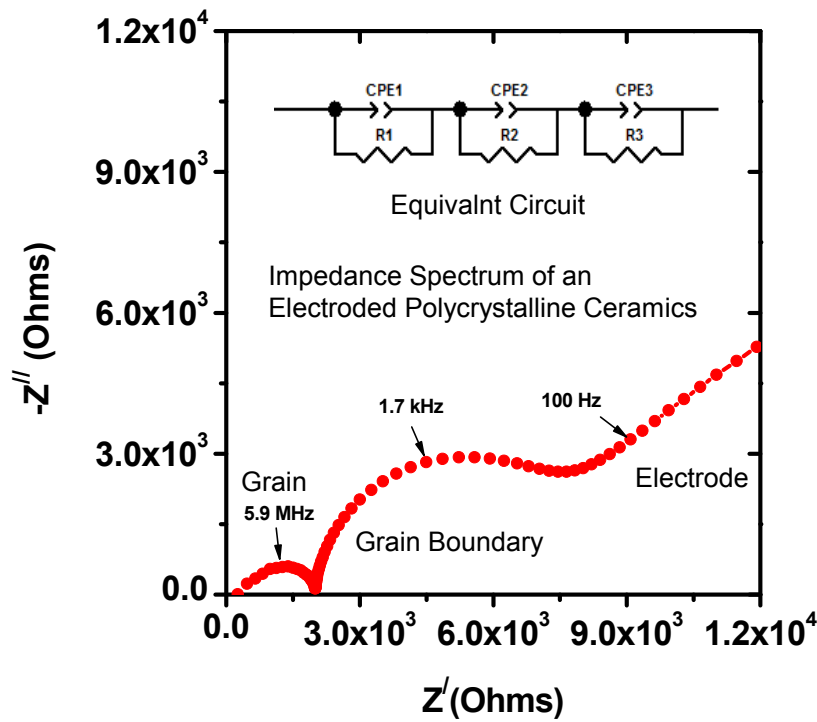


Figure 2-6. Typical impedance spectrum of an electroded polycrystalline ceramic material. The equivalent circuit to fit the spectrum is also shown. CPE and R in the equivalent circuit stands for constant phase element and resistor, respectively.

It is important to note that in the present work, the main focus is to determine the grain ionic conductivity rather than the total ionic conductivity. Thus, the grain ionic resistance was calculated by fitting the observed impedance spectra with the analog

circuit having three parallel pair of resistor-constant phase element in series. The presence of the inductive effect of the experimental setup severely affects the high frequency datasets at high temperatures. To counter this effect, external inductor was also used in the equivalent circuit, while fitting the data. The grain ionic conductivity was calculated using the following relationship,

$$\sigma_{grain} = \frac{1}{R_g} \frac{L}{A} \quad (2-15)$$

where R_g is the grain ionic resistance, L and A are the length and area of the cross-section of the sample, respectively.

CHAPTER 3 MATERIALS AND EXPERIMENTAL PROCEDURES

3.1 Materials Selection

Higher ionically conductive materials are critical for the realization of intermediate temperature range SOFCs. In recent years, doped ceria electrolytes have opened up the possibility for such intermediate temperatures SOFCs, due to their higher ionic conductivity and good thermodynamic stability. Ionic conductivity in doped ceria systems depends upon various factors such as dopant charge valence, dopant ionic radius, dopant concentration, temperature, and oxygen partial pressure. Keeping the last two parameters constant, ionic conductivity primarily depends upon the type of dopants. According to Yahiro et al, the higher the charge valence of the acceptor dopant cation the better is the ionic conductivity.^{56,57} Thus, trivalent doped ceria systems show higher ionic conductivity compared to divalent doped ceria systems. This can be attributed to the lower electrostatic interaction involved in the case of trivalent doped system, between oxygen vacancies and dopant cation sites. These interactions hinder the flow of oxygen vacancies and lower the free oxygen vacancy concentration.⁵² Thus, in order to design higher conductive materials, different trivalent acceptor dopant cations were selected for host ceria.

3.2 Experimental Procedures

In this section, the details of the experimental procedures that were used to synthesize phase pure powders and ceramic samples for different characterizations will be discussed. Figure 3-1 shows the block diagram of the typical powder synthesis, and different ceramic sample characterization techniques.

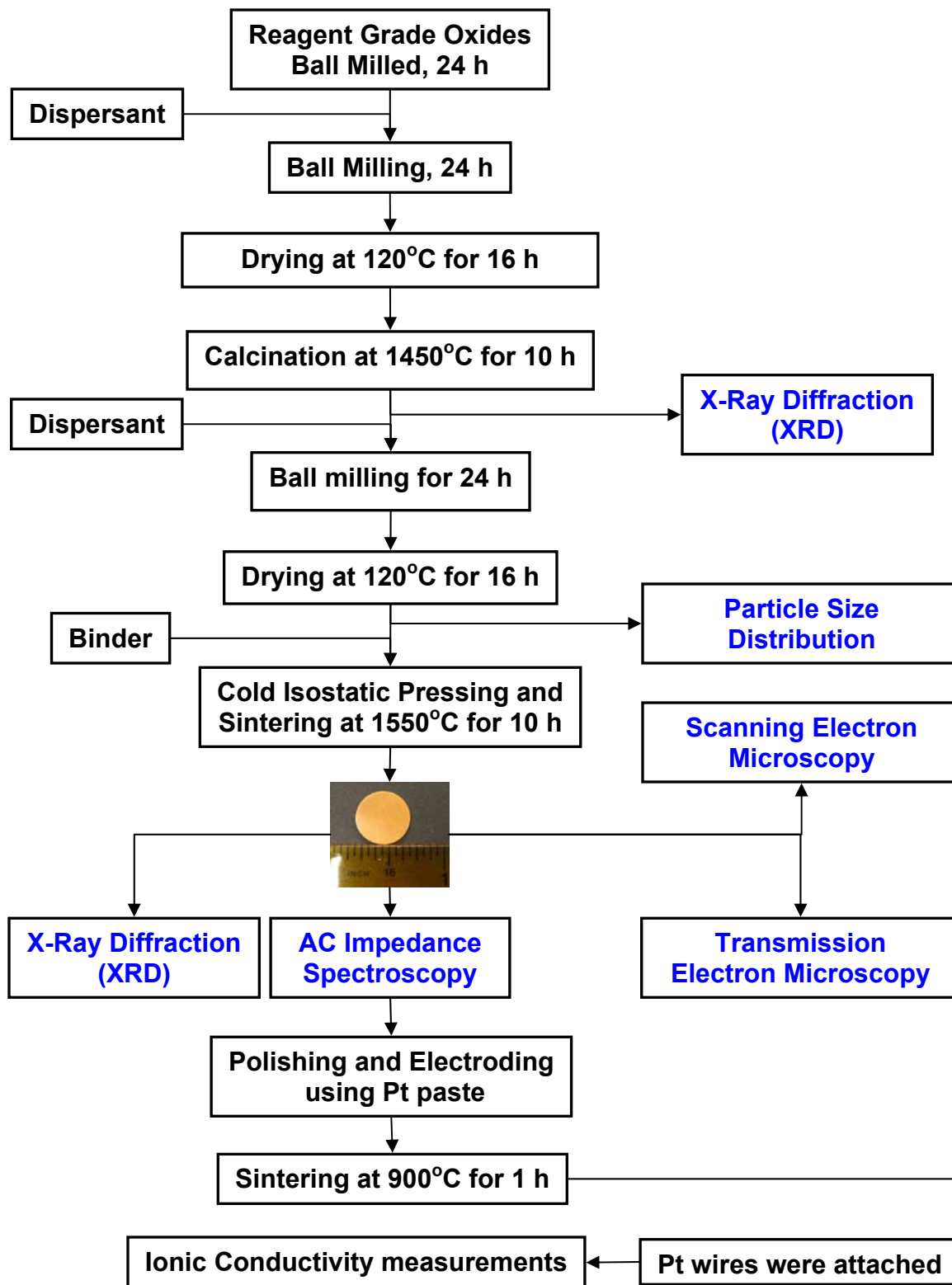


Figure 3-1. Flow chart for the powder synthesis using conventional solid state reaction and different characterization techniques.

3.2.1 Powder Processing

Different processing routes were used to synthesize phase pure doped ceria powders. Conventional solid oxide route was primarily used to synthesize powder in bulk amount. However, the particle size achieved using this technique was usually large compare to other wet chemical routes.⁵⁸ Large particle size results in lowering the surface reactivity of the powder which in turn lowers the sintering kinetics of the material.⁵⁹ Thus, high sintering temperature and time are required for such green ceramic bodies to obtain high theoretical density. Even though high sintering temperature and time increases the diffusion kinetics for sintering process, they are usually avoided for several reasons. Such high sintering temperatures may lead to unwanted interfacial reactions during co-sintering of electrolyte and cathode or anode layers. In addition, very high-temperature sintering can produce micro-cracks; e.g. due to oxygen liberation as a result of reduction of CeO_2 to Ce_2O_3 .⁶⁰ The interest in low temperature sintering is also driven by the need to reduce material processing costs. Furthermore, it has been shown that there is a detrimental effect of sintering at high temperatures on the ionic conductivity.^{61,62} This will be discussed in detail in Chapter 6.

In the present work, all the doped ceria materials were synthesized using conventional solid state sintering under same experimental conditions. These materials were further processed for electrical characterization at high temperatures. Among all the doped ceria systems, the material which shows the highest conductivity was then synthesized using wet chemical route (i.e., co-precipitation technique). Using this process, high purity, homogenous and ultrafine powder can be obtained by calcining at temperatures lower than 1000°C .^{58,63,64}

3.2.1.1 Conventional solid state route

Phase pure powders of $D_x\text{Ce}_{1-x}\text{O}_{2-\delta}$ (where D = trivalent dopant cation, x = dopant content) were synthesized by conventional solid state reaction method, starting from stoichiometric mixtures of $D_2\text{O}_3$ and CeO_2 powders (all with 99.99% purity from Alfa Aesar). Loss on ignition was determined for all the starting powders. Accordingly, the stoichiometric amount of powders were weighed and mixed with de-ionized water and 1 wt% dispersant (Ammonium Polyacrylate) to form 60 vol% solids slurry. The role of dispersant is to keep the dispersed ceramic particles in suspension in the water. Mixing was performed using wet ball milling for 24 h. One of the main disadvantages of using ball milling is that the wear of the grinding media can be fairly high. For ceramic materials used for electrolyte application, the presence of unwanted impurities in the powder is a serious problem. To avoid this, chemically inert and highly pure yttria stabilized zirconia media with 3 and 10 mm diameter spheres were used. The ball milled ceramic slurries were then dried in the oven at 120°C for 16 h. The agglomerated powders were ground using mortar and pestle to fine particles which were subsequently separated out using sieve with the aperture opening of $212\ \mu\text{m}$.

After obtaining the homogeneous mixture of raw oxides, powders were then treated to high temperature for solid state reaction. The calcination temperature and time were optimized for different doped ceria systems. The dissolution of the dopant cations inside the host lattice depends upon its solubility limit at a particular temperature. The width of the solubility increases with the decrease in the ionic radius difference between the host and dopant cations. The maximum solubility exist when the difference between the ionic radii become minimum.⁶⁵ For example, for $\text{Lu}_{0.10}\text{Ce}_{0.90}\text{O}_{2-\delta}$ the calcination temperature and time were optimized to be 1350°C for 10 h.

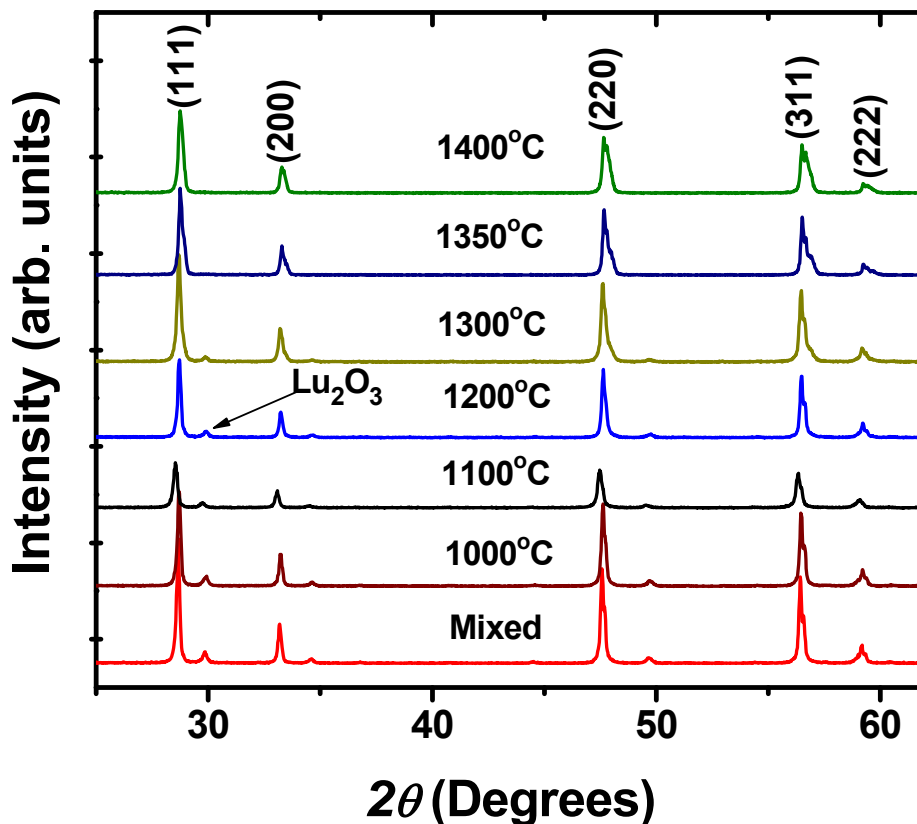


Figure 3-2. XRD patterns of $\text{Lu}_{0.10}\text{Ce}_{0.90}\text{O}_{2-\delta}$ calcined at different temperatures for 10 h.

To verify the complete dissolution of dopants in ceria, phase analysis was performed using X-ray diffraction (XRD). Curved position-sensitive (CPS) diffractometer (INEL, France) was used to obtain the XRD pattern of each composition using $\text{Cu K}\alpha$ radiation. Figure 3-2 shows the XRD profiles of $\text{Lu}_{0.10}\text{Ce}_{0.90}\text{O}_{2-\delta}$ calcined at different temperatures for 10 h. It can be seen around 1350°C, there are no extra peaks of Lu_2O_3 present in the XRD pattern. As Lu^{3+} exhibits similar ionic radius as that of Ce^{4+} , thus it requires lower thermal energy to dissolve in host ceria lattice when compare to other dopant cations which show higher ionic radii ($r_{\text{Lu}}^{\text{VIII}} = 0.977 \text{ \AA}$, $r_{\text{Ce}}^{\text{VIII}} = 0.97 \text{ \AA}$).⁴⁸ In order to widen the solubility limit for other trivalent dopants cations, calcination was performed at 1450°C for 10 h. Figure 3-3 shows the XRD patterns of different doped ceria systems taken at room temperature in air. It can be seen that all the compositions

are phase pure with cubic fluorite structure. In the inset, (200) plane peak of all the compositions is shown. The peak position provides information about the lattice change (expansion or contraction) of the host ceria which will be discussed in Chapter 4 and Chapter 5.

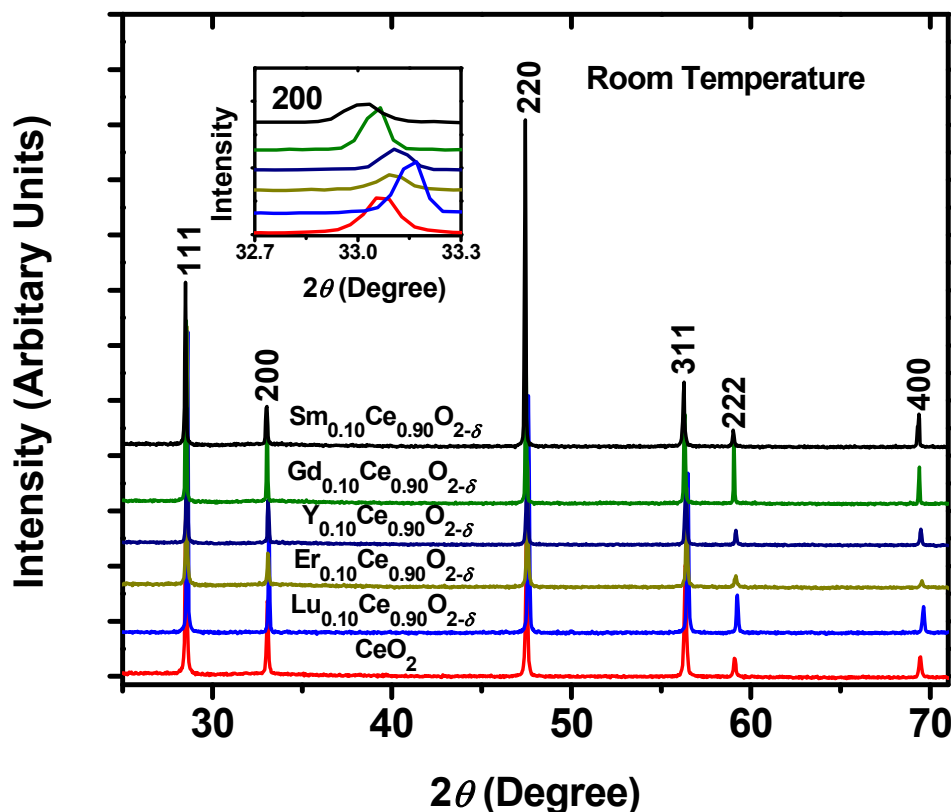


Figure 3-3. XRD patterns of different doped ceria systems calcined at 1450°C for 10 h.

After the calcination, agglomerated powders were again ball-milled for 24 h in de-ionized water, dispersant, forming a 60 vol % slurry. The ball-milled ceramic slurries were then dried in the oven at 120°C for 16 h. The agglomerated powders were ground using mortar and pestle to fine size particles, which were subsequently separated out using sieve with the aperture opening of 212 μm . The particle size distribution of these powders was measured using Beckman Coulter LS13320. Figure 3-4 shows the

number particle size distribution of co-doped ceria ceramic powder synthesized using the experimental procedure described earlier. In order to achieve high density ceramic, it is desired that the particle size should be less than 1 μm with particle size distribution to be narrow and monodisperse.⁵⁹ It can be seen that the most of the particles are less than 2 μm in size with the mean size of 0.84 μm . Further, the particle size distribution is also mono-disperse which is desired for good sintering in reasonable time.

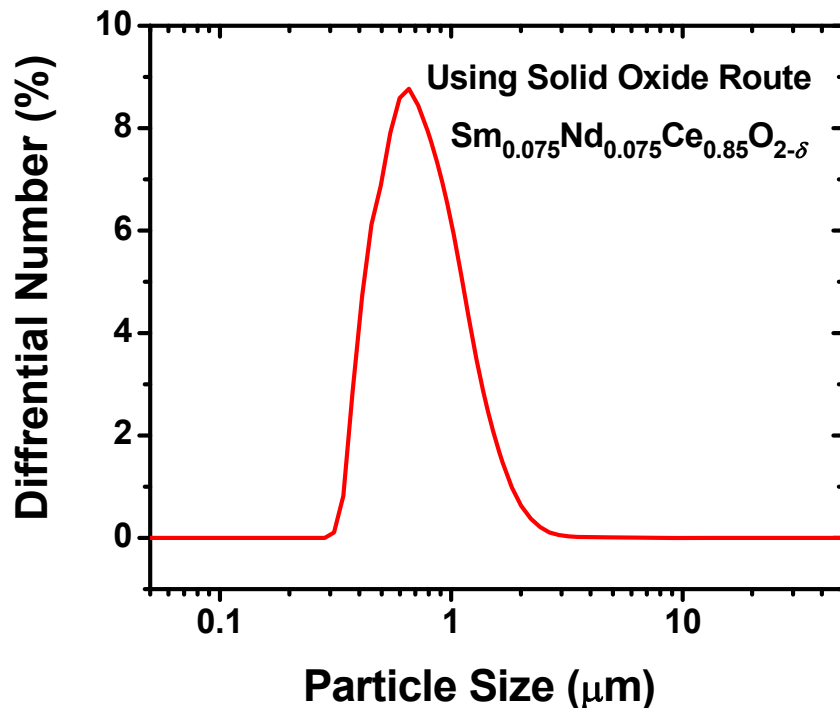


Figure 3-4. Particle size distribution of $\text{Sm}_{0.075}\text{Nd}_{0.075}\text{Ce}_{0.85}\text{O}_{2-\delta}$ synthesized using solid oxide route.

3.2.1.2 Co-precipitation route

The co-precipitation technique was used to synthesize phase pure powder of $\text{Sm}_{0.075}\text{Nd}_{0.075}\text{Ce}_{0.85}\text{O}_{2-\delta}$.⁵⁸ By doing so, the effect of processing on the electrical property of co-doped ceria was studied. One of the main objectives of using wet chemical route is to obtain fine particle size powder which as a result enhance the

sintering kinetic of the ceramic powder. Thus, high density pellets can be obtained using lower sintering temperature and time (especially when compared to conventional solid state route). Highly pure cerium nitrate ($\text{Ce}(\text{NO}_3)_3 \cdot 6\text{H}_2\text{O}$, Alfa Aesar, 99.99%), samarium nitrate ($\text{Sm}(\text{NO}_3)_3 \cdot 6\text{H}_2\text{O}$, Aldrich, 99.999%), and neodymium nitrate ($\text{Nd}(\text{NO}_3)_3 \cdot 6\text{H}_2\text{O}$ Alfa Aesar, 99.9%) were used as a starting raw materials. They were weighed in the stoichiometric proportions and dissolved in de-ionized water to produce aqueous solution. Excess ammonia solution (Acros Organics, 28-30 vol% of NH_3 solution in water) was added to the stirred solution to increase the pH to 12. The addition of ammonia solution results in the formation of yellowish brown color precipitate. The precipitate was filtered and then subsequently dried at 80°C for 12 h. The agglomerated powder was then ground to fine particles using mortar and pestle. The powder was then calcined at 900°C for 10 h in air. The CPS diffractometer was used to obtain the XRD pattern of $\text{Sm}_{0.075}\text{Nd}_{0.075}\text{Ce}_{0.85}\text{O}_{2-\delta}$ using $\text{Cu K}\alpha$ radiation. A monochromator crystal was used to separate out $\text{Cu K}\alpha_1$ from the incident X-ray beam. Peak positions in the XRD pattern were determined by fitting each individual peak with a symmetric Pearson VII profiles to model $\text{Cu K}\alpha_1$ using commercially available software (i.e., Solver add-in within Microsoft Excel spreadsheet package). Figure 3-5 shows the XRD profile of the calcined powder of $\text{Sm}_{0.075}\text{Nd}_{0.075}\text{Ce}_{0.85}\text{O}_{2-\delta}$ taken at room temperature. Powder looks phase pure with cubic fluorite structure. The best estimate of the lattice constant (a_o) was calculated using the least-squares extrapolation method.⁶⁶ The lattice parameter of $\text{Sm}_{0.075}\text{Nd}_{0.075}\text{Ce}_{0.85}\text{O}_{2-\delta}$ synthesized using co-precipitation technique was $5.4299 \pm 0.0013 \text{ \AA}$. The estimated lattice parameter value is close to the value (5.4314 \AA) obtained from the empirical relationship given by Kim.²²

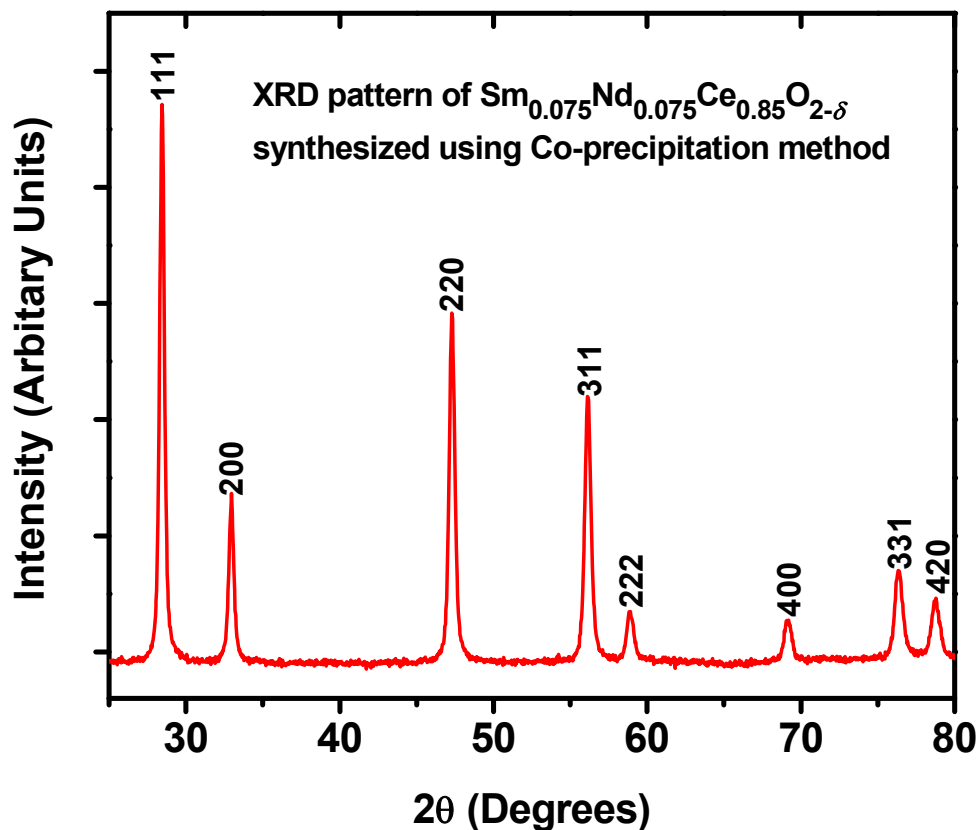


Figure 3-5. XRD pattern of $\text{Sm}_{0.075}\text{Nd}_{0.075}\text{Ce}_{0.85}\text{O}_{2-\delta}$ synthesized using co-precipitation technique.

After the calcination, agglomerated powder was ground using mortar and pestle to fine size particles which were then separated using sieve with the aperture opening of 212 μm . The particle size distribution of the grounded powder was then measured and is shown in Figure 3-6. It can be seen that the particle size of the powder synthesized using co-precipitation is lower than that in solid state method. The most of the particles are less than 0.2 μm in size with the mean size of 0.095 μm . Similar to the conventional solid state route, the particle size distribution obtained using this technique is somewhat narrow and mono-disperse which is desirable for good sinterability.

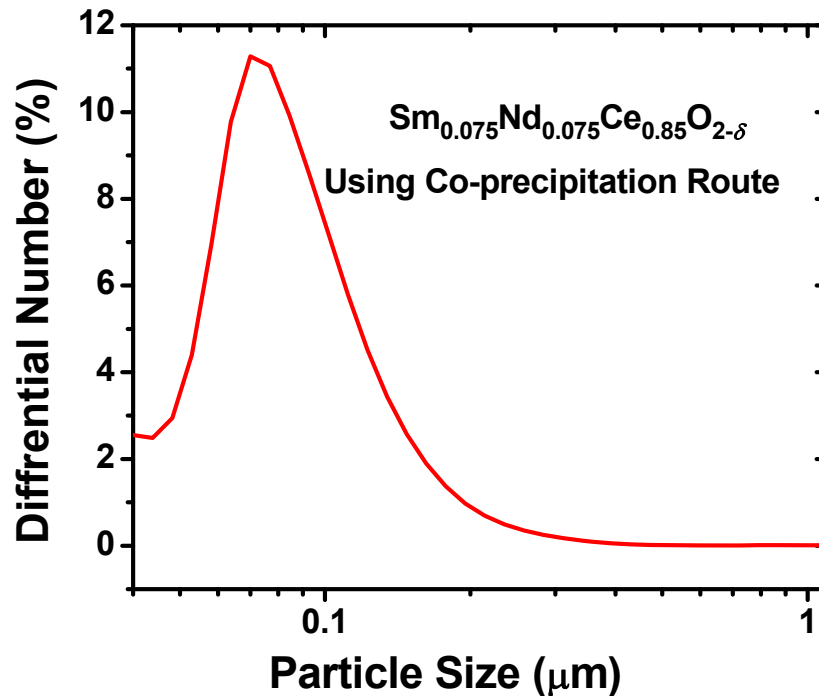


Figure 3-6. Particle size distribution of $\text{Sm}_{0.075}\text{Nd}_{0.075}\text{Ce}_{0.85}\text{O}_{2-\delta}$ synthesized using co-precipitation technique.

3.2.2 Forming

After synthesizing the phase pure powders from conventional solid oxide route and/or co-precipitation techniques, the next step was to fabricate a green ceramic body. Approximately 2 wt% of polyvinyl alcohol (PVA) binder was added into the powder to assist in forming. Powder was then mixed with the binder using a mortar and pestle. This was performed until the powder stopped sticking to the wall of the mortar. The agglomerates were separated from the powder using a sieve with the aperture opening of 212 μm. Powder consisting of fine size particles was then uniaxially pressed into disk-shaped pellets (8 mm in diameter and 4 mm thick) under a pressure of 180 MPa. This was followed by the isostatic pressing at 200 MPa for 3 minutes.

3.2.3 Solid State Sintering

Sintering is a process in which the ceramic green body is heat treated to a temperature (below the melting point) such that its particles adhere to each other to give a desired microstructure. Thus, the porous ceramic body when heated to the sintering temperature, it densify to the theoretical density of the material. This densification rate involves the transport of material which in turn depends upon key process parameters such as particle size, temperature, time and pressure. In this work, all the ceramic samples were sintered in air. Thus, the only parameters which were varied were temperature, time and particle size of the powder. Based on this, the effect of processing conditions on the electrical property of doped ceria is studied.

Although the high sintering temperature and time promotes solid state sintering, it has a detrimental effect on the ionic conductivity of doped ceria materials. Fabrication of highly dense ceramics at lower sintering temperatures and shorter times remains one of the challenges for the application of this material. Microwave sintering technique was used to fabricate dense ceramics of doped ceria at low temperature and time. The effect of microstructure on the ionic conductivity will be discussed in Chapter 6.

3.2.3.1 Conventional sintering

The green ceramic pellets obtained from the phase pure powders synthesized using solid oxide route were sintered in air at 1550°C for 10 h. The pellets pressed from the $\text{Sm}_{0.075}\text{Nd}_{0.075}\text{Ce}_{0.85}\text{O}_{2-\delta}$ powder synthesized using co-precipitation technique were sintered at 1350°C for 10 h. The ramp rate in these runs while heating and cooling was 200°C/hour. Binder burn out was performed at 400°C for 1 h. Densities of the ceramic samples sintered at 1550°C for 10 h were measured in water using Archimedes's principle and were estimated to be 98% of theoretical density or above. However, the

density of the sintered samples fabricated from powder synthesized using co-precipitation was around 93% of theoretical density.

3.2.3.2 Microwave sintering

The green ceramic pellets of $\text{Sm}_{0.075}\text{Nd}_{0.075}\text{Ce}_{0.85}\text{O}_{2-\delta}$ powder synthesized using co-precipitation technique were microwave sintered in a 2.45 GHz microwave furnace (Thermwave Mod III). Microwave furnace was operated at 1.3 kilowatts power output. The microwave sintering was performed at 1450°C for 1 h.

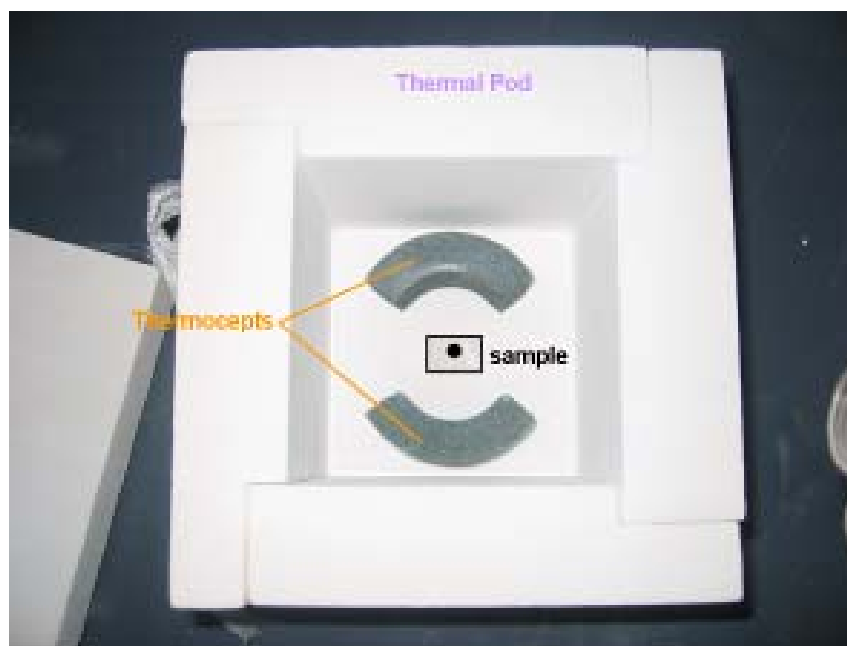


Figure 3-7. Sample placed in the thermal pod for microwave sintering.

Figure 3-7 shows the green ceramic pellet positioned in a zirconia sample holder inside the refractory insulation box or thermal pod. Silicon carbide thermocepts were used to boost the temperature rise of both microwave absorbing samples and non-absorbing or low absorbing materials. They can microwave heat materials through temperature zones where the material does not readily absorb microwave energy at 2.4 GHz. These thermocepts are arranged around the inside wall of the thermal pod. The

Archimedes density of the pellets fabricated from the microwave sintering was estimated to be around 94% of theoretical density.

3.2.4 Sample Preparation for Characterization

After fabricating the high density ceramic pellets, they were processed for different characterizations. In this section, sample fabrication for the different characterization techniques utilized will be discussed.

3.2.4.1 Ionic conductivity

The high temperature ionic conductivity measurements were performed on dense sintered ceramic samples of doped ceria materials. The sintered pellets were polished to obtain planar surfaces. Pt paste (CL11- 5349, Heraeus) was brushed onto both sides of the disk-shaped pellets to serve as the electrode. The pellets were then co-fired at 900°C for 1 h. Pt wires (99.9% pure) with diameter 0.127 mm were attached to the cell using Ag adhesive paste to perform ionic conductivity measurements.

3.2.4.2 X-ray diffraction

High temperature X-ray diffraction was performed on the doped ceria samples to understand the relationships between the crystal structure and ionic conductivity at higher temperatures. After the ionic conductivity measurements, samples were mechanically polished with SiC abrasive papers (of different grit sizes), and subsequently cleaned using sonicator. Pellets were then ground to fine particles using mortar and pestle. X-ray diffraction was performed on the sintered fine particles of doped ceria.

3.2.4.3 Scanning electron microscopy

The microstructural characterization was performed using scanning electron microscope (SEM). The sintered ceramic samples were mechanically polished to a

mirror finish using alumina dispersed polymer grinding discs of different grit size. After polishing, ceramic samples were cleaned using sonication for 30 min. This was followed by thermal etching process. The clean polished surface of ceramic samples was rapidly taken to the temperature 100°C below the respective sintering temperature. The heating ramp rate was 600°C/hour. Samples were kept at the respective temperatures for 1 h. After thermal etching, they were again cleaned using sonication for 30 minutes. They were then coated with carbon for SEM.

3.2.4.4 Transmission electron microscopy

The grain boundary study was performed through conventional TEM, using its various modes of analysis. In conventional TEM, these were mainly bright field (BF) and dark field (DF) imaging, selected area diffraction patterns (SADP), and energy dispersive X-ray analysis (EDX). These were performed on a JEOL JEM-2010 at 200 kV having an ultra thin Be window for EDX, attached with a Link Analyzer.

Sintered disks, 3 - mm in diameter of doped ceria were mechanically polished to a thickness of ~30 μm using Gatan's precision diamond discs of different grades. Using superglue, the ceramic sample was then mounted on the molybdenum TEM sample holder (with the shape of a ring). The sample placed on Mo sample holder was then thinned in the precision ion polishing system (PIPS) with argon ions at an accelerating voltage of 5 kV, which were incident at both surfaces at an angle of 4° to yield a reasonably thin specimen. After 4 to 10 h of ion milling (depending upon the sample thickness), a hole was seen in the centre of the ceramic sample. The samples were then coated with carbon, and were placed under the microscope for microstructural study.

3.2.5 Impedance Spectroscopy Experimental Setup

Ionic conductivity measurements were done using two point probe ac impedance spectroscopy technique. Figure 3-8 shows the electroded ceramic sample, quartz reactor, and impedance spectroscopy setup.

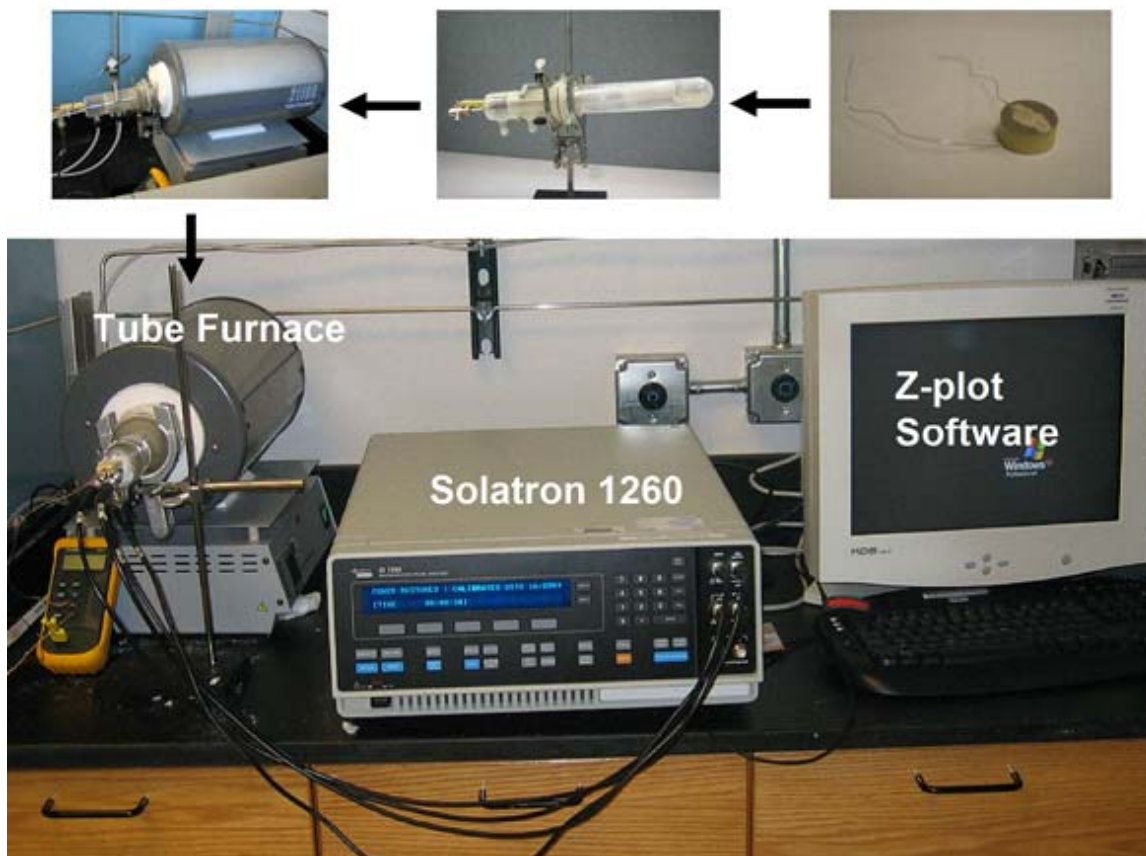


Figure 3-8. AC impedance spectroscopy experimental setup.

Processed ceramic sample was individually heated in a quartz reactor which was placed inside a small tube furnace. The quartz tube consisted of an inlet and outlet for gas flow, and gold wires running through alumina rods coated with platinum for shielding. The gold wires were connected to the Pt wires, which were attached to the Pt electrodes of the ceramic sample using Ag paste. At different temperatures, the complex impedance (Z) of the sample was measured using Solartron 1260 over the

frequency range of 0.10 Hz to 32 MHz. A 50 mV AC voltage was applied and the induced current was measured to produce the impedance spectra. Measurements were performed using 2-point connection to the Solartron. The Solartron 1260 is interfaced with the computer through Z-plot software. Data acquisition was done through Z-plot software. All the measurements were taken in air, in the temperature range of 250°C to 700°C.

CHAPTER 4
IONIC CONDUCTIVITY AND DOPING STRATEGIES FOR IONIC CONDUCTIVITY
ENHANCEMENT

4.1 Ionic Conductivity

Lowering the operating temperature range to intermediate temperatures (500–700 °C) can significantly reduce the cost and extend the SOFC application domain to portable power market sectors.⁶⁷ High ionic conductivity of oxide electrolytes is critical for the development of such SOFCs. Although yttria stabilized zirconia (YSZ) is considered to be the most reliable electrolyte in terms of structural and thermodynamic stability, its lower ionic conductivity in intermediate temperatures restricts SOFC usage to high temperatures (1000°C).^{7,67} In recent years, doped ceria electrolytes have opened up the possibility for such intermediate temperatures SOFCs due to their higher ionic conductivity and good thermodynamic stability.⁹ Among doped ceria electrolytes, $\text{Gd}_{0.10}\text{Ce}_{0.90}\text{O}_{2-\delta}$ is widely accepted to exhibit the highest ionic conductivity.¹³ In search of advanced ceramic materials that show higher ionic conductivity than $\text{Gd}_{0.10}\text{Ce}_{0.90}\text{O}_{2-\delta}$, it is important to investigate the effect of dopants and doping level on the ionic conductivity of the doped ceria materials. This involves investigation of local defect structures or complex defect associates (as mentioned in Chapter 2) for different doped ceria systems. In addition, thermodynamic properties such as activation energy for oxygen diffusion and entropy of the doped ceria system are also influenced by the dopant type and their concentration.^{68,69} Thus, it is essential to understand these relationships, and based on them rationally design higher ionic conductive electrolyte materials.

As mentioned in Chapter 2, ionic conduction in these materials is a thermally activated process. Ionic conductivity (σ) dependence on temperature can be described by Arrhenius relationship,

$$\sigma T = \sigma_o \exp\left(-\frac{\Delta H_m}{kT}\right) \quad (4-1)$$

where σ_o , ΔH_m , k and T are pre-exponential coefficient, migration enthalpy for oxygen diffusion, Boltzmann's constant and absolute temperature, respectively. Equation (4-2) is the detailed form of the abovementioned Arrhenius relationship,

$$\sigma T = \frac{q_v^2}{k} [V_o^{**}] N_o a^2 v_o \exp\left(\frac{\Delta S_m}{k}\right) \exp\left(-\frac{\Delta H_m}{kT}\right) \quad (4-2)$$

where N_o is the number of oxygen sites per unit volume, $[V_o^{**}]$ is the fraction of free mobile oxygen vacancy present in the oxygen sublattice, q_v is the charge oxygen vacancy, a is the ion jump distance, v_o is an appropriate lattice vibration, and ΔS_m and ΔH_m is the entropy and enthalpy change, respectively, during oxygen ion diffusion. However, the above relationship assumes that there are negligible interactions between dopant cations and oxygen vacancies sites. Due to both electrostatic and elastic interactions between these two types of point defects, there is some additional energy barrier involved (in addition to ΔH_m) for oxygen diffusion. Thus, there is a possibility of the formation local defect structures (also discussed in Chapter 2) such as $(D'_A - V_o^{**} - D'_A)$ and $(D'_A - V_o^{**})^*$ (i.e., trimers and dimers, respectively). The additional thermal energy (which can be termed as association energy) is required to break free the oxygen vacancies from these complex defect associates.⁵² Taking $(D'_A - V_o^{**} - D'_A)$

and $(D'_A - V_O^{**})$ defect structures into account, equation (4-2) can be written as equation (4-3) and equation (4-4), respectively.

$$\sigma_i = \frac{q_V^2}{kT} AN_o a^2 v_o \exp\left(\frac{\Delta S_m + \Delta S_{Dimers}}{k}\right) \exp\left(-\frac{\Delta H_m + \Delta H_{Dimers}}{kT}\right) \quad (4-3)$$

$$\sigma_i = \frac{1}{4^{1/3}} \frac{q_V^2}{kT} A^{1/3} c_{dop}^{1/3} N_o a^2 v_o \exp\left(\frac{\Delta S_m + \frac{\Delta S_{Trimers}}{3}}{k}\right) \exp\left(-\frac{\Delta H_m + \frac{\Delta H_{Trimers}}{3}}{kT}\right) \quad (4-4)$$

where ΔH_{Dimers} and ΔS_{Dimers} , and $\Delta H_{Trimers}$ and $\Delta S_{Trimers}$ are the association enthalpy and entropy of dimers and trimers, respectively. A complete derivation of the above relationships can be found in Appendix B. As these defect structures lower the free mobile oxygen vacancy concentration, one of the main objectives while designing the electrolyte material is to minimize this association enthalpy (i.e., ΔH_{Dimers} and $\Delta H_{Trimers}$). The concentration of these defect structures depends on the dopant content and the physical properties of acceptor dopants such as ionic radius, charge valence, polarizability, etc.^{22,70} Hence, the selection of dopants for host ceria based on activation energy is critical for the development of novel electrolytes.

In addition, it can be seen from equations (4-3) and (4-4), that the ionic conductivity also depends upon the entropy of the system. As mentioned in Appendix A, the total entropy of a collection of atoms is a sum of vibrational entropy and configurational entropy.²⁴ The uncertainty in the exact value of energy in which the atoms vibrates in a given energy level constitutes vibrational entropy. On increasing the temperature, the probability of atoms excited to the higher energy level increases, which in turn, increases the vibrational entropy of the system. The change in vibrational entropy as a function of temperature is given in Appendix A. Similar to free mobile

oxygen vacancy concentration (in the pre-exponential term of the Arrhenius relationship), entropy term also depends on the temperature. Further, vibrational entropy is also the function of the characteristic frequency in which the atoms vibrate. Dopants which exhibit stronger bond strength with oxygen ions will show lower thermal entropy, while dopant which shows weaker bond strength will exhibit higher vibrational entropy.²⁴

The total entropy also contains the configurational term which is the measure of the number of ways in which the atom can be arranged in a given number of lattice sites. Thus, using two or more dopants, the number of configurations can be increased which in turn increase the total entropy in the system. Previous works have shown that using two or more dopants can significantly improve the ionic conductivity.^{16,18,19} This was attributed to the increase in configurational entropy which consequently enhances σ_o .^{69,71} In the present work, this approach was taken and the co-dopants were used to suppress the oxygen vacancy ordering with an aim to enhance the ionic conductivity.

4.2 Co-doping Strategies

In the following sections, two different co-doping strategies will be discussed followed by results and discussion. The main objectives in both the strategies are to minimize the association energy and maximize the pre-exponential coefficient (or entropy) which as a result increases the ionic conductivity of the material.

4.2.1 Critical Dopant Ionic Radius

The critical dopant ionic radius was first proposed by Kim²², which was later revisited by many other researchers⁷²⁻⁷⁴. In this section, the effect of co-doping based on critical dopant ionic radius on the ionic conductivity in ceria will be discussed.

4.2.1.1 Theory

As discussed in previous section, activation energy for oxygen diffusion at intermediate temperatures consists of migration enthalpy (ΔH_{mig}) of the oxygen ion, and the association enthalpy (ΔH_{assoc}) of the local defect structures. From previous research it has been found that in the dilute regime, ΔH_{mig} is independent of dopant concentration.⁷⁵ However, with the increase in oxygen vacancy concentration, the probability of the formation of local defect structure increases. Thus, to enhance the ionic conductivity, the minimization of the association of defects is required. As expressed before, this association energy is a function of the coulombic attraction between oxygen vacancies and dopant cations sites and the elastic strain field around the defect complex.²² According to Kilner et al.²¹, maximum ionic conductivity in doped oxide fluorites is achieved when there is minimum elastic strain present in the lattice. Kim²² studied the effect of ionic radius and valence of the dopant cation on the lattice parameter of oxide fluorites and a critical ionic radius, r_c , was defined as the ionic radius of the dopant that neither causes expansion nor contraction of the host fluorite lattice. Specifically, for a trivalent dopant cation in host ceria, r_c was calculated to be 1.038 Å. Figure 4-1 shows the grain (bulk) ionic conductivity as a function of trivalent dopant cation. It is important to note that the grain ionic conductivity data presented in this figure are taken from literature. $Gd_{0.10}Ce_{0.90}O_{2-\delta}$ exhibits the highest grain ionic conductivity among singly doped ceria electrolytes. This is consistent with the critical ionic radius concept as the ionic radius of Gd^{3+} ($r_{Gd,VIII}^{3+} = 0.1053$ nm) is relatively close to the ideal r_c value.⁴⁸

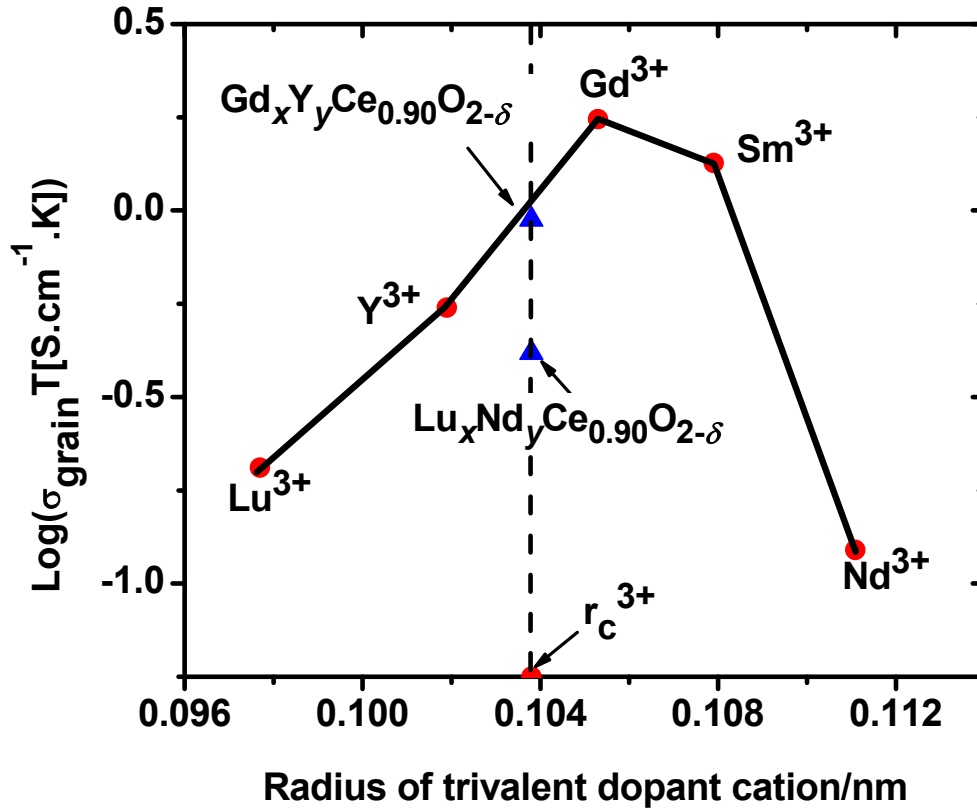


Figure 4-1. Grain ionic (GI) conductivity comparison of $\text{D}_{0.10}\text{Ce}_{0.90}\text{O}_{2-\delta}$ at 400°C . GI conductivity data for $\text{Gd}_{0.10}\text{Ce}_{0.90}\text{O}_{2-\delta}$, $\text{Sm}_{0.10}\text{Ce}_{0.90}\text{O}_{2-\delta}$, $\text{Y}_{0.10}\text{Ce}_{0.90}\text{O}_{2-\delta}$ and $\text{Nd}_{0.10}\text{Ce}_{0.90}\text{O}_{2-\delta}$ are taken after Steele¹³, Zhan et al.⁷⁶, Zhang et al.⁷⁷, and Li et al.⁷⁸, respectively, while $\text{Gd}_{0.056}\text{Y}_{0.044}\text{Ce}_{0.90}\text{O}_{2-\delta}$, $\text{Lu}_x\text{Nd}_y\text{Ce}_{0.90}\text{O}_{2-\delta}$ and $\text{Lu}_{0.10}\text{Ce}_{0.90}\text{O}_{2-\delta}$ are from this work.

4.2.1.2 Materials selection

As Kim²² suggested, ideal trivalent dopant for host ceria should have the ionic radius of 1.038 Å. In the lanthanide series of the periodic table, Tb^{3+} cation with VIII coordination shows ionic radius of 1.040 Å.⁴⁸ Hence, based on critical dopant ionic radius scheme, Tb^{3+} is the ideal dopant for host ceria. Unfortunately, Tb element exists in different valence states. This will promote electronic conduction through the electrolyte and lower the ionic transference number.⁵⁴ In order to test Kim's hypothesis, co-doping pairs were selected based on their ionic radius. Lu^{3+} and Nd^{3+} , and Gd^{3+} and

Y^{3+} were selected as trivalent co-dopant pairs. They were added in a proportion such that the weighed average dopant ionic radius of co-dopants matches r_c . For example if x_{Lu} and x_{Nd} are the proportion of Lu^{3+} and Nd^{3+} co-dopants, then they must satisfy the following equation:

$$x_{Lu}r_{Lu} + x_{Nd}r_{Nd} = (x_{Lu} + x_{Nd})r_c \quad (4-5)$$

where r_{Lu} and r_{Nd} are the ionic radius of trivalent dopant Lu^{3+} and Nd^{3+} with VIII coordination, respectively. By doing so, it was expected that the positive elastic strain due to larger dopant cation (i.e., Nd^{3+} or Gd^{3+}) can be compensated by the negative elastic strain due to smaller dopant cation (i.e., Lu^{3+} or Y^{3+}). This in turn prevents any distortion in fluorite lattice which is usually present in singly doped ceria systems. $Lu_{0.054}Nd_{0.046}Ce_{0.90}O_{2-\delta}$ and $Gd_{0.056}Y_{0.044}Ce_{0.90}O_{2-\delta}$ ceramic samples were synthesized using solid oxide route as described in Chapter 3. In order to study the elastic strain behavior as a function of dopant concentration, different composition of $Lu_xNd_yCe_{1-x-y}O_{2-\delta}$ (where $x+y = 0.05, 0.10, 0.15$ and 0.20) were also synthesized. In addition, to understand the effect of electrostatic interactions alone, $Lu_xCe_{1-x}O_{2-\delta}$ (where $x = 0.05, 0.10,$ and 0.15) was also investigated as the ionic radius of Lu^{3+} is approximately the same as Ce^{4+} ($r_{Lu,VIII}^{3+} = 0.977 \text{ \AA}$ and $r_{Ce,VIII}^{4+} = 0.97 \text{ \AA}$).⁴⁸ Moreover, singly doped ceria $D_{0.10}Ce_{0.90}O_{2-\delta}$ (where $D^{3+} = Y^{3+}, Gd^{3+}, Sm^{3+}$ and Nd^{3+}) samples were also processed under similar experimental procedure.

3.2.1.3 Results and discussion

In this section, relationship between the elastic strain (measured at room temperature) and the ionic conductivity measured at 400°C for co-doped ceria systems

will be discussed. Further, the comparison between the ionic conductivity of co-doped ceria with that of $\text{Gd}_{0.10}\text{Ce}_{0.90}\text{O}_{2-\delta}$ will be presented.

X-ray diffraction analysis: To ensure the complete dissolution of dopant in CeO_2 , phase analysis was performed using X-Ray diffraction (XRD) technique. Figure 4-2 and Figure 4-3 show the XRD profiles of the calcined powders of $\text{Lu}_x\text{Nd}_y\text{Ce}_{1-x-y}\text{O}_{2-\delta}$ (where $x+y = 0.05, 0.10, \text{ and } 0.15$ and 0.20), $\text{Gd}_{0.056}\text{Y}_{0.044}\text{Ce}_{0.90}\text{O}_{2-\delta}$, CeO_2 and $\text{D}_{0.10}\text{Ce}_{0.90}\text{O}_{2-\delta}$ (where $\text{D}^{3+} = \text{Lu}^{3+}, \text{Y}^{3+}, \text{Gd}^{3+}, \text{Sm}^{3+}$ and Nd^{3+}). It can be observed that all the compositions studied are single phase with a cubic fluorite structure like pure CeO_2 .

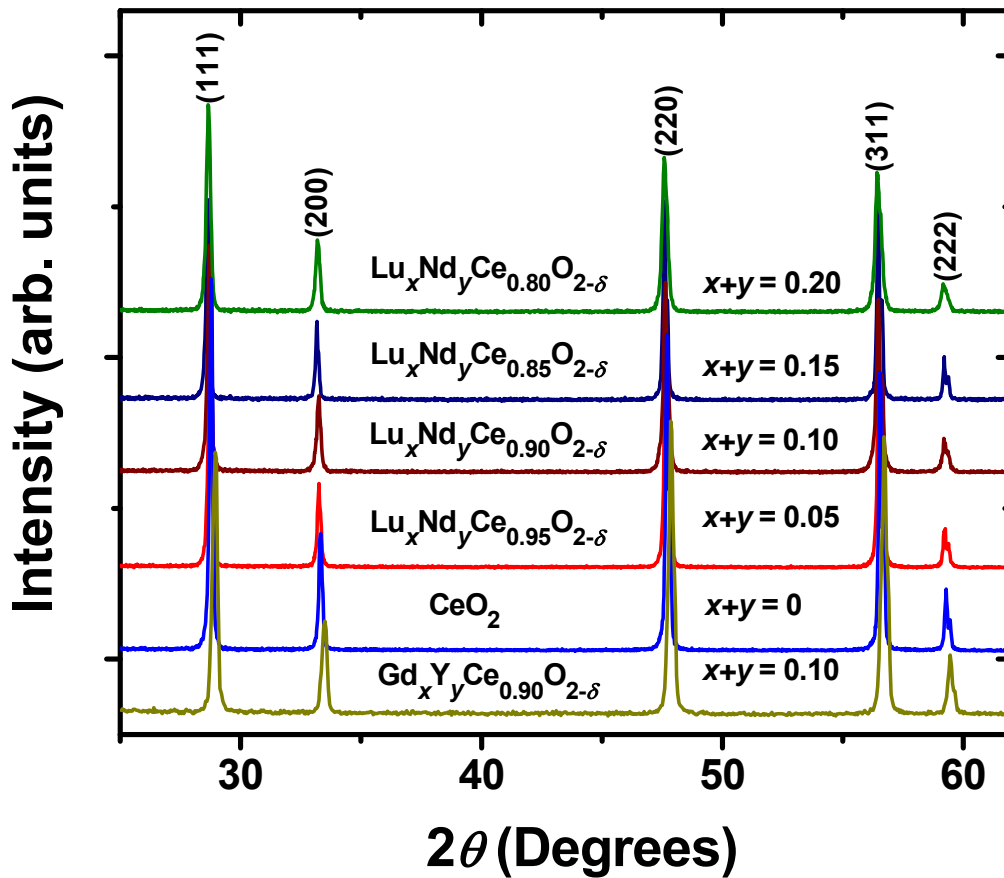


Figure 4-2. XRD profiles of $\text{Lu}_x\text{Nd}_y\text{Ce}_{1-x-y}\text{O}_{2-\delta}$ and $\text{Gd}_{0.056}\text{Y}_{0.044}\text{Ce}_{0.90}\text{O}_{2-\delta}$ taken at room temperature.

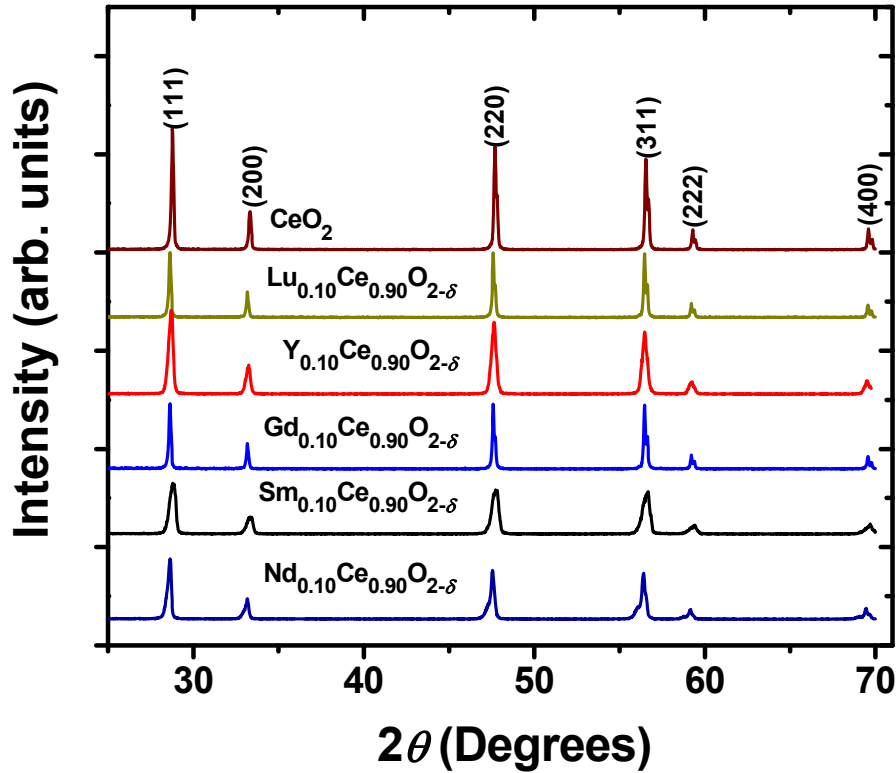


Figure 4-3. XRD profiles of $D_{0.10}Ce_{0.90}O_{2-\delta}$ taken at room temperature.

The effect of total dopant concentration ($x+y$) on the lattice constant a_o of the cubic fluorite structure of $Lu_xNd_yCe_{1-x-y}O_{2-\delta}$ was studied. The a_o of the calcined powders of $Lu_xNd_yCe_{1-x-y}O_{2-\delta}$, and $Lu_xCe_{1-x}O_{2-\delta}$ with different total dopant concentrations was calculated using maximum likelihood estimation method with tungsten as an internal standard.⁷⁹ Figure 4-4 shows the variation of the elastic strain present in the cubic fluorite lattice of $Lu_xNd_yCe_{1-x-y}O_{2-\delta}$, $Nd_xCe_{1-x}O_{2-\delta}$ and $Lu_xCe_{1-x}O_{2-\delta}$ as a function of total dopant concentration. The lattice constant data for the different compositions of $Nd_xCe_{1-x}O_{2-\delta}$ was taken after Stephens et al.⁸⁰ Elastic strain is calculated using the following equation:

$$\text{Elastic strain} = \frac{a_o - a}{a} \quad (4-6)$$

where a is the lattice constant of a pure ceria. Positive and negative elastic strain is respectively observed upon the separate addition of Nd^{3+} and Lu^{3+} . By contrast, there is almost no elastic strain present in the fluorite lattice of $\text{Lu}_x\text{Nd}_y\text{Ce}_{1-x-y}\text{O}_{2-\delta}$, even at high dopant concentrations. This validates the hypothesis that, when combined, the positive elastic strain generated by the addition of the larger Nd^{3+} dopant ion is compensated by the negative elastic strain caused by the addition of smaller Lu^{3+} dopant ion. Further, the lattice parameter of $\text{Gd}_{0.056}\text{Y}_{0.044}\text{Ce}_{0.90}\text{O}_{2-\delta}$ ceramic was calculated using extrapolation method.⁶⁶ The estimated lattice parameter of $\text{Gd}_{0.056}\text{Y}_{0.044}\text{Ce}_{0.90}\text{O}_{2-\delta}$ ($a = 5.4133 \pm 0.0018 \text{ \AA}$) was close to that of standard value of ceria ($a = 5.41134 \text{ \AA}$) at room temperature which is similar to what we obtained in $\text{Lu}_x\text{Nd}_y\text{Ce}_{1-x-y}\text{O}_{2-\delta}$ system.⁴⁷

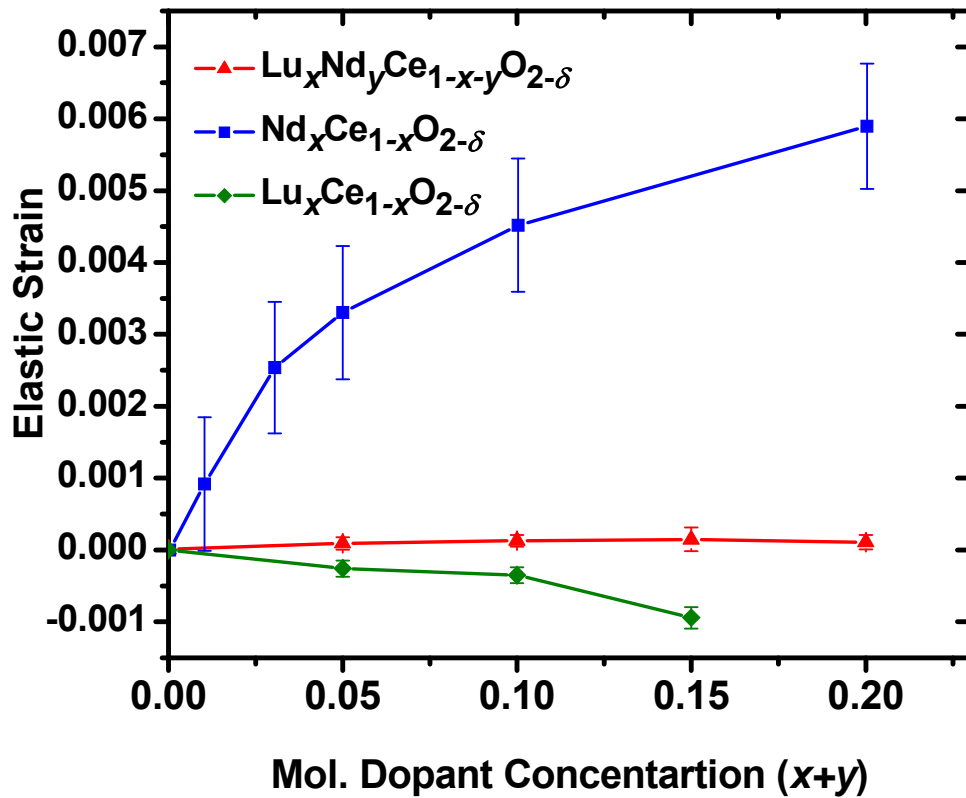


Figure 4-4. Elastic strain as a function of dopant concentration. Lattice parameter data for $\text{Nd}_x\text{Ce}_{1-x}\text{O}_{2-\delta}$ were taken after Stephens et al.^{7,80}

Ionic conductivity: Ionic conductivity measurement was performed using ac impedance spectroscopy from 250 – 700°C, in air. The details of this technique can be found in Chapter 2. Figure 4-5 shows the grain ionic conductivity of $\text{Gd}_{0.10}\text{Ce}_{0.90}\text{O}_{2-\delta}$, $\text{Lu}_{0.054}\text{Nd}_{0.046}\text{Ce}_{0.90}\text{O}_{2-\delta}$, and $\text{Lu}_{0.10}\text{Ce}_{0.90}\text{O}_{2-\delta}$ as a function of temperature. Further, the grain ionic conductivity data of $\text{Gd}_{0.10}\text{Ce}_{0.90}\text{O}_{2-\delta}$ taken from literature were also plotted. It can be seen that the grain ionic conductivity data follows Arrhenius behavior. The typical correlation coefficients for a linear least squares fit lie between 0.9995 and 0.9999. Comparison of the grain ionic conductivity for co-doped ceria with that of singly doped ceria is shown in Figure 4-1. As mentioned earlier, the grain conductivity values of different doped ceria systems are taken from literature. It can be seen that $\text{Lu}_{0.054}\text{Nd}_{0.046}\text{Ce}_{0.90}\text{O}_{2-\delta}$ exhibits higher grain ionic conductivity than either of $\text{Lu}_{0.10}\text{Ce}_{0.90}\text{O}_{2-\delta}$ and $\text{Nd}_{0.10}\text{Ce}_{0.90}\text{O}_{2-\delta}$, which is consistent with the elastic strain behavior observed in Figure 4-4. However, in the intermediate temperature range, the grain ionic conductivity of $\text{Lu}_{0.054}\text{Nd}_{0.046}\text{Ce}_{0.90}\text{O}_{2-\delta}$ is lower than that of $\text{Gd}_{0.10}\text{Ce}_{0.90}\text{O}_{2-\delta}$. Thus, even though $\text{Lu}_{0.054}\text{Nd}_{0.046}\text{Ce}_{0.90}\text{O}_{2-\delta}$ shows higher ionic conductivity than singly doped ceria (Lu^{3+} or Nd^{3+}), its ionic conductivity is less than that of $\text{Gd}_{0.10}\text{Ce}_{0.90}\text{O}_{2-\delta}$. It may be due to the large ionic radius difference between the Lu^{3+} and Nd^{3+} dopant cations ($r_{\text{Lu}^{3+}} = 0.977 \text{ \AA}$ and $r_{\text{Nd}^{3+}} = 1.109 \text{ \AA}$).⁴⁸ On testing the $\text{Gd}_{0.056}\text{Y}_{0.044}\text{Ce}_{0.90}\text{O}_{2-\delta}$ system ($r_{\text{Gd}^{3+}} = 1.053 \text{ \AA}$ and $r_{\text{Y}^{3+}} = 1.019 \text{ \AA}$)⁴⁸, it is found that the ionic conductivity value of $\text{Gd}_{0.056}\text{Y}_{0.044}\text{Ce}_{0.90}\text{O}_{2-\delta}$ lies in between that of $\text{Gd}_{0.10}\text{Ce}_{0.90}\text{O}_{2-\delta}$ and $\text{Y}_{0.10}\text{Ce}_{0.90}\text{O}_{2-\delta}$ (see Figure 4-4). Thus, even though both co-doped ceria systems show minimal elastic strain, their ionic conductivity is less than that of $\text{Gd}_{0.10}\text{Ce}_{0.90}\text{O}_{2-\delta}$. This shows that minimizing elastic strains is good but not enough. Here, it is important to note that in the structure-

property relationship proposed by Kim²², both elastic strain and ionic conductivity are measured in different conditions. Ionic conductivities for all the doped ceria electrolytes were measured at high temperatures ($\sim 400^\circ\text{C}$), while lattice parameters were calculated at room temperature. This will be revisited in the Chapter 5 where structure-property relationships were determined at higher temperatures. That will provide the correct r_c values of the dopant that causes neither expansion nor contraction in the host ceria lattice at high temperatures.

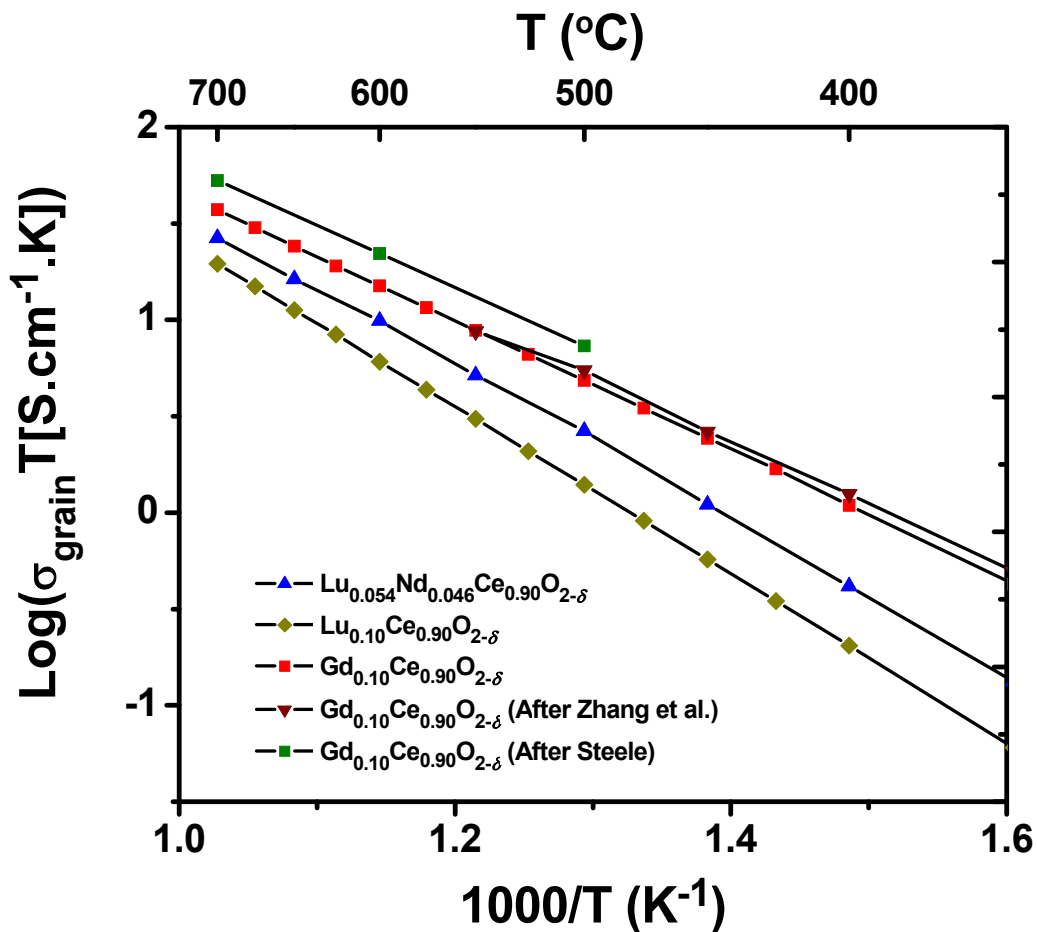


Figure 4-5. Arrhenius plot for the bulk ionic conductivity of $\text{Gd}_{0.10}\text{Ce}_{0.90}\text{O}_{2-\delta}$, $\text{Lu}_{0.10}\text{Ce}_{0.90}\text{O}_{2-\delta}$, and $\text{Lu}_{0.054}\text{Nd}_{0.046}\text{Ce}_{0.90}\text{O}_{2-\delta}$ systems in air. Comparison between the present work and literature^{13,77} for the grain ionic conductivity of $\text{Gd}_{0.10}\text{Ce}_{0.90}\text{O}_{2-\delta}$.

4.2.1.4 Summary and conclusion

Based on critical dopant ionic radius, co-dopant strategy was used to investigate the effect of elastic strain in the lattice on the grain ionic conductivity of the doped ceria. The Lu^{3+} and Nd^{3+} , and Y^{3+} and Gd^{3+} were selected as co-dopant pairs for the host CeO_2 and they were added in a proportion such that the weighed average dopant ionic radius matches r_c for all the compositions. Elastic strain present in $\text{Lu}_x\text{Nd}_y\text{Ce}_{1-x-y}\text{O}_{2-\delta}$ and $\text{Gd}_{0.056}\text{Y}_{0.044}\text{Ce}_{0.90}\text{O}_{2-\delta}$ systems was calculated to be negligible when compared to singly doped ceria systems. It was observed that both $\text{Lu}_{0.054}\text{Nd}_{0.046}\text{Ce}_{0.90}\text{O}_{2-\delta}$ and $\text{Gd}_{0.056}\text{Y}_{0.044}\text{Ce}_{0.90}\text{O}_{2-\delta}$ ceramics show lower grain ionic conductivity than that of $\text{Gd}_{0.10}\text{Ce}_{0.90}\text{O}_{2-\delta}$. The results clearly suggest that the co-dopant strategy based on r_c does not lead to ionic conductivity higher than that of $\text{Gd}_{0.10}\text{Ce}_{0.90}\text{O}_{2-\delta}$. However, r_c proposed by Kim is derived through the empirical relationship, which was obtained for room temperature. The clear view of this co-doping strategy will only be possible, if r_c is obtained at higher temperatures where the ionic conductivity of these materials is measured. This topic will be revisited in the Chapter 5.

4.2.2 Density Functional Theory Calculation

Many of the properties of materials are dependent upon interatomic interactions which include the nuclei-nuclei, nuclei-electron, and electron-electron.⁸¹ Density function theory (DFT) incorporates these interactions by solving Schrödinger's equations typically by using approximations like Kohn-Sham⁸² to obtain electron-electron exchange and correlation functions. DFT provides high materials fidelity and is successfully used to describe different types of material systems (metals, semiconductors, oxides, etc.). A review of the DFT approach to solve materials science related problems can be found elsewhere.⁸¹ In this section, co-doping strategy (for

ceria) based on the DFT prediction of the interaction energy between oxygen vacancy and dopant cation will be described. The ionic conductivity of co-doped ceria with different dopant concentration will be compared with $\text{Gd}_{0.10}\text{Ce}_{0.90}\text{O}_{2-\delta}$. Further, the activation energy and the pre-exponential coefficient of co-doped sample will be presented in detail.

4.2.2.1 Theory

In the recent DFT work by Andersson et al.⁸³ has shown that the total interaction energy values for the oxygen vacancy sitting in nearest neighbor (NN) site and the next to nearest neighbor (NNN) site for Pm^{3+} dopant are almost same. The defect properties were modeled within $3 \times 2 \times 2$ supercells with 4.2 % of dopant content. Figure 4-6 shows the total interaction as a function of dopant ionic radii for different trivalent dopants. This figure is modified after Andersson et al.⁸³ The total interaction energy which is the sum of electrostatic and elastic interaction energies, between trivalent dopant cation site and the oxygen vacancy residing in NN and NNN sites, is calculated for different trivalent dopant cations using DFT calculations. The negative sign in the interaction energy imply attractive interactions. In its original form, Figure 4-6 is plotted between the total interaction energy and the atomic number of the dopant cation. The atomic number was used to describe the doped ceria system as this is the only physical parameter (except for the crystal structure) that is used as an input in DFT calculations. The specification of the atomic number in DFT calculations takes into account ionic radii, and interactions between electrons. However, from the experimental point of view, it is reasonable to plot the interaction energy as a function of ionic radii of the dopant, as this physical property is more relevant while understanding the effect of different dopants on the crystal structure.²²

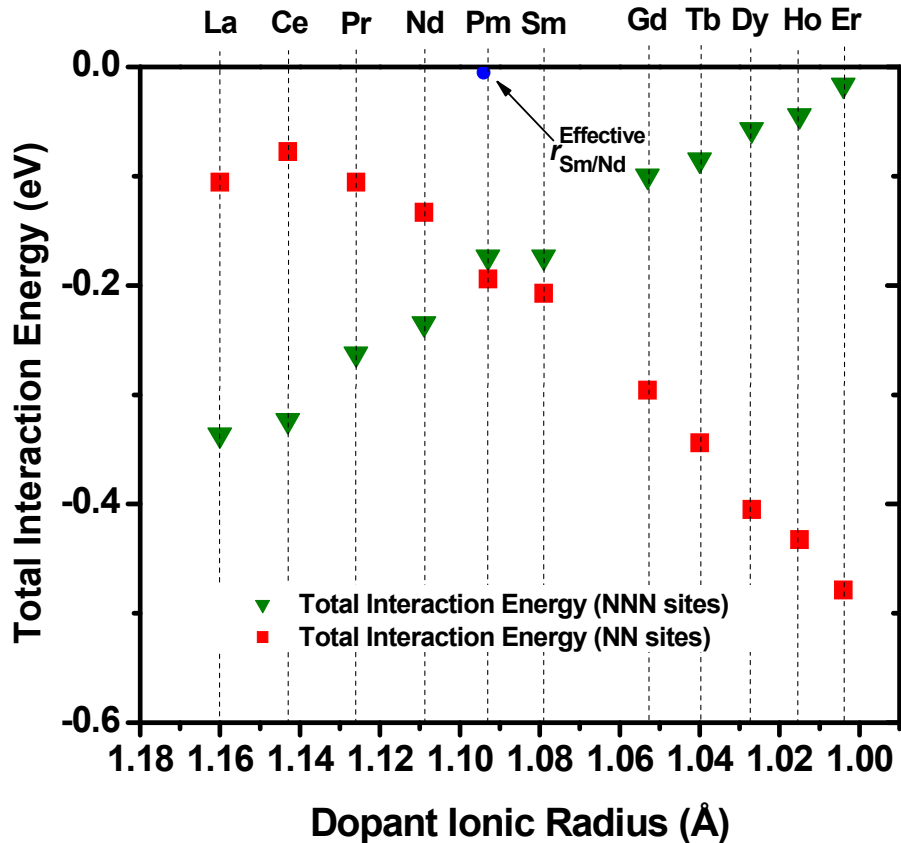


Figure 4-6. Total interaction energy between dopant cation and oxygen vacancy sitting in nearest neighbor (NN) and next to nearest neighbor (NNN) site (of dopant cations) for different trivalent cations.^{48,83}

The main idea of the present co-doping strategy is to maximize the concentration of equi-interaction energy oxygen vacancy sites inside the host ceria lattice. Figure 4-7 shows another view of cubic fluorite structure of doped ceria, where oxygen ions form the lattice and cerium ions (and dopant ions) sit inside the lattice. Here, oxygen vacancy sits in NN site and NNN site of dopant cation. The probability of oxygen vacancy to sit in any particular site depends upon its interaction energy with dopant cation site. The oxygen vacancies will try to diffuse to the sites where the interaction energy is higher. However, once they are trapped in these higher interaction energy sites, they will require additional thermal energy to jump out of there. If all the sites are

of equal interaction energy, then there will be no deep traps for oxygen vacancies. Thus, the probability of oxygen vacancies jump out of the traps increases which will promote diffusion through the material and minimize the concentration of local defect structures.

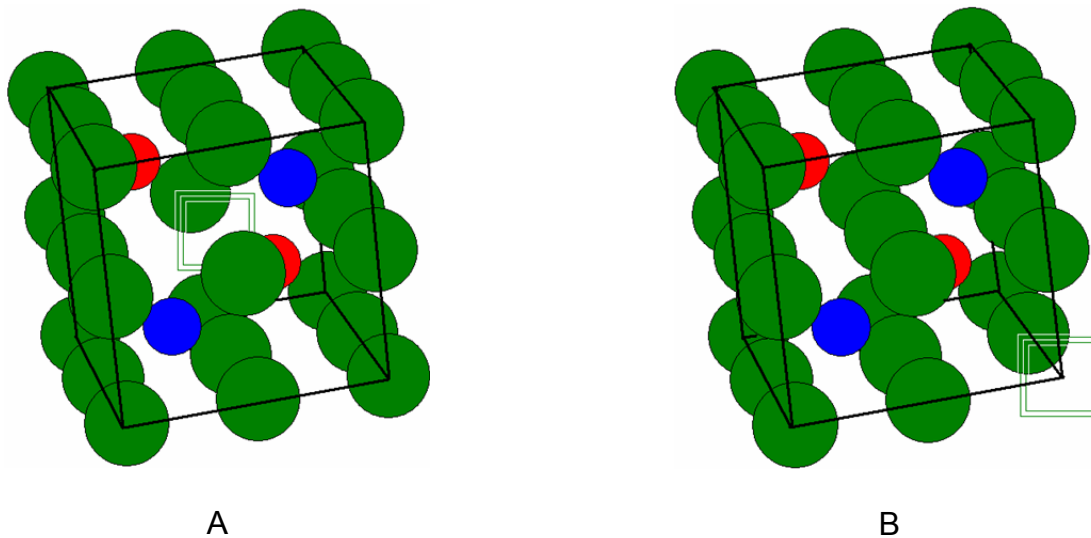


Figure 4-7. Cubic fluorite structure of doped ceria, where oxygen vacancy reside in nearest neighbor (NN) site A) and next to nearest neighbor (NNN) site B) of dopant cation.

It can be seen from Figure 4-6 that for Pm^{3+} , and for ions to the right of Pm^{3+} in the lanthanide series, oxygen vacancy interacts strongly with the dopant cation when it occupies NN position of the dopant cation. Moreover, cations with atomic number less than the Pm^{3+} in the lanthanide series usually hold oxygen vacancies in the NNN position of the dopant cation. Thus, around Pm^{3+} there will be no site preference for oxygen vacancies, resulting in an increase in the number of equi-interaction energy sites which facilitate the oxygen vacancy diffusion. It was predicted then that Pm^{3+} doped ceria should exhibits higher ionic conductivity than any other singly doped ceria material.

4.2.2.2 Materials selection

Using DFT results, it was shown that Pm^{3+} is the ideal trivalent dopant cation for ceria to exhibit highest ionic conductivity. Unfortunately, Pm is radioactive and cannot be used for electrolyte applications. The ideal dopant should have an effective atomic number around Pm^{3+} (61) which shows ionic radius of 1.093 Å.⁴⁸ Therefore, as predicted by Andersson et al., a co-dopant scheme using Sm^{3+} and Nd^{3+} can provide an experimental scenario for testing this hypothesis. In terms of ionic radius, 1:1 Sm:Nd co-doping can be seen as having a weighed average dopant ionic radius ($r_{\text{Sm/Nd}}^{\text{Effective}}$) of 1.094 Å which is close to Pm^{3+} ionic radius of 1.093 Å (shown in Figure 4-6).⁴⁸ Thus, based on the Pm^{3+} atomic number, in the present work the effect of co-dopant pair Sm^{3+} and Nd^{3+} on the ionic conductivity of ceria based electrolyte is investigated. Dopants were added in equal proportion to achieve the effective atomic number of Pm^{3+} , i.e. 61. By doing so, similar total interactions between the oxygen vacancies sitting in NN and NNN sites and the dopant cation are expected, with the consequent enhancement of the ionic conductivity.

In order to study the effect of dopant concentration on the crystal structure and ionic conductivity, polycrystalline samples of $\text{Sm}_{x/2}\text{Nd}_{x/2}\text{Ce}_{1-x}\text{O}_{2-\delta}$ (where $x = 0.01, 0.03, 0.05, 0.08, 0.10, 0.12, 0.15, 0.18, \text{ and } 0.20$) were synthesized by conventional solid state reaction method (as described in Chapter 2). As $\text{Gd}_{0.10}\text{Ce}_{0.90}\text{O}_{2-\delta}$ exhibits the highest ionic conductivity among doped ceria systems, therefore for comparison, phase pure sample of $\text{Gd}_{0.10}\text{Ce}_{0.90}\text{O}_{2-\delta}$ was also processed using the identical experimental procedure. Densities of all the sintered samples were measured in water using Archimedes's principle and were estimated to be 98% of theoretical density or above.⁵³

4.2.2.3 Results and discussion

In this section, the microstructure, lattice parameter, and the ionic conductivity of $\text{Sm}_{x/2}\text{Nd}_{x/2}\text{Ce}_{1-x}\text{O}_{2-\delta}$ will be covered. Also, the comparison between the ionic conductivity of $\text{Sm}_{x/2}\text{Nd}_{x/2}\text{Ce}_{1-x}\text{O}_{2-\delta}$ and $\text{Gd}_{0.10}\text{Ce}_{0.90}\text{O}_{2-\delta}$ will be presented. Further, the effect of dopant concentration on the crystal lattice and the ionic conductivity at intermediate temperatures will be discussed.

Microstructure analysis: The microstructure of the sintered pellets of $\text{Sm}_{x/2}\text{Nd}_{x/2}\text{Ce}_{1-x}\text{O}_{2-\delta}$ was studied using SEM. A typical micrograph of the surface of the $\text{Sm}_{0.05}\text{Nd}_{0.05}\text{Ce}_{0.90}\text{O}_{2-\delta}$ sample is shown in Figure 4-8. There is almost no residual porosity observed in Figure 4-8 which is consistent with the measured density of the sintered pellet. The mean lineal intercept technique was used to determine the mean grain sizes. The average grain size in each sample was found to be in the range of 4 - 5 μm .

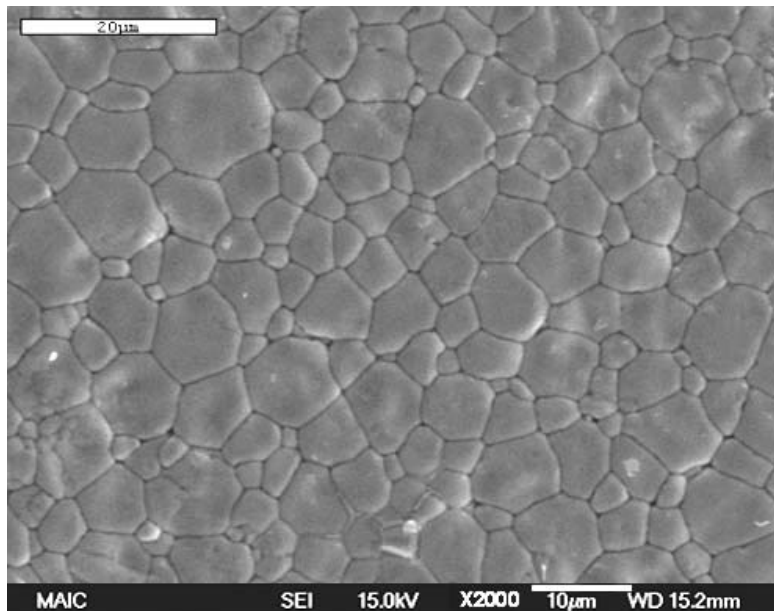


Figure 4-8. Scanning electron micrograph of the surface of $\text{Sm}_{0.05}\text{Nd}_{0.05}\text{Ce}_{0.90}\text{O}_{2-\delta}$ sintered pellet.

X-ray diffraction analysis: To verify the complete dissolution of dopants in ceria, phase analysis was performed using X-ray diffraction (XRD). Curved position-sensitive diffractometer was used to obtain the XRD pattern of each composition using Cu K_{α} radiation. Figure 4-9 shows the XRD profiles measured at room temperature for all the compositions of $\text{Sm}_{x/2}\text{Nd}_{x/2}\text{Ce}_{1-x}\text{O}_{2-\delta}$. Tungsten was used as an internal standard in the powder sample. It can be observed that all the compositions studied are single phase with a cubic fluorite structure like pure CeO_2 .

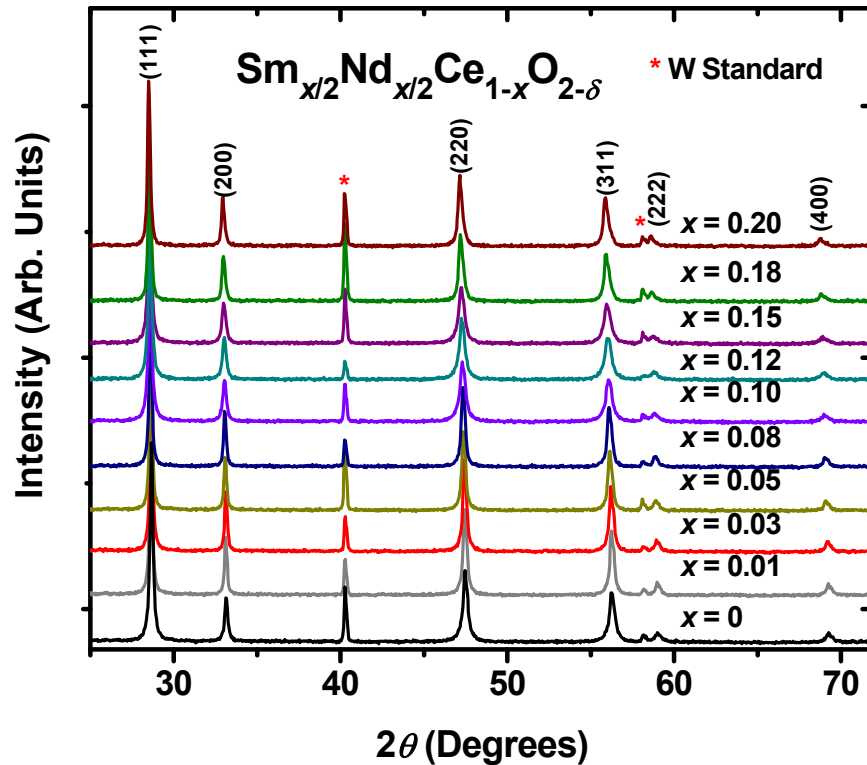


Figure 4-9. XRD patterns of $\text{Sm}_{x/2}\text{Nd}_{x/2}\text{Ce}_{1-x}\text{O}_{2-\delta}$ measured at room temperature. Tungsten was used as an internal standard.

Figure 4-10 shows the (111) and (200) peaks of the materials and (110) peak of the tungsten standard for different dopant concentration. It can be observed that with the increase in the total dopant content (x), (111) and (200) peaks of the material shift to

the lower 2θ angles while (110) peak positions of the tungsten standard remain stable in all the compositions. This clearly indicates that the doped ceria lattice expands with the increase in dopant content.

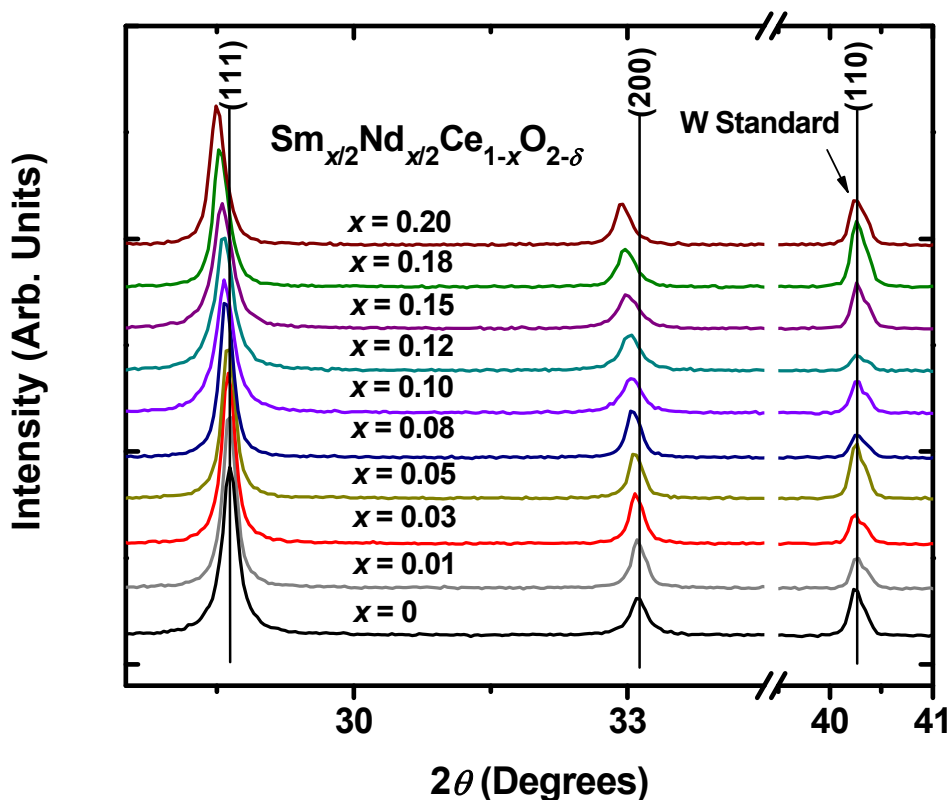


Figure 4-10. Shift in (111) and (200) XRD peaks position of $\text{Sm}_{x/2}\text{Nd}_{x/2}\text{Ce}_{1-x}\text{O}_{2-\delta}$ with increase in dopant concentration (x). Tungsten was used as an internal standard.

Precise lattice constant (a_0) for all the compositions of $\text{Sm}_{x/2}\text{Nd}_{x/2}\text{Ce}_{1-x}\text{O}_{2-\delta}$ was calculated using the least-squares extrapolation method.⁶⁶ Figure 4-11 shows the lattice parameter of $\text{Sm}_{x/2}\text{Nd}_{x/2}\text{Ce}_{1-x}\text{O}_{2-\delta}$ solid solution as a function of total dopant concentration (x). For comparison, the lattice parameter data of $\text{Nd}_x\text{Ce}_{1-x}\text{O}_{2-\delta}$ as a function of dopant content is also shown taken after Stephens et al.⁸⁰ It can be seen that for $\text{Sm}_{x/2}\text{Nd}_{x/2}\text{Ce}_{1-x}\text{O}_{2-\delta}$ system, the lattice parameter increases linearly with the

increase in Sm^{3+} and Nd^{3+} concentration following Vegard's law.⁸⁴ Using a least-squares fitting algorithm, a linear relationship was obtained between the lattice parameters of $\text{Sm}_{x/2}\text{Nd}_{x/2}\text{Ce}_{1-x}\text{O}_{2-\delta}$ and dopant content (x). This can be represented as,

$$a_o(x) = 0.5412 + 0.0154 x \quad (4-7)$$

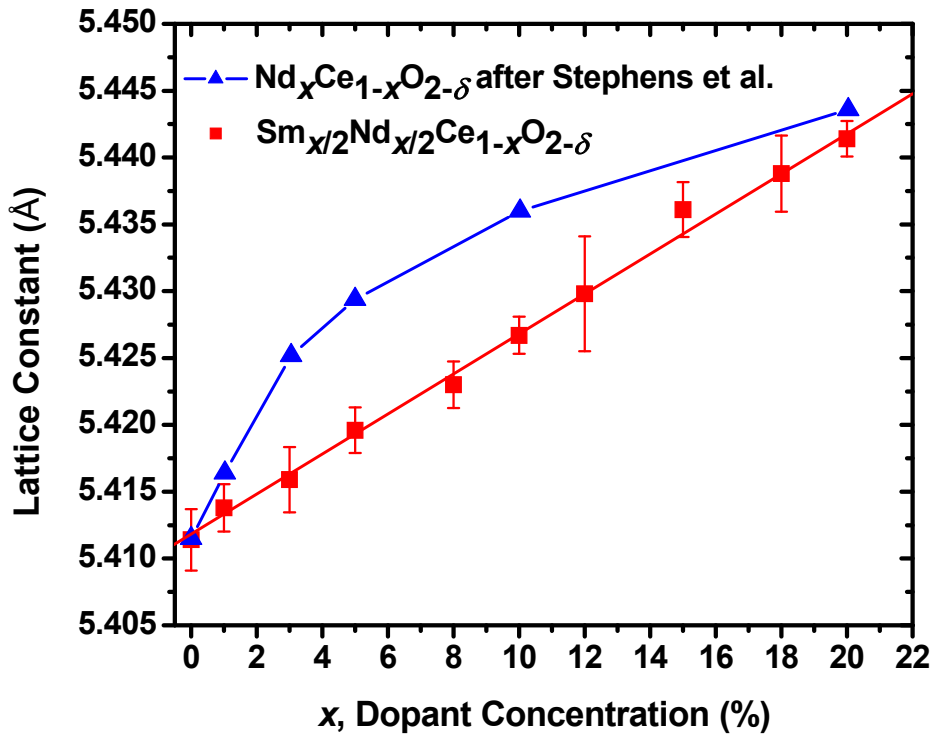


Figure 4-11. Lattice parameter as a function of dopant concentration (mol%) for $\text{Sm}_{x/2}\text{Nd}_{x/2}\text{Ce}_{1-x}\text{O}_{2-\delta}$ and $\text{Nd}_x\text{Ce}_{1-x}\text{O}_{2-\delta}$ taken after Stephens et al.^{67,80}

It is important to note that a gradual non-linear increase in the lattice parameter with dopant concentration was observed in ceria-neodymium system. Similar quadratic expansion was also reported in $\text{Yb}_x\text{Ce}_{1-x}\text{O}_{2-\delta}$, $\text{Dy}_x\text{Ce}_{1-x}\text{O}_{2-\delta}$, $\text{Gd}_x\text{Ce}_{1-x}\text{O}_{2-\delta}$, and $\text{Y}_x\text{Ce}_{1-x}\text{O}_{2-\delta}$ systems.⁸⁵ The lattice parameter behavior for these systems was fitted using the quadratic function of the dopant mole fraction. The first-order term in the quadratic relationship was interpreted as the ionic radii mismatch between the dopant (r_d) and the host cations (r_h), which consequently results in the expansion (for $r_d > r_h$) or

contraction (for $r_d < r_h$) of the host lattice with the increase in dopant concentration. The coefficient of the second-degree term was interpreted as a measure of the degree of ordering present in the material. The decrease in the lattice parameter at higher dopant concentration can be attributed to the effect of the attractive interactions between dopant cations and oxygen vacancies which tend to contract the unit cell.

As seen from equation (4-7), the coefficient of the second-degree term in the lattice parameter - dopant content relationship in $\text{Sm}_{x/2}\text{Nd}_{x/2}\text{Ce}_{1-x}\text{O}_{2-\delta}$ system is essentially negligible. This points to the theory that the oxygen vacancy ordering in $\text{Sm}_{x/2}\text{Nd}_{x/2}\text{Ce}_{1-x}\text{O}_{2-\delta}$ system is significantly lower compared to other ceria based systems.

Ionic conductivity: Ionic conductivity measurement was performed on the sintered pellets of $\text{Sm}_{x/2}\text{Nd}_{x/2}\text{Ce}_{1-x}\text{O}_{2-\delta}$ using the ac impedance spectroscopy technique in air, from 250 –700°C. It is essential to note that it is the grain ionic conductivity that is the intrinsic property of the material; whereas, total conductivity includes microstructural, impurity and other contributions to the samples resistance.⁸⁶ Thus, in the present work, comparison between the grain ionic conductivity rather than the total ionic conductivity for different materials is reported. Figure 4-12 shows the typical impedance spectrum of an electroded polycrystalline ceramic sample of $\text{Sm}_{0.075}\text{Nd}_{0.075}\text{Ce}_{0.85}\text{O}_{2-\delta}$. Three arcs, corresponding to the polarizations of the grain, grain boundary, and the electrode, were shown in the impedance spectrum. The high frequency semi-circle in the spectrum which is associated with intra-grain polarization is also shown in the inset.

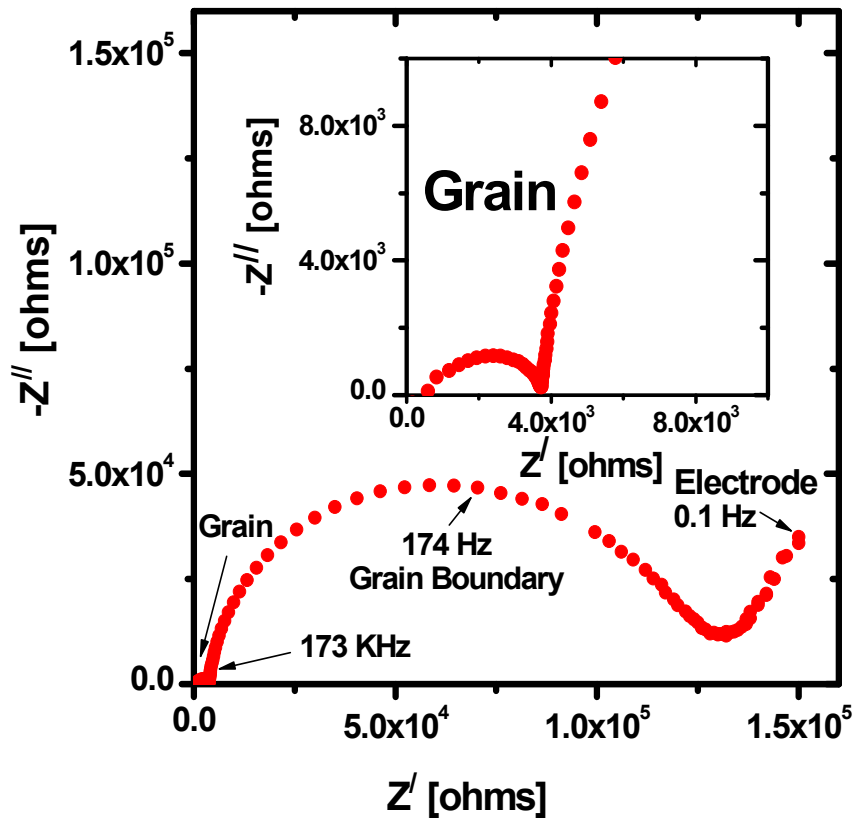


Figure 4-12. Typical impedance spectrum of a polycrystalline $\text{Sm}_{0.075}\text{Nd}_{0.075}\text{Ce}_{0.85}\text{O}_{2.5}$ ceramic measured in air at 300°C. Inset shows the intra-grain polarization contribution.

The grain ionic resistance was calculated by fitting the observed impedance spectrum with the analog equivalent circuit having three parallel resistor-constant phase element (R-CPE) pairs in series. Further details about impedance spectroscopy are given in Chapter 2. The reported grain ionic conductivity for each composition is the average of the grain ionic conductivity values measured for three different test samples of the same composition with varying geometrical aspect ratio. The typical error associated with the values of the reported grain ionic conductivity is < 2%. Furthermore, no density correction has been made on the reported grain ionic conductivity data as the density of all the sintered pellets is 98% of the theoretical density or above.

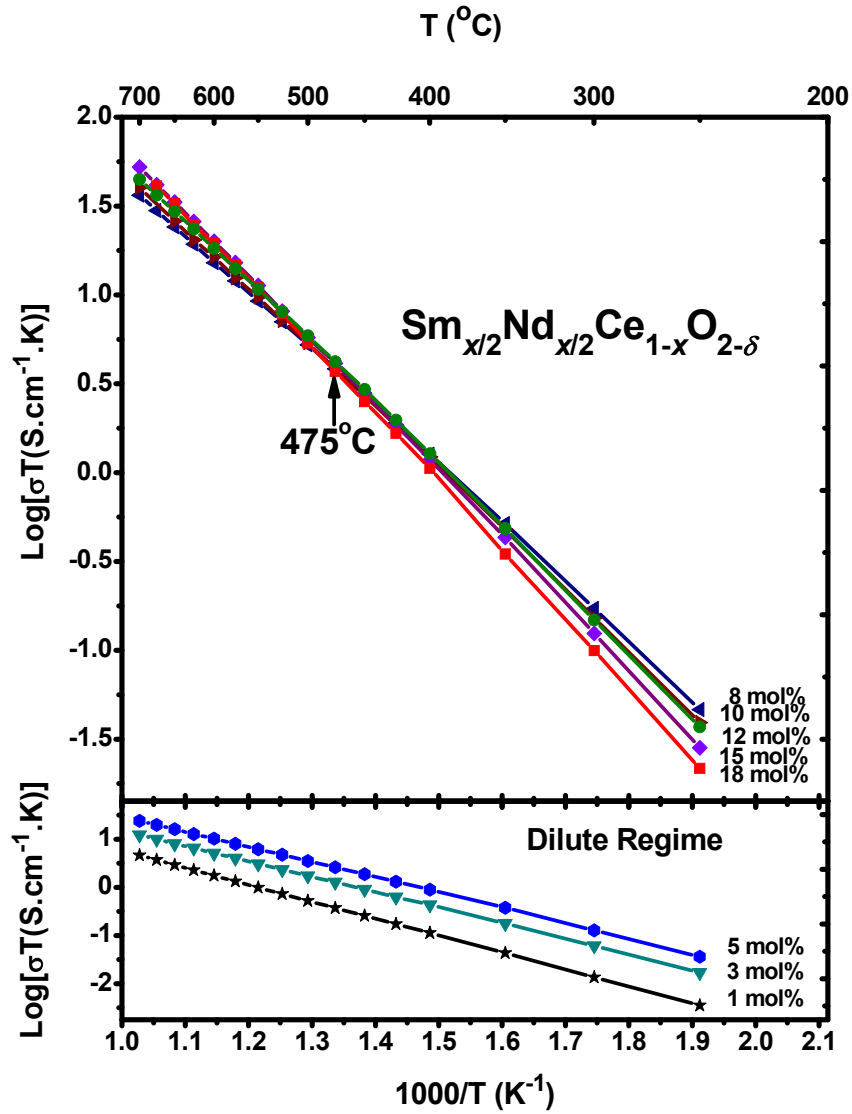


Figure 4-13. Arrhenius plots for the grain ionic conductivity of $\text{Sm}_{x/2}\text{Nd}_{x/2}\text{Ce}_{1-x}\text{O}_{2-\delta}$. Dopant concentration (x) is reported in mol%.

Figure 4-13 shows the Arrhenius plot of the grain ionic conductivity for $\text{Sm}_{x/2}\text{Nd}_{x/2}\text{Ce}_{1-x}\text{O}_{2-\delta}$. In the dilute regime, the grain ionic conductivity increases with the increase in the dopant concentration. This can be explained as there are limited defect interactions, and the ionic conductivity mainly depends upon the oxygen vacancy concentration. However above 5 mol%, the grain ionic conductivity decreases with increase in total dopant concentration (x) in the lower intermediate temperatures ($<$

450°C). This can be attributed to the increase in the defect interactions, which consequently decreases the number of low energy migration paths for oxygen vacancies, and lower the mobile oxygen vacancy concentration.

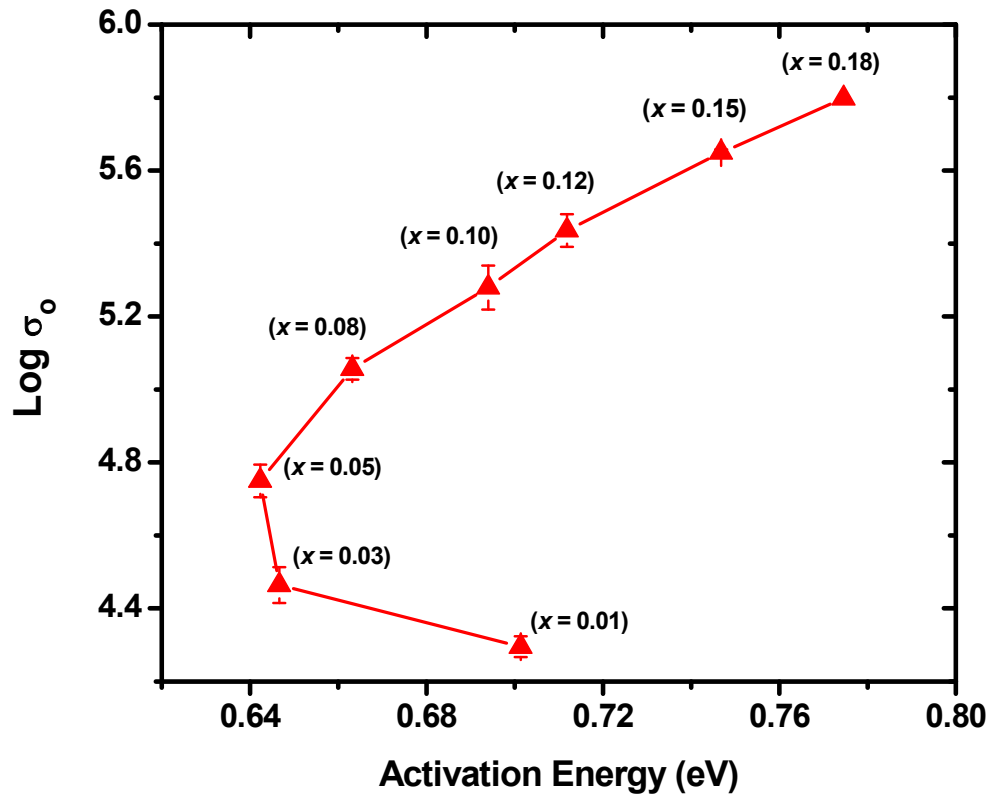


Figure 4-14. $\text{Log } \sigma_0$ as a function of activation energy measured below 475°C for $\text{Sm}_{x/2}\text{Nd}_{x/2}\text{Ce}_{1-x}\text{O}_{2.5}$. Line connecting data points for each composition is shown for visual aid.

Further, it can be seen from the Figure 4-13 that the Arrhenius plots for the grain ionic conductivity of all the compositions (> 5 mol %) converges to a common transition point, i.e. around 475°C. Around this temperature, conductivity becomes independent of dopant concentration. Such behavior was also previously reported in a wide range of materials and is commonly known as Meyer-Neldel rule.⁸⁷ Hohnke reported a similar trend for the ionic conductivity of $\text{Gd}_x\text{Ce}_{1-x}\text{O}_{2.5}$.⁸⁸ Recently, Stephens et al. observed

Meyer-Neldel behavior for the ionic conductivity in $\text{Nd}_x\text{Ce}_{1-x}\text{O}_{2-\delta}$ at higher Nd^{3+} concentration.⁸⁰ Based on the Meyer-Neldel rule, the magnitudes of the pre-exponential factor (σ_o), and activation energy (ΔH) can be linked by a following relationship,

$$\log \sigma_o = \alpha \Delta H + \beta \quad (4-8)$$

where α and β are constants. Figure 4-14 is a plot between the $\log \sigma_o$ and ΔH for $\text{Sm}_{x/2}\text{Nd}_{x/2}\text{Ce}_{1-x}\text{O}_{2-\delta}$. For the higher dopant concentration (> 5 mole %), $\log \sigma_o$ shows a linear relationship with ΔH which is consistent with the above mentioned relationship. Using least-squares linear regression, the values for α and β were found to be 6.6839 and 0.6443, respectively.

According to Almond et al., T_o , which is a common transition point for the Arrhenius plots for the conductivity data of all the composition, corresponds to an order-disorder transition in the mobile ion sublattices in a ionically conductive material.⁸⁹ Thus, above T_o , mobile ions no longer remained ordered on their lattice sites. According to Nowick et al., T_o can be seen as a transition temperature between the stage where most of the carriers are bound at various traps and the stage where all the carriers are free.⁸⁷ This suggests that above T_o , almost all the oxygen vacancies are free to migrate for any dopant concentration. It is difficult to confirm this hypothesis as the Arrhenius conductivity plots of $\text{Sm}_{x/2}\text{Nd}_{x/2}\text{Ce}_{1-x}\text{O}_{2-\delta}$ exhibit a gradual, rather than a sharp, change in slope with temperature. In addition, the extent of formation of local defect structures also increases with the increase in dopant concentration; therefore, higher oxygen vacancy concentration systems will require higher thermal energy (or temperature) for the oxygen vacancies to surpass the dopant interaction barrier.

Furthermore, for the dopant concentration in the dilute regime, Arrhenius plots never exhibit any crossover point.

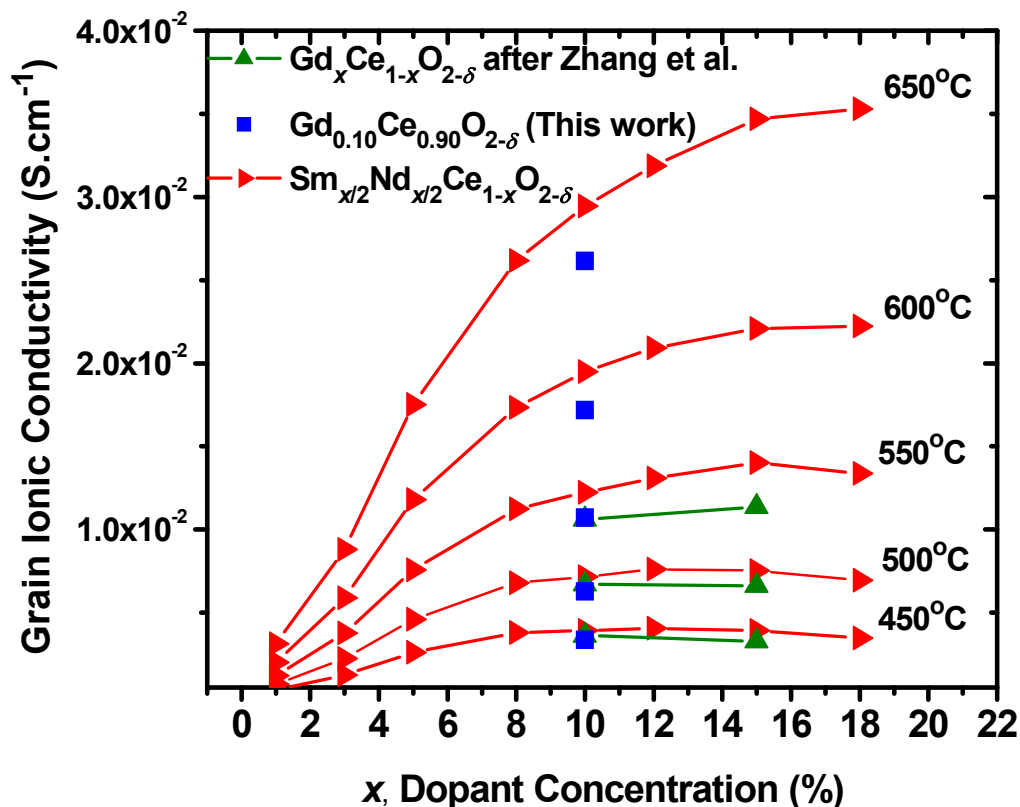


Figure 4-15. Grain ionic conductivity as a function of x , dopant concentration (mol%) in $\text{Sm}_{x/2}\text{Nd}_{x/2}\text{Ce}_{1-x}\text{O}_{2-\delta}$ and $\text{Gd}_x\text{Ce}_{1-x}\text{O}_{2-\delta}$. The grain ionic conductivity of $\text{Gd}_{0.10}\text{Ce}_{0.90}\text{O}_{2-\delta}$ (this work) at different temperatures is also plotted.^{53,67,77}

Figure 4-15 shows the grain ionic conductivity of $\text{Sm}_{x/2}\text{Nd}_{x/2}\text{Ce}_{1-x}\text{O}_{2-\delta}$ at different temperatures. For comparison, measurements of $\text{Gd}_{0.10}\text{Ce}_{0.90}\text{O}_{2-\delta}$ synthesized under identical experimental conditions in our lab are presented, as well as recent data on the same $\text{Gd}_x\text{Ce}_{1-x}\text{O}_{2-\delta}$ composition from Zhang et al.⁷⁷ Our $\text{Gd}_{0.10}\text{Ce}_{0.90}\text{O}_{2-\delta}$ data is comparable with grain ionic conductivity values reported by Zhang et al. At lower temperatures, the grain ionic conductivity of $\text{Sm}_{x/2}\text{Nd}_{x/2}\text{Ce}_{1-x}\text{O}_{2-\delta}$ looks comparable to that of $\text{Gd}_x\text{Ce}_{1-x}\text{O}_{2-\delta}$. However, with the increase in temperature $\text{Sm}_{x/2}\text{Nd}_{x/2}\text{Ce}_{1-x}\text{O}_{2-\delta}$

clearly surpasses $\text{Gd}_x\text{Ce}_{1-x}\text{O}_{2-\delta}$. Among all the compositions of $\text{Sm}_{x/2}\text{Nd}_{x/2}\text{Ce}_{1-x}\text{O}_{2-\delta}$, $\text{Sm}_{0.09}\text{Nd}_{0.09}\text{Ce}_{0.82}\text{O}_{2-\delta}$ exhibits the highest grain ionic conductivity above 600°C ($3.47 \times 10^{-2} \text{ S}\cdot\text{cm}^{-1}$ at 650°C). The reported ionic conductivity is 35% higher than that of GDC. Below 600°C , $\text{Sm}_{0.075}\text{Nd}_{0.075}\text{Ce}_{0.85}\text{O}_{2-\delta}$ is the highest ionically conductive material in doped ceria material.

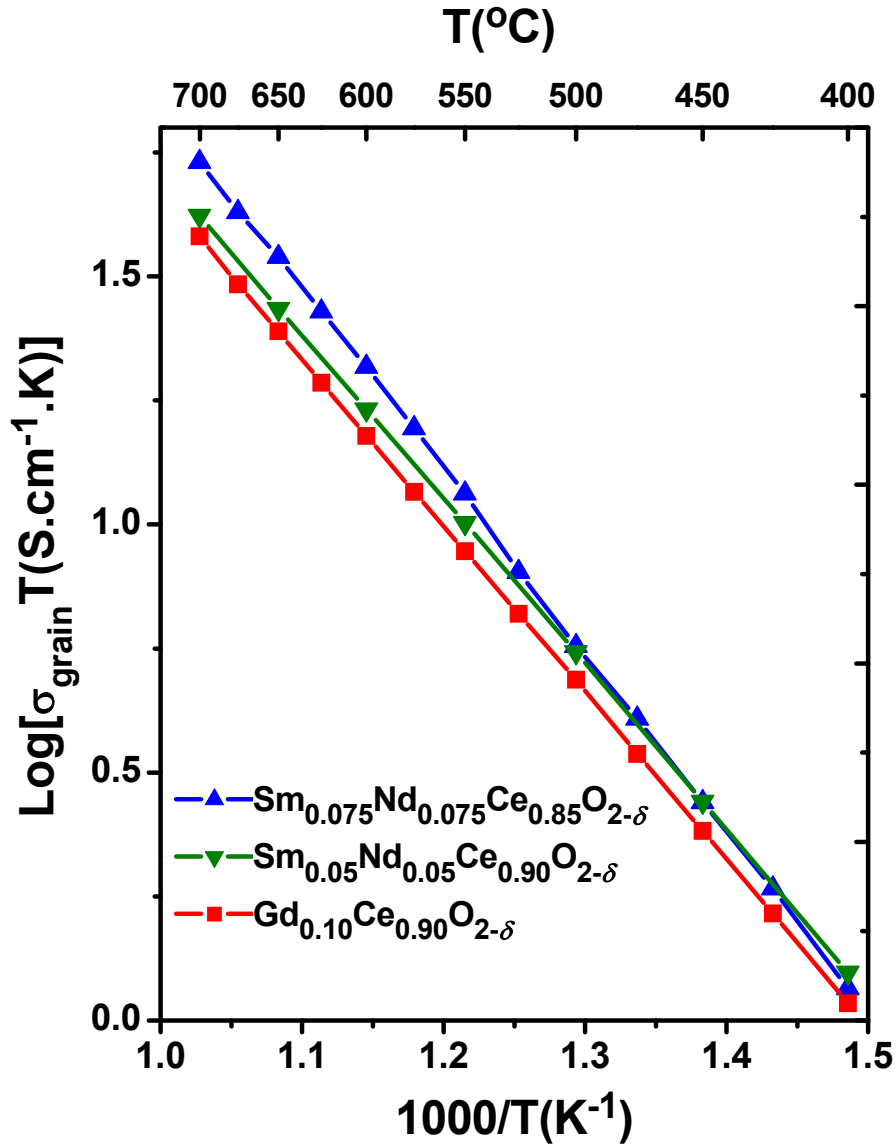


Figure 4-16. Arrhenius plot for the grain ionic conductivity of $\text{Sm}_{0.075}\text{Nd}_{0.075}\text{Ce}_{0.85}\text{O}_{2-\delta}$ and $\text{Sm}_{0.05}\text{Nd}_{0.05}\text{Ce}_{0.90}\text{O}_{2-\delta}$. The grain ionic conductivity of $\text{Gd}_{0.10}\text{Ce}_{0.90}\text{O}_{2-\delta}$ (our work) at different temperatures is also plotted.⁶⁷

At 550°C, the grain ionic conductivity of $\text{Sm}_{0.075}\text{Nd}_{0.075}\text{Ce}_{0.85}\text{O}_{2-\delta}$ and $\text{Sm}_{0.05}\text{Nd}_{0.05}\text{Ce}_{0.90}\text{O}_{2-\delta}$ was found to be $14.0 \times 10^{-3} \text{ S}\cdot\text{cm}^{-1}$ and $12.2 \times 10^{-3} \text{ S}\cdot\text{cm}^{-1}$, respectively. The measured grain ionic conductivity data of $\text{Sm}_{0.075}\text{Nd}_{0.075}\text{Ce}_{0.85}\text{O}_{2-\delta}$ and $\text{Sm}_{0.05}\text{Nd}_{0.05}\text{Ce}_{0.90}\text{O}_{2-\delta}$ was 30% and 14% higher than that of $\text{Gd}_{0.10}\text{Ce}_{0.90}\text{O}_{2-\delta}$ ($\sim 10.7 \times 10^{-3} \text{ S}\cdot\text{cm}^{-1}$), respectively, which is the widely accepted material to exhibit highest ionic conductivity among doped ceria. This is a proof that, on the basis of conductivity, $\text{Sm}_{x/2}\text{Nd}_{x/2}\text{Ce}_{1-x}\text{O}_{2-\delta}$ is the most promising ceria-based electrolyte for SOFCs operating in the intermediate temperature range.

As mentioned earlier, the higher grain ionic conductivity of $\text{Sm}_{x/2}\text{Nd}_{x/2}\text{Ce}_{1-x}\text{O}_{2-\delta}$ electrolytes can be attributed to the increase in the number of equi-interaction energy sites which lower the activation energy and facilitate oxygen ion diffusion in the lattice. In addition to the activation energy, using co-dopants also enhances the configuration entropy of the system which, in turn, increases the pre-exponential factor in the Arrhenius relationship. Figure 4-16 shows the Arrhenius plot for the grain ionic conductivity of $\text{Sm}_{0.05}\text{Nd}_{0.05}\text{Ce}_{0.90}\text{O}_{2-\delta}$, $\text{Sm}_{0.075}\text{Nd}_{0.075}\text{Ce}_{0.85}\text{O}_{2-\delta}$ and $\text{Gd}_{0.10}\text{Ce}_{0.90}\text{O}_{2-\delta}$ in intermediate temperatures. The results clearly show that $\text{Sm}_{0.05}\text{Nd}_{0.05}\text{Ce}_{0.90}\text{O}_{2-\delta}$ exhibits higher grain ionic conductivity than that of $\text{Gd}_{0.10}\text{Ce}_{0.90}\text{O}_{2-\delta}$ at almost all the temperatures. However, in the high intermediate temperature, $\text{Sm}_{0.075}\text{Nd}_{0.075}\text{Ce}_{0.85}\text{O}_{2-\delta}$ is the material that exhibits the highest grain ionic conductivity.⁶⁷ Table 4-1 compares the σ , ΔH , and σ_0 of $\text{Sm}_{0.05}\text{Nd}_{0.05}\text{Ce}_{0.90}\text{O}_{2-\delta}$, $\text{Sm}_{0.075}\text{Nd}_{0.075}\text{Ce}_{0.85}\text{O}_{2-\delta}$ and $\text{Gd}_{0.10}\text{Ce}_{0.90}\text{O}_{2-\delta}$. The error in the values of σ , ΔH , and σ_0 was calculated by measuring the grain ionic conductivity of the test samples with different geometrical aspect ratios. Given the error associated with the experimentation, it can be seen from the Table 4-1

that $\text{Sm}_{0.05}\text{Nd}_{0.05}\text{Ce}_{0.90}\text{O}_{2-\delta}$ exhibits higher σ than that of $\text{Gd}_{0.10}\text{Ce}_{0.90}\text{O}_{2-\delta}$. The result can be attributed to the higher σ_0 and lower ΔH of $\text{Sm}_{0.05}\text{Nd}_{0.05}\text{Ce}_{0.90}\text{O}_{2-\delta}$ than that of $\text{Gd}_{0.10}\text{Ce}_{0.90}\text{O}_{2-\delta}$. This validates the hypothesis that co-dopants based on Pm^{3+} atomic number (with ionic radii in the close proximity to Pm^{3+}) results in the enhancement of grain ionic conductivity. Although, $\text{Sm}_{0.075}\text{Nd}_{0.075}\text{Ce}_{0.85}\text{O}_{2-\delta}$ exhibits the highest ionic conductivity among doped ceria, it shows higher ΔH than that of $\text{Gd}_{0.10}\text{Ce}_{0.90}\text{O}_{2-\delta}$ and $\text{Sm}_{0.05}\text{Nd}_{0.05}\text{Ce}_{0.90}\text{O}_{2-\delta}$. However, it possesses higher σ_0 which shows dominant effect on ionic conductivity compared to ΔH . This indicates that for a high ionic conductive material, both a low ΔH and a maximum σ_0 are required.

Table 4-1. Comparison of the ΔH and $\log \sigma_0$ for $\text{Gd}_{0.10}\text{Ce}_{0.90}\text{O}_{2-\delta}$, $\text{Sm}_{0.05}\text{Nd}_{0.05}\text{Ce}_{0.90}\text{O}_{2-\delta}$ and $\text{Sm}_{0.075}\text{Nd}_{0.075}\text{Ce}_{0.85}\text{O}_{2-\delta}$ measured below 550°C . Further, σ of these oxide materials at 550°C is also reported.⁶⁷

Materials	σ ($\text{S}\cdot\text{cm}^{-1}\cdot\text{K}$)	ΔH (eV)	$\text{Log}_{10} [\sigma_0$ ($\text{S}\cdot\text{cm}^{-1}\cdot\text{K}$)]
$\text{Gd}_{0.10}\text{Ce}_{0.90}\text{O}_{2-\delta}$	$10.7 \pm 0.4 \times 10^{-3}$	0.6900 ± 0.0030	5.184 ± 0.020
$\text{Sm}_{0.05}\text{Nd}_{0.05}\text{Ce}_{0.90}\text{O}_{2-\delta}$	$12.2 \pm 0.3 \times 10^{-3}$	0.6867 ± 0.0003	5.215 ± 0.002
$\text{Sm}_{0.075}\text{Nd}_{0.075}\text{Ce}_{0.85}\text{O}_{2-\delta}$	$14.0 \pm 0.2 \times 10^{-3}$	0.7634 ± 0.0038	5.5565 ± 0.020

Figure 4-17 shows the grain ionic conductivity trend of $\text{Sm}_{x/2}\text{Nd}_{x/2}\text{Ce}_{1-x}\text{O}_{2-\delta}$ as a function of dopant concentration at different temperatures. Initially, the grain ionic conductivity increases with the increase in dopant concentration. However, it reaches a maximum and then substantially drops beyond certain dopant concentration at lower temperatures. Degradation of the grain ionic conductivity at higher dopant concentration is related to the formation of local defect structures, which lowers the mobile oxygen vacancy concentration. Moreover, it is interesting to observe that as the temperature increases, the maxima of the grain ionic conductivity in the Figure 4-17 shifts toward the higher dopant concentration. A similar trend was also observed in $\text{Gd}_x\text{Ce}_{1-x}\text{O}_{2-\delta}$ and $\text{Y}_x\text{Ce}_{1-x}\text{O}_{2-\delta}$ by Zhang et al.⁷⁷ and Tian et al.⁶², respectively. This

behavior indicates the dissociation of complex defect structures (present mainly at higher dopant concentration) at higher temperatures to give mobile oxygen vacancies. Since the ionic conductivity depends mainly on the mobile oxygen vacancy concentration, therefore, with the increase in temperature ionic conductivity maxima shift toward higher dopant concentrations.

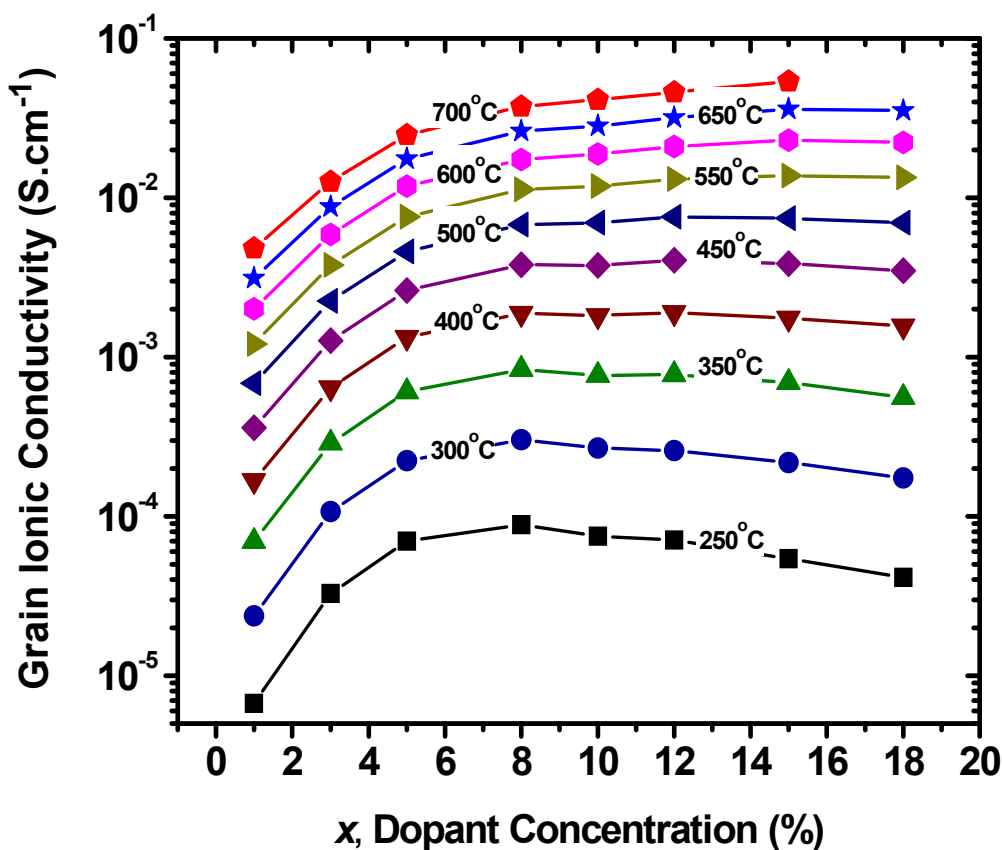


Figure 4-17. Grain ionic conductivity of $\text{Sm}_{x/2}\text{Nd}_{x/2}\text{Ce}_{1-x}\text{O}_{2-\delta}$ as a function of x , dopant concentration (mol%). Lines connecting data points for different temperatures is shown for visual aid.

Since the Arrhenius plot for the grain ionic conductivity exhibits a gradual decrease in the slope at higher intermediate temperatures, it is difficult to distinguish the regimes where the association-dissociation of oxygen vacancies is taking place. As mentioned earlier, the cross-over point of Arrhenius plots for the grain ionic conductivity of

$\text{Sm}_{x/2}\text{Nd}_{x/2}\text{Ce}_{1-x}\text{O}_{2-\delta}$ (for $x > 0.05$) was interpreted as the association - dissociation temperature of oxygen vacancies, hence, for the purpose of this study it is assumed that the transition occurs at 475°C . Using a least-squares algorithm, high and low temperature region of Arrhenius plot is linearly fitted. The fit of the data is generally quite good, with correlation coefficients for a linear least-squares fit between 0.9997 and 0.9999. Activation energy values for the ionic conduction in these materials are calculated from the high and low temperature gradients of the fitted Arrhenius plots.

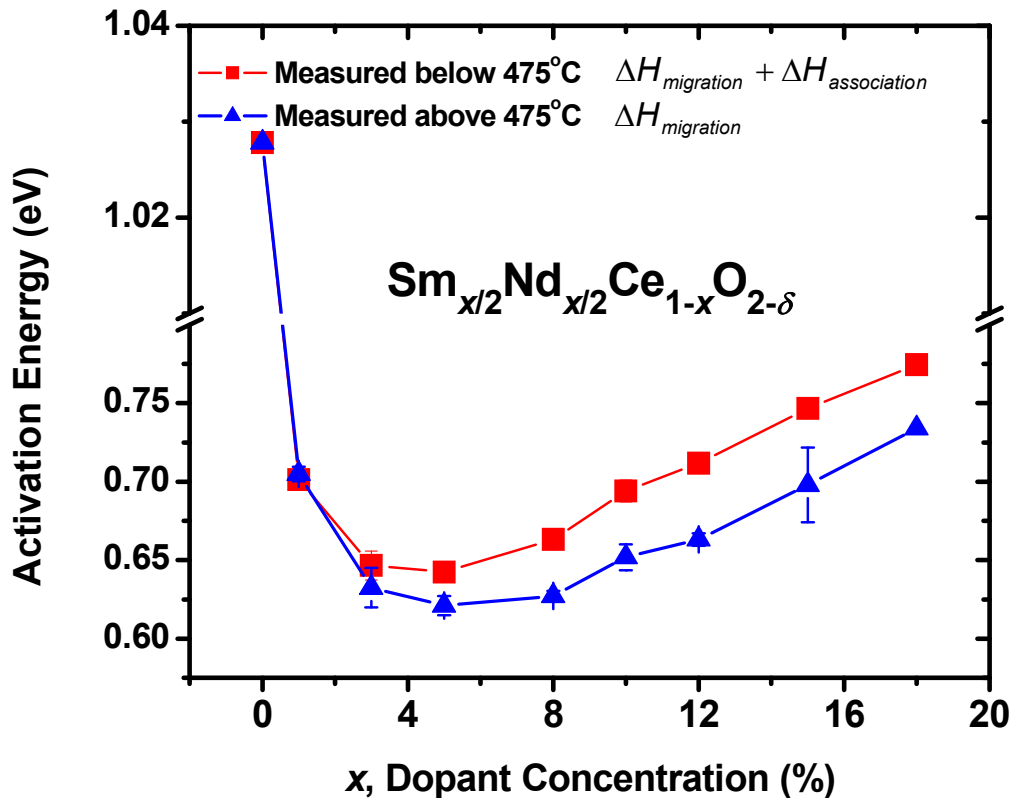


Figure 4-18. Activation energy for oxygen ion diffusion in $\text{Sm}_{x/2}\text{Nd}_{x/2}\text{Ce}_{1-x}\text{O}_{2-\delta}$ measured below 475°C and above 475°C , as a function of x . Line connecting data points for different temperatures is shown for visual aid.

Figure 4-18 shows the plots of activation energy for the grain ionic conductivity of $\text{Sm}_{x/2}\text{Nd}_{x/2}\text{Ce}_{1-x}\text{O}_{2-\delta}$, measured below 475°C and above 475°C , as a function of dopant

concentration (x). The activation energy measured in the range of 475°C - 250°C, can be seen as a sum of two contributions, the association enthalpy ($\Delta H_{\text{association}}$) and migration enthalpy ($\Delta H_{\text{migration}}$). Initially, the addition of dopant cations in ceria decreases the activation energy for oxygen vacancies diffusion. However, around 5 mol% dopant concentrations, activation energy plot exhibits a minimum. A similar trend of activation energy as a function of dopant concentration was earlier reported by Faber et al.¹⁴ for various rare earth oxides doped ceria systems. According to Faber et al., this decrease is due to the presence of attractive interactions between dopant cations and oxygen vacancies, with the increase in dopant concentration leading to an increase in the number of percolation paths. However, above 5 mol% dopant concentration, with increasing dopant concentration, there is an increasing probability that the dopant cations sit in close proximity. This results in the formation of “deep traps” that accommodate all existing mobile oxygen vacancies.¹⁴ Consequently, the oxygen vacancy diffusion paths become more resistive and therefore the activation energy for ionic conduction increases.

As most of the oxygen vacancies above 475°C are assumed to be mobile, the reported activation energy measured above 475°C (in Figure 4-18) is equal to the migration enthalpy of the oxygen ion diffusion. It can be seen that the $\Delta H_{\text{migration}}$ also experiences a minima at 5 mol% dopant concentration. Similar results have been observed for activation energy measured at higher temperatures for $\text{Nd}_x\text{Ce}_{1-x}\text{O}_{2-\delta}$ system, by Stephens et al.⁸⁰ However, based on nuclear magnetic resonance (NMR) studies, Fuda et al.⁹⁰ concluded that the migration enthalpy is independent of dopant concentration. Their results are not in agreement with the migration enthalpy data.

According to Ralph et al.⁹¹, compositional independence of migration enthalpy only holds good in the dilute regime. Assuming the dilute regime in $\text{Sm}_{x/2}\text{Nd}_{x/2}\text{Ce}_{1-x}\text{O}_{2-\delta}$ system extends to 5 mol%, it can be seen that the migration enthalpy decreases with the increase in dopant concentration. This behavior of $\Delta H_{\text{migration}}$ can be explained in terms of continuous network of oxygen vacancies. As the dopant concentration increase in the dilute regime, number of low energy migration paths increase which effectively decrease the migration enthalpy.

4.2.2.4 Summary and conclusion

In search of advanced materials that show improved ionic conductivity, both pre-exponential factor and the activation energy (in the Arrhenius relationship) for oxygen diffusion need to be optimized. Co-dopants were used to suppress the oxygen vacancy ordering and increase the pre-exponential factor in the system. The relative co-dopant concentration was based on the effective atomic number of Pm^{3+} . This novel approach was based on the computational work which suggests using co-dopant with an average effective atomic number of Pm (61). By doing so, the increase in the number of equi-interaction energy sites of oxygen vacancy was expected, which as a result, facilitates oxygen diffusion. This in turn increased the ionic conductivity of the material. Therefore, a co-doping scheme using Sm^{3+} and Nd^{3+} provided the experimental scenario to test this hypothesis. Lattice parameter as a function composition obeys Vegard's law which indicates, short range oxygen ordering in $\text{Sm}_{x/2}\text{Nd}_{x/2}\text{Ce}_{1-x}\text{O}_{2-\delta}$ system is not as pronounced as in other singly doped ceria system. Among all the compositions of $\text{Sm}_{x/2}\text{Nd}_{x/2}\text{Ce}_{1-x}\text{O}_{2-\delta}$, $\text{Sm}_{0.09}\text{Nd}_{0.09}\text{Ce}_{0.82}\text{O}_{2-\delta}$ exhibits the highest grain ionic conductivity above 600°C ($3.47 \times 10^{-2} \text{ S}\cdot\text{cm}^{-1}$ at 650°C). The grain ionic conductivity of $\text{Sm}_{0.09}\text{Nd}_{0.09}\text{Ce}_{0.82}\text{O}_{2-\delta}$ was found to be 35% higher than that of

$Gd_{0.10}Ce_{0.90}O_{2-\delta}$ at 650°C. Below 600°C, $Sm_{0.075}Nd_{0.075}Ce_{0.85}O_{2-\delta}$ is the highest ionically conductive material in doped ceria material. At 550°C, the grain ionic conductivity of $Sm_{0.075}Nd_{0.075}Ce_{0.85}O_{2-\delta}$ was found to be 30% higher than that of $Gd_{0.10}Ce_{0.90}O_{2-\delta}$. Thus, it was shown that co-doping based on Pm atomic number results in the enhancement of ionic conductivity. Further, at higher dopant concentrations, $Sm_{x/2}Nd_{x/2}Ce_{1-x}O_{2-\delta}$ system follows Meyer-Neldel rule. Taking the common transition point of Arrhenius plots as association-dissociation temperature of oxygen vacancies, migration enthalpy in $Sm_{x/2}Nd_{x/2}Ce_{1-x}O_{2-\delta}$ system was calculated. It was shown that the migration enthalpy do have dependence on dopant concentration in dilute regime. Furthermore, shift in the grain ionic conductivity maxima toward higher dopant concentration with the increase in temperature, was observed in $Sm_{x/2}Nd_{x/2}Ce_{1-x}O_{2-\delta}$ system.

4.3 Processing Effects on Ionic Conductivity

In light of the comparison here proposed between singly doped and co-doped electrolytes, it is important to note that, for example, a literature survey of the reported grain ionic conductivity of $Gd_{0.10}Ce_{0.90}O_{2-\delta}$ reveals a wide range of values as presented in Figure 4-1 and Figure 4-19. Inspection of the experimental procedure followed in each work indicates a strong correlation between the powder synthesis technique and the conductivity observed. Typically, co-precipitation techniques lead to higher conductivity values and solid state processing methods result in lower ones.⁶³ Figure 4-19 compares the grain ionic conductivity at 600°C of singly doped ceria reported here with that from literature. Since in our work solid state processing was employed, as expected, the grain ionic conductivity here reported for $Gd_{0.10}Ce_{0.90}O_{2-\delta}$ is lower than that of Steele.¹³ On the other hand, its conductivity is higher that of Reddy et al.⁶¹ Similar is the case with $Sm_{0.10}Ce_{0.90}O_{2-\delta}$. However, our $Nd_{0.10}Ce_{0.90}O_{2-\delta}$ exhibits

much higher grain ionic conductivity than reported by Stephens et al.⁸⁰ and Li et al.⁷⁸ It can be inferred that besides composition, processing related variables such as grain size distribution, dopant redistribution within the grain, grain impurities, and extended grain defects also play a vital role in the enhancement of the grain ionic conductivity of the electrolytes.

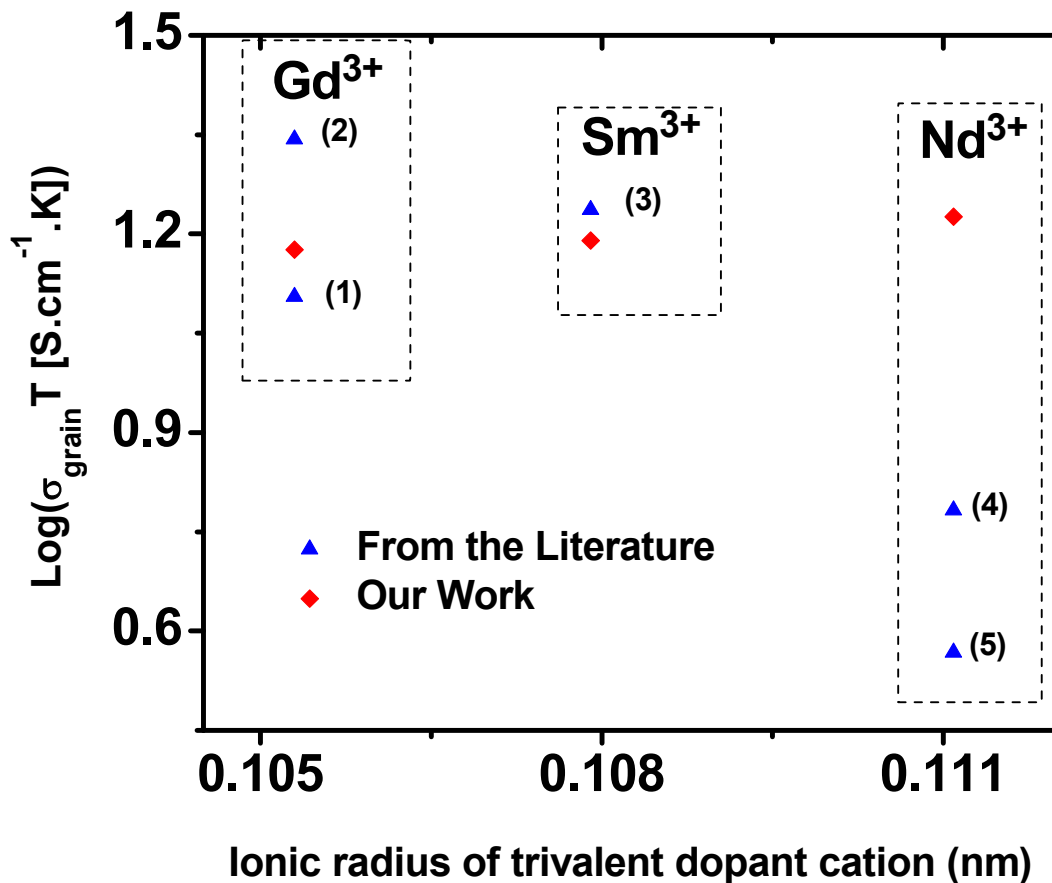


Figure 4-19. Grain ionic conductivity comparison at 600°C between our work and literature. Grain ionic conductivity data (1), (2), (3), (4), and (5) is taken from Reddy et al.⁶¹, Steele¹³, Zhan et al.⁷⁶, Stephens et al.⁸⁰, and Li et al.⁷⁸, respectively.

Clearly, a consistent set of data for the ionic conductivity of all the doped ceria systems is required in which the processing variable to synthesize ceramic samples remain constant. This will provide a clear idea about the ideal dopant for ceria which

shows the highest ionic conductivity, when all the materials are synthesized under similar processing conditions. After identifying the highest ionic conductive material, the ionic conductivity can be improved using lower sintering temperature and higher purity processing conditions. The variation of processing conditions to improve the ionic conductivity of doped ceria will be discussed in the Chapter 6.

CHAPTER 5
STRUCTURE-PROPERTY RELATIONSHIPS IN DOPED CERIA MATERIALS AT
HIGH TEMPERATURES

5.1 Introduction

High ionically conductive electrolyte materials are critical for the development of SOFCs operating in intermediate temperature range. Acceptor doped ceria materials are potential candidates for this application. For a given dopant valence (di- or trivalent) and concentration, oxygen ion conductivity in ceria system depends primarily upon the dopant size. According to Kilner et al.²¹, maximum ionic conductivity is achieved in the system which shows neither contraction nor expansion upon the addition of dopant cation. For example, most of the ionic radii of commonly used dopant cations lie closer to the ionic radius of Ce^{4+} than Zr^{4+} . Thus, it is expected that for the same dopant cation, activation energy for oxygen vacancy diffusion involved in doped CeO_2 systems must be lower than that in doped ZrO_2 . From Chapter 2, it is known that activation energy is comprised of migration and association enthalpies. The migration enthalpy in both the systems is almost comparable; therefore, it is the association enthalpy (of local defect structures) that dictates the oxygen ionic conductivity in the material. Table 5-1 compares the migration and association enthalpies in ZrO_2 and CeO_2 doped with Ca^{2+} .²¹ It can be seen that the association enthalpy in doped CeO_2 system is lower than that in doped ZrO_2 , which clearly indicates that the lower ionic radius difference between the dopant (r_d) and host (r_h) cations, results in higher ionic conductivity.

Although the difference in the host and dopant cations ionic radius ($r_h - r_d$) is important, the creation of oxygen vacancies in the host lattice (to maintain charge neutrality) by the addition of acceptor dopants, also influences the lattice geometry. The presence of oxygen vacancies instead of oxygen anions results in the contraction of the

lattice. Given $(r_h - r_d)$ is negligible, the increase in the dopant concentration results in the contraction of the host lattice.⁹² For example, as presented in Chapter 4, in $\text{Lu}_x\text{Ce}_{1-x}\text{O}_{2-\delta}$ system, although the ionic radius difference between Lu^{3+} and Ce^{4+} is very small ($r_{\text{Lu, VIII}}^{3+} = 0.977 \text{ \AA}$ and $r_{\text{Ce, VIII}}^{4+} = 0.97 \text{ \AA}$), the increase in the dopant concentration contracts the host ceria lattice.^{7,48}

Table 5-1. Activation energies for ZrO_2 and CeO_2 systems doped with Ca^{2+} .²¹

Activation Energy	Ca-doped ZrO_2	Ca-doped CeO_2
Migration Enthalpy (eV)	0.68	0.61
Association Enthalpy (eV)	1.00	0.64

Aleksandrov et al.⁹³ estimated the lattice strain in $\text{Y}_2\text{O}_3\text{-ZrO}_2$ solid solution as a function of dopant concentration, which was later modified by Ingel et al.⁹⁴, by adding the dopant size effect on the lattice. However, the proposed model does not fit to other fluorite AO_2 type oxide (where A is a cation) systems, as it does not precisely take into account the effect of oxygen vacancies. In order to compensate the oxygen ion vacancies, some arbitrary values of ionic radii were used. Glushkova et al.⁹² used both ionic radius difference (between host and dopant cations), and the oxygen vacancies creation factors into account to describe the change in the lattice constant of lanthanide doped fluorite oxides. The contraction of the lattice due to the formation of oxygen vacancies was described in terms of an effective oxygen-ionic radius, which becomes smaller with the increase in dopant content. The effective oxygen ionic radius ($r_{\text{O}}^{\text{effective}}$) was defined as,

$$r_{\text{O}}^{\text{effective}} = 1.38(1 - m)^{\frac{1}{3.6}} \quad (5-1)$$

where 1.38 Å is the ionic radius of O²⁻ (four-fold co-ordination), m is the molar concentration of lanthanide oxide (LnO_{1.5}), and 3.6 is the correction factor for the association of oxygen vacancies. The units of $r_O^{effective}$ is Å. The model shows good agreement with the experimental data for LnO_{1.5}-ZrO₂ and LnO_{1.5}-HfO₂ systems. However, lattice parameter calculated from the model shows deviation from the measured values for LnO_{1.5}-CeO₂ and LnO_{1.5}-ThO₂ systems. The deviation is even larger, if alkaline dopant cations are used instead of LnO_{1.5}.

Kim²² studied the elastic strain formed in the host fluorite oxide lattice by the substitution of acceptor dopant cations for host cations. Using multiple regression analysis, empirical relationship for the lattice parameter change in the doped ceria system, as a function of the difference in the ionic radius between host and dopant cation ($r_h - r_d$), dopant valence and dopant concentration was established for room temperature. Equation (5-2) shows the lattice change for the ceria solid solutions,

$$a_{Ce} = 5.413 + \sum_k (0.22\Delta r_k + 0.0015\Delta z_k)m_k \quad (5-2)$$

where a_{Ce} (in Å) is the lattice parameter of the ceria solid solution at room temperature, Δr_k (in Å) is the ionic radius difference ($r_k - r_h$) between k^{th} dopant (r_k) and host (r_h) cations, Δz_k is the valence difference ($z_k - z_h$) between k^{th} dopant (z_k) and host (z_h) cations, and m_k is the mole percent of the k^{th} dopant cation. It was assumed that the solid solution of doped ceria obeys Vegard's law i.e., a linear relationship exists between lattice parameter and concentration of solute.⁸⁴

Using equation (5-2), the critical ionic radius (r_c) of the dopant was proposed. Dopant with ionic radius equal to r_c , will neither cause expansion nor contraction in the host fluorite oxide lattice. For the trivalent dopant cation and host ceria, r_c was

determined to be 1.038 Å.²² Based on Kilner et al.'s prediction, dopant with r_c is the ideal dopant for ceria to show highest ionic conductivity. Thus, the ionic conductivity in doped ceria materials depends upon the difference ($|r_d - r_c|$) between the ionic radius of the dopant cation and r_c . The lower the $|r_d - r_c|$ value for a particular dopant, the higher the ionic conductivity for that system is expected to be. Using a similar argument, Kim suggested that Gd^{3+} exhibits the highest ionic conductivity as the ionic radius of Gd^{3+} ($r_{Gd,III}^{3+} = 1.053 \text{ Å}$) lies close to r_c .⁴⁸

Hong et al.⁷⁴ proposed a model to estimate lattice parameter of trivalent doped ceria at room temperature using a different approach. Oxygen vacancy was considered to be one of the species, and a radius (r_{V_o}) was assigned to it which was assumed to be constant with respect to dopant concentration and dopant ionic radius. Thus, r_{V_o} has a unique value for a given solid solution. Using this approach, lattice parameter (a) as a function of dopant concentration (x) and dopant ionic radius (r_d) was proposed and is given by,

$$a = \frac{4}{\sqrt{3}} \times 0.9971 \times [r_d - r_{Ce} - 0.25 \times r_o + 0.25 \times r_{V_o}] \times x + \frac{4}{\sqrt{3}} \times 0.9971 \times [r_{Ce} + r_o] \quad (5-3)$$

where r_{Ce} and r_o are the ionic radius of Ce^{4+} and O^{2-} , respectively. Equation (5-3) obeys Vegard's law. Using this model, the critical ionic radius (r_c) for the trivalent dopant cation was proposed for ceria, the definition of which is similar to Kim's definition of r_c . The r_c is defined for which the Vegard's slope = 0. For the trivalent dopant cations, the r_c value is estimated to be 1.024 Å by plotting measured values of Vegard's slopes for a number of dopant cations against the dopant cation ionic radius.

In the literature, it has been reported that Sm^{3+} and Gd^{3+} are the ideal dopants for ceria to show higher conductivity among other dopant cations.^{9,71} The ionic radius of Sm^{3+} ($r_{\text{Sm,VIII}}^{3+} = 1.079 \text{ \AA}$) is higher than that of Gd^{3+} and shows $|r_d - r_c|$ value of 0.041 \AA .⁴⁸ The r_c value is taken from the Kim's²² proposed model. Also, it is known that Dy^{3+} shows lower ionic conductivity than that of Gd^{3+} and Sm^{3+} .⁹ The $|r_d - r_c|$ value is lowest for Dy^{3+} (0.011 \AA), when compared with Gd^{3+} (0.015 \AA), and Sm^{3+} (0.041 \AA). These results contradict Kilner et al.'s hypothesis.

It is important to note that the r_c derived by Kim, was obtained from the elastic strain (or lattice parameter) measured at room temperature. The ionic conductivity of doped ceria electrolyte materials is usually measured between 400°C to 700°C . It may be possible that the r_c value increases with the increasing temperature. Hence, it is important to test the Kilner et al.'s hypothesis by obtaining r_c value at higher temperatures.²¹ Also important is the fact that the ionic conductivity of these electrolyte materials depend upon processing variables.^{7,63} Keeping the processing conditions constant, it is important to synthesize ceria based materials with different trivalent dopants. This will provide a consistent set of ionic conductivity data that can be used to obtain elastic strain – conductivity relationships at higher temperatures.

As discussed by Inaba et al.⁹ in the review of ceria based electrolytes, trivalent acceptor cations as dopants exhibit higher ionic conductivity than divalent cations in ceria, therefore, in the present work, trivalent cations were used as dopants for host ceria. Polycrystalline ceramic materials of $\text{D}_{0.10}\text{Ce}_{0.90}\text{O}_{2-\delta}$ (where $\text{D}^{3+} = \text{Lu}^{3+}, \text{Yb}^{3+}, \text{Er}^{3+}, \text{Y}^{3+}, \text{Dy}^{3+}, \text{Gd}^{3+}, \text{Sm}^{3+}, \text{Nd}^{3+}$) were synthesized under similar experimental conditions described in Chapter 3. In addition to this, different compositions of $\text{Sm}_{x/2}\text{Nd}_{x/2}\text{Ce}_{1-x}\text{O}_{2-\delta}$

($x = 0.01, 0.03, 0.05, 0.08, 0.10, 0.12, 0.15, 0.20$) were also processed using same experimental procedures. Ionic conductivity measurements were performed using two-point probe ac impedance spectroscopy, from 250°C to 700°C in air. This was followed by high temperature X-ray diffraction (XRD) of the crushed sintered samples of doped ceria materials from room temperature to 600°C. Curved position sensitive diffractometer CPS120 (with modified Debye - Scherrer geometry) was used to perform high temperature XRD. A monochromator crystal was used to separate out Cu $K_{\alpha 1}$ from the incident X-ray beam. The ground powders were placed on top of an alumina tube, inside a water-cooled furnace. Furnace temperature was controlled using a commercial software with 2°C tolerance. Samples were first heated to 600°C, and then measurements were performed at different temperatures (in air), while the furnace temperature is lowered. A ramp rate of 8°C/minute was maintained for the furnace to heat up to 600°C and then cool down to room temperature. Before the start of the data acquisition at any temperature, around 10 minutes of waiting time was given for the material to come into equilibrium with the temperature. Data acquisition at each temperature was performed for 1 h. Peak positions in the XRD pattern were determined by fitting each individual peak with a symmetric Pearson VII profile to model Cu $K_{\alpha 1}$ using a commercially available software (i.e., Solver add-in within Microsoft Excel spreadsheet package). The best estimate of the lattice constant was calculated using the extrapolation method.⁶⁶ This method corrects for the most common error in lattice parameter determination, that of vertical sample displacement.⁹⁵ Further information about this method is given in Appendix D.

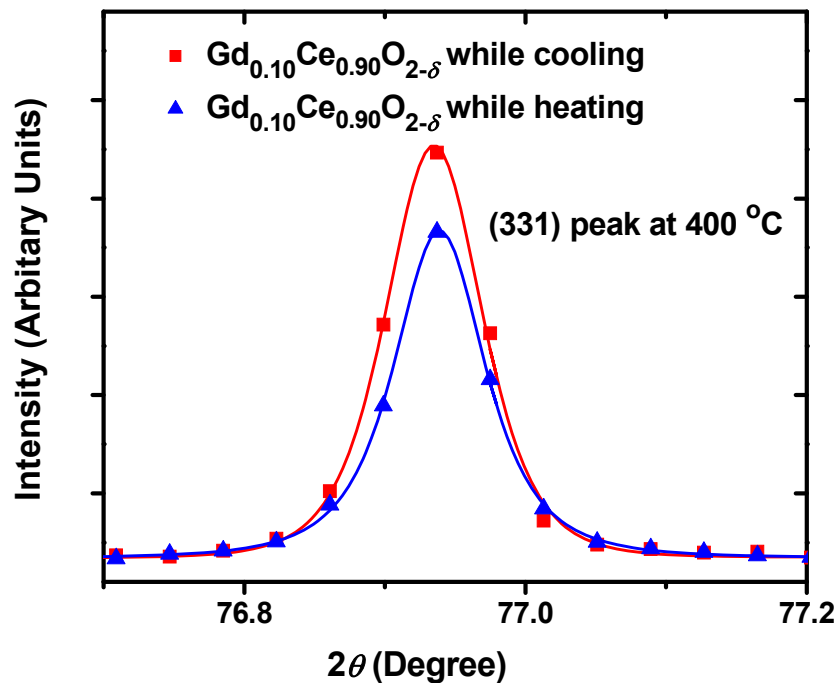


Figure 5-1. The (331) peak in XRD profiles of $Gd_{0.10}Ce_{0.90}O_{2-\delta}$ measured at $400^{\circ}C$ in different ramping conditions. Dots are the experimental data, and the line is the symmetric Pearson VII function peak fit.

In order to confirm that the XRD patterns obtained while the furnace is cooling down and heating up are same, measurements were taken for $Gd_{0.10}Ce_{0.90}O_{2-\delta}$ ceramic in both situations. Figure 5-1 shows the fitted (331) peak of $Gd_{0.10}Ce_{0.90}O_{2-\delta}$ at $400^{\circ}C$ in air. The fitted peak profile parameters for both the conditions are given below (in Table 5-2).

Table 5-2. Fitted (331) XRD peak profile parameters for $Gd_{0.10}Ce_{0.90}O_{2-\delta}$ at $400^{\circ}C$, measured while the furnace is heating up and cooling down.

	2θ (Degrees)	Full width of half max. (Degrees)
Heating	76.939	0.077
Cooling	76.935	0.081

It can be seen that in both profiles, peak position values are very close to each other. This clearly indicates that there is no evidence of significant thermal hysteresis present in the material.

5.2 Crystal Structure of Trivalent Acceptor Doped Ceria at High Temperature

5.2.1 High Temperature X-Ray Diffraction

High temperature XRD patterns were taken for different doped ceria systems at temperatures ranging from 25°C to 600°C, in air. Figure 5-2 and Figure 5-3 show the XRD profiles of $\text{Sm}_{0.10}\text{Ce}_{0.90}\text{O}_{2-\delta}$ and $\text{Lu}_{0.10}\text{Ce}_{0.90}\text{O}_{2-\delta}$, respectively, measured at different temperatures. All the patterns look similar to that of pure ceria shown in Chapter 2, which clearly indicates that, both $\text{Sm}_{0.10}\text{Ce}_{0.90}\text{O}_{2-\delta}$ and $\text{Lu}_{0.10}\text{Ce}_{0.90}\text{O}_{2-\delta}$ ceramics, remain phase pure cubic at intermediate temperature range in air.

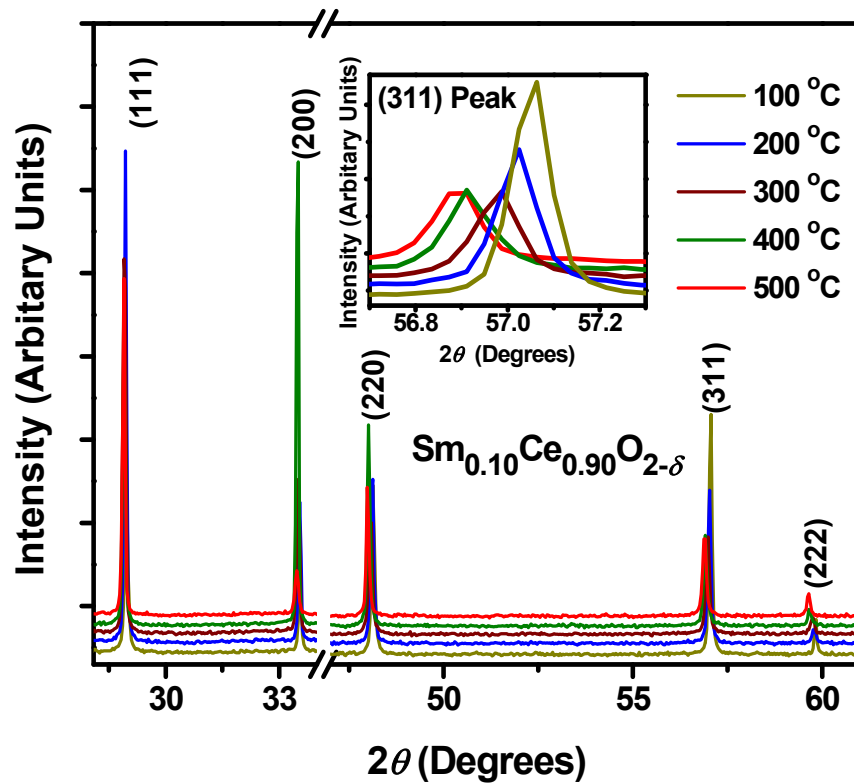


Figure 5-2. XRD profiles of measured $\text{Sm}_{0.10}\text{Ce}_{0.90}\text{O}_{2-\delta}$ at different temperature in air.

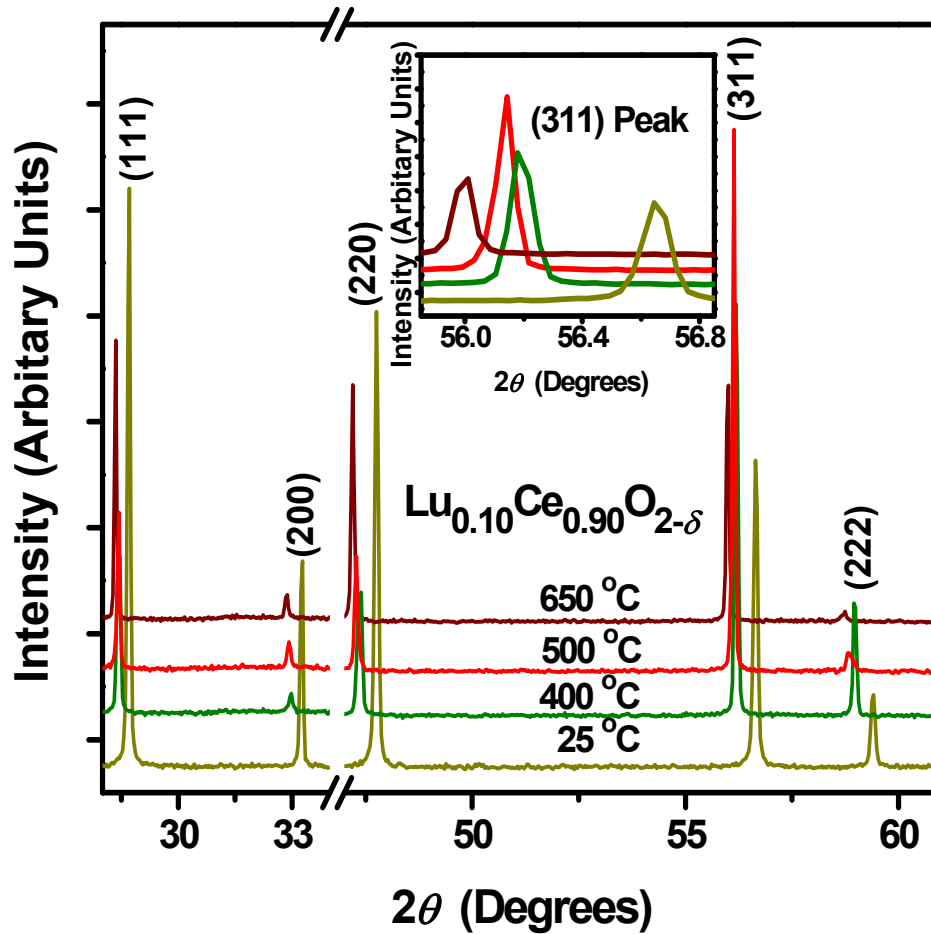


Figure 5-3. XRD profiles of measured $\text{Lu}_{0.10}\text{Ce}_{0.90}\text{O}_{2-\delta}$ at different temperature in air.

In the insets of Figure 5-2 and Figure 5-3, the (311) peak of the XRD patterns measured at different temperatures for $\text{Sm}_{0.10}\text{Ce}_{0.90}\text{O}_{2-\delta}$ and $\text{Lu}_{0.10}\text{Ce}_{0.90}\text{O}_{2-\delta}$, respectively, are also shown. With the increase in temperature, the (311) peak shifts toward lower 2θ angle which indicates the thermal expansion of the lattice of doped ceria system. The XRD profiles measured for other doped ceria systems at higher temperatures are presented in Appendix C. All the doped ceria materials are phase pure with no extra peaks of other phase present in XRD profiles.

5.2.2 Lattice Strain

5.2.2.1 Thermal strain

The solid oxide electrolyte is an essential component of SOFC device which operates in the temperature range between 400°C to 800°C. Together with electrolyte, an SOFC consists of an anode, a cathode, and interconnector. Thus, the device can be regarded as a typical example of composite materials. For such composite materials to avoid thermal stresses at high temperatures, it is required that all the components of the materials possess nearly the same thermal expansion coefficient over a wide temperature range.^{96,97} For example, it is recognized that the highest accepted mismatch in thermal expansion coefficient between cathode and electrolyte materials should not exceed 30%.⁹⁸ Higher difference in thermal expansion results in the mechanical fracture of the components during the heating and cooling cycles of the device. Hence, thermal properties of SOFC components are essential for this application. Since the present work is devoted on the study of solid oxide electrolytes, therefore in this section, thermal expansion coefficient of doped ceria electrolytes will be discussed.

The linear thermal expansion coefficient (α) of a material can be defined as the fractional change in length with the change in temperature at constant pressure, or

$\left(\frac{1}{l_o} \frac{\Delta l}{\Delta T} \right)_P$ where l_o is the original length.²⁴ It is well known that the thermal expansion is

related to the shape of the potential energy – inter-atomic distance between atoms in the crystal lattice. The larger the asymmetry in the shape of the potential energy curve, the higher the thermal expansion coefficient of the material. Further, asymmetry of the energy well depends upon the bond strength between the two atoms. Weak bond

strength materials will show higher asymmetry, and consequently higher thermal expansion coefficient. For example, thermal expansion coefficient of solid Ar is in the range of $10^{-3} / ^\circ\text{C}$, while for most of ceramics and metals, it is in range of $10^{-5} / ^\circ\text{C}$.²⁴

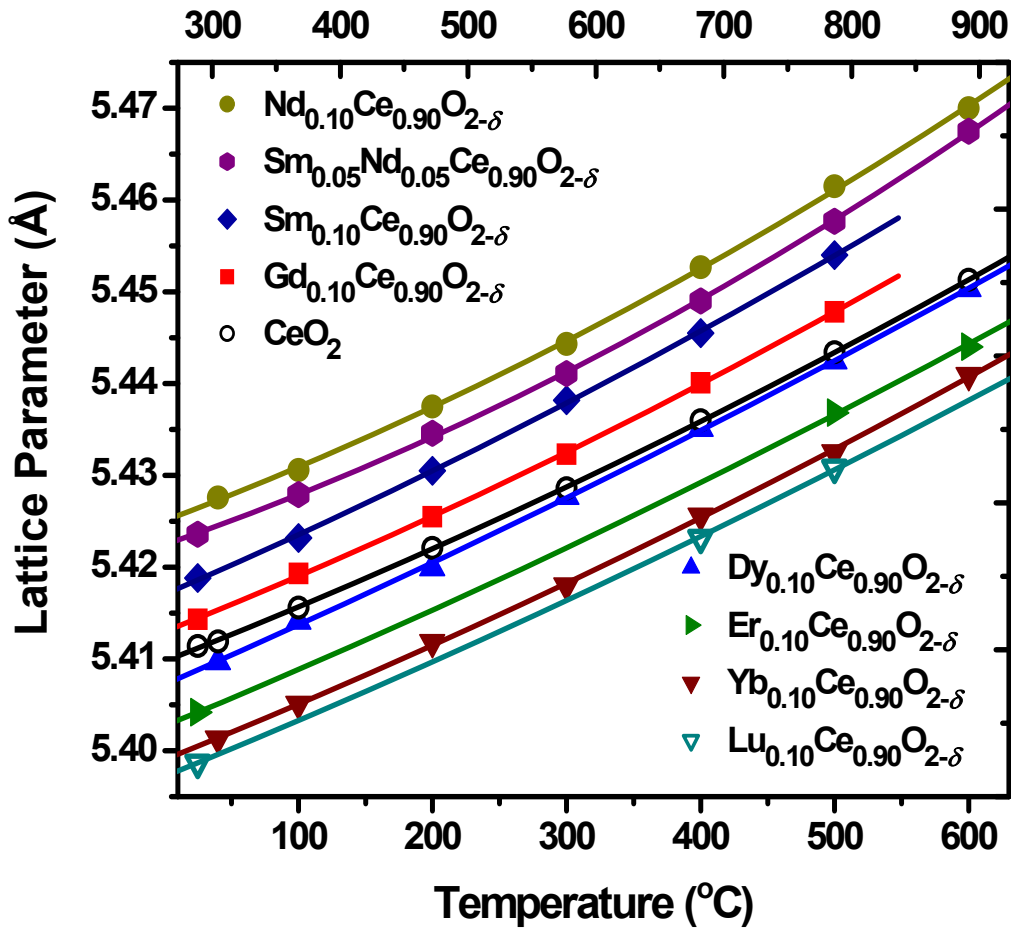


Figure 5-4. Thermal expansion of $\text{D}_{0.10}\text{Ce}_{0.90}\text{O}_{2-\delta}$ ceramic systems (where $\text{D}^{3+} = \text{Lu}^{3+}$, Yb^{3+} , Er^{3+} , Dy^{3+} , Gd^{3+} , Sm^{3+} , $\text{Sm}^{3+}/\text{Nd}^{3+}$, Nd^{3+}) in air. Polynomial equation was used to fit the thermal expansion of doped ceria systems.

Since the thermal expansion coefficient normally increases with the increase in temperature, it is usually written in terms of temperature as,

$$\alpha = b_0 + b_1T + \frac{c}{T^2} \quad (5-4)$$

where b_0 , b_1 , and c are constants independent of temperature.⁹⁶ Figure 5-4 shows the lattice expansion of the of $D_{0.10}Ce_{0.90}O_{2-\delta}$ (where $D^{3+} = Lu^{3+}, Yb^{3+}, Er^{3+}, Y^{3+}, Dy^{3+}, Gd^{3+}, Sm^{3+}, Sm^{3+}/Nd^{3+}, Nd^{3+}$) ceramic systems with the increase in temperature. The curves shown in the Figure 5-4 are plotted as a function of temperature (with Kelvin as a unit) and are fitted using a least square algorithm to the following polynomial,

$$a = a_0 \left(b_0 T + \frac{b_1 T^2}{2} - \frac{c}{T} + d \right) \quad (5-5)$$

where d is a constant, a and a_0 are the lattice parameter of the material at any given temperature and at room temperature, respectively.

Table 5-3. Thermal expansion coefficient (α) constants for different doped ceria systems.

Doped Ceria Electrolyte Materials (with different trivalent dopants)	Thermal Expansion Coefficient (α) Constants		
	b_0 (1/K) $\times 10^{-10}$	B_1 (1/K ²) $\times 10^{-9}$	c (K) $\times 10^{-1}$
$Yb_{0.10}Ce_{0.90}O_{2-\delta}$	1.48	8.70	7.58
$Dy_{0.10}Ce_{0.90}O_{2-\delta}$	1.48	8.76	8.61
$Gd_{0.10}Ce_{0.90}O_{2-\delta}$	1.48	9.69	6.24
$Sm_{0.10}Ce_{0.90}O_{2-\delta}$	1.48	10.21	5.55
$Sm_{0.05}Nd_{0.05}Ce_{0.90}O_{2-\delta}$	1.48	10.57	4.46
$Nd_{0.10}Ce_{0.90}O_{2-\delta}$	1.47	11.21	3.63
CeO_2	1.48	8.85	7.01

Table 5-3 shows the thermal expansion coefficient constants (i.e., b_0 , b_1 , and c) of doped ceria systems, obtained through fitting. For $Lu_{0.10}Ce_{0.90}O_{2-\delta}$, and $Er_{0.10}Ce_{0.90}O_{2-\delta}$ ceramic systems, the curve cannot be fitted as there was insufficient number of experimentally measured data points. In Figure 5-4, the line connecting data points for these materials is plotted for visual aid.

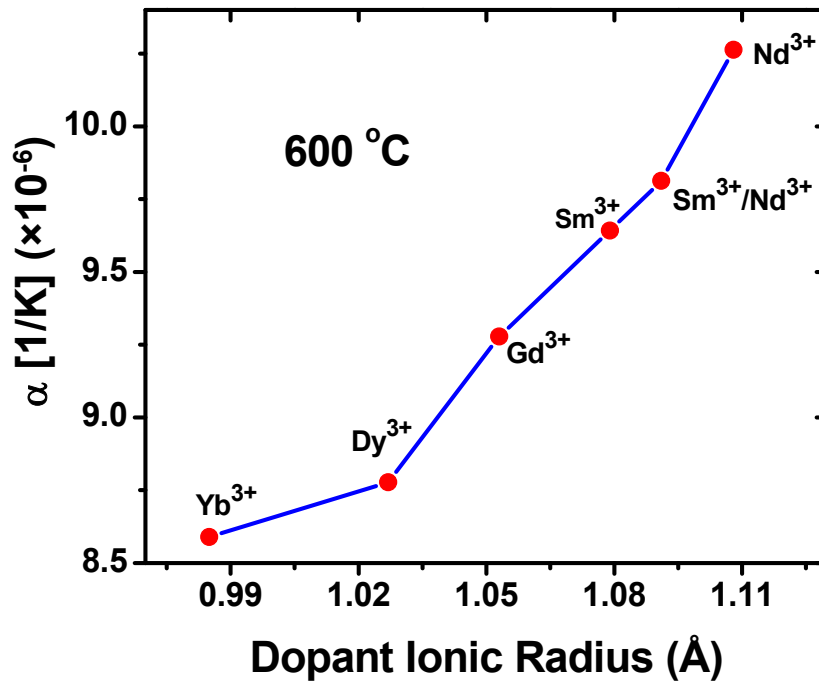


Figure 5-5. Thermal expansion coefficient (at 600°C) as a function of dopant ionic radius for $D_{0.10}Ce_{0.90}O_{2-\delta}$ systems. Line connecting data is for visual aid.

According to Hayashi et al.⁹⁹, the thermal expansion coefficient is dependent on the total binding energy of the material. This binding energy can be influenced by changing the bond distances between anions and cations, and also by creating oxygen vacancies inside the material. It becomes smaller with the increase in the ionic distance between anions and cations. Further, with the formation of oxygen vacancies the binding energy in the crystal decreases.⁹⁹ Keeping the oxygen vacancy concentration (or dopant content i.e., 10 mol%) fixed, the incorporation of dopant cations with different ionic radii results in the change in Ce-O and D-O distances (Dopant cation = D^{3+}). This is critical as it determines whether the total binding energy in the system increase or decrease. As Hayashi et al.^{97,99} suggested, the lower the total binding energy in the material, the higher the thermal expansion coefficient. Figure 5-5 shows the effect on α (at 600°C) with the change in dopant ionic radius. It can be seen that with the increase

in the ionic radius of the dopant, the thermal expansion coefficient for doped ceria systems at this temperature increases. This suggests that the total binding energy involved in the system decreases with the increase in ionic radii of the dopant. Thus, Nd^{3+} dopant cation shows lower binding energy than Yb^{3+} cations.

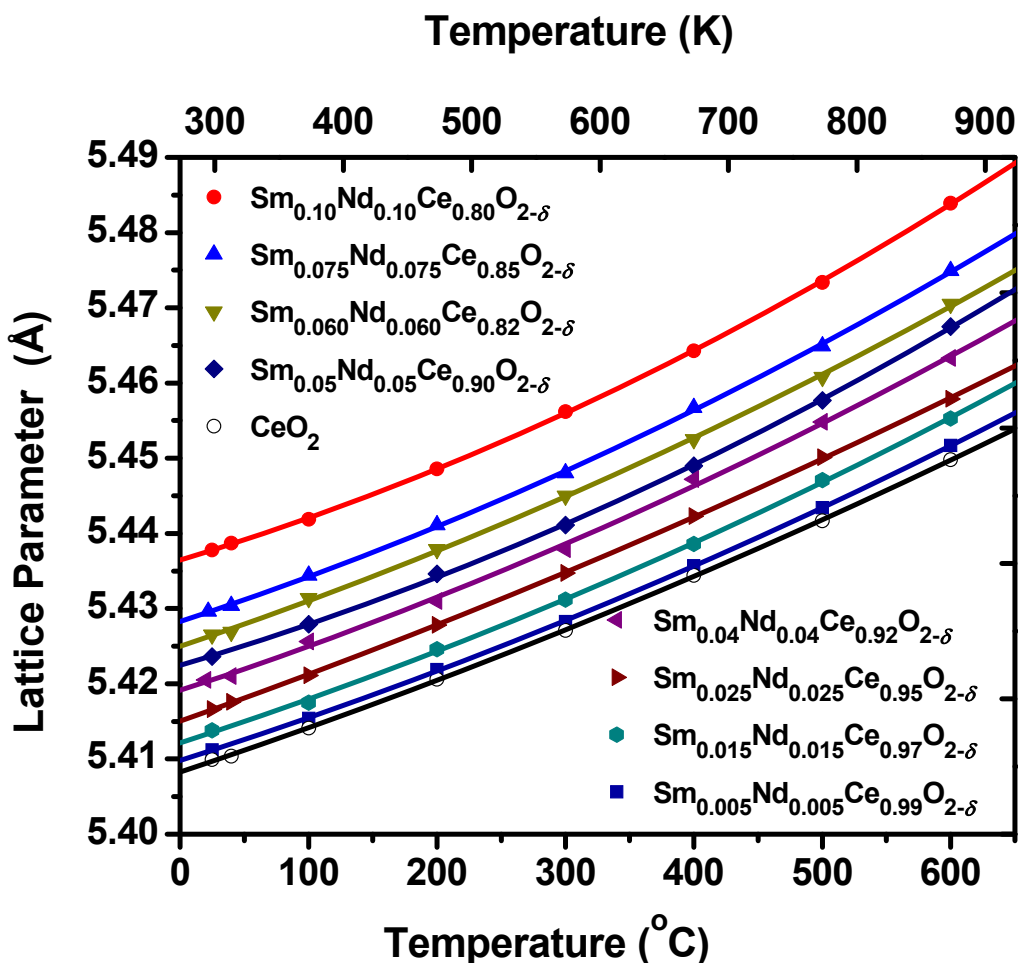


Figure 5-6. Thermal expansion of $\text{Sm}_{x/2}\text{Nd}_{x/2}\text{Ce}_{1-x}\text{O}_{2-\delta}$ ceramic systems (where $x = 0.01, 0.03, 0.05, 0.08, 0.10, 0.12, 0.15,$ and 0.20) in air. Polynomial equation (given in text) was used to fit the thermal expansion of doped ceria systems.

The thermal lattice expansion for the different compositions of $\text{Sm}_{x/2}\text{Nd}_{x/2}\text{Ce}_{1-x}\text{O}_{2-\delta}$ was also measured using high temperature XRD. Figure 5-6 shows the thermal expansion curve for $\text{Sm}_{x/2}\text{Nd}_{x/2}\text{Ce}_{1-x}\text{O}_{2-\delta}$ system. As expected, all the curves exhibit

non-linear behavior. They were fitted using equation (5-5). Table 5-4 shows the thermal expansion coefficient constants (i.e., b_0 , b_1 , and c) of doped ceria systems, used in equation (5-4).

Table 5-4. Thermal expansion coefficient (α) constants for $\text{Sm}_{x/2}\text{Nd}_{x/2}\text{Ce}_{1-x}\text{O}_{2-\delta}$.

$\text{Sm}_{x/2}\text{Nd}_{x/2}\text{Ce}_{1-x}\text{O}_{2-\delta}$	Thermal Expansion Coefficient (α) Constants		
	$b_0 (1/\text{K}) \times 10^{-10}$	$b_1 (1/\text{K}^2) \times 10^{-9}$	$c (\text{K}) \times 10^{-1}$
$\text{Sm}_{0.005}\text{Nd}_{0.005}\text{Ce}_{0.99}\text{O}_{2-\delta}$	1.478	9.275	5.778
$\text{Sm}_{0.015}\text{Nd}_{0.015}\text{Ce}_{0.97}\text{O}_{2-\delta}$	1.478	9.731	5.469
$\text{Sm}_{0.040}\text{Nd}_{0.040}\text{Ce}_{0.92}\text{O}_{2-\delta}$	1.475	10.019	5.700
$\text{Sm}_{0.05}\text{Nd}_{0.05}\text{Ce}_{0.90}\text{O}_{2-\delta}$	1.480	10.210	5.550
$\text{Sm}_{0.060}\text{Nd}_{0.060}\text{Ce}_{0.88}\text{O}_{2-\delta}$	1.474	10.312	5.451
$\text{Sm}_{0.075}\text{Nd}_{0.075}\text{Ce}_{0.85}\text{O}_{2-\delta}$	1.473	10.597	5.520
$\text{Sm}_{0.010}\text{Nd}_{0.010}\text{Ce}_{0.80}\text{O}_{2-\delta}$	1.471	11.314	4.085

Figure 5-7 shows the effect on α (at 600°C) with the change in dopant content in ceria. It can be seen that with the increase in the dopant concentration, the thermal expansion coefficient for doped ceria systems (at this temperature) increases. Zhou et al.¹⁰⁰ and Hayashi et al.⁹⁷ observed similar results for $\text{Y}_x\text{Ce}_{1-x}\text{O}_{2-\delta}$ and $\text{Gd}_x\text{Ce}_{1-x}\text{O}_{2-\delta}$, respectively. According to Hayashi et al., this trend can be explained by the formation of oxygen vacancy, which reduces the binding energy of the system. For example, in $\text{Gd}_x\text{Ce}_{1-x}\text{O}_{2-\delta}$ system, the Ce-O distance decreases with the increase of Gd content, while Gd-O bond length remains almost unchanged with increase in x .⁹⁹ However, the increase in the binding energy due to the decrease in Ce-O distances is lower than the decrease in binding energy during the creation of oxygen vacancies. This results in the lowering of binding energy which explains the higher thermal expansion coefficient with the increase in dopant concentration.

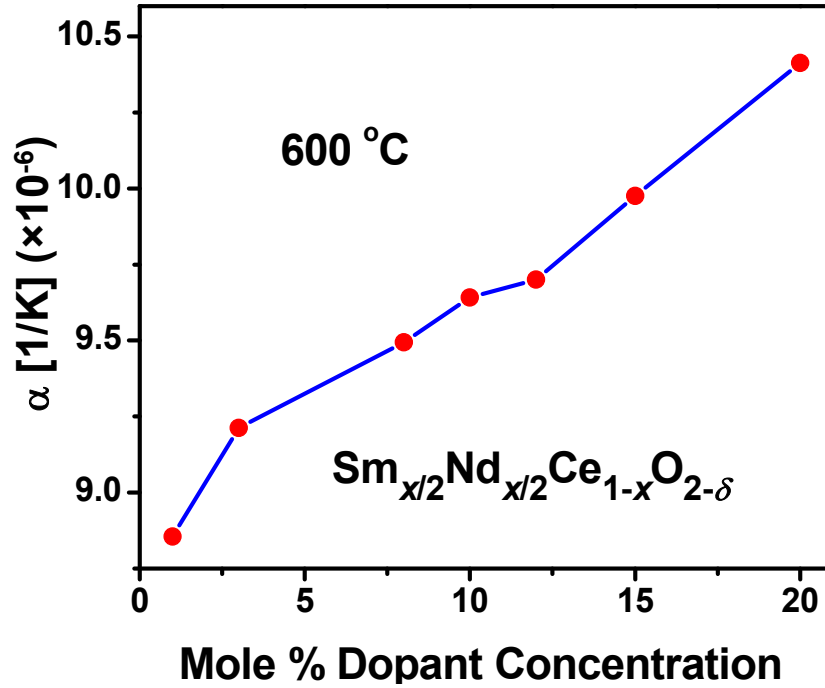


Figure 5-7. Thermal expansion coefficient (α) at 600°C for $\text{Sm}_{x/2}\text{Nd}_{x/2}\text{Ce}_{1-x}\text{O}_{2-\delta}$ as a function of dopant concentration. Line connecting data is for visual aid.

5.2.2.2 Chemical strain

The formation of point defects has an influence on the lattice dimension of the host crystal structure.¹⁰¹ These point defects have their own specific volume generally different from that of their host lattice, and are non-uniformly distributed in the host crystal structure.¹⁰² This results in the mechanical strain in the lattice which is also called chemical strain. For example, addition of trivalent dopant cation (D^{3+}) results in the formation of D'_{Ce} and $V_{\text{O}}^{\bullet\bullet}$ point defects in the host ceria lattice. Both these defects independently affect the lattice dimension of host ceria crystal structure. For D'_{Ce} point defect, the ionic radius mismatch between the host and dopant cations ($r_h - r_d$) governs the nature of chemical elastic strain in the lattice. In the case $r_h < r_d$, the addition of D'_{Ce} point defect, results in the expansion of host lattice. However, if $r_h > r_d$, the lattice will

contract.²¹ To maintain charge neutrality in the system, $V_{\text{O}}^{\bullet\bullet}$ point defect is also created (in addition to D'_{Ce}). Hong et al.⁷⁴ estimated the effective oxygen vacancy radius for ceria to be 1.164 Å at room temperature which is significantly smaller than the radius of the oxide ion of 1.38 Å.^{48,74} Thus, it can be said incorporation of oxygen vacancies result in the contraction of the host lattice. For example, at room temperature, the lattice constant of $\text{Lu}_{0.10}\text{Ce}_{0.90}\text{O}_{2-\delta}$ (5.3987 Å) is lower than that of pure ceria (5.41134 Å), even though $r_h - r_d$ value is almost negligible ($r_{\text{Lu, VIII}}^{3+} = 0.977$ Å and $r_{\text{Ce, VIII}}^{4+} = 0.97$ Å).^{7,47,48}

The effect of both the point defects on the host lattice will decide the nature of elastic strain present in the host lattice. The extent (or magnitude) of the elastic strain is a function of the concentration of these point defects. In the present section, the chemical strain (or lattice strain) by incorporating trivalent dopant cations (of different physical properties) inside the ceria lattice, from room temperature to 600°C will be discussed. Also, the effect of dopant concentration (x) on the lattice parameter of $\text{Sm}_{x/2}\text{Nd}_{x/2}\text{Ce}_{1-x}\text{O}_{2-\delta}$ ceramic at higher temperature is investigated.

As presented in the previous section, according to Kim's²² proposed empirical relationship for doped ceria, at room temperature, lattice parameter change in doped ceria system is linearly dependent on the ionic radius mismatch between the host and dopant cations. Similar type of linear relationship was also given by Hong et al.⁷⁴ in their work on rare earth element doped ceria electrolytes. However, whether this linear dependency also exists at higher temperatures, where these materials are normally operated is still unknown.

In order to investigate the effect of dopant ionic radius on the lattice parameter at higher temperatures, different doped ceria systems ($D_{0.10}Ce_{0.90}O_{2-\delta}$) were synthesized under the same experimental conditions, as described in Chapter 3. The dopant content (and thus expected oxygen vacancy concentration) in these systems is kept constant to study the separate effect of ionic radius mismatch between host and dopant cations. The high temperature lattice parameters were estimated using XRD described earlier in this chapter.

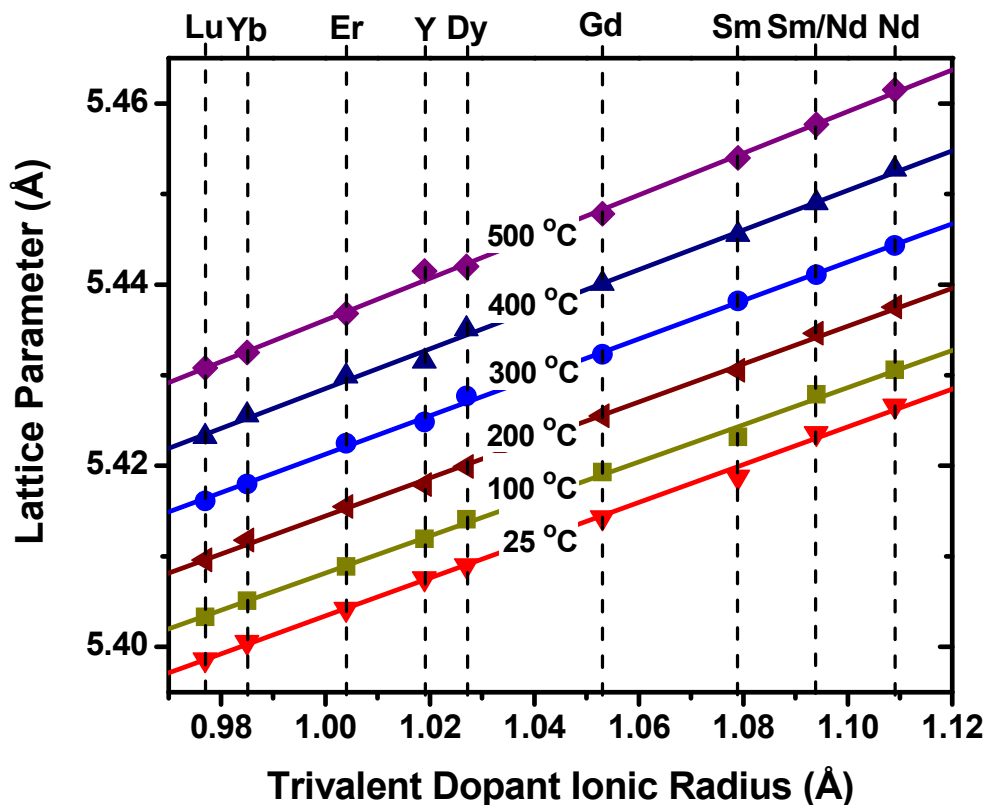


Figure 5-8. Lattice expansion of $D_{0.10}Ce_{0.90}O_{2-\delta}$ systems as a function of dopant ionic radius. The linear least-square algorithm was used to fit the data.

Figure 5-8 shows the isothermal curves for the lattice expansion of doped ceria as a function of dopant ionic radius. It can be seen even at higher temperatures, lattice

parameter shows a linear dependency on the dopant ionic radius. All the curves were fitted using a linear least-square fit.

Table 5-5. Relationship between lattice parameter (a) and dopant ionic radius (r_d) for $D_{0.10}Ce_{0.90}O_{2-\delta}$ at different temperatures.

Temperature ($^{\circ}C$)	Relationship between lattice parameter (a) and dopant ionic radius (r_d). The units of a and r_d are in \AA .
25	$a = 0.2088 \times r_d + 5.1946$
100	$a = 0.2049 \times r_d + 5.2033$
200	$a = 0.2096 \times r_d + 5.2049$
300	$a = 0.2122 \times r_d + 5.2090$
400	$a = 0.2189 \times r_d + 5.2096$
500	$a = 0.2302 \times r_d + 5.2059$

Table 5-5 shows the lattice parameter and dopant ionic radius relationships obtained by linearly fitting each isothermal curve in Figure 5-8. The empirical relationship proposed by Kim²² (taking 10 mole % dopant concentration and trivalent dopant cations) for room temperature is given below.

$$a = 0.2200 \times r_d + 5.185 \quad (5-6)$$

where a is the lattice parameter of the $D_{0.10}Ce_{0.90}O_{2-\delta}$ and r_d is the ionic radius of the trivalent dopant cation. The units of a and r_d are in \AA . It is important to note that Kim's lattice constant of pure ceria is 0.00166 higher than the standard value of 5.41134 \AA .⁴⁷ Kim verified the relationship against considerable amount of data, and the typical uncertainty in the parameters was observed to be 0.003 \AA . Although in the present work, the relationship between lattice parameter and ionic radius of dopant follows a

linear behavior, the obtained linear fit for $D_{0.10}Ce_{0.90}O_{2-\delta}$ (at room temperature) does not match with the relationship proposed by Kim.

The effect of dopant concentration on the lattice parameter of doped ceria systems is already discussed in Chapter 4. According to Mogensen et al.⁷³, doped ceria solid solutions should follow Vegard's law. However, experimentally it has been observed for various singly doped ceria systems that lattice parameter exhibits quadratic behavior with dopant concentration.^{80,85} The second degree term in the quadratic expansion or contraction (depending upon the ionic radius mismatch between dopant and host cations) has been interpreted as due to interactions between the point defects. In the dilute regime, the host lattice parameter change is not affected by these interactions as the point defects (in this case D'_{Ce} and V_{O}^{**}) are usually far away from each other. However, with the increase in dopant content, the probability of V_{O}^{**} sitting next to D'_{Ce} increases. This results in the formation of stable local defect structures (such as $D' - V_{O}^{**} - D'$) which tend to contract the host ceria lattice, and, thus, precludes Vegard's law behavior. However, in $Sm_{x/2}Nd_{x/2}Ce_{1-x}O_{2-\delta}$ system, it has been shown that at room temperature, the lattice expands linearly as a function of dopant concentration.⁶⁷ The second degree in the lattice expansion of $Sm_{x/2}Nd_{x/2}Ce_{1-x}O_{2-\delta}$ system is negligible which indicates that the local defect structures in this system are not as pronounced as in other systems. In the present work, lattice parameter relationships as a function of dopant content in $Sm_{x/2}Nd_{x/2}Ce_{1-x}O_{2-\delta}$ system at higher temperatures were determined. Different polycrystalline sintered samples of $Sm_{x/2}Nd_{x/2}Ce_{1-x}O_{2-\delta}$ (where $x = 0.01, 0.03, 0.05, 0.08, 0.10, 0.12, 0.15,$ and 0.20) were synthesized using the conventional solid oxide route (described in Chapter 3). Sintered

pellets were crushed into fine particles using mortar and pestle. The XRD profiles were collected at high temperatures as described earlier.

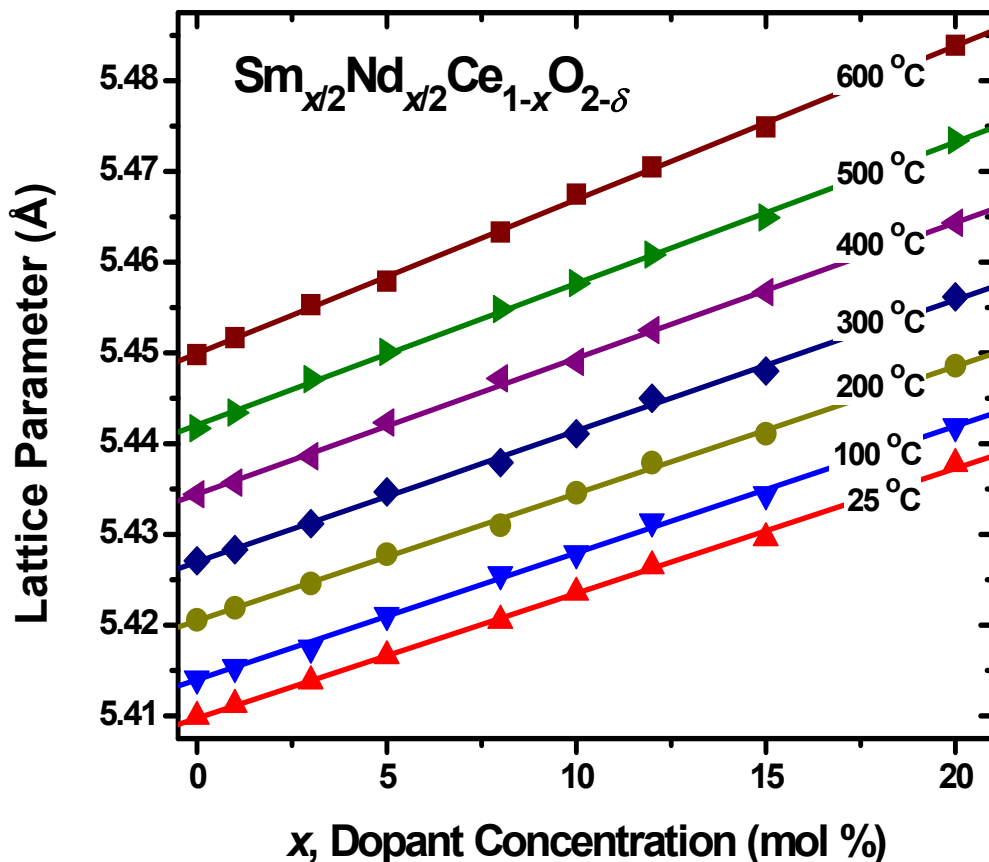


Figure 5-9. Lattice expansion in $\text{Sm}_{x/2}\text{Nd}_{x/2}\text{Ce}_{1-x}\text{O}_{2-\delta}$ system as a function of dopant concentration at different temperatures.

Figure 5-9 shows the lattice expansion of $\text{Sm}_{x/2}\text{Nd}_{x/2}\text{Ce}_{1-x}\text{O}_{2-\delta}$ as a function of dopant concentration at different temperatures. It can be seen that in all the temperatures, $\text{Sm}_{x/2}\text{Nd}_{x/2}\text{Ce}_{1-x}\text{O}_{2-\delta}$ system follows linear behavior i.e., Vegard's law. All the curves are fitted using a linear least-squares fit. Table 5-6 shows the fitted linear relationship for $\text{Sm}_{x/2}\text{Nd}_{x/2}\text{Ce}_{1-x}\text{O}_{2-\delta}$ system at different temperatures.

Table 5-6. Relationship between lattice parameter (a) and dopant content (x) for $\text{Sm}_{x/2}\text{Nd}_{x/2}\text{Ce}_{1-x}\text{O}_{2-\delta}$ system at higher temperatures.

Temperature ($^{\circ}\text{C}$)	Relationship between lattice parameter (a) and dopant content (x). The unit of a is \AA .
25	$a = 0.00138(2) \times x + 5.40973(21)$
100	$a = 0.00140(2) \times x + 5.41398(24)$
200	$a = 0.00140(2) \times x + 5.42050(22)$
300	$a = 0.00145(3) \times x + 5.42694(27)$
400	$a = 0.00150(2) \times x + 5.43444(22)$
500	$a = 0.00156(2) \times x + 5.44205(18)$
600	$a = 0.00170(2) \times x + 5.44992(21)$

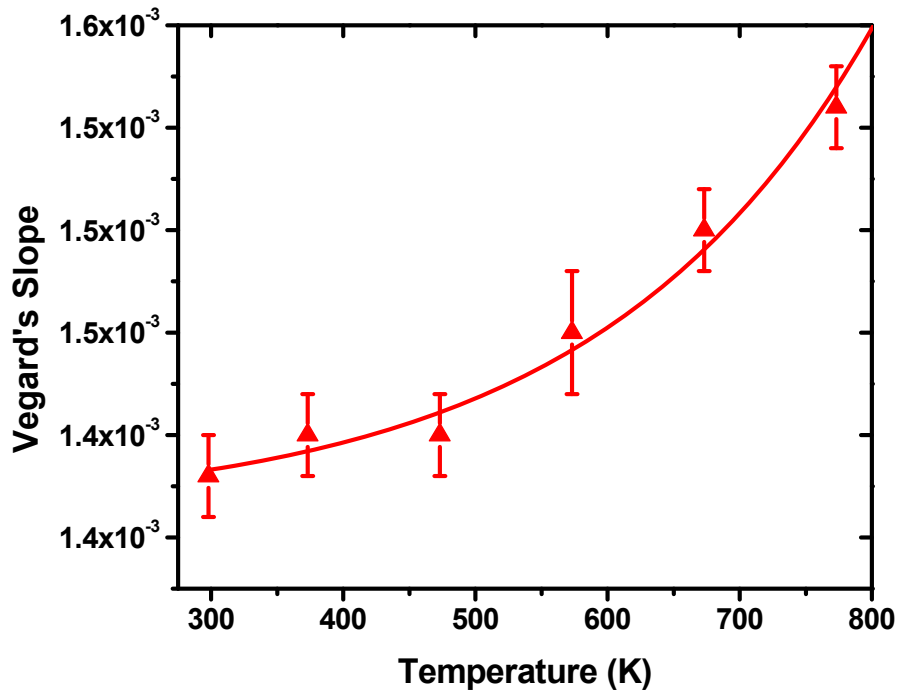


Figure 5-10. Vegard's slope as a function of temperature for $\text{Sm}_{x/2}\text{Nd}_{x/2}\text{Ce}_{1-x}\text{O}_{2-\delta}$ system. The experimental data is fitted using an exponential curve.

The slope of the fitted line is termed as Vegard's slope. Figure 5-10 shows the variation of Vegard's slope (S_V) with temperature. It can be seen that the S_V in the

$\text{Sm}_{x/2}\text{Nd}_{x/2}\text{Ce}_{1-x}\text{O}_{2-\delta}$ system increases with the increase in temperature. The variation of the estimated S_V datasets with temperature was then fitted using different curve equations. The best fit was observed using exponential curve, with R^2 value of 0.9947. The relationship between S_V and the absolute temperature (T) is given below,

$$S_V = 0.00136 + 5.1453 \times 10^{-6} \exp(0.00479 \times T) \quad (5-7)$$

According to Kim²², S_V is the algebraic sum of elastic and electrostatic interactions among the point defects in the doped fluorite oxide system. The solubility limit of a solute depends on the elastic energy in the lattice which is introduced when a dopant cation (with different ionic radius and charge valence than host cation) is incorporated into the host lattice. The higher the elastic strain energy, the smaller the extent of solubility. This elastic strain energy (ΔE) in a substitutional solid solution is defined as,

$$\Delta E = \frac{2}{3} G V_o \left(\frac{V}{V_o} - 1 \right)^2 \quad (5-8)$$

where G is a the shear modulus, and V_o and V are the molar volume of a pure metal and its solid solution. As doped ceria exhibits the cubic fluorite structure, the molar volume in equation (5-8) can be written in terms of lattice parameter.

$$\Delta E = \frac{2}{3} G V_o \left(\left(\frac{\Delta a + a_o}{a_o} \right)^3 - 1 \right)^2 \quad (5-9)$$

where a_o is the lattice constant of the pure ceria and Δa is the change in lattice constant after the incorporation of dopant. Since $\Delta a \ll a_o$, therefore, ΔE can be written as,

$$\Delta E = 6 G V_o \Delta a^2 \quad (5-10)$$

Now, Δa can be described in terms of Vegard's slope (S_V). Therefore,

$$\Delta E = 6GV_o S_V^2 c^2 \quad (5-11)$$

where c is the concentration of solute. As mentioned earlier, the extent of solubility depends inversely upon the elastic strain energy (ΔE). Using equation (5-11), it can be said that the solubility limit of the dopant increases with the decrease in S_V .

$$s \propto \frac{1}{S_V^2} \quad (5-12)$$

It is well known that the extent of solubility widens with the increase in temperature. Thus, following equation (5-12), it is expected that with the increase in temperature, S_V should decrease. However, Vegard's slope in $\text{Sm}_{x/2}\text{Nd}_{x/2}\text{Ce}_{1-x}\text{O}_{2-\delta}$ system increases with the increase in temperature (as shown in Figure 5-10). This indicates there is an additional term involved in the Vegard's slope, which with the increase in temperature becomes predominant compared to elastic and electrostatic interaction energy. Also, it is important to note that with the increase in temperature, the extent of solubility depends not only on the elastic energy but also on the entropy term ($-T\Delta S$). Thus, it is the Gibb's free energy (ΔG) which governs the solubility limit rather than the elastic energy (ΔE).

5.3 Ionic Conductivity of Trivalent Acceptor Doped Ceria at High Temperatures

Due to higher ionic conductivity and good thermodynamic stability, doped ceria materials open up the possibility of SOFCs operating at intermediate temperatures. Ionic conductivity in these materials takes place through the oxygen vacancy diffusion mechanism. The concentration of oxygen vacancies which are the charge carriers in these oxide materials is dependent on the amount of acceptor dopant content present in the host oxide. For the same dopant concentration, ionic conductivity differs for different type of dopants. For example, the trivalent dopant cation system shows higher

ionic conductivity compared to the divalent dopant cation system.⁹ Also, Gd^{3+} is widely accepted to show highest ionic conductivity.¹³ This difference in ionic conductivity occurs due to the interactions which exist among various types of point defects. The highest ionic conductivity is shown in the dopant cation system where these interactions are minimal. This condition leads to oxygen vacancy with higher mobility without any type of local ordering. Numerous studies have been done to understand the effect of different dopants on the oxygen vacancy diffusion in doped ceria materials.^{11,14,56,75,103} However, as mentioned in Chapter 4, a wide range of ionic conductivity data have been reported in the literature.^{13,63,77} Examination of the experimental procedure followed in each work indicates a strong correlation between the processing conditions and the conductivity observed. Typically, powder synthesized using co-precipitation technique exhibits higher ionic conductivity than that processed through solid state route.⁶³ In order to identify the best dopant cations for ceria, and to establish the relationships between dopant physical properties and ionic conductivity, it is essential to develop a consistent set of ionic conductivity data for all the doped ceria systems synthesized using the same experimental conditions. This will provide a clear idea about the ideal dopant for ceria, which shows the highest ionic conductivity, when all the materials are synthesized under similar processing conditions.

In the present work, $D_{0.10}Ce_{0.90}O_{2-\delta}$ systems (where $D^{3+} = Lu^{3+}, Yb^{3+}, Er^{3+}, Y^{3+}, Dy^{3+}, Gd^{3+}, Sm^{3+}$ and Nd^{3+}) were synthesized using solid oxide route as described in Chapter 3. Dopant concentration in these systems is kept fixed, to investigate the effect of ionic radius mismatch between host and dopant cations on the ionic conductivity. In addition, to study the effect of dopant concentration on the ionic conductivity, different

compositions of $\text{Sm}_{x/2}\text{Nd}_{x/2}\text{Ce}_{1-x}\text{O}_{2-\delta}$ were also synthesized under similar experimental conditions. The ionic conductivity measurements were taken on the Pt electroded sintered samples using two-point probe electrochemical impedance spectroscopy from 250°C to 700°C in air. Complex impedance measurements were taken over the frequency range from 10 MHz to 0.1 Hz. It is essential to note that in the present work, the grain ionic conductivity which is the fundamental material property, rather than the overall ionic conductivity (which includes microstructural, impurities and other contributions) of doped ceria systems is reported. Further, the reported grain ionic conductivity for each composition is the average grain ionic conductivity values measured for three different samples of the same composition with varying geometrical aspect ratio. The typical error associated with the values of the reported grain ionic conductivity is < 2%.

Figure 5-11 shows the grain ionic conductivity comparison of $\text{D}_{0.10}\text{Ce}_{0.90}\text{O}_{2-\delta}$ materials synthesized using similar experimental procedures, measured at different temperatures in air. The grain ionic conductivity values of $\text{Sm}_{0.05}\text{Nd}_{0.05}\text{Ce}_{0.90}\text{O}_{2-\delta}$ are also shown. The weighed average ionic radius of the dopant cations (i.e., Sm^{3+} and Nd^{3+}) was taken as an effective ionic radius of $\text{Sm}^{3+}/\text{Nd}^{3+}$ (i.e., 1.094 Å) while plotting this graph. From the Figure 5-11, it can be seen that with the increase in dopant ionic radius, the ionic conductivity increases. Even though the dopant ionic radius of Lu^{3+} is very close to that of Ce^{4+} , the grain ionic of $\text{Lu}_{0.10}\text{Ce}_{0.90}\text{O}_{2-\delta}$ exhibits the lowest ionic conductivity in all the temperatures. This may be due to the electrostatic interactions between dopant cations and oxygen vacancies which restrain oxygen vacancy diffusion inside the crystal lattice. At higher ionic radius of the dopant cation, the ionic

conductivity data of $D_{0.10}Ce_{0.90}O_{2-\delta}$ seems to reach saturation (with increasing dopant ionic radius). However, between 500°C and 600°C, $Nd_{0.10}Ce_{0.90}O_{2-\delta}$ shows the highest ionic conductivity among other trivalent acceptor doped ceria systems with similar dopant concentration. It is also important to note that the ionic conductivity of co-doped ceria (i.e., $Sm_{0.05}Nd_{0.05}Ce_{0.90}O_{2-\delta}$) lies between that of $Sm_{0.10}Ce_{0.90}O_{2-\delta}$ and $Nd_{0.10}Ce_{0.90}O_{2-\delta}$ for all the temperatures.

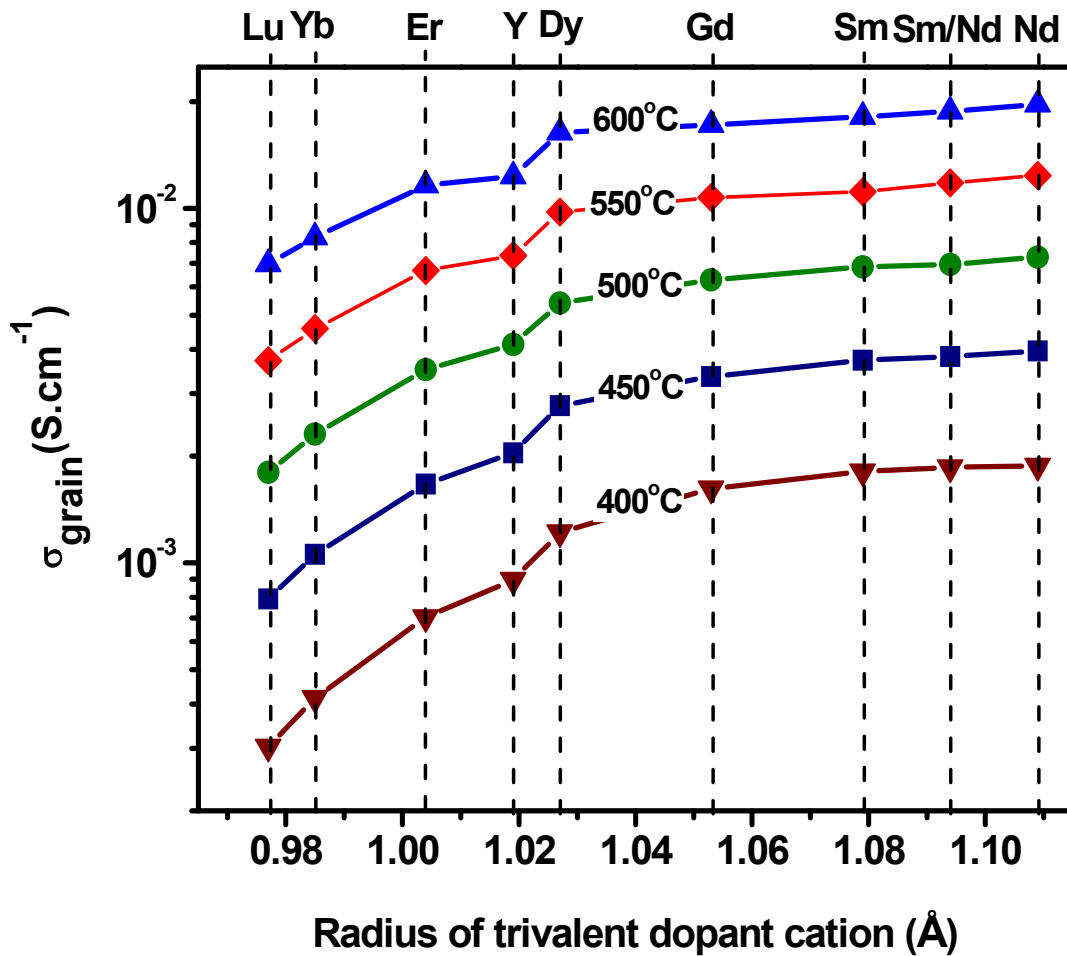


Figure 5-11. Grain ionic conductivity comparison of different doped ceria materials (with 10 mol% dopant content). All the materials were synthesized using solid oxide route.

A recent study by Kamiya et al. on Nd-doped ceria system has shown that $\text{Nd}_{0.23}\text{Ce}_{0.77}\text{O}_{2-\delta}$ exhibits higher oxygen diffusion coefficient than $\text{Y}_{0.20}\text{Ce}_{0.80}\text{O}_{2-\delta}$.¹⁰⁴ Also, the obtained oxygen diffusion coefficient value for $\text{Nd}_{0.23}\text{Ce}_{0.77}\text{O}_{2-\delta}$ is close to that of $\text{Gd}_{0.31}\text{Ce}_{0.69}\text{O}_{2-\delta}$ and $\text{Y}_{0.40}\text{Ce}_{0.60}\text{O}_{2-\delta}$. It is well known that the ionic conductivity is directly proportional to the oxygen diffusion coefficient, which depends upon the concentration of mobile charge carriers. Based on the oxygen diffusion coefficient of $\text{Nd}_{0.23}\text{Ce}_{0.77}\text{O}_{2-\delta}$ and $\text{Gd}_{0.31}\text{Ce}_{0.69}\text{O}_{2-\delta}$, it can be said that there is less association of point defects in Nd-doped ceria system.¹⁰⁴ Further, the activation energy for oxygen ion diffusion in these cubic fluorite structure oxides is inversely proportional to the lattice spacing in the unit cell. As doping with Nd^{3+} leads to a higher lattice parameter compared to Gd^{3+} and Y^{3+} in doped ceria, the activation energy in Nd-doped CeO_2 is lower than that of Y-doped CeO_2 and Gd-doped CeO_2 .⁹ These results indicate that doping with Nd^{3+} is much more effective compared to Gd^{3+} and Y^{3+} .

The ionic conductivity as a function of dopant concentration in $\text{Sm}_{x/2}\text{Nd}_{x/2}\text{Ce}_{1-x}\text{O}_{2-\delta}$ system is already discussed in Chapter 4. Figure 5-12 shows the 3-dimensional graph between the grain ionic conductivity, dopant concentration and temperature. For all the temperatures, the ionic conductivity initially increases with the increase in dopant content. It reaches maximum at certain dopant concentration, and then degrades. The decrease in the ionic conductivity at higher dopant concentration can be attributed to the increase in the concentration of local defect structures. These stable defect structures hinder the flow of oxygen vacancies, and thus lower the mobile oxygen vacancy concentration.

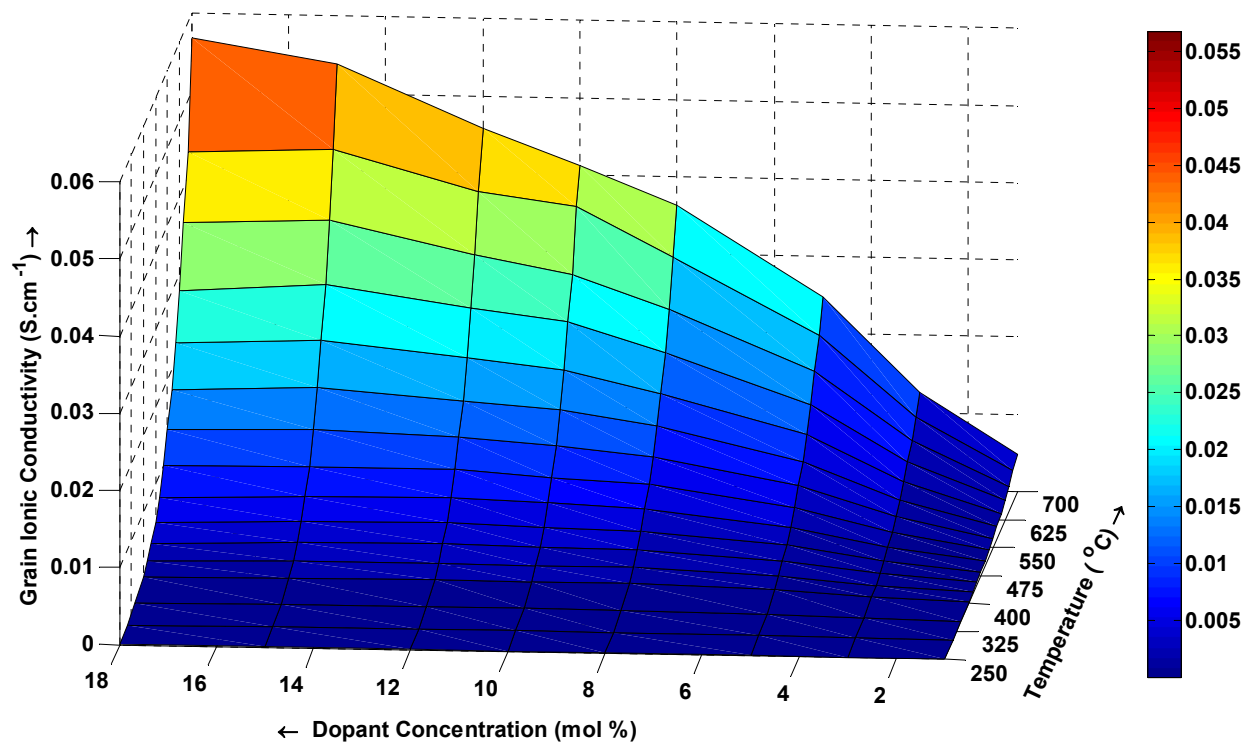


Figure 5-12. Grain ionic conductivity as a function of dopant concentration and temperature.

Figure 5-13 shows the 3-dimensional graph between the normalized grain ionic conductivity, dopant concentration, and temperature. The ionic conductivity of all the compositions at a given temperature is normalized by the maximum ionic conductivity obtained at that temperature. The graph shows that with the increase in temperature, the ionic conductivity maximum shifts toward higher dopant concentration. This behavior indicates the dissociation of complex defect structures (present mainly at higher dopant concentration) at higher temperatures to give mobile oxygen vacancies. Since the ionic conductivity depends mainly on the mobile oxygen vacancy concentration, with increase in temperature, ionic conductivity maximum shift toward higher dopant concentrations.

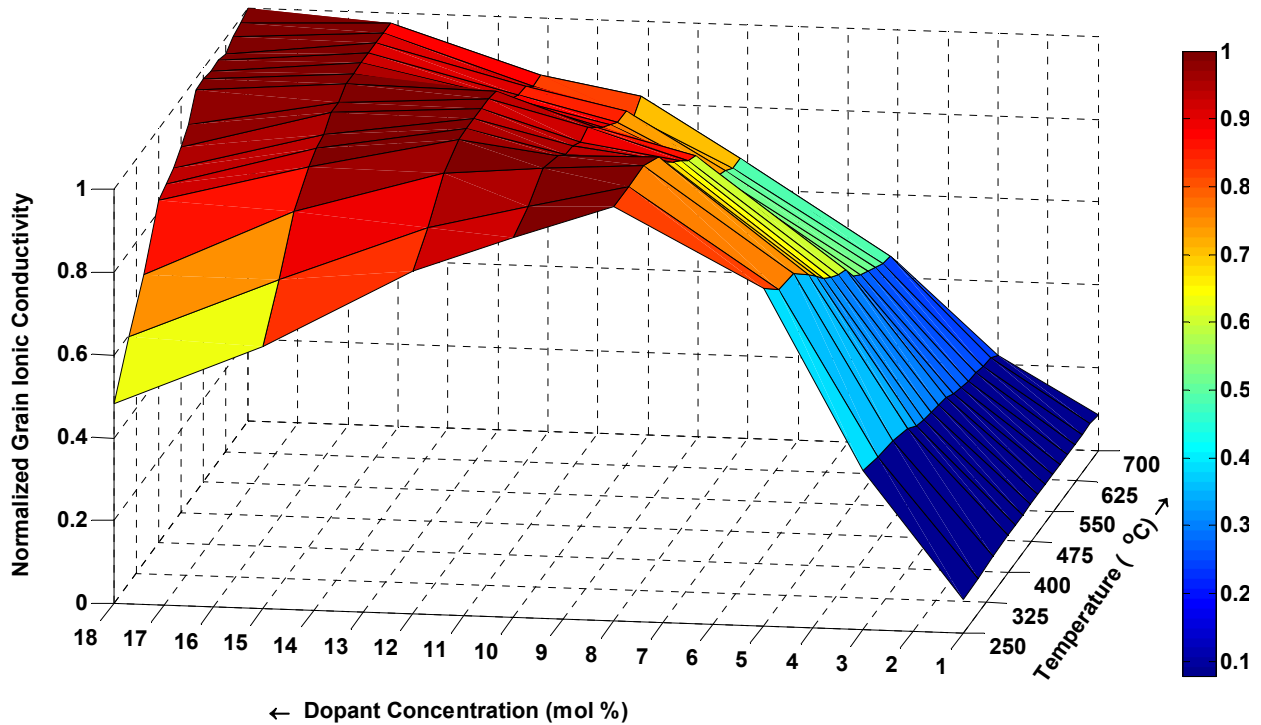


Figure 5-13. Normalized grain ionic conductivity as a function of dopant concentration and temperature.

5.3.1 Activation Energy

As discussed in Chapter 4, the activation energy for oxygen vacancy diffusion inside the crystal lattice, is the sum of migration enthalpy ($\Delta H_{Migration}$) of oxygen vacancy and association enthalpy ($\Delta H_{Association}$) of local defect structures. The $\Delta H_{Migration}$ is defined as the amount of energy required for the oxygen vacancy to jump from one oxygen ion site to another oxygen ion site, assuming there are no interactions offered from the point defects residing next to oxygen vacancy site. At lower temperatures, point defects (oxygen vacancies and dopant cations) usually interact with each other to form stable local defect structures. Thus, an additional amount of energy is required to dissociate oxygen vacancies from these local defect structures at these temperatures. This additional energy is termed as association enthalpy or $\Delta H_{Association}$. In this

temperature range, activation energy is the sum of $\Delta H_{Migration}$ and $\Delta H_{Association}$. According to Steele¹³, above 400°C, most of the oxygen vacancies overcome the dopant cations interaction barrier, and are free to diffuse inside the crystal lattice. Thus, activation energy for oxygen vacancy diffusion above this temperature can be considered to be equal to $\Delta H_{Migration}$. However, experimentally there is no such set temperature at which this transition takes place. Typically, the Arrhenius conductivity plots of these oxide materials exhibit a gradual, rather than a sharp, change in slope with temperature. Therefore, using Arrhenius conductivity plot, it is difficult to separate $\Delta H_{Association}$ from the total activation energy. In the present work, activation energy is determined from the Arrhenius plot of the ionic conductivity data measured from 250°C to 700°C for $D_{0.10}Ce_{0.90}O_{2-\delta}$ systems. It was assumed that the change in slope is negligible in the Arrhenius plots.

Figure 5-14 shows the activation energy for oxygen vacancy diffusion in different doped ceria systems with 10 mol% dopant concentration. For comparison, activation energy in co-doped ceria systems of $Gd_{0.056}Y_{0.044}Ce_{0.90}O_{2-\delta}$ and $Sm_{0.05}Nd_{0.05}Ce_{0.90}O_{2-\delta}$ is also shown. The weighed average ionic radius of the dopant cations (i.e., Gd^{3+} and Y^{3+} , and Sm^{3+} and Nd^{3+}) was taken as an effective ionic radius of Gd^{3+}/Y^{3+} (i.e., 1.038 Å) and Sm^{3+}/Nd^{3+} (i.e., 1.094 Å), respectively, while plotting this graph. The error bar associated with the activation energy value in Figure 5-14 was determined by measuring activation energy values in three different test samples of similar composition. Initially, with the increase in dopant ionic radius, activation energy decreases. It reaches minimum at $Sm_{0.10}Ce_{0.90}O_{2-\delta}$ (0.662 ± 0.002 eV), and then increases. $Nd_{0.10}Ce_{0.90}O_{2-\delta}$ (0.672 ± 0.004 eV) exhibits higher activation energy than

$\text{Sm}_{0.10}\text{Ce}_{0.90}\text{O}_{2-\delta}$ system but lower activation energy than $\text{Sm}_{0.05}\text{Nd}_{0.05}\text{Ce}_{0.90}\text{O}_{2-\delta}$ (0.676 ± 0.004 eV) and $\text{Gd}_{0.10}\text{Ce}_{0.90}\text{O}_{2-\delta}$ (0.678 ± 0.003 eV) systems. Interestingly, for co-doped ceria i.e., $\text{Gd}_{0.056}\text{Y}_{0.044}\text{Ce}_{0.90}\text{O}_{2-\delta}$ (0.719 ± 0.003 eV), activation energy is in between that of $\text{Y}_{0.10}\text{Ce}_{0.90}\text{O}_{2-\delta}$ (0.764 ± 0.002 eV) and $\text{Gd}_{0.10}\text{Ce}_{0.90}\text{O}_{2-\delta}$. As mentioned earlier, in order to design higher ionically conductive materials, activation energy for oxygen vacancy diffusion needs to be minimized. From Figure 5-14, it is clear that the trivalent dopant with ionic radius within the range of 1.05 Å to 1.11 Å exhibits lower activation energy, and consequently, higher ionic conductivity.

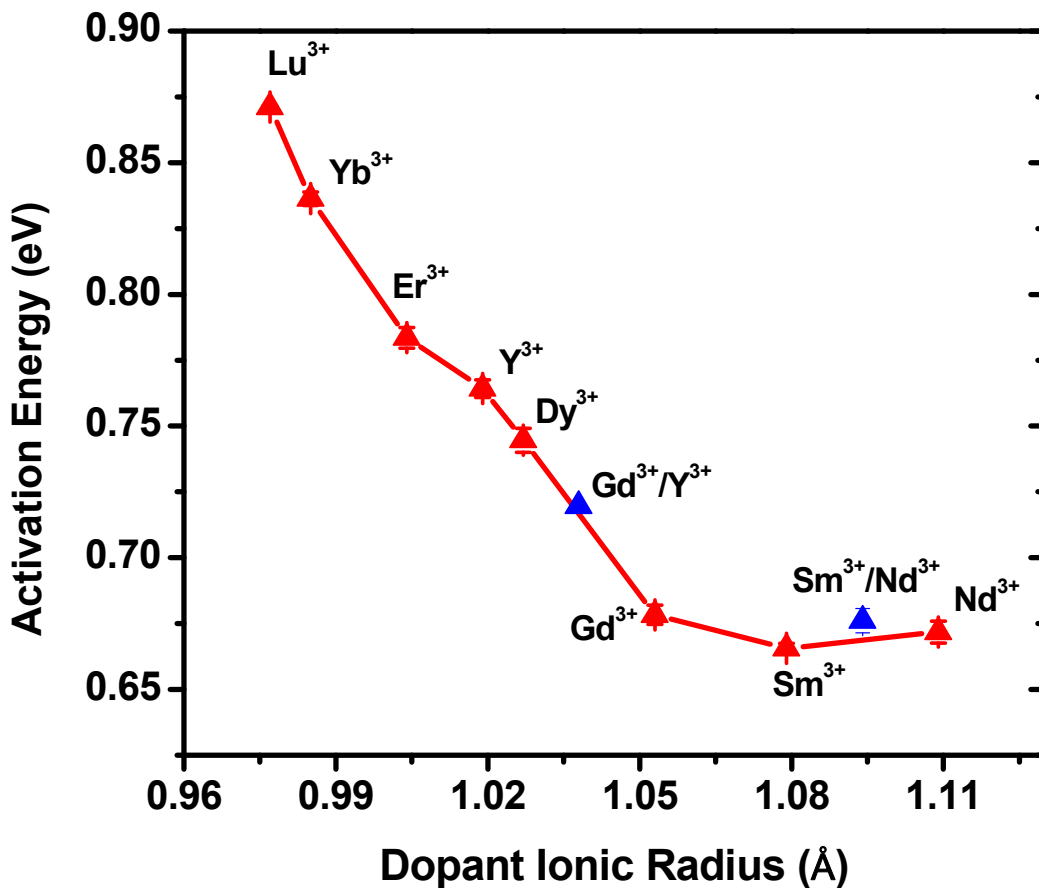


Figure 5-14. Activation energy for oxygen vacancy diffusion determined from the Arrhenius plot of the ionic conductivity data measured from 250°C to 700°C in doped ceria systems with 10 mol% dopant.

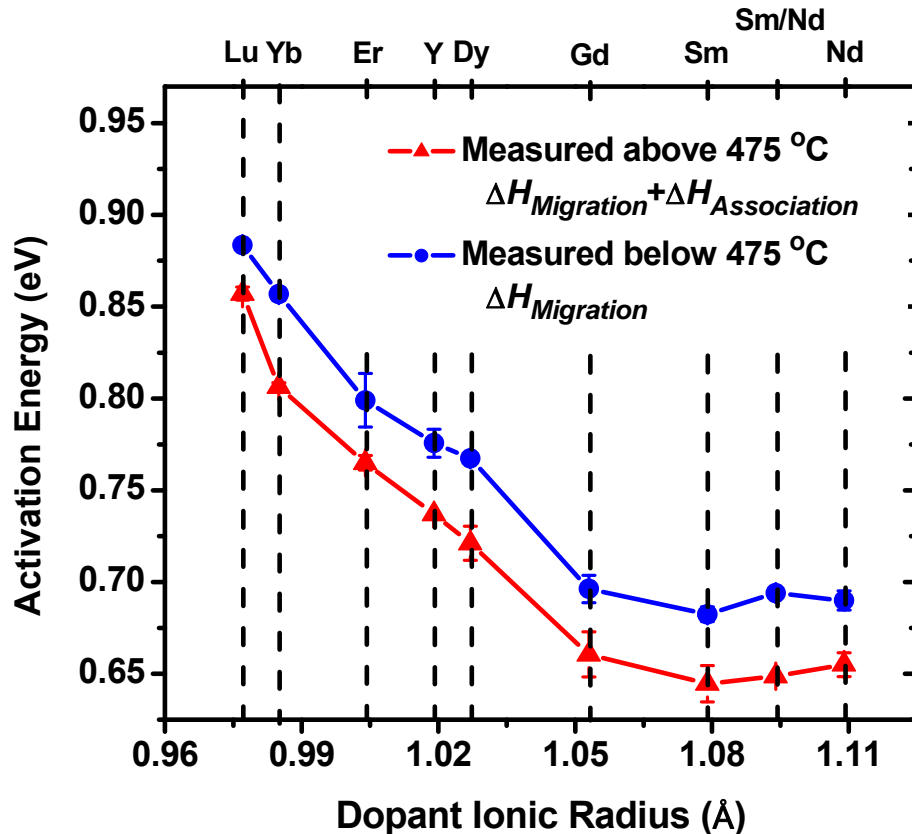


Figure 5-15. Migration and Association enthalpies for oxygen vacancy diffusion determined from the Arrhenius plot of doped ceria systems.

While describing the activation energy for oxygen diffusion in $\text{Sm}_{x/2}\text{Nd}_{x/2}\text{Ce}_{1-x}\text{O}_{2-\delta}$ system in Chapter 4, the Meyer-Neldel rule was discussed. According to this rule, the Arrhenius plots for the grain ionic conductivity of all the compositions (> 5 mol % dopant concentration) converges to a common transition temperature point (T_o). Around this temperature, conductivity becomes independent of dopant concentration. According to Nowick et al., T_o can be seen as a transition temperature between the stage where most of the carriers are bound at various traps and the stage where all the carriers are free.⁸⁷ This suggests that above T_o , almost all the oxygen vacancies are free to migrate for any dopant concentration. Since the Arrhenius plot for the grain ionic conductivity exhibits a gradual decrease in the slope at higher intermediate temperatures, it is

difficult to confirm this hypothesis. However, in order to distinguish between migration and association enthalpies, it was assumed that the association - dissociation transition occurs at T_o . For $\text{Sm}_{x/2}\text{Nd}_{x/2}\text{Ce}_{1-x}\text{O}_{2-\delta}$ system, T_o is found to be around 475°C. In the present study, it was further assumed that the transition temperature for all the doped ceria systems is around 475°C. Using a least-squares algorithm, the high and low temperature region of Arrhenius plot was linearly fitted. The fit of the data was generally quite good, with correlation coefficients for linear least-squares fit between 0.9997 and 0.9999. Activation energy values for the ionic conduction in these materials were calculated from the high and low temperature gradients of the fitted Arrhenius plots.

Figure 5-15 shows the activation energy for the grain ionic conductivity of $\text{D}_{0.10}\text{Ce}_{0.90}\text{O}_{2-\delta}$ systems, measured below 475°C and above 475°C, as a function of dopant cation ionic radius. The activation energy measured in the range of 475 °C - 250°C is a sum of $\Delta H_{\text{association}}$ and $\Delta H_{\text{migration}}$, while the activation energy measured above 475°C is equal to $\Delta H_{\text{migration}}$. It can be seen that both the curves show similar behavior. The migration enthalpy decreases with the increase in dopant ionic radius and reaches a minimum at $\text{Sm}_{0.10}\text{Ce}_{0.90}\text{O}_{2-\delta}$ (0.645 ± 0.009 eV), and then increases. According to Nowick et al., $\Delta H_{\text{migration}}$ should be independent of dopant cations physical properties and most importantly dopant concentration. Using this argument, Nowick et al. measured the ionic conductivity of highly pure CeO_2 , and separately estimated the migration enthalpy to be 0.67 eV.¹⁰⁵ Wang et al.¹⁰³ studied the dielectric and anelastic loss originating in the $(Y_{\text{Ce}}' - V_{\text{O}}^{\bullet\bullet})'$ defect pair. The activation energy for the relaxation process was estimated to be 0.64 eV. Similarly, Kilner et al. and Hohnke reported the migration enthalpy to be 0.6 eV and 0.61 eV, respectively, for doped ceria systems.^{88,106}

The literature results are not in agreement with the migration enthalpy data presented in this work. The data presented in Figure 5-15 indicates that there might be some additional energy term involved in the total activation energy.

The activation energy for oxygen diffusion as a function of dopant concentration in $\text{Sm}_{x/2}\text{Nd}_{x/2}\text{Ce}_{1-x}\text{O}_{2-\delta}$ system is already discussed in Chapter 4. The migration enthalpy in $\text{Sm}_{x/2}\text{Nd}_{x/2}\text{Ce}_{1-x}\text{O}_{2-\delta}$ system exhibits dependency on dopant content which is again not in agreement with the above mentioned literature.

5.3.2 Pre-Exponential Coefficient

The pre-exponential term in the Arrhenius relationship for the ionic conductivity of these oxide materials is described in Chapter 2. The pre-exponential factor (σ_0) is a complex function of different variables, and can be written as,

$$\sigma_0 = q_v^2 [V_O^{\bullet\bullet}] N_o a^2 v_o \exp\left(\frac{\Delta S_m}{k}\right) \quad (5-13)$$

where q_v is the charge of an oxygen vacancy, $[V_O^{\bullet\bullet}]$ is the fraction of mobile oxygen vacancies, N_o is the number of oxygen ion sites per unit volume, a is the ion jump distance, v_o is an appropriate lattice vibration, and ΔS_m is the entropy change during oxygen ion diffusion. In order to develop higher ionically conductive materials, it is essential to select dopant cations which show a high pre-exponential coefficient. In the present work, the pre-exponential coefficient in the Arrhenius ionic conductivity plot in doped ceria systems is compared. Figure 5-16 shows the pre-exponential factor of $\text{D}_{0.10}\text{Ce}_{0.90}\text{O}_{2-\delta}$ systems. It is important to note that the reported pre-exponential coefficient is determined from the intercept of the Arrhenius plot, assuming there is no change in the slope at higher temperatures, due to the release of oxygen vacancies

from local defect structures. It can be seen that the pre-exponential coefficient shows a similar trend when compared with activation energy in doped ceria systems shown in Figure 5-14. It decreases with the increase in dopant ionic radius. $\text{Sm}_{0.10}\text{Ce}_{0.90}\text{O}_{2-\delta}$ exhibits the lowest while $\text{Lu}_{0.10}\text{Ce}_{0.90}\text{O}_{2-\delta}$ shows the highest pre-exponential coefficient value.

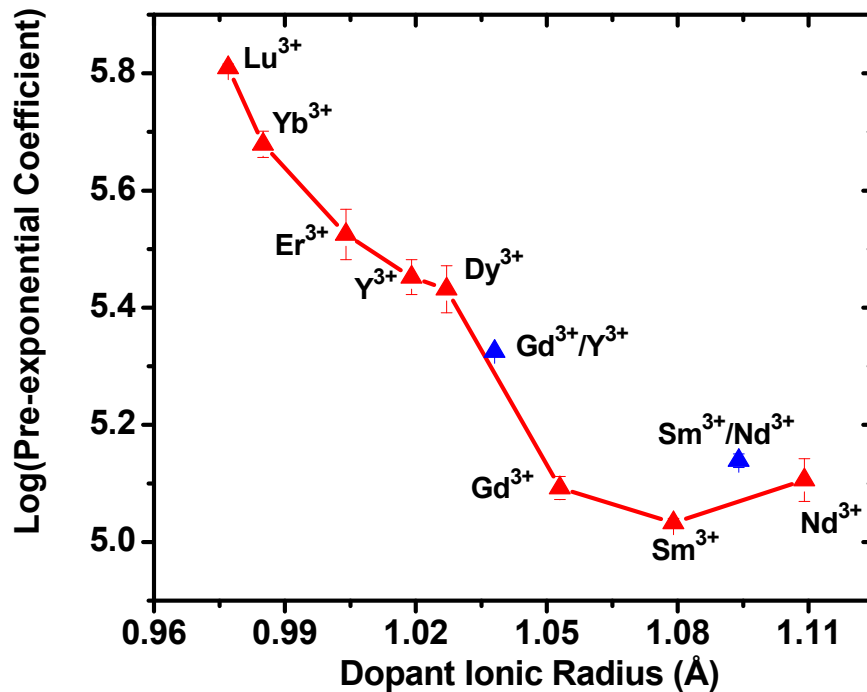


Figure 5-16. Pre-exponential coefficient in the Arrhenius ionic conductivity plot of $\text{D}_{0.10}\text{Ce}_{0.90}\text{O}_{2-\delta}$ systems.

The higher pre-exponential coefficient of $\text{Lu}_{0.10}\text{Ce}_{0.90}\text{O}_{2-\delta}$ may be attributed to the higher lattice vibration (ν_o) in this system. As shown in Figure 5-8, among all the doped ceria systems, $\text{Lu}_{0.10}\text{Ce}_{0.90}\text{O}_{2-\delta}$ shows the lowest lattice parameter. It is expected that ions in this system, are comparatively closer to each other, and exhibit stronger bond strength. The two ions (with unlike charges) inside the crystal lattice can be seen as a

harmonic oscillator where two blocks (of similar mass) are attached with the spring. The vibration frequency (ν_o) of the spring is given by,

$$\nu_o = \frac{1}{2\pi} \sqrt{\frac{k}{m}} \quad (5-14)$$

where m is the mass of the block and k is the spring constant. The k depends upon the stiffness of the spring, which in turn determines the force required to stretch the spring. Similarly, ions with stronger bond strength will show higher stiffness, and consequently, higher vibration frequency.

After reaching the minimum at Sm^{3+} , the pre-exponential coefficient again increases with the increase in the ionic radius of the dopant. $\text{Nd}_{0.10}\text{Ce}_{0.90}\text{O}_{2-\delta}$ shows a higher pre-exponential coefficient than that of $\text{Sm}_{0.10}\text{Ce}_{0.90}\text{O}_{2-\delta}$. This may be due to the increase in the lattice spacing of $\text{Sm}_{0.10}\text{Ce}_{0.90}\text{O}_{2-\delta}$, which results in the increase in the jump distance (a) of the oxygen vacancy. From the present work, it is known that the activation energy of $\text{Nd}_{0.10}\text{Ce}_{0.90}\text{O}_{2-\delta}$ is higher than that of $\text{Sm}_{0.10}\text{Ce}_{0.90}\text{O}_{2-\delta}$. Although, the ionic conductivity depends upon both the activation energy and the pre-exponential coefficient, it is the latter that is contributing more towards ionic conductivity in this dopant ionic radius range. Since, the pre-exponential coefficient value of $\text{Nd}_{0.10}\text{Ce}_{0.90}\text{O}_{2-\delta}$ is higher than that of $\text{Sm}_{0.10}\text{Ce}_{0.90}\text{O}_{2-\delta}$, $\text{Nd}_{0.10}\text{Ce}_{0.90}\text{O}_{2-\delta}$ exhibits higher ionic conductivity.

As discussed in Chapter 4, co-doping in ceria can lead to the increase in configurational entropy of the system, which consequently enhances the pre-exponential coefficient value. For $\text{Sm}_{0.05}\text{Nd}_{0.05}\text{Ce}_{0.90}\text{O}_{2-\delta}$ system, the pre-exponential coefficient was higher than that of $\text{Nd}_{0.10}\text{Ce}_{0.90}\text{O}_{2-\delta}$ and $\text{Sm}_{0.10}\text{Ce}_{0.90}\text{O}_{2-\delta}$. However,

$\text{Gd}_{0.056}\text{Y}_{0.044}\text{Ce}_{0.90}\text{O}_{2-\delta}$ exhibits a pre-exponential coefficient value between that of $\text{Gd}_{0.10}\text{Ce}_{0.90}\text{O}_{2-\delta}$ and $\text{Y}_{0.10}\text{Ce}_{0.90}\text{O}_{2-\delta}$ ceramics.

Experimentally, it is difficult to separate out the contribution from different variables on the pre-exponential coefficient value. Thus, a computational approach, like density functional theory, may be extremely helpful to investigate the effect of each variable independently. This work will allow better understanding of the pre-exponential factor for different type of acceptor dopants shown in Figure 5-16. This will allow selecting next generation co-dopants, which not only show higher pre-exponential coefficient values, but also lower activation energies for oxygen vacancy diffusion.

5.4 Revisiting Critical Dopant Ionic Radius

In the introduction of this chapter, it was mentioned that fluorite structured oxides exhibit maximum ionic conductivity when doped with an trivalent cation that causes very little expansion or contraction of the lattice. To support this argument, it has been said that doped ZrO_2 exhibits lower ionic conductivity than that of doped CeO_2 , because most of the trivalent dopant cations show ionic radius that closely lie to that of Ce^{4+} than Zr^{4+} . Thus, the ionic radius mismatch between host and dopant cations will be smaller in doped ceria systems compared to doped ZrO_2 . This leads to more elastic strain in doped ZrO_2 system, and consequently, lower ionic conductivity. However, among doped ceria systems, Lu^{3+} cation shows the lowest ionic conductivity even though the ionic radius of Lu^{3+} is very close to that of Ce^{4+} . The addition of acceptor dopant cations creates oxygen vacancies (to achieve electrical neutrality), which also leads to the contraction of the lattice. In the literature, different approaches were taken to estimate the effect of dopant cations inside the fluorite oxide lattice. Using multiple regression analysis, Kim proposed the empirical relationship between the ionic radius of the dopant

cation dissolved in ceria (and other fluorite structure oxides). A critical ionic radius (r_c) for the dopant cation is defined which on substituting for host cation does not change the lattice parameter. Based on lattice strain – ionic conductivity relationship, cation with ionic radius r_c , is the ideal dopant for ceria to exhibit the highest ionic conductivity. The r_c value obtained from Kim's²² proposed model for the trivalent dopant cations in ceria was estimated to be 1.038 Å. In the same line, Hong et al.⁷⁴ derived r_c value to be 1.024 Å, using a model in which radius was assigned to oxygen vacancy. In principle, the r_c value can be derived from the plot of lattice parameter versus dopant ionic radius for a number of different oxide solutions of the same concentration. Eguchi et al. published such a plot using eight lanthanide oxides with 20 mol% dopant concentration.¹⁰ The r_c value obtained from the graph is 1.010 Å. Mogensen et al. reported different r_c values derived from the past literature, ranging from 1.010 Å to 1.038 Å.⁷³

It is widely accepted that Gd^{3+} dopant cation exhibits the highest ionic conductivity among doped ceria materials.¹³ According to Kim, Gd^{3+} shows the highest ionic conductivity because the ionic radius of Gd^{3+} (1.053 Å) lies very close to the r_c value (1.038 Å).⁴⁸ In Chapter 4, co-doping strategy was discussed in which co-dopants were added such that the weighed average dopant ionic radius matches to the r_c value. The ionic conductivity obtained from the co-doped ceria was lower than that of Gd-doped ceria with the same total dopant concentration. The r_c value reported in all the past work is obtained from the plot of dopant cation ionic radius and lattice expansion measured at room temperature. The ionic conductivity (which is measured at high temperatures) results indicate that there might be an increase in r_c value toward Nd^{3+}

ionic radius value, at higher temperatures. To test this hypothesis, in the present work, lattice expansion as a function of dopant cation ionic radius is measured at higher temperatures. The r_c value is obtained, where the lattice parameter mismatch between doped ceria and pure ceria becomes zero. This work will not only provide the r_c value at higher temperatures, but also verify Kilner et al.'s hypothesis, that maximum ionic conductivity is achieved in the system when the dopant cation substitute for host cation without any change in lattice.

Table 5-7. Critical dopant ionic radius for trivalent acceptor dopant cation for host ceria, for different temperatures.

Temperature (°C)	Critical dopant ionic radius (r_c) value (Å)
25°C	1.0311 Å
100°C	1.0293 Å
200°C	1.0291 Å
300°C	1.0278 Å
400°C	1.0274 Å
500°C	1.0252 Å

The relationship between the lattice parameter of $D_{0.10}Ce_{0.90}O_{2-\delta}$ as a function of dopant cation ionic radius, at higher temperatures is shown earlier in this chapter in Table 5-5. The lattice parameter of doped ceria depends linearly upon dopant cation ionic radius, even at higher temperatures. The lattice parameter of pure CeO_2 as a function of temperature was also determined using the same experimental procedure (given in Chapter 3). The lattice parameter of pure ceria was estimated to be 5.4099 Å, at room temperature. The Joint Committee on Powder Diffraction Standards card 34-0394 for ceria shows the lattice parameter value of 5.41134 Å.⁴⁷ The difference in the

estimated and standard value (0.00144 Å) was adjusted in all the lattice parameter values that were determined using this procedure. Table 5-7 shows the r_c value determined at different temperatures. At room temperature, the r_c value was estimated to be 1.0311 Å which is in between the values reported by Kim et al. (1.038 Å) and Hong et al. (1.024 Å). With the increase in temperature, the r_c value decreases.

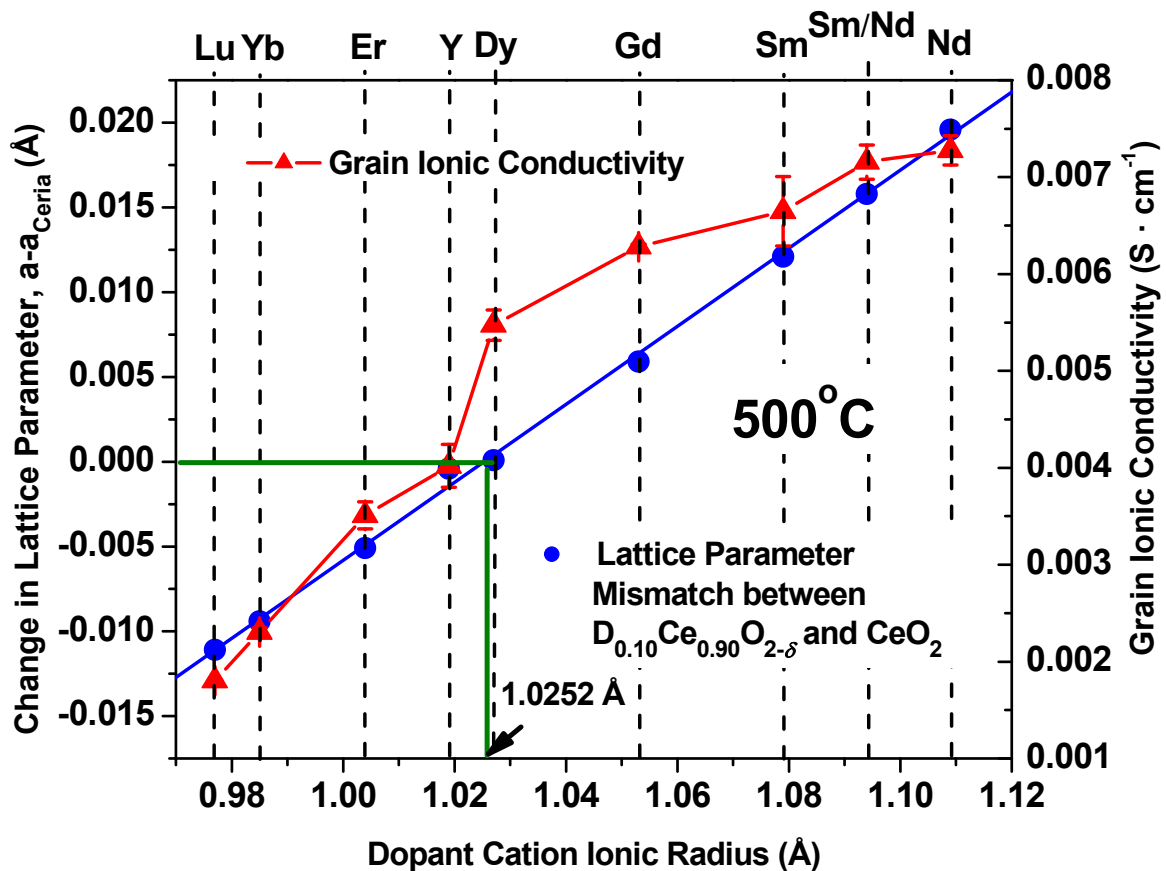


Figure 5-17. Lattice parameter mismatch between $D_{0.10}Ce_{0.90}O_{2-\delta}$ and pure ceria, as a function of dopant cation ionic radius at 500°C. The grain ionic conductivity of $D_{0.10}Ce_{0.90}O_{2-\delta}$ at 500°C is also shown.

Figure 5-17 shows the lattice parameter mismatch between $D_{0.10}Ce_{0.90}O_{2-\delta}$ (a) and pure ceria, as a function of dopant cation ionic radius, at 500°C. It can be seen that for dopant cations with ionic radius less than 1.025 Å, the mismatch is negative, while dopant cations which show higher ionic radius than 1.025 Å, the mismatch is positive.

At 1.025 Å, there is no mismatch between doped ceria system and pure ceria. Figure 5-17 also compares the grain ionic conductivity of different doped ceria systems as a function of dopant cation ionic radius, at 500°C. Assuming Kilner et al.²¹'s hypothesis is correct, Dy³⁺ should exhibit the highest ionic conductivity, as its ionic radius (1.027 Å) is very close to the r_c value. However, it can be seen that the grain ionic conductivity continues to increase even for the dopant cations which show ionic radius higher than the r_c value. The Nd_{0.10}Ce_{0.90}O_{2-δ} cation exhibits the highest ionic conductivity among all the other doped ceria materials, with lattice parameter difference with pure ceria ~0.0196 Å at 500°C. This clearly indicates that the Kilner et al.²¹'s structure-ionic conductivity relationship is not applicable in doped ceria materials.

In Chapter 4, DFT work performed by Andersson et al.⁸³ on the total interaction energy for different trivalent dopant cations was shown. Since the oxygen vacancy site preference in Pm³⁺ to reside in nearest neighbor site or next to neighbor site of dopant cation is almost the same, therefore it was predicted that Pm³⁺ is the ideal dopant cation for ceria. However, DFT calculations were performed at 0 K. As Nd³⁺ lies next to Pm³⁺ in the lanthanide series, therefore there is a possibility that the cross-over of the total interaction energies shown in Figure 4-6 shifts toward Nd³⁺ at higher temperatures. Thus, for Nd-doped ceria system, the number of equi-interaction energy sites is comparatively higher compared to other doped ceria materials. Future work is required to further investigate this possibility in detail.

5.5 Summary and Conclusions

To design higher ionically conductive doped ceria materials, it is imperative to relate the crystal structure with ionic conductivity at higher temperatures. In this work, crystal structure of different doped ceria systems were characterized at higher

temperature using XRD. All the compositions exhibit cubic fluorite structure similar to that of pure ceria. Both thermal and chemical elastic strains in the different systems of doped ceria were determined by estimating the lattice parameter at higher temperatures. The thermal expansion coefficient increases with the increase in dopant ionic radius and dopant concentration. The lattice parameter shows linear behavior with dopant ionic radius, from room temperature to 500°C. Also, the $\text{Sm}_{x/2}\text{Nd}_{x/2}\text{Ce}_{1-x}\text{O}_{2-\delta}$ system obeys Vegard's law, even at high temperatures.

As ionic conductivity depends upon the processing conditions, a wide range of ionic conductivity values is reported for any given doped ceria system. Thus, it was difficult to compare the ionic conductivity data from the literature. In order to understand the ionic conductivity trend among different trivalent acceptor doped ceria materials, processing variables in the synthesis of these materials were kept constant. A consistent set of ionic conductivity data (at higher temperatures) was prepared for the different doped ceria materials ($\text{D}_{0.10}\text{Ce}_{0.90}\text{O}_{2-\delta}$) synthesized under similar experimental conditions. Dopant concentration in these compositions is fixed to understand the separate effect of dopant ionic radius. Among trivalent acceptor dopant cations, Nd^{3+} cation exhibits the highest ionic conductivity in ceria. To study the effect of dopant content, different compositions of $\text{Sm}_{x/2}\text{Nd}_{x/2}\text{Ce}_{1-x}\text{O}_{2-\delta}$ ceramics were also synthesized. Initially, with the increase in the dopant concentration, the ionic conductivity increases. It reaches maximum at certain dopant concentration, and then degrades. Among all the tested doped ceria systems, $\text{Sm}_{0.075}\text{Nd}_{0.075}\text{Ce}_{0.85}\text{O}_{2-\delta}$ exhibits the highest ionic conductivity, at 500°C in air.

According to Kilner et al., for a fluorite structure oxides maximum ionic conductivity is achieved by alloying it with dopant cations which show minimum elastic strain in the host lattice. Following this hypothesis, Kim introduced the critical dopant ionic radius (r_c) concept for doped ceria materials. The r_c was defined as the ionic radius of the dopant cation that causes no elastic strain in the host lattice. Thus, dopant with ionic radius with r_c value should exhibit the highest ionic conductivity in ceria. On comparing the ionic conductivity of all the doped ceria materials synthesized under similar experimental conditions, it was observed that Nd^{3+} exhibits the highest ionic conductivity. However, ionic radius of Nd^{3+} is far away from the r_c value. It is important to note that in the structure (r_c) – property (ionic conductivity) relationship proposed by Kim²², both the parameters were measured in different conditions (temperatures). In order to verify the r_c concept, r_c values were determined at temperatures where the ionic conductivity is measured. The graph between the elastic strain and the dopant cation ionic radius was plotted at higher temperatures, to derive r_c values. The r_c value decreases with the increase in temperature. At 500°C, r_c value was estimated to be 1.0252 Å for trivalent dopant cations in host ceria. The r_c value obtained at 500°C lies close to the ionic radius of Dy^{3+} . However, it is Nd^{3+} that exhibits the highest ionic conductivity. This clearly indicates that the Kilner et al.'s hypothesis is not applicable for doped ceria materials.

CHAPTER 6 PROCESSING EFFECTS ON THE IONIC CONDUCTIVITY

6.1 Introduction

In Chapter 4, a comparison between the ionic conductivity data for singly doped ceria systems taken from literature was shown. A wide range of grain ionic conductivity values have been reported for a material with similar composition.⁷ A careful survey of the experimental procedures from literature, it indicates that processing variables show an effect on the ionic conductivity of the material. Typically, powder synthesized using wet chemical route exhibit higher ionic conductivity compared to conventional solid state route.⁵⁸ The soft chemical route is capable of producing relatively higher purity, homogeneous, and ultrafine powder at low temperatures.^{58,63,64} For the polycrystalline ceramic electrolyte materials, the presence of even slight concentration of impurities is deleterious to both the grain and the grain boundary conductivities.^{107,108} Typically in all the ceramic processing techniques, SiO₂ is a ubiquitous background impurity.¹⁰⁹ It is difficult to avoid its presence even when using a relatively pure sample. Zhang et al.¹⁰⁷ studied the influence of SiO₂ content on the grain and the grain boundary ionic conductivity in Gd_xCe_{1-x}O_{2-δ} system. It was shown that with the increase in SiO₂ content, the grain ionic conductivity consistently decreases. Similar results have been reported by Martin et al.¹¹⁰ in SiO₂ doped ZrO₂ system. With the increase in SiO₂ content from 1 wt % to 10 wt%, grain conductivity of 8 mol% yttrium stabilized zirconia at 400°C decreases by approximately 25 %. According to Zhang et al.¹⁰⁷, this decrease in the conductivity can be explained by the dissolution of SiO₂ in Gd_xCe_{1-x}O_{2-δ} crystallites. At higher temperatures, small amount of SiO₂ dissolve inside the doped

ceria lattice, either at substitutional (shown in equation 6-1) or interstitial sites (shown in equation 6-2).



The Si^{4+} cation entering the lattice as a substitution for Ce^{4+} does not create any charge carriers inside the lattice, however due to the difference in the ionic radius between the Si^{4+} ($r_{\text{Si,VIII}}^{4+} = 0.4 \text{ \AA}$) and Ce^{4+} ($r_{\text{Ce,VIII}}^{4+} = 0.97 \text{ \AA}$) results in the elastic strain which not only hinders the mobility of oxygen vacancies but also increases the association activation energy of local defect structures (discussed in Chapter 2). According to the Hume-Rothery rules, for the substitutional dissolution, the ionic radius mismatch between the host and dopant cations of less than 15 % is required. The ionic radius mismatch between the Si^{4+} and Ce^{4+} case is quite large for Si^{4+} to substitute for Ce^{4+} . Thus, there is a higher probability that Si^{4+} cations reside on the interstitial sites. It can be seen from equation (6-2), interstitial point defects results in the consumption of oxygen vacancies which are the charge carrier in these oxide materials. This type of dissolution mechanism also results in the degradation of ionic conductivity.

In polycrystalline ceramic samples grain boundaries also have a significant role to the overall ionic conductivity. The deleterious effect of impurities on the grain boundary conductivity has been recognized in doped ceria ceramic for over 10 years.^{62,111} The impurities incorporated during the powder processing tend to segregate near the grain boundaries during sintering and grain growth. Figure 6-1 shows high resolution images of doped ceria systems from our work. Figure 6-1 A) shows continuous layer of an segregated phase present in the grain boundary of $\text{Gd}_{0.10}\text{Ce}_{0.90}\text{O}_{2.5}$. The layer is

around 2 nm in thickness. Figure 6-1 B) shows the glassy amorphous phase formed on the three-grain junction in the sintered $\text{Sm}_{0.05}\text{Nd}_{0.05}\text{Ce}_{0.90}\text{O}_{2-\delta}$ ceramic sample. Both the samples were synthesized using solid state reaction. The partial or complete blocking of charge carriers by these segregated impurities leads to higher grain boundaries resistivity.

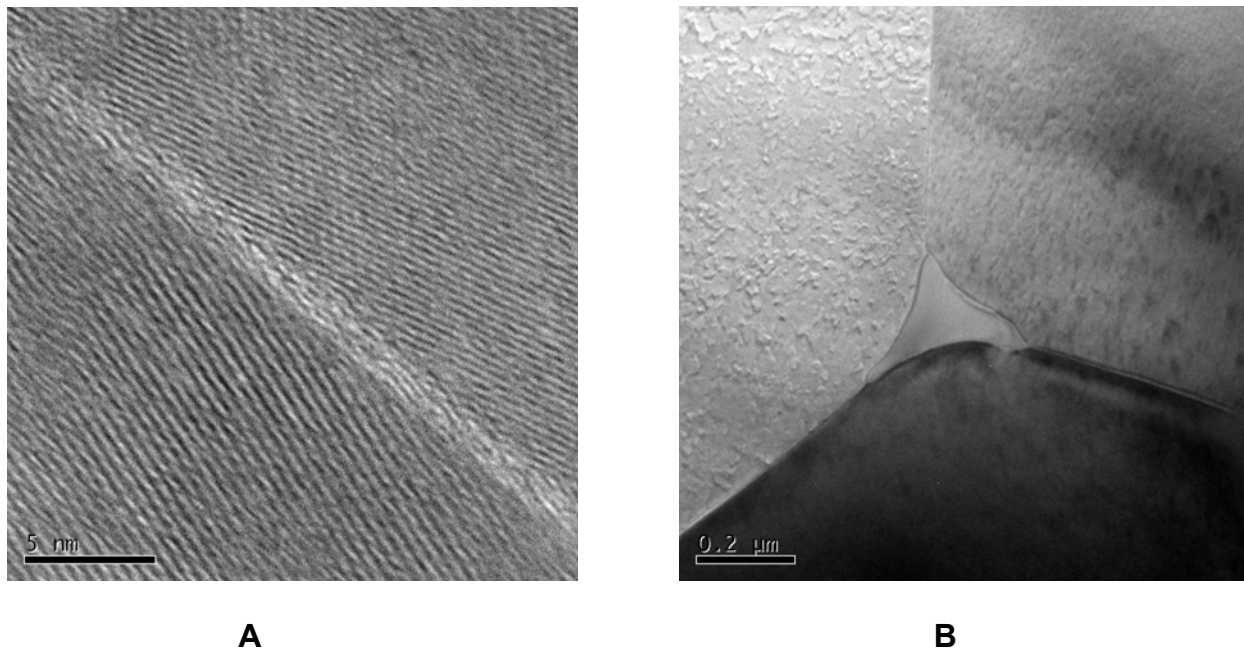


Figure 6-1. A) Continuous layer of an siliceous phase in the grain boundary of $\text{Gd}_{0.10}\text{Ce}_{0.90}\text{O}_{2-\delta}$ B) Glassy phase formed at the three-grain junction in $\text{Sm}_{0.05}\text{Nd}_{0.05}\text{Ce}_{0.90}\text{O}_{2-\delta}$.

Using transmission electron microscopy, Gerhardt et al.¹¹² studied the grain boundaries in doped ceria systems. The presence of Si in the form of a continuous glassy phase is responsible for the large decrease in the effective ionic conductivity in these materials. Even a few hundred ppm of a siliceous impurity can increase the grain-boundary resistivity of $\text{Gd}_{0.10}\text{Ce}_{0.90}\text{O}_{2-\delta}$ by up to 100 times.^{112,113} According to Steele¹³, for a highly pure $\text{Gd}_{0.10}\text{Ce}_{0.90}\text{O}_{2-\delta}$ sample, the grain boundary impedance cannot be detected above 500°C. However, for an impure $\text{Gd}_{0.10}\text{Ce}_{0.90}\text{O}_{2-\delta}$ sample, the

total ionic conductivity is mainly dominated by grain boundary conductivity, upto 1000°C. This clearly suggests the need for highly pure materials for the electrolyte application in SOFCs.

In addition to the impurities, the processing of the final microstructure from the starting powder also affects the ionic conductivity. Recent work by Eposito et al.¹¹⁴, have shown that the sharp grains and the unrelaxed grain boundary interfaces lead to higher grain boundary conductivity in doped ceria systems. Such microstructure possesses grain boundaries that are considered to be highly defective and segregation-free. In order to obtain such grain boundary structure, fast firing was performed to promote lattice diffusion of the material (from the grain boundary source) which results in the densification (rather than the grain growth and coarsening) in the polycrystalline green ceramic.

Also, it is well known that the acceptor dopant cations in ceria materials have tendency to segregate near the grain boundaries.¹¹⁵ This results in the formation of Schottky barrier for oxygen vacancy diffusion which significantly degrades the ionic conductivity in polycrystalline ionic materials. Dopant segregation can be attributed to the ionic radius mismatch between the dopant and host cations. In addition, the positive potential of the grain boundary core act as a driving force in segregating dopant cations near the grain boundary.¹¹⁶ Also, at high sintering temperatures, acceptor cations are sufficiently mobile to segregate to the grain boundary core, and accumulate in the space-charge layer as a result of elastic strain and electrostatic interactions with the positively charged grain boundary core. Thus, it is essential to lower the sintering temperature and time of the green ceramic material, such that the sintering process

does not provide enough thermal drive for the acceptor dopant cation to segregate near the grain boundary. One of the approach, as pointed out by Herring¹¹⁷, to lower the sintering temperature is to reduce the particle size of the starting powder. The densification can be enhanced by using nano-size powder which exhibits higher surface energy to drive mass diffusion transport.¹¹⁸ Other approach to synthesize dense ceria samples at lower temperatures is by using transition metal oxides sintering additives which promote densification.^{119,120} However, following this methodology may have a detrimental effects on the electrical properties of the material.^{121,122}

In recent years, microwave heating have gained lot of interest especially in the fabrication of ceramic materials with controlled microstructure.¹²³ In comparison to the conventional direct heating, microwave heating of ceramics offers lot of advantages. It not only promotes the material densification in a considerably reduced processing time and temperature, but also provides uniform heat treatment (via volumetric heating) and rapid heating rate which improve the material properties and microstructure. It has been reported for alumina that the microstructure evolution in the microwave and conventional sintering are not the same, and that the microwave sintering produces finer-grained alumina.¹²⁴ Recently, Rambabu et al.¹²⁵ reported 92 % relative theoretical density of the ceramic samples of CeO₂ synthesized using microwave sintering at 1200°C for 60 min. In the present work, microwave sintering was used as a fast firing technique to obtain dense polycrystalline ceramics with sharp grains and unrelaxed grain boundary interfaces.

In Chapter 4, a novel co-doped ceria system was designed that exhibits higher ionic conductivity than Gd-doped ceria. After identifying the co-dopants for the host

ceria, optimization of the dopant concentration was performed. This leads to the development of $\text{Sm}_{0.075}\text{Nd}_{0.075}\text{Ce}_{0.85}\text{O}_{2-\delta}$ material that exhibits 30 % higher ionic conductivity than $\text{Gd}_{0.10}\text{Ce}_{0.90}\text{O}_{2-\delta}$, at 550°C in air. In the previous work, co-doped samples were synthesized using solid state reaction. As mentioned earlier, this ceramic processing technique may contain impurities which degrade the ionic conductivity of the materials. To capture the full potential of $\text{Sm}_{0.075}\text{Nd}_{0.075}\text{Ce}_{0.85}\text{O}_{2-\delta}$ material, powder was synthesized using co-precipitation technique. This will not only improve the grain ionic conductivity but also promotes transport of charge carriers across the grain boundaries. Further, microwave sintering was used as a fast firing technique to obtain unrelaxed grain boundary interfaces that can further enhance the grain boundary conductivity of the material.

6.2 Experimental Procedures

The experimental details for the processing of phase pure powder of $\text{Sm}_{0.075}\text{Nd}_{0.075}\text{Ce}_{0.85}\text{O}_{2-\delta}$ using co-precipitation technique, and the microwave sintering of the green ceramic sample are given in Chapter 3. Figure 6-2 compares the temperature - time profile in the conventional sintering, and the microwave sintering. The conventional sintering of the $\text{Sm}_{0.075}\text{Nd}_{0.075}\text{Ce}_{0.85}\text{O}_{2-\delta}$ sample was performed at 1550°C for 10 h while the microwave sintering was done at 1450°C for 1 h. The area under the curve shown in Figure 6-2 is proportional to the thermal energy given to the ceramic sample during each sintering process.

The particle size distribution in $\text{Sm}_{0.075}\text{Nd}_{0.075}\text{Ce}_{0.85}\text{O}_{2-\delta}$ powder obtained using co-precipitation technique was mono-disperse with most of the particles were below 0.2 μm in size. The mean particle size was around 0.095 μm . Similarly, powder synthesized using conventional solid oxide route exhibits mono-disperse particle size distribution.

However, the average particle size obtained through this process was 0.84 μm . Microwave sintering was performed on the green ceramic sample using the powder synthesized with co-precipitation technique; while the conventional solid state sintering was performed on the sample with the powder synthesized using the solid oxide route. The density of the ceramic sample obtained using microwave sintering was around 94 % of theoretical density, while in the case of conventional sintering it was above 98 % of theoretical density. For convenience, in the text abbreviations are used for both the samples (shown in Table 6-1).

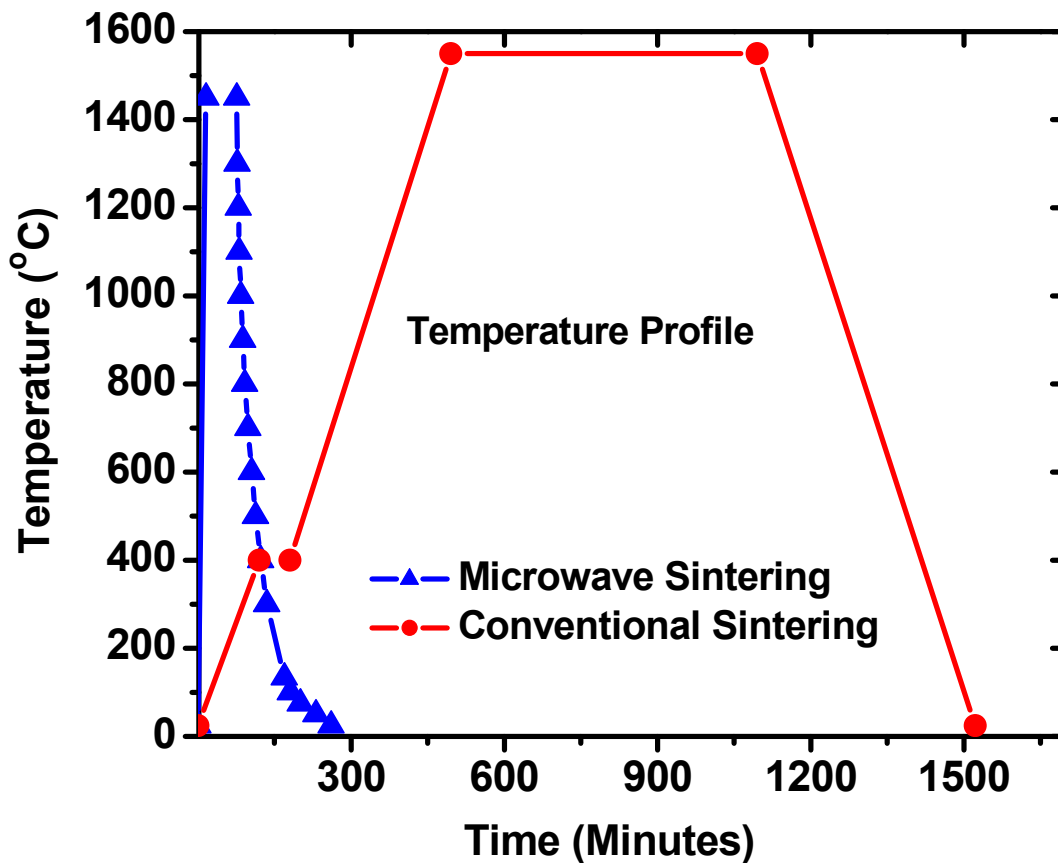


Figure 6-2. Comparison of the temperature – time profile in conventional solid state sintering and microwave sintering.

Table 6-1. Abbreviation of samples synthesized using different techniques.

Sample	Abbreviation
Conventional Sintering + Solid Oxide Route	Sam _{CoSo}
Microwave Sintering + Co-precipitation Route	Sam _{MiCo}

The microstructural analysis was performed using both scanning electron microscopy (SEM) and transmission electron microscopy (TEM). Electron dispersive X-rays spectroscopy (EDXS) was used for chemical compositional analysis in the material. Details for the sample preparation for both the characterizations are described in Chapter 3. The ionic conductivity measurements were performed using two-point probe impedance spectroscopy (discussed in Chapter 2) from 250°C to 700°C, in air.

6.3 Results and Discussion

6.3.1 Microstructure

Figure 6-3 shows the SEM images of Sam_{CoSo} and Sam_{MiCo}. Due to the large particle size of the starting powder, and the higher sintering temperature and time, the grain size in Sam_{CoSo} is much larger compared to Sam_{CoMi}. The grain size in the sample synthesized through solid state reaction method is in the range of 4 – 7 μm. The arrows in the microstructure image of the Sam_{CoSo} sample show the curved nature of the grain boundaries. According to Eposito et al.¹¹⁴, this type of grain boundaries are relaxed and in equilibrium state. The fast firing in the Sam_{MiCo} sample, results in the finer grained microstructure. The grain size using microwave sintering is in the range of 0.5 - 1 μm. In order to study the grain boundary in Sam_{MiCo} sample, TEM was performed on Sam_{MiCo} sample.

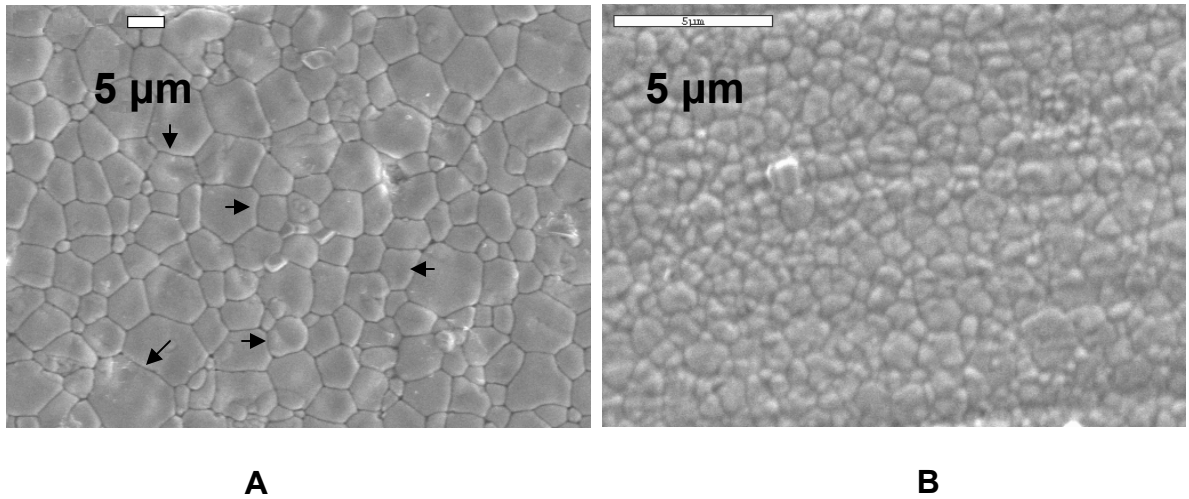


Figure 6-3. SEM images of A) Conventional sintering + Solid oxide route B) Microwave sintering + Co-precipitation technique.

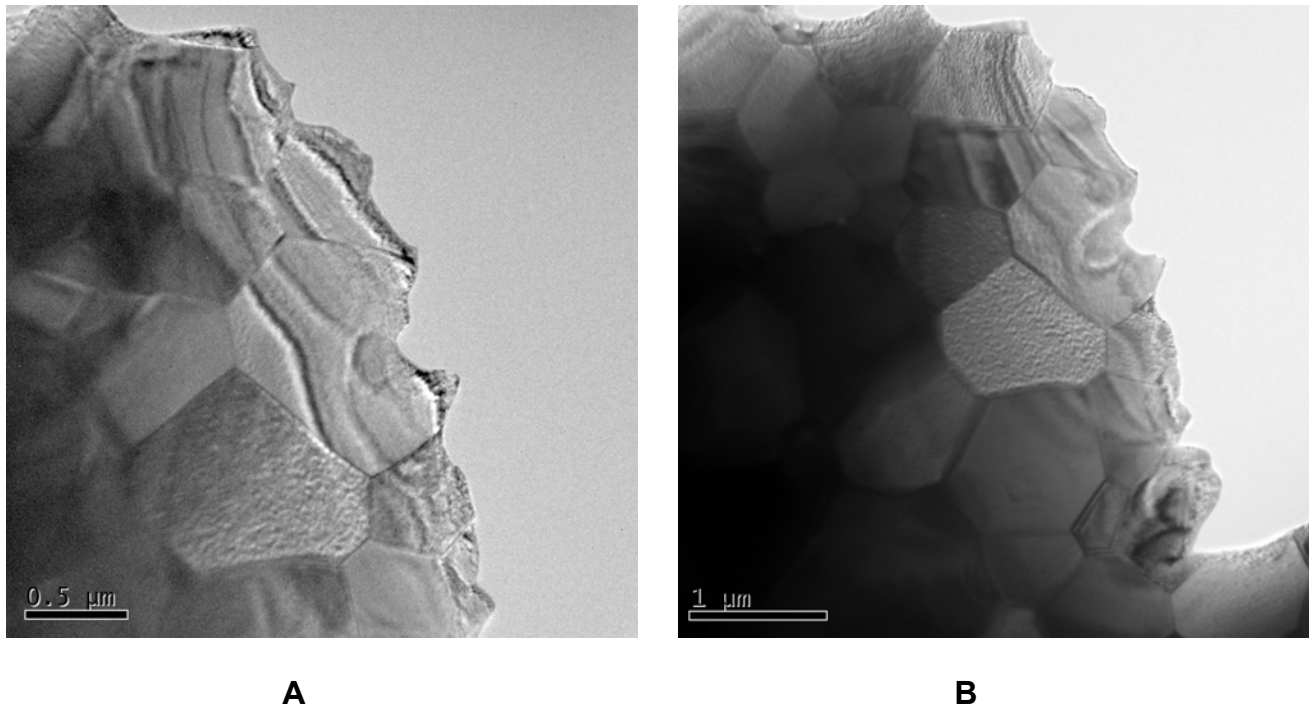


Figure 6-4. TEM images of the microwave sintered $\text{Sm}_{0.075}\text{Nd}_{0.075}\text{Ce}_{0.85}\text{O}_{2-\delta}$ sample.

Figure 6-4 shows the microstructure of the Sm_{MgCo} sample. It can be seen that the grains are finer with sharp grain boundaries. Clearly, uniform and rapid heating of the ceramic sample does not provide enough time for grain growth. Thus, there is no grain boundary interface relaxation in the Sm_{MgCo} sample. Figure 6-5 compares the

typical grain boundary observed in both the samples. Typically, the width of the grain boundary in the pure polycrystalline ceramic sample is in the range 1 - 2 nm.¹²⁶ As discussed in the introduction, in order to reduce the grain boundary surface energy most of the siliceous impurities segregate near the grain boundaries. Therefore, depending upon the segregation of the dopant and impurities, the grain boundary thickness can increase to above 2 nm.¹¹⁵ In the sample synthesized using co-precipitation and microwave sintering, it can be seen that the width of the grain boundary is quite small (<1 nm). This clearly suggests that the segregation near the grain boundaries is minimal in the sample, and the impurities present in the material are very low. In contrast to Sam_{MiCo} sample, the grain boundary width in Sam_{CoSo} is quite large (~2 nm). This may be due to the segregation of acceptor dopant cations or due to the presence of impurities near the grain boundary.

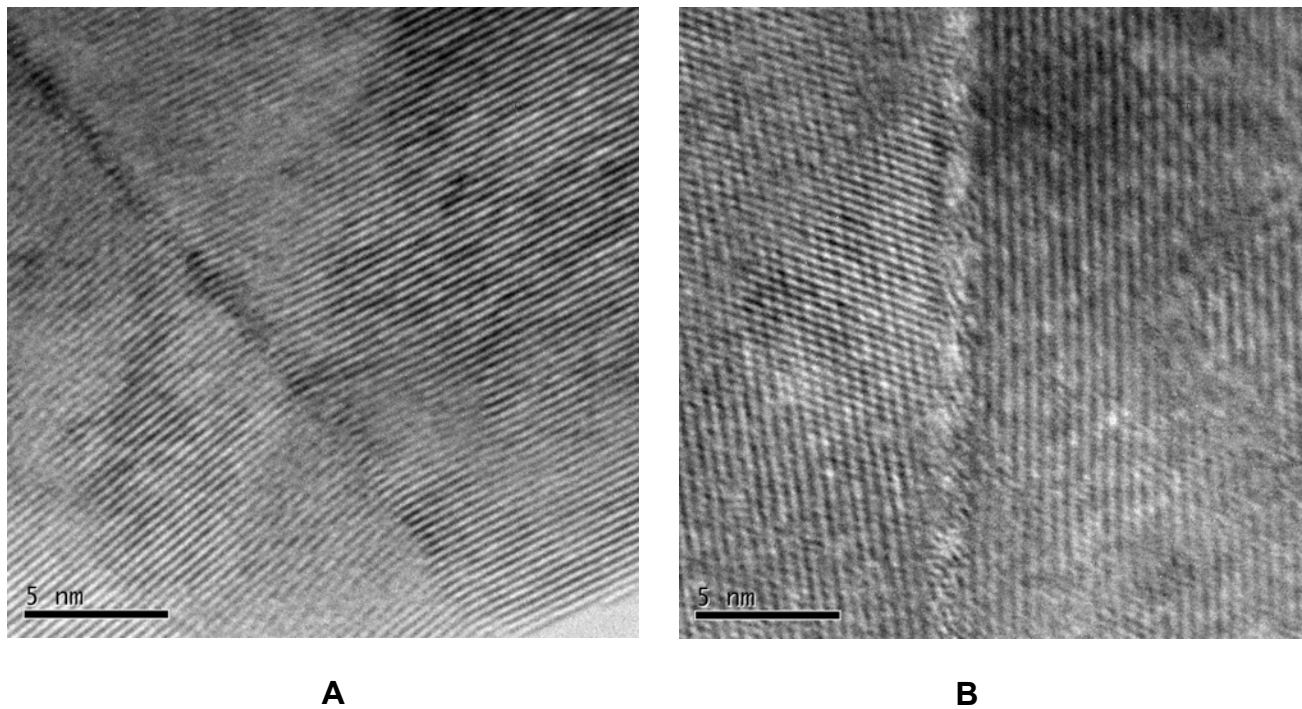


Figure 6-5. Grain boundary in the polycrystalline ceramic synthesized using A) microwave sintering and B) conventional solid state sintering.

EDXS was performed for chemical compositional analysis in the grain boundary of Sm_{CoSo} sample. Figure 6-6 shows the EDX spectrum at the grain boundary for the sample synthesized using solid oxide route and solid state sintering. The extent of dopant segregation profile across the grain boundary cannot be determined using line scan EDXS, as it is difficult to resolve the peaks of Ce, Sm and Nd in the EDX spectrum. However, in the EDXS result shown in Figure 6-6, Si peak was detected. This suggests the presence of Si near the grain boundaries. This is consistent with literature, which states that solid oxide processing route to process powder usually contains higher impurity content.

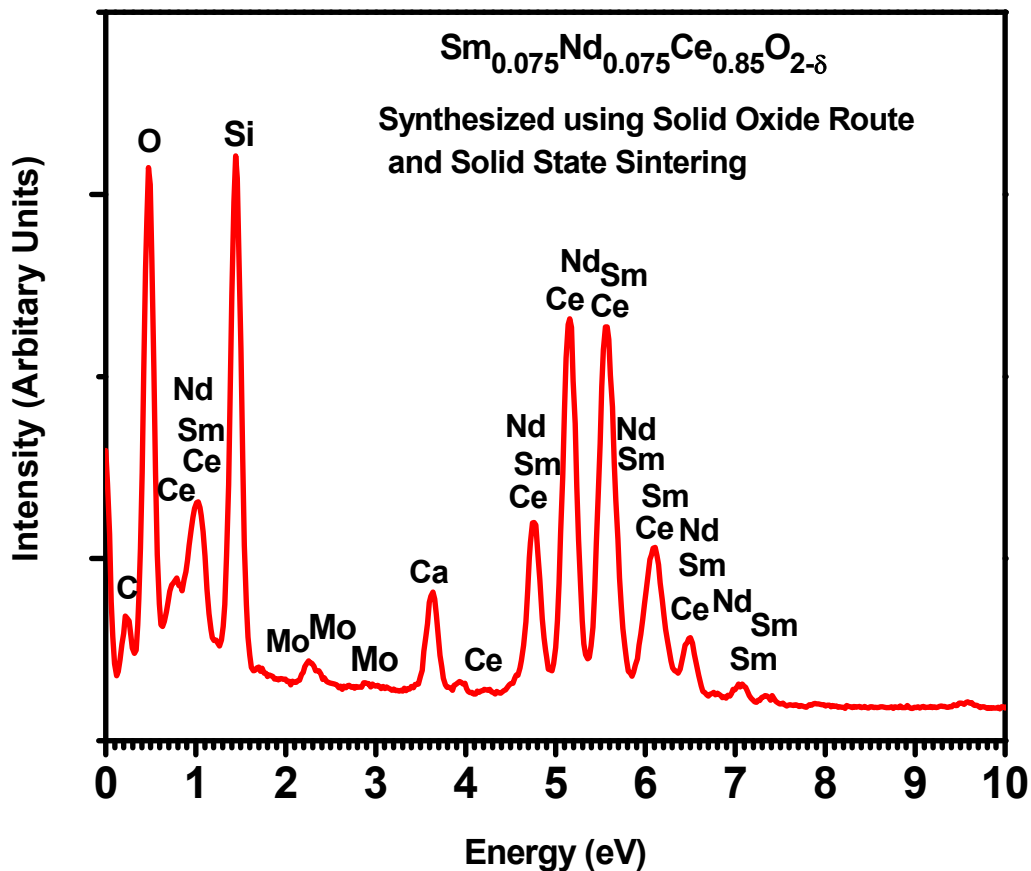


Figure 6-6. EDX spectrum of Sm_{CoSo} sample.

6.3.2 Ionic Conductivity

Figure 6-7 shows the normalized impedance spectra of an electroded polycrystalline ceramic samples of $\text{Sm}_{0.075}\text{Nd}_{0.075}\text{Ce}_{0.85}\text{O}_{2-\delta}$ synthesized using different processing routes, taken at 350°C in air.

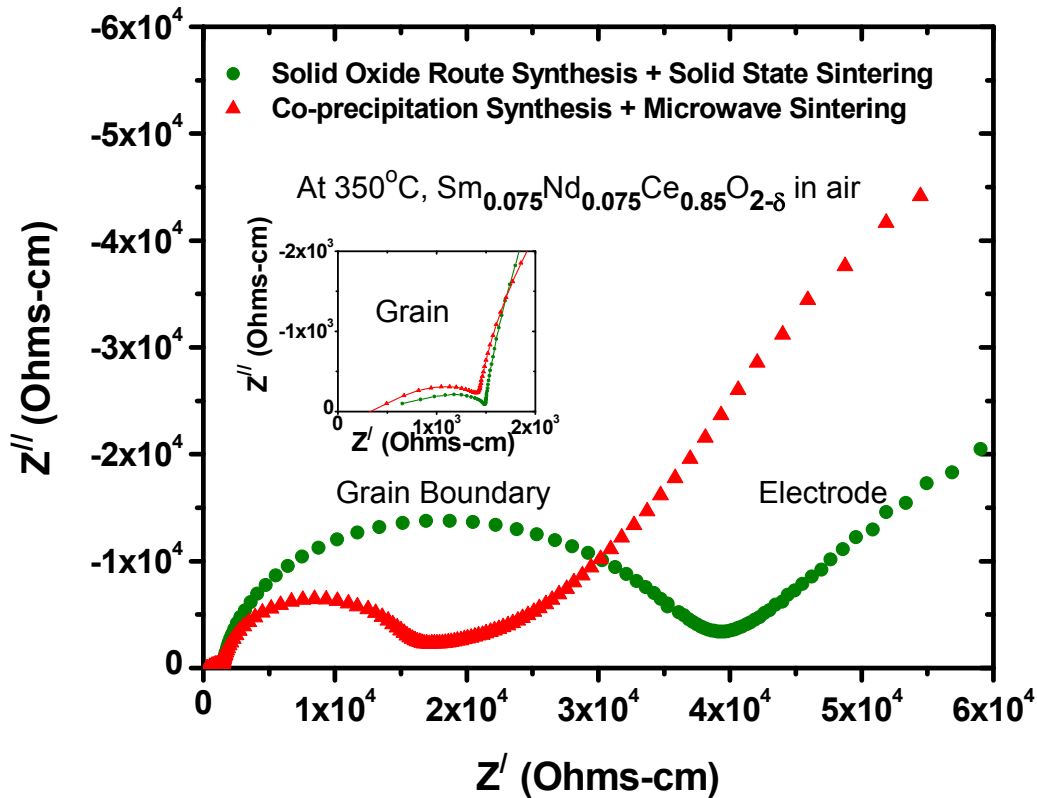


Figure 6-7. Impedance spectrum of Sm_{MiCo} and Sm_{CoSo} samples at 350°C, in air.

On comparing different $\text{Sm}_{0.075}\text{Nd}_{0.075}\text{Ce}_{0.85}\text{O}_{2-\delta}$ ceramic samples at 350°C, it can be seen that the intra-grain polarization semicircle in Sm_{MiCo} sample looks smaller when compared with Sm_{CoSo} . This may be attributed to the siliceous impurities present in the Sm_{CoSo} sample which dissolve inside the crystal lattice (using interstitial mechanism), and consume the oxygen vacancies which are the charge carriers in these oxide materials. Similarly, the impedance of the grain boundary polarization semi-circle for the Sm_{CoMi} sample is smaller than that of Sm_{CoSo} , which is consistent with the

microstructural features observed in the previous section. The sharp and un-relaxed grain boundary interfaces formed in the fast firing results in the lower grain boundary impedance in Sm_{MICo} sample. Further, the rapid and homogeneous heating during the microwave sintering does not provide sufficient time for the acceptor dopant cations to segregate near the grain boundaries. Also, due to the higher purity powder (synthesized using co-precipitation technique), extrinsic siliceous impurities are almost absent in the Sm_{MICo} sample.

As reported in Chapter 4, at 550°C , the grain ionic conductivity of $\text{Sm}_{0.075}\text{Nd}_{0.075}\text{Ce}_{0.85}\text{O}_{2-\delta}$ synthesized using conventional solid oxide route is $14 \times 10^{-3} \text{ S}\cdot\text{cm}^{-1}$. The conductivity value is 30% higher than that of $\text{Gd}_{0.10}\text{Ce}_{0.90}\text{O}_{2-\delta}$ synthesized using the same experimental conditions. Figure 6-8 shows the Arrhenius plot for the grain and the total ionic conductivity in Sm_{MICo} and Sm_{CoSo} samples. In addition, the Arrhenius plot for the grain and the total ionic conductivity of $\text{Gd}_{0.10}\text{Ce}_{0.90}\text{O}_{2-\delta}$ synthesized using solid oxide route is also shown. The sample synthesized using microwave sintering and co-precipitation technique, shows higher grain ionic conductivity than that of Sm_{CoSo} . At 550°C , the grain ionic conductivity of $\text{Sm}_{0.075}\text{Nd}_{0.075}\text{Ce}_{0.85}\text{O}_{2-\delta}$ of Sm_{MICo} sample is $15 \times 10^{-3} \text{ S}\cdot\text{cm}^{-1}$, which is around 45 % higher than that of $\text{Gd}_{0.10}\text{Ce}_{0.90}\text{O}_{2-\delta}$ ($\sim 10.7 \times 10^{-3} \text{ S}\cdot\text{cm}^{-1}$).

Table 6-2 shows the grain ionic conductivity value of $\text{Sm}_{0.075}\text{Nd}_{0.075}\text{Ce}_{0.85}\text{O}_{2-\delta}$ at 600°C , synthesized using different processing techniques. For comparison, the grain ionic conductivity value of $\text{Gd}_{0.10}\text{Ce}_{0.90}\text{O}_{2-\delta}$ taken after Steele¹³ is also shown. It is important to note that the grain ionic conductivity reported by Steele is the highest ever reported for $\text{Gd}_{0.10}\text{Ce}_{0.90}\text{O}_{2-\delta}$. It can be seen from the Table 6-2 that

$\text{Sm}_{0.075}\text{Nd}_{0.075}\text{Ce}_{0.85}\text{O}_{2-\delta}$ synthesized using microwave sintering and co-precipitation technique exhibits higher grain ionic conductivity than that of $\text{Gd}_{0.10}\text{Ce}_{0.90}\text{O}_{2-\delta}$ reported by Steele. This result shows the potential of $\text{Sm}_{0.075}\text{Nd}_{0.075}\text{Ce}_{0.85}\text{O}_{2-\delta}$ as an electrolyte material for solid oxide fuel cells.

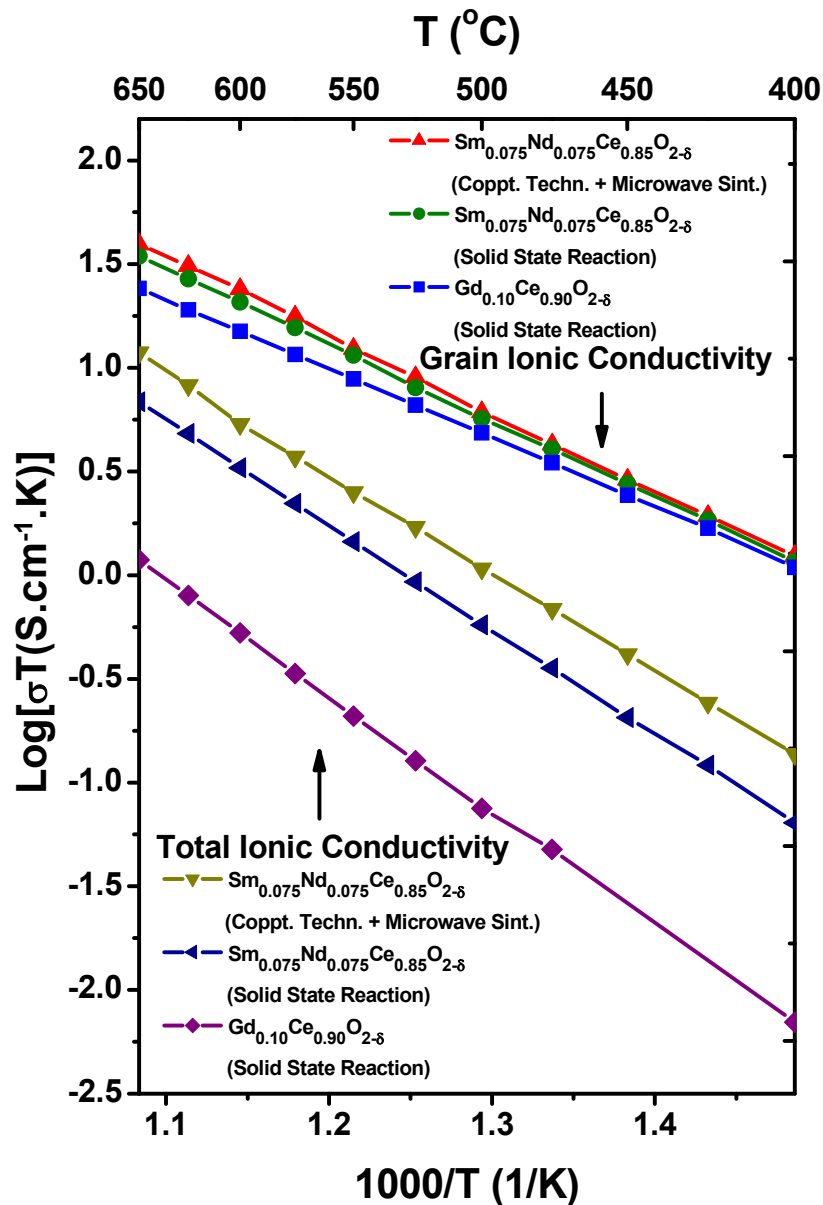


Figure 6-8. Arrhenius plot for the ionic conductivity of $\text{Sm}_{0.075}\text{Nd}_{0.075}\text{Ce}_{0.85}\text{O}_{2-\delta}$ and $\text{Gd}_{0.10}\text{Ce}_{0.90}\text{O}_{2-\delta}$ materials.

Table 6-2. Comparison of the grain ionic conductivity of $\text{Sm}_{0.075}\text{Nd}_{0.075}\text{Ce}_{0.85}\text{O}_{2-\delta}$ and $\text{Gd}_{0.10}\text{Ce}_{0.90}\text{O}_{2-\delta}$ at 600°C .

	Sm_{CoMi}	Sm_{CoSo}	$\text{Gd}_{0.10}\text{Ce}_{0.90}\text{O}_{2-\delta}$ (taken after Steele)
Grain Ionic Conductivity ($\text{S}\cdot\text{cm}^{-1}$)	2.74×10^{-2}	2.37×10^{-2}	2.50×10^{-2}

The total ionic conductivity of both $\text{Gd}_{0.10}\text{Ce}_{0.90}\text{O}_{2-\delta}$ and $\text{Sm}_{0.075}\text{Nd}_{0.075}\text{Ce}_{0.85}\text{O}_{2-\delta}$ samples is lower than their corresponding grain ionic conductivity. This is basically due to the lower grain boundary conductivity contribution towards the total ionic conductivity. Typically, the grain boundary ionic conductivity of acceptor doped ceria is two orders of magnitude lower than the corresponding grain ionic conductivity values, depending upon the dopant concentration and temperature.¹¹⁵ Thus, the lower grain boundary conductivity results in lower total ionic conductivity. Further, the total ionic conductivity of Sm_{CoMi} sample is higher than that of Sm_{CoSo} . This is consistent with the microstructural results discussed earlier. Since Sm_{CoMi} sample exhibits higher purity compared with Sm_{CoSo} sample, therefore, the grain boundary impurity phase blocking is comparatively lower in Sm_{CoMi} sample. In addition, the fast firing in the microwave sintering does not provide sufficient time for dopant cations or impurities to segregate the near the grain boundaries in the material. Further work need to be performed to separate out the individual effect of the powder synthesis, and the microwave sintering on the total ionic conductivity.

Further, from Figure 6-8, it can be seen that the $\text{Sm}_{0.075}\text{Nd}_{0.075}\text{Ce}_{0.85}\text{O}_{2-\delta}$ synthesized using solid stat sintering route exhibits higher total ionic conductivity than $\text{Gd}_{0.10}\text{Ce}_{0.90}\text{O}_{2-\delta}$. This can be attributed to the comparatively higher grain and grain boundary resistivity of $\text{Gd}_{0.10}\text{Ce}_{0.90}\text{O}_{2-\delta}$. It is already shown in previous chapter that

$\text{Sm}_{0.075}\text{Nd}_{0.075}\text{Ce}_{0.85}\text{O}_{2-\delta}$ exhibits higher grain ionic conductivity than that of $\text{Gd}_{0.10}\text{Ce}_{0.90}\text{O}_{2-\delta}$. However, the main contribution to the total resistivity of $\text{Gd}_{0.10}\text{Ce}_{0.90}\text{O}_{2-\delta}$ is from the grain boundary resistivity. The lower grain boundary conductivity of $\text{Gd}_{0.10}\text{Ce}_{0.90}\text{O}_{2-\delta}$ may be associated with the Gd^{3+} segregation near the positively charged grain boundaries. The segregation of dopant blocks the oxygen vacancy diffusion across the grain boundaries. Future work is required to investigate the chemical compositional analysis near the grain boundaries and to study the extent of dopant segregation in these two materials.

6.4 Summary and Conclusions

In recent years, ionic conductivity of doped ceria electrolyte materials has been extensively studied. In literature a wide range of ionic conductivity data for Gd-doped ceria (which is commonly used for electrolyte application) are given. After inspecting the experimental procedures followed in the work, it was observed that powder synthesized using wet chemical route usually shows higher ionic conductivity when compared with powder synthesized using solid state reaction. Further, from literature it is known that the higher sintering time and temperature leads to lower grain boundary conductivity due to the segregation of acceptor dopant cations (or impurities) near the grain boundaries. In order to prevent any segregation, fast firing technique to sinter ceramics is usually preferred over conventional sintering. This will promote lattice diffusion of material during sintering process, which results in sharp grains with un-relaxed grain boundaries. In the work presented in the previous chapter, co-doping in ceria leads to the development of $\text{Sm}_{0.075}\text{Nd}_{0.075}\text{Ce}_{0.85}\text{O}_{2-\delta}$ electrolyte, which exhibits 30% higher grain ionic conductivity than $\text{Gd}_{0.10}\text{Ce}_{0.90}\text{O}_{2-\delta}$. However, $\text{Sm}_{0.075}\text{Nd}_{0.075}\text{Ce}_{0.85}\text{O}_{2-\delta}$ was synthesized using solid state reaction method. In the

present chapter, $\text{Sm}_{0.075}\text{Nd}_{0.075}\text{Ce}_{0.85}\text{O}_{2-\delta}$ powder was synthesized using co-precipitation technique. This results in ultrafine particle size powder with lower impurity content. Sintering of the compacted green ceramic sample was carried out using microwave heating, at 1450°C for 1 h. Microstructure of the microwave sintered ceramic sample shows the sharp grains with clean grain boundaries. Ionic conductivity was measured using two-point probe ac impedance spectroscopy technique. Both the grain and the total conductivity was higher in the sample synthesized using co-precipitation technique and microwave sintered, when compared with the sample synthesized using conventional solid state reaction method. At 550°C , the obtained grain ionic conductivity was around 45 % higher than that of $\text{Gd}_{0.10}\text{Ce}_{0.90}\text{O}_{2-\delta}$. On comparing with Steele's $\text{Gd}_{0.10}\text{Ce}_{0.90}\text{O}_{2-\delta}$ (which is the best ever reported grain ionic conductivity data for $\text{Gd}_{0.10}\text{Ce}_{0.90}\text{O}_{2-\delta}$), the grain ionic conductivity of $\text{Sm}_{0.075}\text{Nd}_{0.075}\text{Ce}_{0.85}\text{O}_{2-\delta}$ sample synthesized using co-precipitation technique and microwave sintering, was 10 % higher at 600°C in air. The blocking effect of grain boundaries is higher in the solid state reaction sample compared to the sample synthesized using co-precipitation technique and microwave sintering. This can be attributed to the higher dopant cation and impurities segregation near the grain boundaries in the sample synthesized using conventional solid state reaction. These results indicate the combined effect of the powder synthesis route and the sintering technique on the ionic conductivity in doped ceria materials. Higher purity ceramic processing route, and the low temperature and time sintering technique are essential to obtain better conductivity in these materials. However, further work needs to be done to separate out the individual effect of powder synthesis technique and microwave sintering on the grain boundary ionic conductivity.

CHAPTER 7 BUTTON CELL PERFORMANCE TESTING

7.1 Introduction

Lowering the operating temperature of solid oxide fuel cells (SOFCs) requires development of novel materials that exhibit improved properties at intermediate temperatures. In the present work, focus is on designing higher ionically conductive materials for the electrolyte application in SOFCs. Using co-doping strategy, it has been shown in Chapter 4, that $\text{Sm}_{0.075}\text{Nd}_{0.075}\text{Ce}_{0.85}\text{O}_{2-\delta}$ exhibits 30 % higher ionic conductivity than the commercially employed $\text{Gd}_{0.10}\text{Ce}_{0.90}\text{O}_{2-\delta}$ (GDC) electrolyte at 550°C, in air. In the present chapter, the potential of $\text{Sm}_{0.075}\text{Nd}_{0.075}\text{Ce}_{0.85}\text{O}_{2-\delta}$ as an alternative electrolyte to GDC will be further investigated by testing the performance of SOFC device with flat-plate design. It is the most common cell design which offers simple cell geometry and multiple fabrication options. Further information about the cell design is discussed elsewhere.⁶ The performance of the SOFC device at intermediate temperatures will be discussed in this chapter.

The fabrication of the anode-supported prototype SOFC devices was assisted by Jin-Soo Ahn, graduate student in Materials Science & Engineering Department at University of Florida.

7.2 Experimental Procedure

An anode-supported prototype SOFC is fabricated, with $\text{Sm}_{0.075}\text{Nd}_{0.075}\text{Ce}_{0.85}\text{O}_{2-\delta}$ electrolyte deposited on NiO-GDC composite anode using the conventional colloidal process. The $\text{La}_{0.6}\text{Sr}_{0.4}\text{Co}_{0.2}\text{Fe}_{0.8}\text{O}_{3-\delta}$ - GDC composite is used as a cathode. Figure 7-1 shows the schematic of an anode-supported flat-plate design of SOFC.

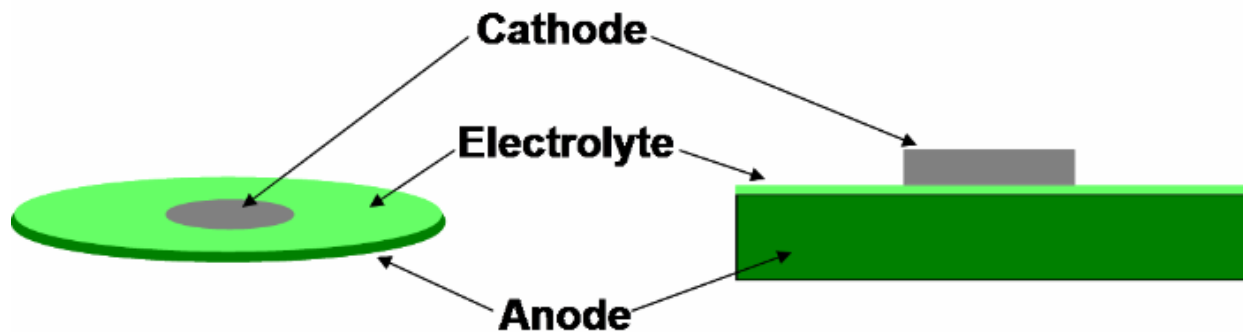


Figure 7-1. Schematic of anode-supported prototype solid oxide fuel cell.

The NiO - GDC anode supports were synthesized by tape casting a mixture of NiO (Alfa Aesar, 99% purity, CAS 1313) and GDC (Rhodia, LOT H-050708) powders. The powder mixture contains 65 weight % of NiO. Both the raw oxide powders were accordingly weighed (to obtain 150 g batch of powder mixture), and are mixed to the organic mixture of toluene (23.5 cm³) and ethanol (21.5 cm³), with 1.5 g of solspere (Air Products and Chemicals) which act as a dispersant in the slurry. The role of dispersant is to keep the dispersed ceramic particles in suspension in the dispersing medium. Further, a mixture of di-n butyl Phthalate (Alfa Aesar) (6.13 cm³ in volume), and polyethylene glycol (Fisher scientific) (1.2 g in weight) was added as a plasticizer, while polyvinyl butyral (Acros organic) (6.1 cm³ in volume) was added as a binder to this slurry. Mixing was performed using ball milling for 24 h. After ball milling, the resulting slurry was transferred to a vacuum chamber, for de-airing. This process prevents any formation of pinhole defects or cracking (during tape casting), due to the air bubbles trapped inside the slurry. During the de-airing process, the slurry was constantly stirred with magnetic stirrer to avoid solidification of the slurry surface. The slurry was then tape-casted using tape-cast (Procast from DHI, Inc.). The NiO - GDC tape was subsequently dried for 2 h at 100 °C. Circular green tapes with 32 mm diameter were

then punched out from the tape. Figure 7-2 shows the green tape and the circular punched tape of NiO-GDC. The circular anode tapes were partially sintered at 900 °C for 2 h.

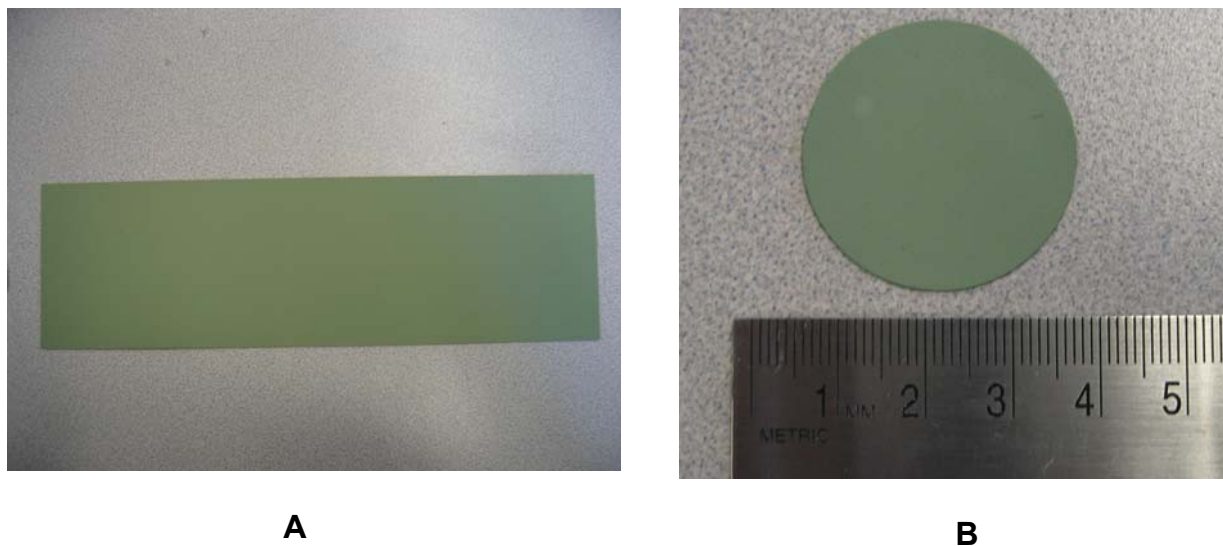


Figure 7-2. Green tape of NiO-GDC. A) and the circular punched tape B).

The co-precipitation technique was used to synthesize phase pure powder of $\text{Sm}_{0.075}\text{Nd}_{0.075}\text{Ce}_{0.85}\text{O}_{2-\delta}$. One of the main objectives of using wet chemical route is to obtain fine particle size powder, which as a result enhances the sintering kinetic of the ceramic powder. Thus, highly dense ceramic electrolyte can be synthesized using lower sintering temperature and time. The details about the powder synthesis using co-precipitation technique are provided in Chapter 3. The particle size distribution in $\text{Sm}_{0.075}\text{Nd}_{0.075}\text{Ce}_{0.85}\text{O}_{2-\delta}$ powder obtained using co-precipitation technique was mono-disperse with most of the particles were below 0.2 μm in size. The mean particle size was around 0.095 μm . For the deposition of electrolyte on anode support, the $\text{Sm}_{0.075}\text{Nd}_{0.075}\text{Ce}_{0.85}\text{O}_{2-\delta}$ powder synthesized using co-precipitation technique was ball milled for 24 h, in ethanol medium with solspere as a dispersing agent. After 24 h of ball milling, appropriate amount of polyvinyl butyral and di-n butyl phthalate were added

into the slurry. The ceramic slurry was again ball-milled for another 24 h. Before the deposition, ceramic slurry was sonicated for 10 minutes. The ceramic slurry of $\text{Sm}_{0.075}\text{Nd}_{0.075}\text{Ce}_{0.85}\text{O}_{2-\delta}$ was then deposited twice onto the anode (NiO-GDC) surface using pipette. The electrolyte deposited anode samples were subsequently, heat-treated at 120 °C for 5 h. The bi-layered structure of the electrolyte and anode was then co-sintered at 1550 °C for 4 h using a 3 °C/minute ramp rate in air.

Cathode ink was prepared by mixing $\text{La}_{0.6}\text{Sr}_{0.4}\text{Co}_{0.2}\text{Fe}_{0.8}\text{O}_{3-\delta}$ (Praxair Specialty Ceramics, 99.9% purity) and the GDC (Rhodia) powders in a 1:1 weight ratio, using mortar and pestle. The alpha-terpineol and ethanol were added as a solvent, and polyvinyl butyral and di-n butyl phthalate were used as a binder and plasticizer, respectively. After mixing and grinding the cathode ink in mortar and pestle for 1 h, the ink was brush-painted evenly onto the $\text{Sm}_{0.075}\text{Nd}_{0.075}\text{Ce}_{0.85}\text{O}_{2-\delta}$ electrolyte (deposited on NiO/GDC tape). The first layer of cathode ink was dried in an oven at 120°C for 1 h. The second layer of the same cathode ink was then evenly brush painted on top of the first layer. After applying the cathode on top of the electrolyte, samples were then fired at 1100 °C for 1 h. Pt paste (CL11- 5349, Heraeus), as a current collector, was brush-painted onto both electrodes along with Pt mesh, and Au connecting wires. Samples with current collectors and connecting wires were then finally heat-treated at 900°C for 1 h. Figure 7-3 shows the flow chart for the complete experimental procedure for the fabrication of the prototype of solid oxide fuel cell sample. After the heat treatment, button cells were mounted on the ZrO_2 reactor for testing the power density in the intermediate temperature range.

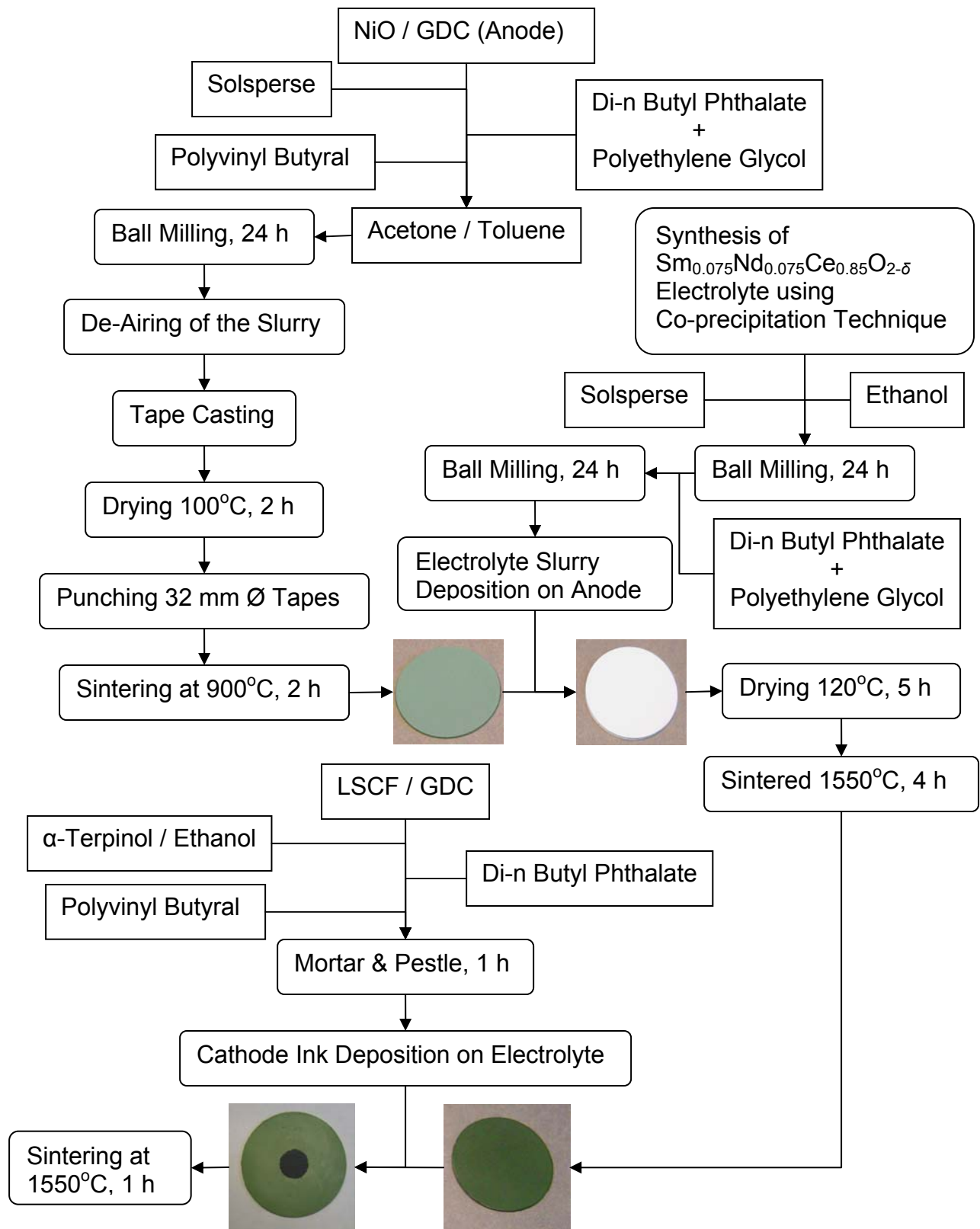


Figure 7-3. Flow chart for the fabrication of anode-supported prototype SOFC.

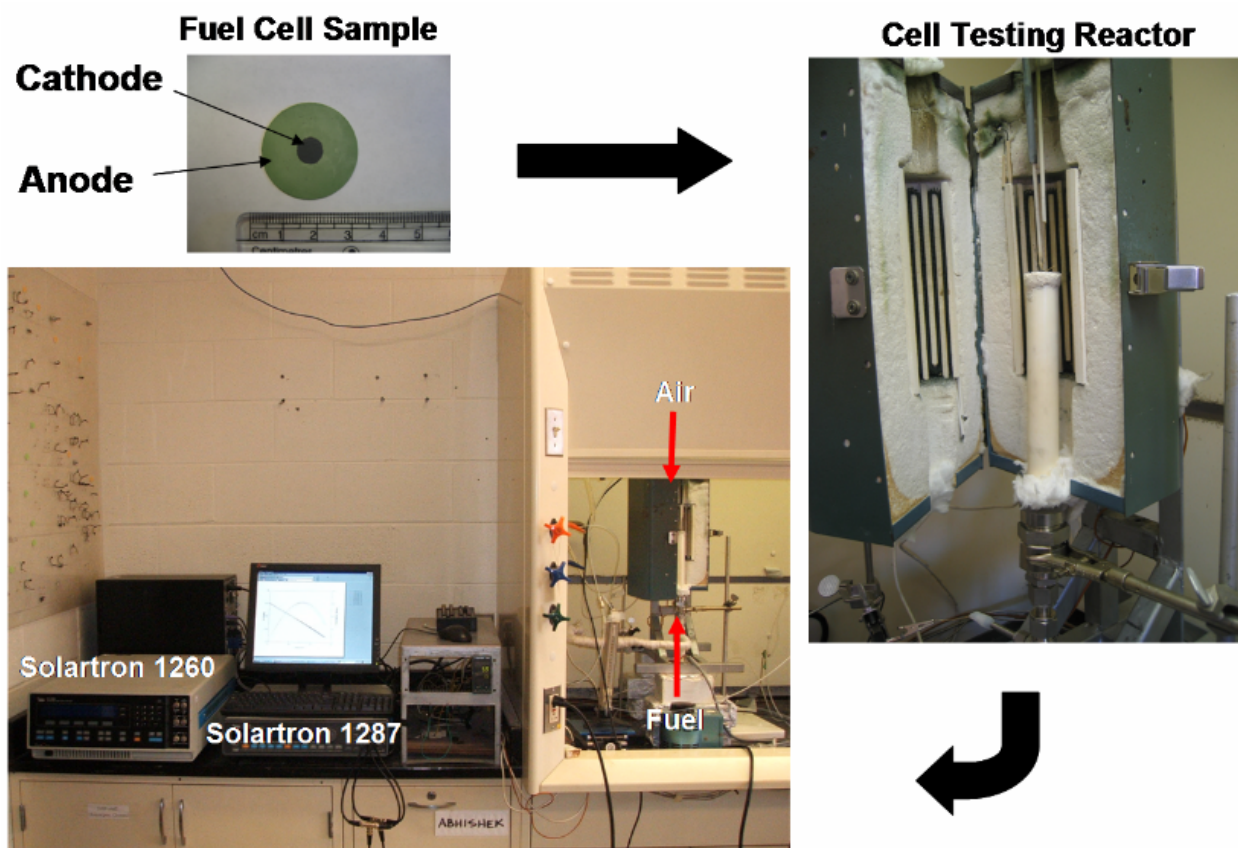


Figure 7-4. Experimental setup for the I-V characteristics measurement of the test SOFC sample.

Figure 7-4 shows the experimental setup for the current-voltage characteristics measurements of the SOFC sample at different temperatures. The fuel cell samples were sealed (anode side) to a zirconia tube in a custom-made testing apparatus using two-part ceramabond sealant (a mixture of 517-powder and 517-liquid from Aremco). The setup was then placed into a furnace, cured, and taken up to testing temperature. Dry air and H_2/H_2O gas mixtures were used as the oxidant and fuel gases, respectively. Flow rates were maintained using mass flow controllers. The $90 \text{ cm}^3/\text{minute}$ of dry air and wet hydrogen (3 volume % H_2O) were supplied to the cathode and anode side, respectively. The cell open circuit potential (OCP) was monitored using a Solartron

1287 potentiostat until a stable value was reached, and the current-voltage (I-V) measurements were taken with the same instrument. The impedance measurement was carried out at open circuit conditions using two-point probes ac impedance spectroscopy technique. A Par-stat 2273 (Princeton Applied Research) frequency response analyzer was used for impedance measurement. Impedance spectra were measured from 10 kHz to 0.01 Hz, at different temperatures. From the high frequency intercept of the impedance spectrum with the real axis, the ohmic ASR value was calculated (after normalizing the resistance according to cathode area). Electrode ASR value was determined from the difference between the low and high frequency intercepts (after normalizing the resistance according to cathode area).

Field emission scanning electron microscope (FE-SEM) was used to visualize the microstructure of the fuel cell sample. In order to view the cross-section of all the three layers (anode, electrolyte, and cathode) of the cell, the test sample was fractured through the electrodes. The fractured sample was embedded in epoxy-resin, and was mechanically polished.

7.3 Results and Discussion

7.3.1 Particle Size

Figure 7-5 shows the number particle size distribution of the $\text{Sm}_{0.075}\text{Nd}_{0.075}\text{Ce}_{0.85}\text{O}_{2-\delta}$ and the commercially obtained $\text{La}_{0.6}\text{Sr}_{0.4}\text{Co}_{0.2}\text{Fe}_{0.8}\text{O}_{3-\delta}$ (LSCF) powders. The particle size distribution of the phase pure $\text{Sm}_{0.075}\text{Nd}_{0.075}\text{Ce}_{0.85}\text{O}_{2-\delta}$ powder synthesized using co-precipitation technique was measured using Beckman Coulter LS13320. The particle size distribution of LSCF powder is provided by the company. In order to achieve high density ceramic electrolyte, it is desired that the particle size should be less than 1 μm with particle size distribution to be narrow and

monodisperse. It can be seen that the $\text{Sm}_{0.075}\text{Nd}_{0.075}\text{Ce}_{0.85}\text{O}_{2-\delta}$ particles exhibit size less than 1 μm , with the mean size of 0.095 μm . Further, the particle size distribution is also monodisperse which is desired for good sintering in reasonable time.

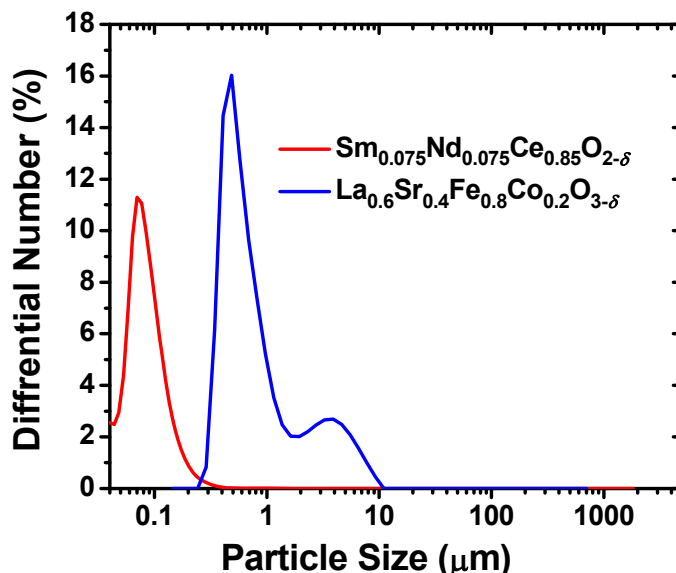


Figure 7-5. Particle size distribution of $\text{Sm}_{0.075}\text{Nd}_{0.075}\text{Ce}_{0.85}\text{O}_{2-\delta}$ synthesized using co-precipitation technique and $\text{La}_{0.6}\text{Sr}_{0.4}\text{Co}_{0.2}\text{Fe}_{0.8}\text{O}_{3-\delta}$ (obtained from Praxair Specialty Ceramics).

The GDC powder obtained from Rhodia comprised of very fine particles of size less than 100 nm.¹²⁷ These particles form aggregates due to their high surface area. On the other hand, the NiO particles are mostly micron-sized.¹²⁷ The performance of the SOFC also depends upon the electrode reactions which primarily take place at triple phase boundaries (TPB) of electrolyte, electrode and air. Increasing the TPB length, increases the electrode reaction sites which consequently enhances the performance of SOFCs. The electrodes consist of smaller particles result in larger TPB lengths. Thus, the lower particle size is typically required to increase the surface reactivity, and reduce the activation polarization. However, lowering the particle size enhances the densification of the electrode. The dry air and oxygen gas can easily pass through the

dense cathode; however, it is difficult for a dense anode to provide fuel rapidly to the reaction sites, and to remove water molecules efficiently. This results in the increase in the concentration polarization. To avoid this issue, the micron-sized NiO powder was used in the fabrication of anode tape. The LSCF powder used for the cathode exhibit the number particle size distribution which is bi-modal, with most of the particles around 1 μm in size (shown in Figure 7-5).

7.3.2 Microstructural Analysis

Figure 7-6 shows the microstructure view of the cross-section of the fuel cell, and the surface of $\text{Sm}_{0.075}\text{Nd}_{0.075}\text{Ce}_{0.85}\text{O}_{2-\delta}$ electrolyte. It can be seen both in the cross-sectional and surface micrographs, that the electrolyte is densely sintered except for a few isolated residual pores. From the SEM image, the thickness of the $\text{Sm}_{0.075}\text{Nd}_{0.075}\text{Ce}_{0.85}\text{O}_{2-\delta}$ electrolyte is estimated to be $\sim 5 \mu\text{m}$. This suggests that the $\text{Sm}_{0.075}\text{Nd}_{0.075}\text{Ce}_{0.85}\text{O}_{2-\delta}$ electrolyte can be easily deposited with conventional ceramic routes such as colloidal deposition. As expected, the nickel (reduced form of NiO) particles in the anode are exceptionally larger compared to LSCF particles in the cathode. This is mainly due to the large particle size of the starting powder i.e., NiO. Although, the hydrogen oxidation in the anode side is kinetically more favorable than oxygen reduction in the cathode side, the significantly large particle size of the Ni near the electrolyte and anode interface can cause high anodic polarization, at low temperatures.

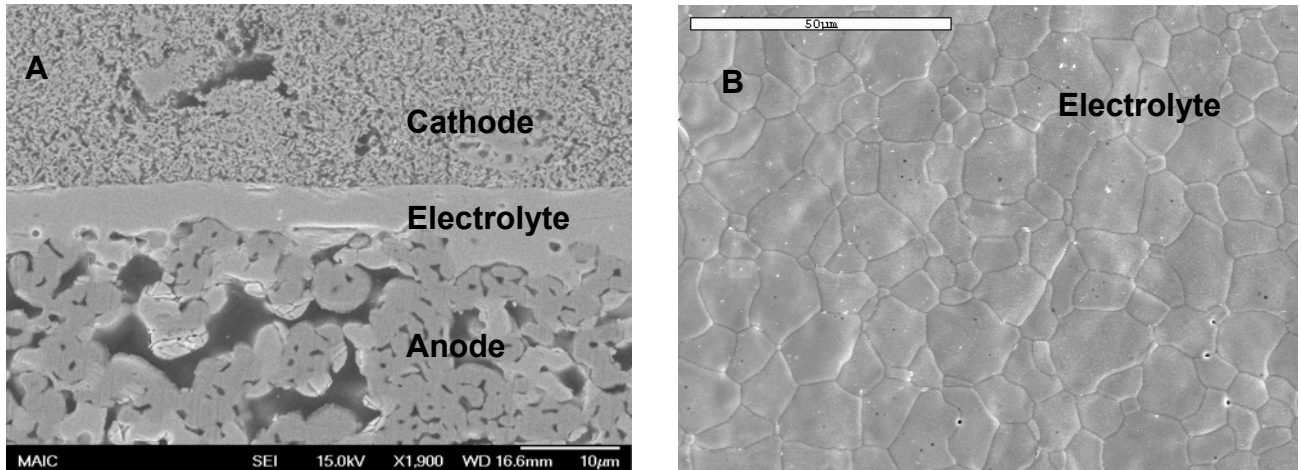


Figure 7-6. FE-SEM images of A) cross-section view of electrodes and electrolyte, and B) surface of the electrolyte.

7.3.3 Impedance Analysis

Figure 7-7 shows the impedance spectrum of the test SOFC sample at 650, 600, 550 and 500°C. Using impedance spectroscopy, it is possible to separate out the electrode and the ohmic contributions to the total area specific resistance (ASR) value at each temperature.

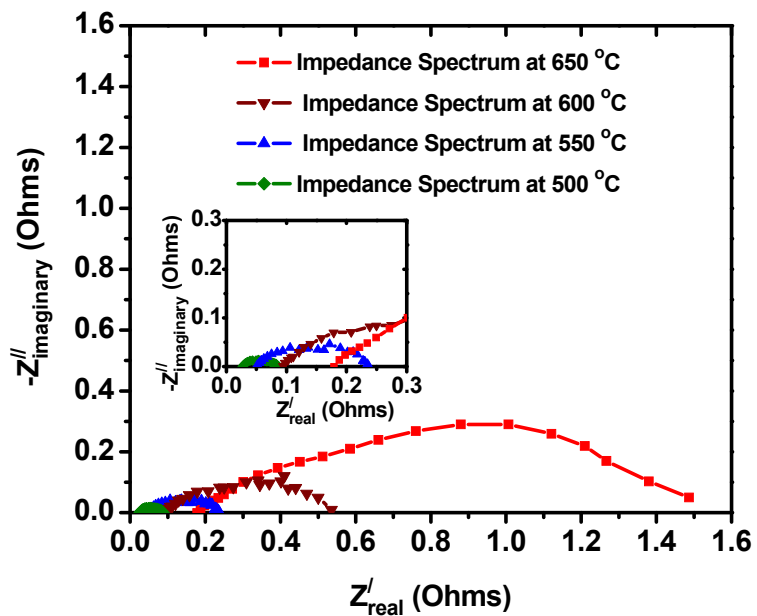


Figure 7-7. Impedance spectrum of the SOFC cell measured at different temperatures.

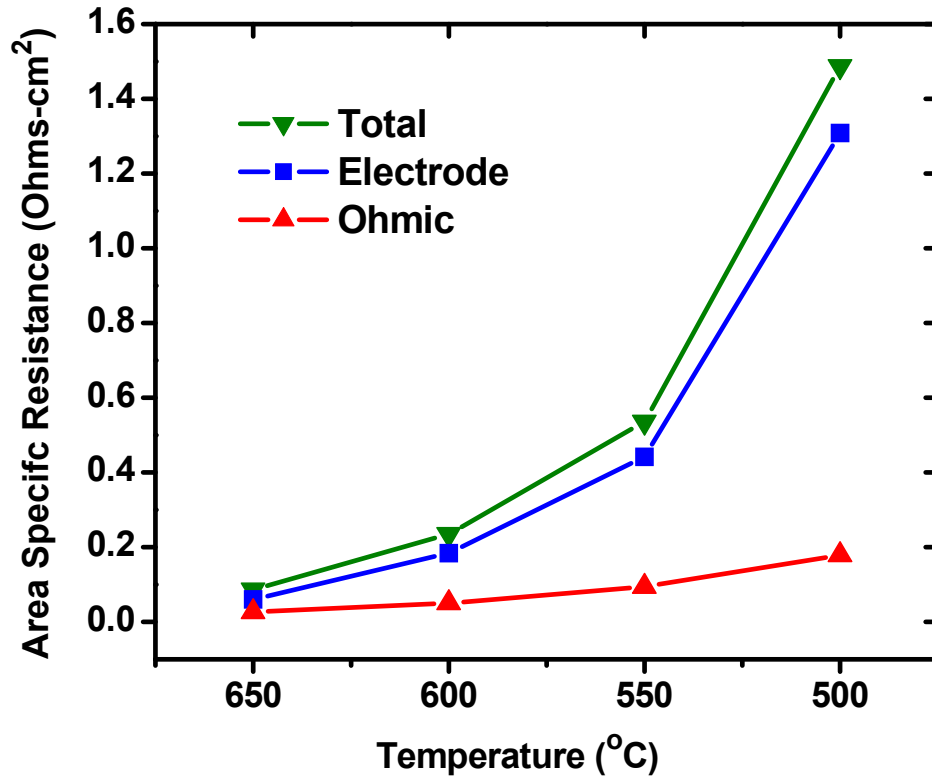


Figure 7-8. Area specific resistance at different temperatures.

Figure 7-8 shows the electrode and the ohmic ASR values separated from the total ASR at different temperatures. The rapid increase in the total ASR value with the decrease in temperature is mainly due to the significant increase in the electrode polarization. On the other hand, ohmic ASR value stays relatively low even at lower temperatures.

The total ASR values were also calculated from the gradient of the linearly fitted I-V curves. Table 7-1 shows the comparison between the total ASR values obtained from the impedance measurements and I-V characteristics. Impedance measurements were done under open circuit condition, therefore while fitting the I-V curve, the region near zero current was taken into account. Both ASR values from the I-V characteristics and

the impedance measurement are comparable in all temperatures except 500°C. The ohmic contribution towards the total ASR at each temperature is tabulated in

Table 7-1. Comparison between the total ASR obtained from I-V characteristic and impedance measurement. The ohmic contribution towards the total ASR is also shown.

Temperature (°C)	ASR _{I-V} (Ohms-cm ²)	ASR _{Impedance} (Ohms-cm ²)	% Ohmic
650	0.083	0.087	30.78 %
600	0.244	0.235	21.74 %
550	0.507	0.536	17.54 %
500	1.189	1.487	12.03 %

As shown in Table 7-1, at 650°C the ohmic contribution toward the total ASR is 30%. However, with the decreasing temperature ohmic ASR % contribution becomes smaller. At 500°C, the ohmic contribution to the total ASR value is only 12.03%. This can be explained by two aspects. First, the high activation energy of the oxygen reduction reaction results in higher resistance from the cathode at low temperatures. Secondly, without the anode functional layer, large particles of NiO at the anode-electrolyte interface lowers the hydrogen oxidation reaction kinetics which results in additional resistance. At this point, due to the limitation of two point impedance measurement, we cannot decide which electrode ASR is dominant.

7.3.4 Power Density

Figure 7-9 shows the I-V characteristics of the prototype of SOFC with Sm_{0.075}Nd_{0.075}Ce_{0.85}O_{2-δ} electrolyte at various temperatures, ranging from 500°C to 650°C. The flow rate of 90 cm³/minute of dry air and wet hydrogen was maintained in cathode and anode side, respectively. The open circuit potential (OCP) values obtained

from this test cell were 0.72, 0.79, 0.77 and 0.84 V at 650°C, 600°C, 550°C and 500°C, respectively. The obtained OCP values were close to the typical OCP values achieved in the cell with GDC as an electrolyte, using similar experimental setup.¹²⁷ The open circuit potential value of the tested cell is also dependent upon the properties of sealant used in the device. The gas sealant should be highly dense with minimal porosity, and also match the thermal expansion coefficient of $\text{Sm}_{0.075}\text{Nd}_{0.075}\text{Ce}_{0.85}\text{O}_{2-\delta}$ electrolyte. Future work need to be performed to identify materials to be used as sealant for SOFCs based on $\text{Sm}_{0.075}\text{Nd}_{0.075}\text{Ce}_{0.85}\text{O}_{2-\delta}$ electrolyte.

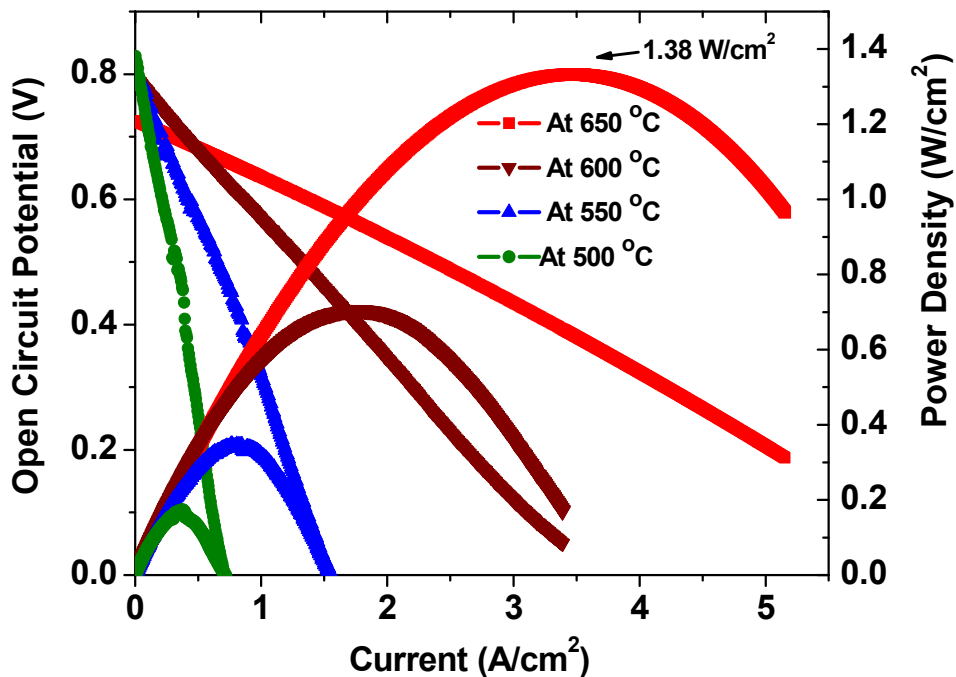


Figure 7-9. The I-V characteristics of the prototype SOFC sample with $\text{Sm}_{0.075}\text{Nd}_{0.075}\text{Ce}_{0.85}\text{O}_{2-\delta}$ electrolyte at various temperatures ranging from 500 to 650°C in 90 cm³/minute of both dry air and wet hydrogen.

Figure 7-9 also shows the power density as a function of current. The maximum power densities achieved in the test cell were 1.38, 0.71, 0.34 and 0.17 W/cm² at 650, 600, 550, and 500°C, respectively. Considering the lower OCP values in the test cell, the obtained power densities are exceptionally high. This can be contributed to the high

ionic conductivity of $\text{Sm}_{0.075}\text{Nd}_{0.075}\text{Ce}_{0.85}\text{O}_{2-\delta}$ electrolyte. Also, it is important to note that the I-V characteristics and the maximum power density of the SOFC is a function of numerous processing and material variables. For this reason, the potential of $\text{Sm}_{0.075}\text{Nd}_{0.075}\text{Ce}_{0.85}\text{O}_{2-\delta}$ electrolyte cannot be directly compared with that of GDC using I-V characteristics. Comparison between the ionic conductivity of $\text{Sm}_{0.075}\text{Nd}_{0.075}\text{Ce}_{0.85}\text{O}_{2-\delta}$ and GDC electrolyte was investigated in detail in Chapter 4.^{53,67} However, the performance testing results clearly suggest that the $\text{Sm}_{0.075}\text{Nd}_{0.075}\text{Ce}_{0.85}\text{O}_{2-\delta}$ electrolyte material can successfully generate high power density in SOFCs operating in the intermediate temperature range.

Further, it is well known that the ionic phase in the electrode composite also have an effect on the SOFC efficiency.^{128,129} Higher ionic conductive material in the electrodes significantly enhances the power density of the SOFC. As $\text{Sm}_{0.075}\text{Nd}_{0.075}\text{Ce}_{0.85}\text{O}_{2-\delta}$ exhibit higher ionic conductivity than GDC, it is expected this will further improve the performance of SOFCs. The optimization of the processing parameters involved while replacing GDC with $\text{Sm}_{0.075}\text{Nd}_{0.075}\text{Ce}_{0.85}\text{O}_{2-\delta}$ material in the electrode composites is left as a future work.

7.4 Summary and Conclusion

The performance testing of the novel co-doped ceria material as an electrolyte was performed by fabricating anode – supported prototype of SOFC. The electrolyte was deposited on top of the porous NiO-GDC anode tape using conventional colloidal technique. The microstructure results show that the deposited layer of $\text{Sm}_{0.075}\text{Nd}_{0.075}\text{Ce}_{0.85}\text{O}_{2-\delta}$ ceramic is highly dense with very few residual pores present. The LSCF-GDC composite was used as a cathode, which was brushed on top of the dense sintered electrolyte layer. The current-voltage characteristics were measured at

different temperatures, using 90 cm³/minute of dry air and wet hydrogen in cathode and anode sides, respectively. The exceptionally high power density of 1.38 W/cm² was obtained at 650°C. The power density of the tested cell shows that the Sm_{0.075}Nd_{0.075}Ce_{0.85}O_{2-δ} ceramic can successfully generate higher performance in SOFCs working in intermediate temperature range. The ASR values obtained from impedance measurements matches very closely with that measured using I-V characteristics. On lowering the temperature, the ohmic contribution towards the total ASR decreases. This implies that the electrode contribution to the total ASR value is significantly higher at lower temperatures. By replacing the ionic phase in the electrode composite from GDC to Sm_{0.075}Nd_{0.075}Ce_{0.85}O_{2-δ} can further improve the performance of SOFCs operating in the intermediate temperature range.

CHAPTER 8 SUMMARY AND FUTURE WORK

8.1 Summary

Solid oxide fuel cell (SOFC) is a promising technology for the future electrical power generation, as it shows high efficiency, low emissions and fuel flexibility. In order to promote the development of SOFCs for a variety of energy needs, it is essential to lower the operating temperature to the intermediate temperature range (400 – 700°C). This will not only lower the fabrication and maintenance cost, but also improves the reliability of SOFCs. However, with current SOFC materials lowering the operating temperature increases the ohmic losses, and degrades the performance and efficiency of the system. Thus, it is required to develop materials for all the components of SOFC that exhibit improved properties in the intermediate temperatures. This work focused on the development of higher ionic conductive materials for electrolyte applications in the intermediate temperature range.

In recent years, doped ceria materials have received significant attention for electrolyte application, due to their high ionic conductivity and good thermodynamic stability in intermediate temperatures. Until this work, among doped ceria materials, $\text{Gd}_{0.10}\text{Ce}_{0.90}\text{O}_{2-\delta}$ exhibited the highest ionic conductivity at intermediate temperatures. The main goal of this work was to further enhance the ionic conductivity in doped ceria systems. Two different doping strategies were used on ceria such that the interactions between point defects formed by the substitution of acceptor dopant cations for host Ce^{4+} cations, become minimal. Also, it is essential to maximize the pre-exponential coefficient (in the Arrhenius relationship) which is the function of configurational entropy. Co-dopants were used to suppress the oxygen vacancy ordering, and increase the

configurational entropy of the system. The co-dopants pairs were selected based on the individual dopant ionic radius, to test two different doping strategies i.e., critical ionic radius concept, and the results from density functional theory (DFT).

According to the critical dopant ionic radius concept, it was suggested that the ideal dopants for ceria to exhibit higher ionic conductivity, should possess ionic radius closer to the critical dopant ionic radius (r_c) value. The r_c is the ionic radius of the dopant that on addition to the host fluorite structure of ceria causes no lattice elastic strain. In order to test this hypothesis, co-dopant pairs were selected and added in host ceria such that the weighed average ionic radius of co-dopants matches r_c value. On comparing the ionic conductivity of the novel ceramic materials with that of $\text{Gd}_{0.10}\text{Ce}_{0.90}\text{O}_{2-\delta}$ synthesized under similar experimental conditions, it was observed that the electrolyte based on the critical dopant ionic radius concept (i.e., $\text{Lu}_x\text{Nd}_y\text{Ce}_{1-x-y}\text{O}_{2-\delta}$ and $\text{Gd}_{0.056}\text{Y}_{0.044}\text{Ce}_{0.90}\text{O}_{2-\delta}$) exhibit lower grain ionic conductivity than that of $\text{Gd}_{0.10}\text{Ce}_{0.90}\text{O}_{2-\delta}$ material.

Another novel doping strategy based on recent DFT results was tested which suggests using co-dopant with an average effective atomic number of Pm ($Z = 61$). By doing so, the increase in the number of equi-interaction energy sites of oxygen vacancy was expected, which as a result, facilitates oxygen diffusion. This in turn increased the ionic conductivity of the material. Therefore, a co-doping scheme using Sm^{3+} and Nd^{3+} provided the experimental scenario to test this hypothesis. It was found that the lattice parameter as a function composition obeys Vegard's law which indicates short range oxygen ordering in $\text{Sm}_{x/2}\text{Nd}_{x/2}\text{Ce}_{1-x}\text{O}_{2-\delta}$ system is not as pronounced as in other singly doped ceria system. The grain ionic conductivity of $\text{Sm}_{0.05}\text{Nd}_{0.05}\text{Ce}_{0.90}\text{O}_{2-\delta}$ was found to

be higher than that of $\text{Gd}_{0.10}\text{Ce}_{0.90}\text{O}_{2-\delta}$. Among all the compositions (x) of $\text{Sm}_{x/2}\text{Nd}_{x/2}\text{Ce}_{1-x}\text{O}_{2-\delta}$, $\text{Sm}_{0.09}\text{Nd}_{0.09}\text{Ce}_{0.82}\text{O}_{2-\delta}$ exhibits the highest grain ionic conductivity above 600°C ($3.47 \times 10^{-2} \text{ S}\cdot\text{cm}^{-1}$ at 650°C). The grain ionic conductivity of $\text{Sm}_{0.09}\text{Nd}_{0.09}\text{Ce}_{0.82}\text{O}_{2-\delta}$ was found to be 35% higher than that of $\text{Gd}_{0.10}\text{Ce}_{0.90}\text{O}_{2-\delta}$ at 650°C . Below 600°C , $\text{Sm}_{0.075}\text{Nd}_{0.075}\text{Ce}_{0.85}\text{O}_{2-\delta}$ is the highest ionically conductive material in doped ceria material. At 550°C , the grain ionic conductivity of $\text{Sm}_{0.075}\text{Nd}_{0.075}\text{Ce}_{0.85}\text{O}_{2-\delta}$ was found to be 30% higher than that of $\text{Gd}_{0.10}\text{Ce}_{0.90}\text{O}_{2-\delta}$. Thus, it was shown that the co-doping based on Pm atomic number results in enhanced ionic conductivity. In addition, at higher dopant concentrations, $\text{Sm}_{x/2}\text{Nd}_{x/2}\text{Ce}_{1-x}\text{O}_{2-\delta}$ system follows Meyer-Neldel rule. Taking the common transition point of Arrhenius plots as association-dissociation temperature of oxygen vacancies, migration enthalpy in $\text{Sm}_{x/2}\text{Nd}_{x/2}\text{Ce}_{1-x}\text{O}_{2-\delta}$ system was calculated. It was shown that the migration enthalpy does depend on dopant concentration in the dilute regime. Furthermore, shift in the grain ionic conductivity maxima toward higher dopant concentration with the increase in temperature, was observed in $\text{Sm}_{x/2}\text{Nd}_{x/2}\text{Ce}_{1-x}\text{O}_{2-\delta}$ system.

Ionic conductivity also depends upon the processing conditions. There are a wide range of ionic conductivity values for $\text{Gd}_{0.10}\text{Ce}_{0.90}\text{O}_{2-\delta}$ reported in literature. In order to understand the ionic conductivity trend among different trivalent acceptor doped ceria materials, processing variables in the synthesis of these materials were kept constant. Thus, in the present work, a consistent ionic conductivity data set was prepared for different doped ceria materials ($\text{D}_{0.10}\text{Ce}_{0.90}\text{O}_{2-\delta}$) synthesized using similar experimental conditions. Dopant concentration in these compositions is fixed to understand the effect of dopant ionic radius. Among trivalent acceptor dopant cations, Nd^{3+} exhibits the

highest ionic conductivity in the host ceria. To study the effect of dopant content, different compositions of $\text{Sm}_{x/2}\text{Nd}_{x/2}\text{Ce}_{1-x}\text{O}_{2-\delta}$ ceramics were also synthesized. Initially, with the increase in the dopant concentration, the ionic conductivity increases. It reaches maximum at certain dopant concentration, and then significantly decreases. Among all the tested doped ceria systems, $\text{Sm}_{0.075}\text{Nd}_{0.075}\text{Ce}_{0.85}\text{O}_{2-\delta}$ exhibited the highest ionic conductivity, at 500°C in air.

Among all the trivalent acceptor dopants, Nd^{3+} exhibited the highest ionic conductivity in ceria. However, the ionic radius of Nd^{3+} is far away from the r_c value. It is important to note that in the structure (r_c) – property (ionic conductivity) relationship proposed by Kim²², both the parameters were measured in different conditions (temperatures). In order to verify the r_c concept, r_c values were determined at temperatures where the ionic conductivity is measured. The graph between the elastic strain and the dopant cation ionic radius was plotted at higher temperatures, to derive r_c values. The r_c value decreased with the increase in temperature. At 500°C, the r_c value was estimated to be 1.0252 Å for trivalent dopant cations in host ceria. The r_c value obtained at 500°C lies closest to Dy^{3+} ionic radius. However, it is Nd^{3+} that exhibits the highest ionic conductivity. This clearly indicated that the r_c concept is not applicable for doped ceria materials.

In order to investigate the effect of processing on the ionic conductivity, different processing routes were used to synthesize material. From literature, it is reported that the powder synthesized using wet chemical route usually shows higher ionic conductivity than conventional solid oxide route. Further, it is also known that higher sintering times and temperatures lead to lower grain boundary conductivity due to the

segregation of acceptor dopant cations (and impurities) near the grain boundaries. In order to prevent any segregation, fast firing technique to sinter ceramics is usually preferred over conventional sintering. As $\text{Sm}_{0.075}\text{Nd}_{0.075}\text{Ce}_{0.85}\text{O}_{2-\delta}$ exhibited the highest ionic conductivity among the tested doped ceria materials, therefore in the present work, $\text{Sm}_{0.075}\text{Nd}_{0.075}\text{Ce}_{0.85}\text{O}_{2-\delta}$ powder was synthesized using co-precipitation technique. Sintering of the compacted green ceramic sample was done using microwave heating, at 1450°C for 1 h. Microstructure of the microwave sintered ceramic sample shows sharp grains with clean grain boundaries. Both the grain and the total ionic conductivity were higher in the sample synthesized using co-precipitation technique and microwave sintering, when compared with the sample synthesized using conventional solid state reaction method. At 550°C , the obtained grain ionic conductivity was around 45 % higher than that of $\text{Gd}_{0.10}\text{Ce}_{0.90}\text{O}_{2-\delta}$. Comparison with Steele¹³'s $\text{Gd}_{0.10}\text{Ce}_{0.90}\text{O}_{2-\delta}$ (which is the best ever reported grain ionic conductivity data for $\text{Gd}_{0.10}\text{Ce}_{0.90}\text{O}_{2-\delta}$), the grain ionic conductivity of $\text{Sm}_{0.075}\text{Nd}_{0.075}\text{Ce}_{0.85}\text{O}_{2-\delta}$ sample synthesized using co-precipitation technique and microwave sintering, was 10 % higher at 600°C in air. The blocking effect of the grain boundaries is higher in the solid state reaction sample compared with the sample synthesized using co-precipitation technique and microwave sintering. This can be attributed to the segregation of dopant cations and impurities near the grain boundaries in the sample synthesized using conventional solid state reaction. These results indicated the combined effect of the powder synthesis route and the sintering technique on the ionic conductivity in doped ceria materials.

After developing the higher ionically conductive material, performance testing of an anode – supported prototype of SOFC based on $\text{Sm}_{0.075}\text{Nd}_{0.075}\text{Ce}_{0.85}\text{O}_{2-\delta}$ electrolyte was

performed. The electrolyte was deposited on top of the porous NiO- $\text{Gd}_{0.10}\text{Ce}_{0.90}\text{O}_{2-\delta}$ anode tape using conventional colloidal technique. The microstructure showed that the deposited layer of $\text{Sm}_{0.075}\text{Nd}_{0.075}\text{Ce}_{0.85}\text{O}_{2-\delta}$ ceramic is highly dense with very few residual pores present. The $\text{La}_{0.6}\text{Sr}_{0.4}\text{Co}_{0.2}\text{Fe}_{0.8}\text{O}_{3-\delta}$ - $\text{Gd}_{0.10}\text{Ce}_{0.90}\text{O}_{2-\delta}$ composite was used as a cathode, which was brushed on top of the dense sintered electrolyte layer. The current - voltage characteristics were measured at different temperatures, using 90 $\text{cm}^3/\text{minute}$ of dry air and wet hydrogen in cathode and anode sides, respectively. The exceptionally high power density of $1.38 \text{ W}/\text{cm}^2$ was obtained at 650°C . The power density of the tested cell shows that the $\text{Sm}_{0.075}\text{Nd}_{0.075}\text{Ce}_{0.85}\text{O}_{2-\delta}$ ceramic can successfully generate higher performance in SOFCs working in intermediate temperature range.

8.2 Future Work

8.2.1 Doping Strategy

As mentioned in Chapter 1, the main scientific approach to achieve the goal of developing higher ionic conductive materials is to identify the doping strategy. It was shown in Chapter 4 that Pm is the ideal dopant to exhibit the highest ionic conductivity. Since Pm is a radioactive element, and cannot be used for this application, therefore co-dopant strategy based on Sm^{3+} and Nd^{3+} was used on ceria. This leads to the development of highly ionically conductive $\text{Sm}_{0.075}\text{Nd}_{0.075}\text{Ce}_{0.85}\text{O}_{2-\delta}$ material. Future work is needed to further test this strategy using Gd^{3+} and Nd^{3+} as co-dopant pair.

Using multiple trivalent dopants suppresses the oxygen vacancy ordering, and increases the configurational entropy of the system.⁶⁷ This, in turn, enhances the ionic conductivity of the material. In addition, from Chapter 5, it is clear that the dopant cations exhibiting the ionic radius in the range of 1.05 \AA to 1.11 \AA show low activation

energy for oxygen diffusion. Since dopant ionic radius of Gd^{3+} , Sm^{3+} and Nd^{3+} cations lie in this range, it would be interesting to study the ionic conductivity of $Gd_{x/3}Sm_{x/3}Nd_{x/3}Ce_{1-x}O_{2-\delta}$ system in detail.

Also, in Chapter 5, it is shown that Nd^{3+} dopant cation exhibits the highest ionic conductivity among all the other trivalent dopant cations. However, the ionic conductivity result does not follow the host and dopant cations ionic radius mismatch concept. Therefore, work is required to study in detail the crystal structure and the grain ionic conductivity in $Nd_xCe_{1-x}O_{2-\delta}$ system. As grain boundary is the integral part of the polycrystalline ceramic material, the study of the grain boundary ionic conductivity for different compositions in $Nd_xCe_{1-x}O_{2-\delta}$ system need to be performed. Finally, work is required for the optimization of dopant content in $Nd_xCe_{1-x}O_{2-\delta}$ system to obtain higher ionic conductivity.

8.2.2 Ionic Conductivity

Among all the tested doped ceria compositions, $Sm_{0.075}Nd_{0.075}Ce_{0.85}O_{2-\delta}$ exhibits the highest grain ionic conductivity in the intermediate temperature range, in air. However, under real operation, the solid oxide electrolyte is also exposed to reducing environment at the anode side. Thus, it is important to measure the ionic conductivity of $Sm_{0.075}Nd_{0.075}Ce_{0.85}O_{2-\delta}$ as a function of partial pressure of oxygen. Further, in reducing conditions ($\sim 10^{-20}$ atmosphere) and at high temperatures ($\sim 1000^\circ C$), CeO_2 is prone to change its valence state from Ce^{4+} to Ce^{3+} , which promotes electronic conduction in the material. This not only degrades the associated cell efficiency, but also expands the material (due to the formation of additional oxygen vacancies) which has a deleterious effect on the mechanical properties.⁷³ Thus, for $Sm_{0.075}Nd_{0.075}Ce_{0.85}O_{2-\delta}$ electrolyte, it is

required to measure the transference number of $\text{Sm}_{0.075}\text{Nd}_{0.075}\text{Ce}_{0.85}\text{O}_{2-\delta}$ in reducing atmospheres.

In Chapter 5, a trend for the pre-exponential factor (in Arrhenius relationship) was shown as a function of the trivalent dopant ionic radius. Since pre-exponential factor depends upon numerous variables (shown in Appendix B), it is difficult to de-convolute the contribution from different variables toward the pre-exponential factor. Thus, a computational approach, like density functional theory, may be extremely helpful to investigate the effect of each variable independently. This work will allow better understanding of the pre-exponential factor for different type of acceptor dopants. Using this knowledge, novel doping strategy can be designed (to develop higher ionically conductive materials) for ceria and related fluorite based oxides.

8.2.3 Processing

In Chapter 6, it has been shown that the ionic conductivity depends on processing conditions. Samples synthesized using co-precipitation technique and microwave sintering exhibit higher grain and total ionic conductivity, than the samples prepared through solid state reaction method. As described in chapter 6, microwave sintering is a fast firing technique in which the microstructure with fine grain size is obtained. Thus, it is important to study the effect of the microwave sintering over the microstructure of doped ceria material. Further, the amount of impurities segregation (near the grain boundary core) is also dependent upon the orientation of the grains forming the grain boundary. The high angle grain boundaries can accommodate more impurities when compared with low angle grain boundaries. Future work is required to study in detail the grain boundary configuration in the microwave sintered samples. Furthermore, ionic conductivity measurements need to be performed on the conventional sintered ceramic

samples formed using the powder synthesized from co-precipitation technique. This will separate out the effect of the powder synthesis route on the ionic conductivity of the material.

8.2.4 Performance Testing

In Chapter 7, it was shown that the $\text{Sm}_{0.075}\text{Nd}_{0.075}\text{Ce}_{0.85}\text{O}_{2-\delta}$ electrolyte material can successfully generate high power density in SOFCs operating in the intermediate temperature range. At 650°C , exceptionally high power density of 1.38 W/cm^2 was obtained using $90 \text{ cm}^3/\text{minute}$ of dry air and wet hydrogen in cathode and anode sides. However, with the decrease in temperature, the power density of the tested cell degrades significantly. This is basically due to the rapid increase in the electrode area specific resistance (ASR) with the decrease in temperature. This electrode ASR can be lowered by replacing the ionic phase in the electrode composite. It is well known that the ionic phase in the electrode composite also have an effect on the SOFC efficiency. Higher ionic conductive material in the electrodes significantly enhances the power density of the SOFC. As $\text{Sm}_{0.075}\text{Nd}_{0.075}\text{Ce}_{0.85}\text{O}_{2-\delta}$ exhibit higher ionic conductivity than GDC, it is expected this will further improve the performance of SOFCs.^{128,129} The optimization of the processing parameters involved while replacing GDC with $\text{Sm}_{0.075}\text{Nd}_{0.075}\text{Ce}_{0.85}\text{O}_{2-\delta}$ material in the electrode composites is left as a future work.

In addition, without the anode functional layer, large particles of NiO at the anode-electrolyte interface lowers the hydrogen oxidation reaction kinetics which results in additional resistance.¹²⁷ Thus, using anode functional layer in the interface of anode and electrolyte can substantially improve the performance of SOFCs operating in the intermediate temperature range. Further, the open circuit potential value of the tested cell is also dependent upon the properties of sealant used in the device. The gas

sealant should be highly dense with minimal porosity, and also match the thermal expansion coefficient of $\text{Sm}_{0.075}\text{Nd}_{0.075}\text{Ce}_{0.85}\text{O}_{2-\delta}$ electrolyte. Future work need to be done to identify materials to be used as sealant for SOFCs based on $\text{Sm}_{0.075}\text{Nd}_{0.075}\text{Ce}_{0.85}\text{O}_{2-\delta}$ electrolyte.

APPENDIX A
DEFECT CHEMISTRY AND THERMODYNAMIC IN POINT DEFECTS

Diffusion in oxide solids can only take place due to the presence of imperfections (point defects) in the lattice. For example, Schottky defect in MgO results in the formation of a pair of Mg^+ and O^{2-} vacancies in the bulk crystal. The V_O^{**} defects play the role of charge carriers and enable O_2 gas to diffuse through the solid material.



Even though introduction of defects involve breaking of bonds, there is a finite concentration of defects always present in the crystal structure at all the temperature above 0 K. This is attributed to the entropy increase due to the presence of these defects. The total entropy of a collection of atoms can be written as a sum of configurational entropy (ΔS_{config}) and vibrational entropy (or thermal entropy) (ΔS_{vibra}).

$$\Delta S = \Delta S_{config} + \Delta S_{vibra} \quad (A-2)$$

Thus, if x mole fraction of certain type of point defect, then the entropy change (ΔS) due to the formation of these defects is,

$$\Delta S = -k[x \ln(x) + (1-x) \ln(1-x)] + xk \ln \frac{v'}{v} \quad (A-3)$$

where k , v , and v' are Boltzmann's constant, the vibrational frequency of atoms far away from oxygen vacancy, and the vibrational frequency of atoms in close proximity to oxygen vacancy, respectively.

If the energy needed to form these defect is ΔH_{for} Joules per mole then the increase in enthalpy (ΔH) is,

$$\Delta H = x \times \Delta H_{for} \dots\dots\dots (A-4)$$

The total change in Gibb's free energy (ΔG) is

$$\Delta G = \Delta H - T\Delta S \quad (\text{A-5})$$

From (A-3) and (A-4),

$$\Rightarrow \Delta G = x\Delta H_{for} + kT[x\ln(x) + (1-x)\ln(1-x)] + xkT\ln\frac{v'}{v} \quad (\text{A-6})$$

The concentration of defect at which the minimum in ΔG occurs (i.e., $\frac{\partial(\Delta G)}{\partial x}$), is the equilibrium concentration (x_{eq}) of defect for a particular temperature,

$$x_{eq} = \exp\left(-\frac{\Delta H_{for} - T\Delta S_{vib}}{RT}\right) \quad (\text{A-7})$$

Thus, the final expression does not contain the configuration entropy term but only depends upon the change in Gibb's energy by the formation of a single defect.

APPENDIX B
IONIC CONDUCTIVITY AND DEFECT COMPLEXES

B.1 Oxygen Ion Conductivity

Oxygen ion conductivity (σ_i) in a solid oxide electrolyte obeys Arrhenius relationship,

$$\sigma_i = \sigma_o \exp\left(-\frac{\Delta H_m}{kT}\right) \quad (\text{B-1})$$

where σ_o , ΔH_m , k , and T pre-exponential coefficient, migration enthalpy, and Boltzmann constant. Oxygen vacancy conductivity can be expressed in terms of oxygen vacancy mobility as,

$$\sigma_v = [V_o^{**}] N_o q_v \mu_v \quad (\text{B-2})$$

where N_o is the number of oxygen sites per unit volume (cm^{-3}), $[V_o^{**}]$ is the fraction of mobile oxygen vacancy present in the anion sublattice, and q_v and μ_v are the charge and mobility of oxygen vacancies, respectively. According to the Nernst – Einstein relationship, oxygen vacancy mobility can be described with the corresponding diffusivity (D_v).

$$\mu_v = \frac{q_v D_v}{kT} \quad (\text{B-3})$$

The oxygen vacancy diffusivity can be written as,

$$D_v = a^2 \nu_o \exp\left(\frac{\Delta S_m}{k}\right) \exp\left(-\frac{\Delta H_m}{kT}\right) \quad (\text{B-4})$$

where a is the ion jump distance, ν_o is an appropriate lattice vibration, and ΔS_m is the entropy change during oxygen ion diffusion. Oxygen ion diffusivity can be describe in terms of oxygen vacancy diffusivity as,

$$D_i = [V_O^{\bullet\bullet}]D_V \quad (\text{B-5})$$

From (B-4) and (B-5),

$$D_i = [V_O^{\bullet\bullet}]a^2v_o \exp\left(\frac{\Delta S_m}{k}\right) \exp\left(-\frac{\Delta H_m}{kT}\right) \quad (\text{B-6})$$

The oxygen ion mobility (μ_i) can be written as,

$$\mu_i = \frac{q_V}{kT} [V_O^{\bullet\bullet}]a^2v_o \exp\left(\frac{\Delta S_m}{k}\right) \exp\left(-\frac{\Delta H_m}{kT}\right) \quad (\text{B-7})$$

Using (B-7) and (B-2), oxygen ion conductivity can be written as

$$\sigma_i = \frac{q_V^2}{kT} [V_O^{\bullet\bullet}]C_oN_o a^2v_o \exp\left(\frac{\Delta S_m}{k}\right) \exp\left(-\frac{\Delta H_m}{kT}\right) \quad (\text{B-8})$$

where C_o is the mole fraction of oxygen ions present in the material,

$$\Rightarrow \sigma_i = \frac{q_V^2}{kT} [V_O^{\bullet\bullet}](1-[V_O^{\bullet\bullet}])N_o a^2v_o \exp\left(\frac{\Delta S_m}{k}\right) \exp\left(-\frac{\Delta H_m}{kT}\right) \quad (\text{B-9})$$

For smaller values of $[V_O^{\bullet\bullet}]$ equation (B-9) can be approximated as,

$$\sigma_i = \frac{q_V^2}{kT} [V_O^{\bullet\bullet}]N_o a^2v_o \exp\left(\frac{\Delta S_m}{k}\right) \exp\left(-\frac{\Delta H_m}{kT}\right) \quad (\text{B-10})$$

B.2 Defect Complexes

In equation (B-10), it is assumed that there are no interactions between dopant cations and oxygen vacancies sites. However, the presence of elastic and electrostatic interactions between these two point defects result in the formation of local defect structures such as $(D'_A - V_O^{\bullet\bullet} - D'_A)$ and $(D'_A - V_O^{\bullet\bullet})^{\bullet}$. At lower dopant concentration, it can be assume that only dimers (i.e., $(D'_A - V_O^{\bullet\bullet})^{\bullet}$) are present in the material. However, with the increase in dopant concentration, the probability that oxygen vacancy has more than one dopant cation in the neighboring position rapidly increases. Thus, at higher

dopant concentration, the presence of trimers (i.e., $(D'_A - V_O^{**} - D'_A)$) is more likely. In the following section, equation (B-10) is modified taken into consideration both dimers and trimers.

B.2.1 Dimers

In this section, equation (B-10) is modified assuming that only dimers are present.



Applying the law of mass-action,

$$K_{Dimers} = \left(\frac{[D'_{Ce}] \times [V_O^{**}]}{[(D'_{Ce} - V_O^{**})^{\bullet}]} \right) \quad (B-12)$$

where K_{dimers} is the equilibrium constant. From charge neutrality relationship,

$$[(D'_{Ce} - V_O^{**})^{\bullet}] + 2[V_O^{**}] = [D'_{Ce}] \quad (B-13)$$

For full association of defects,

$$[(D'_{Ce} - V_O^{**})^{\bullet}] \gg [V_O^{**}] \quad (B-14)$$

$$[(D'_{Ce} - V_O^{**})^{\bullet}] = [D'_{Ce}] = c_{dop} \quad (B-15)$$

where c_{dop} is the concentration of dopant cations. Thus, equation [12] becomes,

$$K_{Dimers} = [V_O^{**}] \quad (B-16)$$

Now, equilibrium constant K_{Dimers} is a function of temperature (T) and can be written as,

$$K_{Dimers} = A \exp\left(-\frac{\Delta G_{Dimers}}{kT}\right) \quad (B-17)$$

$$K_{Dimers} = A \exp\left(-\frac{\Delta H_{Dimers} - T\Delta S_{Dimers}}{kT}\right) \quad (B-18)$$

where A , ΔG_{Dimers} , ΔH_{Dimers} , and ΔS_{Dimers} are the pre-exponential constant for the reaction, Gibb's free energy, enthalpy, and entropy of association, respectively. Using (B-16) and (B-17),

$$[V_{O}^{**}] = A \exp\left(-\frac{\Delta H_{Dimers} - T\Delta S_{Dimers}}{kT}\right) \quad (B-19)$$

Inputting the equation (B-19) into (B-10),

$$\sigma_i = \frac{q_V^2}{kT} A \exp\left(-\frac{\Delta H_{Dimers} - T\Delta S_{Dimers}}{kT}\right) N_o a^2 v_o \exp\left(\frac{\Delta S_m}{k}\right) \exp\left(-\frac{\Delta H_m}{kT}\right) \quad (B-20)$$

$$\Rightarrow \sigma_i = \frac{q_V^2}{kT} A N_o a^2 v_o \exp\left(\frac{\Delta S_m + \Delta S_{Dimers}}{k}\right) \exp\left(-\frac{\Delta H_m + \Delta H_{Dimers}}{kT}\right) \quad (B-21)$$

Equation (B-21) is the modified equation (B-10) assuming only dimers as a local defect structure present.

B.2.2 Trimers

In this section, it is assumed that only trimers local defect structures are present while modifying equation (B-10).

$$(D'_{Ce} - V_{O}^{**} - D'_{Ce})^{\times} \rightarrow 2D'_{Ce} + V_{O}^{**} \quad (B-22)$$

Applying the law of mass-action,

$$K_{Trimers} = \left(\frac{[D'_{Ce}]^2 \times [V_{O}^{**}]}{[(2D'_{Ce} - V_{O}^{**})^{\times}]}\right) \quad (B-23)$$

where $K_{Trimers}$ is the equilibrium constant. From charge neutrality relationship,

$$2[V_{O}^{**}] = [D'_{Ce}] \quad (B-24)$$

Using equation (B-23) and (B-24),

$$K_{Trimers} = \left(\frac{4[V_{O}^{\bullet\bullet}]^3}{[(2D'_{Ce} - V_{O}^{\bullet\bullet})^{\times}]} \right) \quad (B-25)$$

For full association of defects,

$$[(2D'_{Ce} - V_{O}^{\bullet\bullet})^{\times}] \gg [V_{O}^{\bullet\bullet}] \quad (B-26)$$

$$[(2D'_{Ce} - V_{O}^{\bullet\bullet})^{\times}] = c_{dop} \quad (B-27)$$

where c_{dop} is the total dopant concentration expressed as a site fraction of the cation site. Similar to dimers case, equilibrium constant $K_{Trimers}$ is a function of temperature (T) and can be written as,

$$K_{Trimers} = A \exp\left(-\frac{\Delta G_{Trimers}}{kT}\right) \quad (B-28)$$

$$K_{Trimers} = A \exp\left(-\frac{\Delta H_{Trimers} - T\Delta S_{Trimers}}{kT}\right) \quad (B-29)$$

where A , $\Delta G_{Trimers}$, $\Delta H_{Trimers}$, and $\Delta S_{Trimers}$ are the pre-exponential constant for the reaction, Gibb's free energy, enthalpy, and entropy of association, respectively. Using equation (B-25), (B-27), and (B-29),

$$[V_{O}^{\bullet\bullet}] = \frac{1}{4^{1/3}} A^{1/3} c_{dop}^{1/3} \exp\left(-\frac{\Delta H_{Trimers} - T\Delta S_{Trimers}}{3kT}\right) \quad (B-30)$$

Inputting the equation (B-30) into (B-10),

$$\sigma_i = \frac{1}{4^{1/3}} \frac{q_V^2}{kT} A^{1/3} c_{dop}^{1/3} N_o a^2 v_o \exp\left(\frac{\Delta S_m + \frac{\Delta S_{Trimers}}{3}}{k}\right) \exp\left(-\frac{\Delta H_m + \frac{\Delta H_{Trimers}}{3}}{kT}\right) \quad (B-31)$$

Equation (B-31) is the modified equation (B-10) assuming only trimers as a local defect structure present. The conductivity should follow above trends at higher dopant concentration, when the probability of the presence of trimers is higher.

APPENDIX C
HIGH TEMPERATURE XRD PATTERNS OF CERIA COMPOUNDS

In this section, XRD profiles of doped ceria systems at high temperatures are shown.

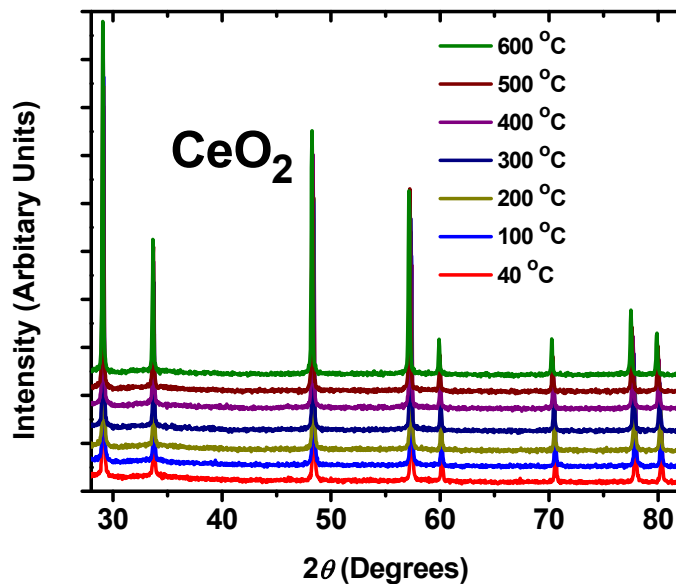


Figure C-1. XRD profiles of pure ceria collected at high temperatures.

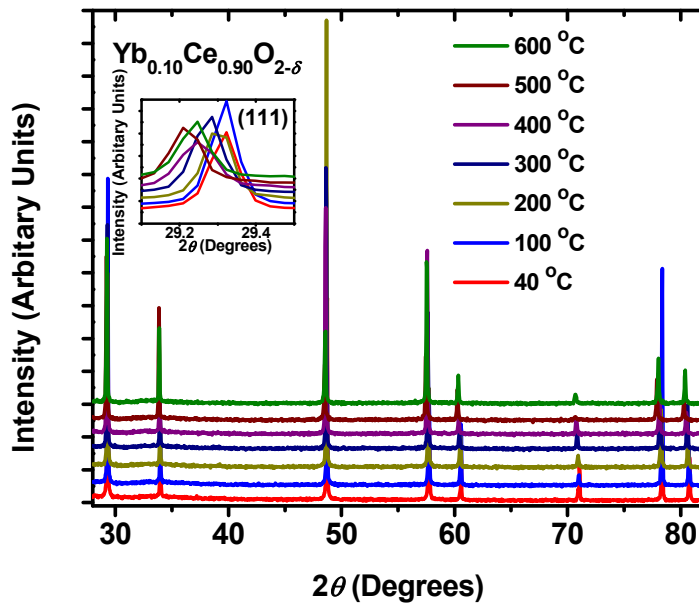


Figure C-2. XRD profiles of $\text{Yb}_{0.10}\text{Ce}_{0.90}\text{O}_{2-\delta}$ collected at high temperatures.

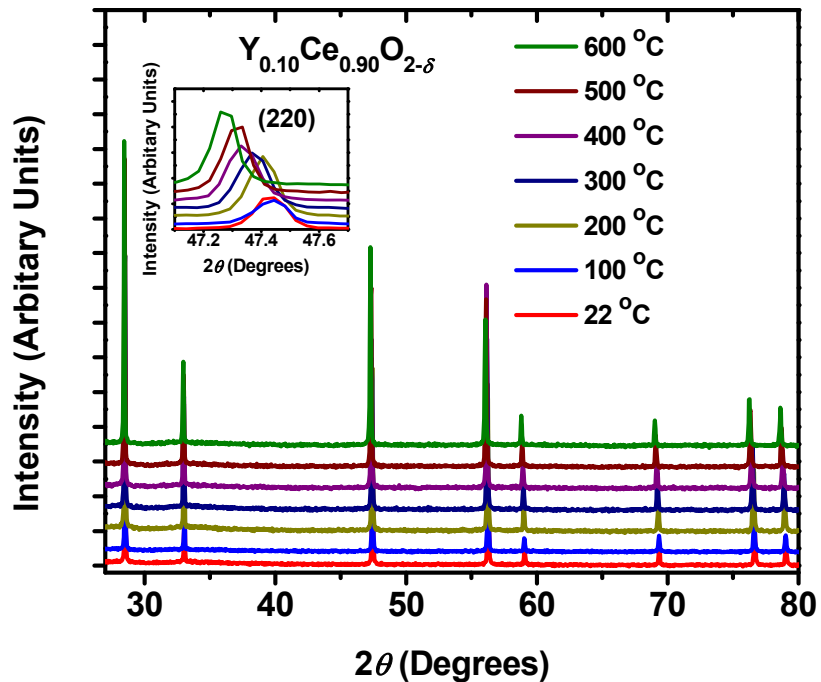


Figure C-3. XRD profiles of Y_{0.10}Ce_{0.90}O_{2-δ} collected at high temperatures.

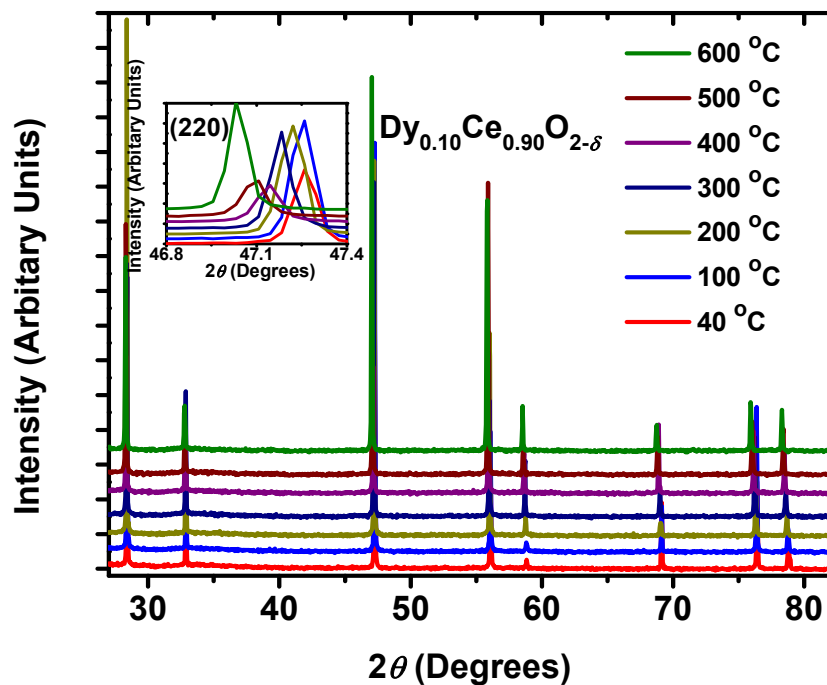


Figure C-4. XRD profiles of Dy_{0.10}Ce_{0.90}O_{2-δ} collected at high temperatures.

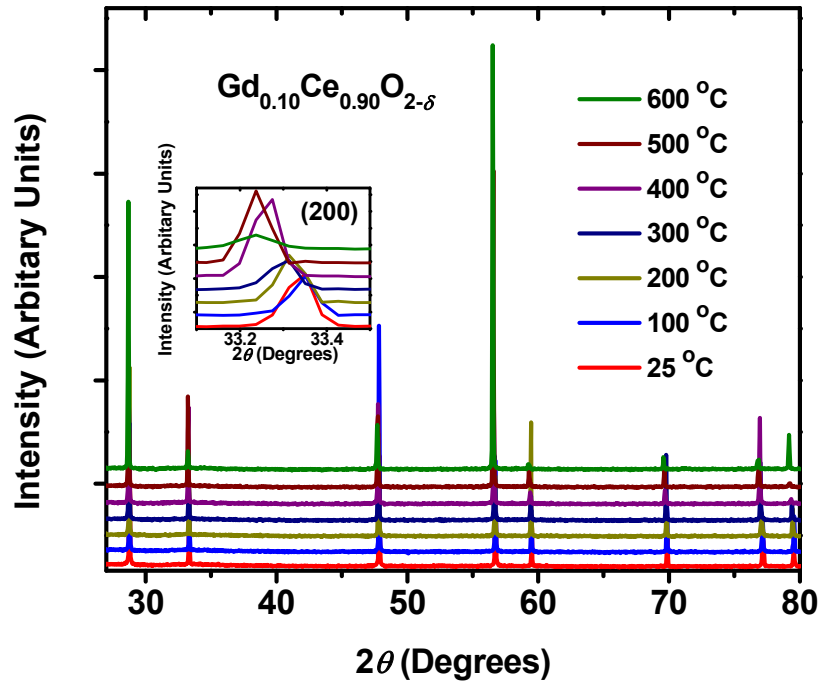


Figure C-5. XRD profiles of $\text{Gd}_{0.10}\text{Ce}_{0.90}\text{O}_{2-\delta}$ collected at high temperatures.

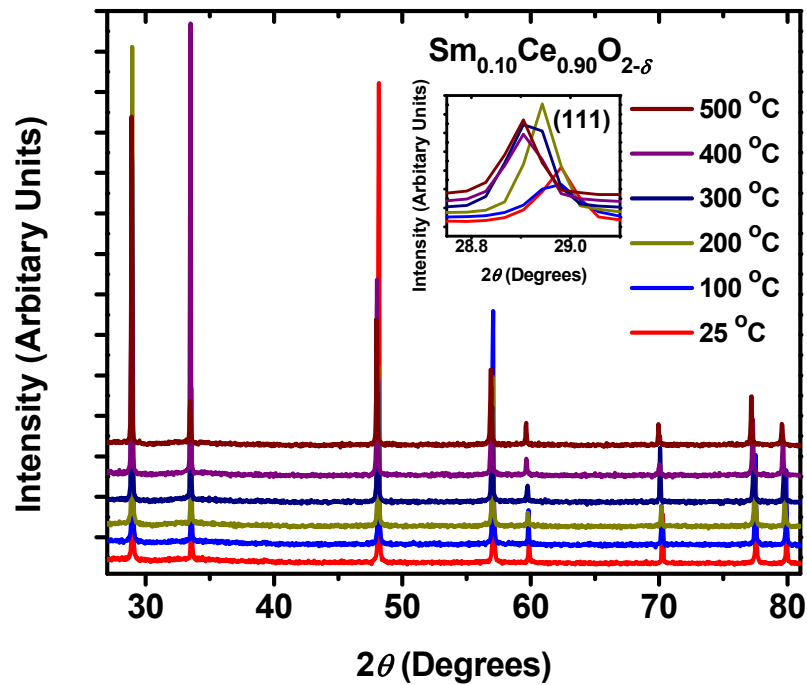


Figure C-6. XRD profiles of $\text{Sm}_{0.10}\text{Ce}_{0.90}\text{O}_{2-\delta}$ collected at high temperatures.

APPENDIX D
EXTRAPOLATION METHOD TO CALCULATE LATTICE PARAMETER

The curved position sensitive (CPS) diffractometer (INEL, France) was used to collect X-ray diffraction profiles of doped ceria materials using Cu K_{α} radiation. Monochromator crystal was used to separate out Cu $K_{\alpha 1}$ from the incident X-ray beam. Peak positions in the XRD pattern were determined by fitting each individual peak with a symmetric Pearson VII profiles to model Cu $K_{\alpha 1}$ using a commercially available software (i.e., Solver add-in within Microsoft Excel spreadsheet package). Extrapolation method was used to estimate the lattice parameter of doped ceria materials. This method can be used to correct for vertical sample displacements within certain limits. Thus, it is not essential to use internal standard to obtain the experimental offset in 2θ position. Information regarding this technique can be found elsewhere.⁶⁶ For a given XRD profile, lattice parameter (a) was determined for each individual peak using the following relationship,

$$a = \frac{\lambda}{2 \sin \theta} \sqrt{h^2 + k^2 + l^2} \quad (\text{D-1})$$

The measured lattice parameters were then plotted as a function of $\cos^2\theta$. The scattered data was then linearly fitted using least-square algorithm. The fitted line is in the form of the following relationship,

$$a = a_o + k \cos^2 \theta \quad (\text{D-2})$$

where a_o is the true estimation of the lattice parameter, and a is the apparent lattice parameter calculated from the angular position of a particular peak and k is the constant depending upon the sample vertical displacement. The implication of equation (D-2) is that the best estimate of lattice parameter, a_o , can be obtained by plotting a with respect

to $\cos^2\theta$, and extrapolating it to $\cos^2\theta = 0$. Figure D-1 shows apparent lattice parameter and $\cos^2\theta$ plots for pure ceria material taken at different temperatures. It can be seen that with the increase in temperature the intercept is also increasing which indicates the thermal lattice expansion of ceria.

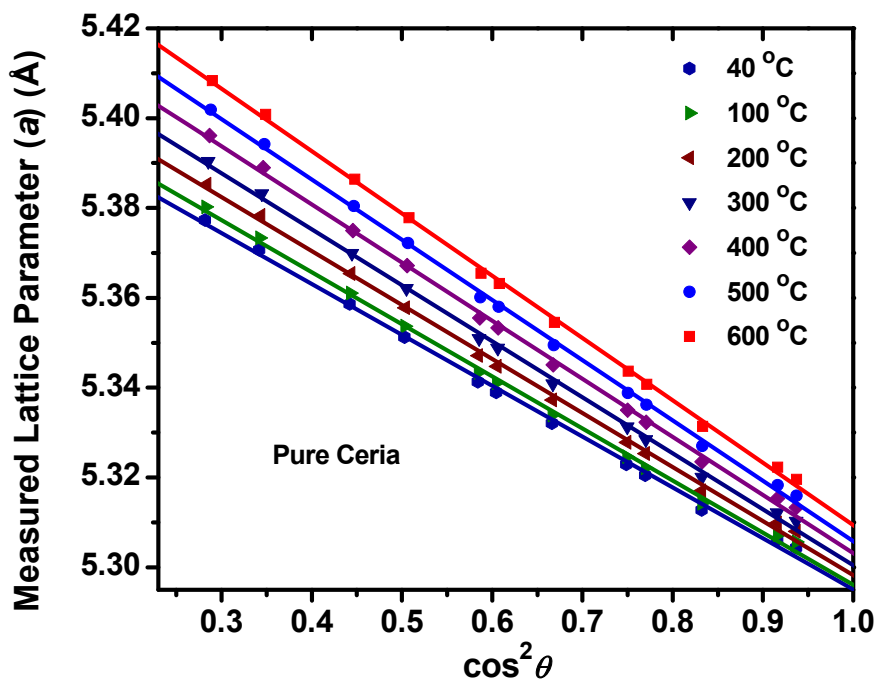


Figure D-1. Plot of calculated lattice parameter, a with respect to $\cos^2\theta$ for pure ceria at different temperatures.

LIST OF REFERENCES

1. Energy Information Administration, 5th May 2008 (<http://www.eia.doe.gov>).
2. Energy Information Administration (Official Energy Statistics from the U.S. Government), 5th May 2008 (<http://www.eia.doe.gov/environment.html>).
3. National Renewable Energy Laboratory (NREL), 20th June 2008 (<http://www.nrel.gov>).
4. Fuel Cell Vehicles, 15th May 2008 (<http://www.fueleconomy.gov/feg/fuelcell.shtml>).
5. N.Q. Minh, "Ceramic Fuel-Cells," *J. Am. Ceram. Soc.*, **76** [3] 563-88 (1993).
6. N.Q. Minh, and T. Takahashi, *Science and Technology of Ceramic Fuel Cells*, Elsevier Science B. V., Amsterdam, 1995.
7. S. Omar, E.D. Wachsman, and J.C. Nino, "A co-doping approach towards enhanced ionic conductivity in fluorite-based electrolytes," *Solid State Ionics*, **177** [35-36] 3199-203 (2006).
8. NETL: Solid State Energy Conversion Alliance (SECA), 15th May 2008 (www.seca.doe.gov).
9. H. Inaba, and H. Tagawa, "Ce_{1-x}Y_xO_{2-x/2}-Based Solid Electrolytes - Review," *Solid State Ionics*, **83** [1-2] 1-16 (1996).
10. K. Eguchi, T. Setoguchi, T. Inoue, and H. Arai, "Electrical-Properties of Ceria-Based Oxides and Their Application to Solid Oxide Fuel-Cells," *Solid State Ionics*, **52** [1-3] 165-72 (1992).
11. R.T. Dirstine, R.N. Blumenthal, and T.F. Kuech, "Ionic-Conductivity of Calcia, Yttria, and Rare Earth Doped Cerium Dioxide," *J. Electrochem. Soc.*, **126** [2] 264-9 (1979).
12. V. Butler, C.R.A. Catlow, B.E.F. Fender, and J.H. Harding, "Dopant Ion Radius and Ionic-Conductivity in Cerium Dioxide," *Solid State Ionics*, **8** [2] 109-13 (1983).
13. B.C.H. Steele, "Appraisal of Ce_{1-x}Gd_yO_{2-x/2} Electrolytes for IT-SOFC Operation at 500° C," *Solid State Ionics*, **129** [1-4] 95-110 (2000).
14. J. Faber, C. Geoffroy, A. Roux, A. Sylvestre, and P. Abelard, "A Systematic Investigation of the DC-Electrical Conductivity of Rare-Earth Doped Ceria," *Appl. Phys. A: Mater. Sci. Process.*, **49** [3] 225 (1989).

15. X.Q. Sha, Z. Lu, X.Q. Huang, J.P. Miao, Z.G. Liu, X.S. Xin, Y.H. Zhang, and W.H. Su, "Influence of the Sintering Temperature on Electrical Property of the $\text{Ce}_{0.8}\text{Sm}_{0.1}\text{Y}_{0.1}\text{O}_{1.9}$ electrolyte," *J. Alloys Compd.*, **433** [1-2] 274-8 (2007).
16. J. Van Herle, D. Seneviratne, and A.J. McEvoy, "Lanthanide Co-Doping of Solid Electrolytes: AC Conductivity Behaviour," *J. Eur. Ceram. Soc.*, **19** [6-7] 837-41 (1999).
17. N. Kim, B.H. Kim, and D. Lee, "Effect of Co-Dopant Addition on Properties of Gadolinia-Doped Ceria Electrolyte," *J. Power Sources*, **90** [2] 139-43 (2000).
18. F.Y. Wang, S.Y. Chen, W. Qin, S.X. Yu, and S.F. Cheng, "Study on Gd and Mg Co-Doped Ceria Electrolyte for Intermediate Temperature Solid Oxide Fuel Cells," *Catal. Today*, **97** [2-3] 189-94 (2004).
19. X.Q. Sha, Z. Lu, X.Q. Huang, J.P. Miao, Z.H. Ding, X.S. Xin, and W.H. Su, "Study on La and Y Co-Doped Ceria-Based Electrolyte Materials," *J. Alloys Compd.*, **428** [1-2] 59-64 (2007).
20. X.Q. Sha, Z. Lu, X.Q. Huang, J.P. Miao, L. Jia, X.S. Xin, and W.H. Su, "Preparation and Properties of Rare Earth Co-Doped $\text{Ce}_{0.8}\text{Sm}_{0.2-x}\text{Y}_x\text{O}_{1.9}$ Electrolyte Materials for SOFC," *J. Alloys Compd.*, **424** [1-2] 315-21 (2006).
21. J.A. Kilner, and R.J. Brook, "A Study of Oxygen Ion Conductivity in Doped Nonstoichiometric Oxides," *Solid State Ionics*, **6** [3] 237-52 (1982).
22. D.J. Kim, "Lattice-Parameters, Ionic Conductivities, and Solubility Limits in Fluorite-Structure MO_2 Oxide ($\text{M} = \text{Hf}^{4+}, \text{Zr}^{4+}, \text{Ce}^{4+}, \text{Th}^{4+}, \text{U}^{4+}$) Solid-Solutions," *J. Am. Ceram. Soc.*, **72** [8] 1415-21 (1989).
23. P.J. Gellings, and H.J.M. Bouwmeester, *The CRC Handbook of Solid State Electrochemistry*, CRC Press Inc, Boca Raton, 1996.
24. M.W. Barsoum, *Fundamentals of Ceramics*, McGraw Hill, Bristol, 1997.
25. A.J. Moulson, and J.M. Herbert, *Electroceramics: Materials, Properties, and Applications*, Wiley, Chichester, 2003.
26. A.M. Adams, F.T. Bacon, and R.G.T. Watson, *Fuel Cells*, Academic Press, New York, 1963.
27. B.C.H. Steele, "Material Science and Engineering: The Enabling Technology for the Commercialisation of Fuel Cell Systems," *J. Mater. Sci.*, **36** [5] 1053-68 (2001).
28. C. Berger, *Handbook of Fuel Cell Technology*, Prentice-Hall Inc., New Jersey, 1968.
29. A.J. Appleby, *Fuel Cell Handbook*, Van Nostrand Reinhold, New York, 1989.

30. L.J.N. Blomen, and M.N. Mugerwa, Fuel Cell Systems, Plenum, New York, 1993.
31. A.J. Appleby, "Issues in Fuel Cell Commercialization," *J. Power Sources*, **58** [2] 153-76 (1996).
32. H.H. Möbius, "On the History of Solid Electrolyte Fuel Cells," *J. Solid State Electrochem.*, **1** [July] 2-16 (1997).
33. E. Baur, and H. Preis, "On Fuel Chains with Fixed Cables," *Z. Elektro. Angew. Phys. Chem.*, **43** 727-32 (1937).
34. L. Blum, H.P. Buchkremer, S. Gross, A. Gubner, L.G.J. de Haart, H. Nabelek, W.J. Quadackers, U. Reisgen, M.J. Smith, R. Steinberger-Wilckens, R.W. Steinbrech, F. Tietz, and I.C. Vinke, "Solid Oxide Fuel Cell Development at Forschungszentrum Juelich," *Fuel Cells*, **7** [3] 204-10 (2007).
35. M. Sahibzada, B.C.H. Steele, K. Hellgardt, D. Barth, A. Effendi, D. Mantzavinos, and I.S. Metcalfe, "Intermediate Temperature Solid Oxide Fuel Cells Operated with Methanol Fuels," *Chem. Eng. Sci.*, **55** [16] 3077-83 (2000).
36. S.C. Singhal, and S. Gopalan, *Processing and Characterization of Electrochemical Materials and Devices*. The American Ceramic Society, Ceramic Transactions: Westerville, 1996; Vol. 109.
37. C. Wagner, "The Mechanism of Electric Supply Lines in Neon Lamps," *Naturwissenschaften*, **31** 265-8 (1943).
38. T.H. Etsell, and S.N. Flengas, "Electrical Properties of Solid Oxide Electrolytes," *Chem. Rev.*, **70** [3] 339-76 (1970).
39. H. Yokokawa, N. Sakai, T. Horita, K. Yamaji, and M.E. Brito, "Electrolytes for Solid-Oxide Fuel Cells," *Mater. Res. Soc. Bull.*, **30** [8] 591-5 (2005).
40. N.X. Jiang, and E.D. Wachsman, "Structural Stability and Conductivity of Phase-Stabilized Cubic Bismuth Oxides," *J. Am. Ceram. Soc.*, **82** [11] 3057-64 (1999).
41. V.V. Kharton, F.M.B. Marques, and A. Atkinson, "Transport Properties of Solid Oxide Electrolyte Ceramics: A Brief Review," *Solid State Ionics*, **174** [1-4] 135-49 (2004).
42. X.D. Wu, Q. Liang, D. Weng, J. Fan, and R. Ran, "Synthesis of CeO₂-MnO_x Mixed Oxides and Catalytic Performance Under Oxygen-Rich Condition," *Catal. Today*, **126** [3-4] 430-5 (2007).
43. S.M. Mathew, S.B. Umbarkar, and M.K. Dongare, "NO_x Storage Behavior of BaO in Different Structural Environment in NSR Catalysts," *Catal. Commun.*, **8** [8] 1178-82 (2007).

44. Z.I. Onsan, "Catalytic Processes for Clean Hydrogen Production from Hydrocarbons," *Turk. J. Chem.*, **31** [5] 531-50 (2007).
45. M.I. Soumelidis, R.K. Stobart, and R.A. Jackson, "A Chemically Informed, Control-Oriented Model of a Three-Way Catalytic Converter," *Proceedings of the I Mech E Part D Journal of Automobile Engineering*, **221** [D9] 1169-82 (2007).
46. S. Yabe, and T. Sato, "Cerium Oxide for Sunscreen Cosmetics," *J. Solid State Chem.*, **171** [1-2] 7-11 (2003).
47. JCPDS - International Committee for Diffraction Data Card 34 - 0394. In.
48. R.D. Shannon, "Revised Effective Ionic-Radii and Systematic Studies of Interatomic Distances in Halides and Chalcogenides," *Acta Crystallogr., Sect. A*, **32** [Sep1] 751-67 (1976).
49. B.C.H. Steele, *Ceramic Oxygen Ion Conductors and Their Technological Applications*. The Institute of Materials: London, 1996.
50. T. Kudo, and K. Fueki, *Solid State Ionics*, Kodansha/VCH, Tokyo, 1990.
51. T. Takahashi, *Physics of Electrolytes*, Academic Press, London, 1972.
52. D.M. Smyth, *The Defect Chemistry of Metal Oxides*, Oxford University Press, Inc., New York, 2000.
53. S. Omar, E.D. Wachsman, and J.C. Nino, "Higher Conductivity Sm³⁺ and Nd³⁺ Co-Doped Ceria-Based Electrolyte Materials," *Solid State Ionics*, **178** 1890-7 (2008).
54. G.B. Balazs, and R.S. Glass, "AC-Impedance Studies of Rare-Earth-Oxide Doped Ceria," *Solid State Ionics*, **76** [1-2] 155-62 (1995).
55. J.R. Macdonald, and E. Barsoukov, *Impedance Spectroscopy: Theory, Experiment, and Applications*, John Wiley & Sons, New York, 1987.
56. H. Yahiro, K. Eguchi, and H. Arai, "Electrical-Properties and Reducibilities of Ceria Rare Earth Oxide Systems and Their Application to Solid Oxide Fuel-Cell," *Solid State Ionics*, **36** [1-2] 71-5 (1989).
57. H. Yahiro, T. Ohuchi, K. Eguchi, and H. Arai, "Electrical-Properties and Microstructure in the System Ceria Alkaline-Earth Oxide," *J. Mater. Sci.*, **23** [3] 1036-41 (1988).
58. I. Mahata, G. Das, R.K. Mishra, and B.P. Sharma, "Combustion Synthesis of Gadolinia Doped Ceria Powder," *J. Alloys Compd.*, **391** [1-2] 129-35 (2005).
59. N.M. Rahaman, *Ceramic Processing*, CRC Taylor & Francis, Boca Raton, 2007.

60. A. Tsoga, A. Naoumidis, and D. Stover, "Total Electrical Conductivity and Defect Structure of ZrO_2 - CeO_2 - Y_2O_3 - Gd_2O_3 Solid Solutions," *Solid State Ionics*, **135** [1-4] 403-9 (2000).
61. K.R. Reddy, and K. Karan, "Sinterability, Mechanical, Microstructural, and Electrical Properties of Gadolinium-Doped Ceria Electrolyte for Low-Temperature Solid," *J. Electroceram.*, **15** [1] 45-56 (2005).
62. C.Y. Tian, and S.W. Chan, "Ionic Conductivities, Sintering Temperatures and Microstructures of Bulk Ceramic CeO_2 Doped with Y_2O_3 ," *Solid State Ionics*, **134** [1-2] 89-102 (2000).
63. R.S. Torrens, N.M. Sammes, and G.A. Tompsett, "Characterisation of $(CeO_2)_{0.8}(GdO_{1.5})_{0.2}$ Synthesised Using Various Techniques," *Solid State Ionics*, **111** [1-2] 9-15 (1998).
64. S.W. Zha, C.R. Xia, and G.Y. Meng, "Effect of Gd (Sm) Doping on Properties of Ceria Electrolyte for Solid Oxide Fuel Cells," *J. Power Sources*, **115** [1] 44-8 (2003).
65. C. Keller, U. Berndt, H. Engerer, and L. Leitner, "Phase Equilibria in Thorium Oxide - Lanthanide Oxide Systems," *J. Solid State Chem.*, **4** [3] 453-65 (1972).
66. A. Pramanick, S. Omar, J.C. Nino, and J.L. Jones, "Lattice Parameter Determination using a Curved Position Sensitive Detector and Application to $Sm_xNd_xCe_{1-2x}O_{2-\delta}$ Ceramics," unpublished (2007).
67. S. Omar, E.D. Wachsman, and J.C. Nino, "Higher Ionic Conductive Ceria Based Electrolytes for SOFCs," *Appl. Phys. Lett.*, **91** 144106 (2007).
68. L. Minervini, M.O. Zacate, and R.W. Grimes, "Defect Cluster Formation in M_2O_3 -Doped CeO_2 ," *Solid State Ionics*, **116** [3-4] 339-49 (1999).
69. H. Yamamura, E. Katoh, M. Ichikawa, K. Kakinuma, T. Mori, and H. Haneda, "Multiple Doping Effect on the Electrical Conductivity in the $(Ce_{1-x-y}La_xM_y)O_{2-\delta}$ (M = Ca, Sr) System," *Electrochemistry*, **68** [6] 455-9 (2000).
70. E.D. Wachsman, S. Boyapati, and N. Jiang, "Effect of Dopant Polarizability on Oxygen Sublattice Order in Phase-Stabilized Cubic Bismuth Oxides," *Ionics*, **7** 1-6 (2001).
71. F.Y. Wang, B.Z. Wan, and S.F. Cheng, "Study on Gd^{3+} and Sm^{3+} Co-Doped Ceria-Based Electrolytes," *J. Solid State Electrochem.*, **9** [3] 168-73 (2005).
72. P. Li, I.W. Chen, J.E. Pennerhahn, and T.Y. Tien, "X-Ray Absorption Studies of Ceria with Trivalent Dopants," *J. Am. Ceram. Soc.*, **74** [5] 958-67 (1991).

73. M. Mogensen, N.M. Sammes, and G.A. Tompsett, "Physical, Chemical and Electrochemical Properties of Pure and Doped Ceria," *Solid State Ionics*, **129** [1-4] 63-94 (2000).
74. S.J. Hong, and A.V. Virkar, "Lattice-Parameters and Densities of Rare-Earth-Oxide Doped Ceria Electrolytes," *J. Am. Ceram. Soc.*, **78** [2] 433-9 (1995).
75. K. Fuda, K. Kishio, S. Yamachi, and K. Fueki, "Study on Vacancy Motion in Y₂O₃-Doped CeO₂ by O-17 NMR Technique," *J. Phys. Chem. Solids*, **46** [10] 1141-6 (1985).
76. Z.L. Zhan, T.L. Wen, H.Y. Tu, and Z.Y. Lu, "AC Impedance Investigation of Samarium-Doped Ceria," *J. Electrochem. Soc.*, **148** [5] A427-A32 (2001).
77. T.S. Zhang, J. Ma, L.B. Kong, S.H. Chan, and J.A. Kilner, "Aging Behavior and Ionic Conductivity of Ceria-Based Ceramics: A Comparative Study," *Solid State Ionics*, **170** [3-4] 209-17 (2004).
78. L.P. Li, X.M. Lin, G.S. Li, and H. Inomata, "Solid Solubility and Transport Properties of Ce_{1-x}Nd_xO_{2-δ} Nanocrystalline Solid Solutions by a Sol-Gel Route," *J. Mater. Res.*, **16** [11] 3207-13 (2001).
79. Y. Tsur, and C.A. Randall, "Analysis of X-Ray Powder Diffraction Data Using the Maximum Likelihood Estimation Method," *J. Am. Ceram. Soc.*, **83** [8] 2062-6 (2000).
80. I.E.L. Stephens, and J.A. Kilner, "Ionic Conductivity of Ce_{1-x}Nd_xO_{2-x/2}," *Solid State Ionics*, **177** [7-8] 669-76 (2006).
81. A.E. Mattsson, P.A. Schultz, M.P. Desjarlais, T.R. Mattsson, and K. Leung, "Designing meaningful density functional theory calculations in materials science - a primer," *Modelling and Simulation in Materials Science and Engineering*, **13** [1] R1-R31 (2005).
82. W. Kohn, and L.J. Sham, "Self-Consistent Equations Including Exchange and Correlation Effects," *Physical Review*, **140** [4A] 1133-& (1965).
83. D.A. Andersson, S.I. Simak, N.V. Skorodumova, I.A. Abrikosov, and B. Johansson, "Optimization of Ionic Conductivity in Doped Ceria," *Proc. Natl. Acad. Sci. U. S. A.*, **103** 3518 (2006).
84. L. Vegard, and H. Dale, "Tests on Mixed Crystals and Alloys," *Z. Kristallogr.*, **67** [1] 148-62 (1928).
85. T.C. Parks, and D.J.M. Bevan, "Mixed Oxides of Type MO₂ (Fluorite)-MO_{1.5} VI : Phase Relationships in Systems CeO₂-SmO_{1.5} and CeO₂-NdO_{1.5}," *Rev. Chim. Miner.*, **10** [1-2] 15-28 (1973).

86. J.E. Bauerle, "Study of Solid Electrolyte Polarization by a Complex Admittance Method," *J. Phys. Chem. Solids*, **30** [12] 2657-70 (1969).
87. A.S. Nowick, W.K. Lee, and H. Jain, "Survey and Interpretation of Pre-Exponentials of Conductivity," *Solid State Ionics*, **28** 89-94 (1988).
88. D.K. Hohnke, "Ionic-Conduction in Doped Oxides with the Fluorite Structure," *Solid State Ionics*, **5** [Oct] 531-4 (1981).
89. D.P. Almond, and A.R. West, "The Activation Entropy for Transport in Ionic Conductors," *Solid State Ionics*, **23** [1-2] 27-35 (1987).
90. K. Fuda, K. Kishio, S. Yamauchi, K. Fueki, and Y. Onoda, "O-17 NMR-Study of Y₂O₃-Doped CeO₂," *J. Phys. Chem. Solids*, **45** [11-1] 1253-7 (1984).
91. J.M. Ralph, and J.A. Kilner, *Enhancement of the ionic conductivity in ceria gadolinia solid solutions*. The European Solid Oxide Fuel Cell Forum: Oslo, 1996.
92. V.B. Glushkova, L.V. Sazonova, and F. Hanic, "Lattice Parameters of Cubic Solid Solutions in the System $uR_2O_3-(1-u)MO_2$," *Ceram. Int.*, **4** [4] 176-8 (1978).
93. V.I. Aleksandrov, G.E. Valyano, B.V. Lukin, V.V. Osiko, A.E. Rautbort, V.M. Tatarintsev, and V.N. Filatova, "Structure of Single-Crystals of Stabilized Zirconium Dioxide," *Inorg. Mater.*, **12** [2] 235-8 (1976).
94. R.P. Ingel, and D. Lewis, "Lattice-Parameters and Density for Y₂O₃-Stabilized ZrO₂," *J. Am. Ceram. Soc.*, **69** [4] 325-32 (1986).
95. B.D. Cullity, and S.R. Stock, *Elements of X-ray Diffraction*, Prentice Hall, New Jersey, 3rd 1978.
96. T. Hisashige, Y. Yamamura, and T. Tsuji, "Thermal Expansion and Debye temperature of Rare Earth-Doped Ceria," *J. Alloys Compd.*, **408** 1153-6 (2006).
97. H. Hayashi, M. Kanoh, C.J. Quan, H. Inaba, S.R. Wang, M. Dokiya, and H. Tagawa, "Thermal Expansion of Gd-Doped Ceria and Reduced Ceria," *Solid State Ionics*, **132** [3-4] 227-33 (2000).
98. W. Zajac, K. Swierczek, and J. Molenda, "Thermochemical Compatibility Between Selected (La,Sr)(Co,Fe,Ni)O₃ Cathodes and Rare Earth Doped Ceria Electrolytes," *J. Power Sources*, **173** [2] 675-80 (2007).
99. H. Hayashi, T. Saitou, N. Maruyama, H. Inaba, K. Kawamura, and M. Mori, "Thermal Expansion Coefficient of Yttria Stabilized Zirconia for Various Yttria Contents," *Solid State Ionics*, **176** [5-6] 613-9 (2005).

100. X.L. Zhou, M.X. Zhu, F.J. Deng, G.Y. Meng, and X.Q. Liu, "Electrical Properties, Sintering and Thermal Expansion Behavior of Composite Ceramic Interconnecting Materials, $\text{La}_{0.7}\text{Ca}_{0.3}\text{CrO}_{3-d}/\text{Y}_{0.2}\text{Ce}_{0.8}\text{O}_{1.9}$ for SOFCs," *Acta Mater.*, **55** [6] 2113-8 (2007).
101. N. Swaminathan, and J. Qu, "Interactions Between Non-Stoichiometric Stresses and Defect Transport in a Tubular Electrolyte," *Fuel Cells*, **7** [6] 453-62 (2007).
102. M. Greenberg, E. Wachtel, I. Lubomirsky, J. Fleig, and J. Maier, "Elasticity of Solids with a Large Concentration of Point Defects," *Adv. Funct. Mater.*, **16** [1] 48-52 (2006).
103. D.Y. Wang, D.S. Park, J. Griffith, and A.S. Nowick, "Oxygen-Ion Conductivity and Defect Interactions in Yttria-Doped Ceria," *Solid State Ionics*, **2** [2] 95-105 (1981).
104. M. Kamiya, E. Shimada, Y. Ikuma, M. Komatsu, H. Haneda, S. Sameshima, and Y. Hirata, "Oxygen Self-Diffusion in Cerium Oxide Doped with Nd," *J. Mater. Res.*, **16** [1] 179-84 (2001).
105. A.S. Nowick, D.Y. Wang, D.S. Park, and J. Griffith, *Oxygen-Ion Conductivity and Defect Structure of CeO_2 Doped with CaO and Y_2O_3* . North - Holland: Amsterdam, 1979.
106. J.A. Kilner, and B.C.H. Steele, *Nonstoichiometric Oxides*. Academic Press: New York, 1981.
107. T.S. Zhang, J. Ma, S.H. Chan, P. Hing, and J.A. Kilner, "Intermediate-Temperature Ionic Conductivity of Ceria-Based Solid Solutions as a Function of Gadolinia and Silica Contents," *Solid State Sci.*, **6** [6] 565-72 (2004).
108. Y.H. Cho, P.S. Cho, G. Auchterlonie, D.K. Kim, J.H. Lee, D.Y. Kim, H.M. Park, and J. Drennan, "Enhancement of Grain-Boundary Conduction in Gadolinia-Doped Ceria by the Scavenging of Highly Resistive Siliceous Phase," *Acta Mater.*, **55** [14] 4807-15 (2007).
109. T.S. Zhang, J. Ma, L.B. Kong, P. Hing, Y.J. Leng, S.H. Chan, and J.A. Kilner, "Sinterability and Ionic Conductivity of Co-Precipitated $\text{Ce}_{0.8}\text{Gd}_{0.2}\text{O}_{2-\delta}$ Powders Treated via a High-Energy Ball-Milling Process," *J. Power Sources*, **124** [1] 26-33 (2003).
110. M.C. Martin, and M.L. Mecartney, "Grain Boundary Ionic Conductivity of Yttrium Stabilized Zirconia as a Function of Silica Content and Grain Size," *Solid State Ionics*, **161** [1-2] 67-79 (2003).
111. T.S. Zhang, J. Ma, Y.Z. Chen, L.H. Luo, L.B. Kong, and S.H. Chan, "Different conduction behaviors of grain boundaries in SiO_2 -containing 8YSZ and CGO20 electrolytes," *Solid State Ionics*, **177** [13-14] 1227-35 (2006).

112. R. Gerhardt, and A.S. Nowick, "Grain-Boundary Effect in Ceria Doped with Trivalent Cations .1. Electrical Measurements," *J. Am. Ceram. Soc.*, **69** [9] 641-6 (1986).
113. R. Gerhardt, A.S. Nowick, M.E. Mochel, and I. Dumler, "Grain-Boundary Effect in Ceria Doped with Trivalent Cations .2. Microstructure and Microanalysis," *J. Am. Ceram. Soc.*, **69** [9] 647-51 (1986).
114. V. Esposito, and E. Traversa, "Design of Electroceramics for Solid Oxide Fuel Cell Applications: Playing with Ceria," *J. Am. Ceram. Soc.*, **91** [4] 1037-51 (2008).
115. X. Guo, and R. Waser, "Electrical Properties of the Grain Boundaries of Oxygen Ion Conductors: Acceptor-Doped Zirconia and Ceria," *Prog. Mater. Sci.*, **51** [2] 151-210 (2006).
116. X. Guo, and Y. Ding, "Grain boundary space charge effect in zirconia - Experimental evidence," *J. Electrochem. Soc.*, **151** [1] J1-J7 (2004).
117. C. Herring, "Effect of Change of Scale on Sintering Phenomena," *J. Appl. Phys.*, **21** [4] 301-3 (1950).
118. Y.C. Zhou, and M.N. Rahaman, "Effect of Redox Reaction on the Sintering Behavior of Cerium Oxide," *Acta Mater.*, **45** [9] 3635-9 (1997).
119. J.D. Nicholas, and L.C. De Jonghe, "Prediction and evaluation of sintering aids for Cerium Gadolinium Oxide," *Solid State Ionics*, **178** [19-20] 1187-94 (2007).
120. G.S. Lewis, A. Atkinson, B.C.H. Steele, and J. Drennan, "Effect of Co addition on the lattice parameter, electrical conductivity and sintering of gadolinia-doped ceria," *Solid State Ionics*, **152** 567-73 (2002).
121. E. Jud, Z. Zhang, W. Sigle, and L.J. Gauckler, "Microstructure of Cobalt Oxide Doped Sintered Ceria Solid Solutions," *J. Electroceram.*, **16** [3] 191-7 (2006).
122. V. Gil, J. Tartaj, C. Moure, and P. Duran, "Effect of Bi₂O₃ Addition on the Sintering and Microstructural Development of Gadolinia-Doped Ceria Ceramics," *J. Eur. Ceram. Soc.*, **27** [2-3] 801-5 (2007).
123. K.H. Brosnan, G.L. Messing, and D.K. Agrawal, "Microwave Sintering of Alumina at 2.45 GHz," *J. Am. Ceram. Soc.*, **86** [8] 1307-12 (2003).
124. M.A. Janney, and H.D. Kimrey, *Microwave Sintering of Alumina at 28 GHz*. American Ceramic Society: Westerville, 1988.
125. B. Rambabu, S. Ghosh, and H. Jena, "Novel Wet-Chemical Synthesis and Characterization of Nanocrystalline CeO₂ and Ce_{0.8}Gd_{0.2}O_{1.9} as Solid Electrolyte for Intermediate Temperature Solid Oxide Fuel Cell (IT-SOFC) Applications," *J. Mater. Sci.*, **41** [22] 7530-6 (2006).

126. D. Perez-Coll, D. Marrero-Lopez, P. Nunez, S. Pinol, and J.R. Frade, "Grain Boundary Conductivity of $\text{Ce}_{0.8}\text{Ln}_{0.2}\text{O}_{2-d}$ Ceramics (Ln = Y, La, Gd, Sm) with and without Co-Doping," *Electrochim. Acta*, **51** [28] 6463-9 (2006).
127. J.S. Ahn, H.S. Yoon, and E.D. Wachsman, "Performance of IT-SOFC with $\text{Ce}_{0.9}\text{Gd}_{0.1}\text{O}_{1.95}$ Functional Layer at the Interface of $\text{Ce}_{0.9}\text{Gd}_{0.1}\text{O}_{1.95}$ Electrolyte and Ni- $\text{Ce}_{0.9}\text{Gd}_{0.1}\text{O}_{1.95}$ Anode," *Proc. - Electrochem. Soc.*, Submitted (2008).
128. T. Kenjo, S. Osawa, and K. Fujikawa, "High-Temperature Air Cathodes Containing Ion Conductive Oxides," *J. Electrochem. Soc.*, **138** [2] 349-55 (1991).
129. E.P. Murray, and S.A. Barnett, "(La,Sr) MnO_3 -(Ce,Gd) O_{2-x} Composite Cathodes for Solid Oxide Fuel Cells," *Solid State Ionics*, **143** [3-4] 265-73 (2001).

BIOGRAPHICAL SKETCH

Shobit Omar was born in 19th of October 1980, in Jhansi, Uttar Pradesh, India. His father is an electrical engineer, and ran a small scale industry in Jhansi. His mother is a homemaker, while his elder brother is an electrical engineer and works in a software company in Pune, India. Following the footsteps of his father and brother, Shobit Omar always dreamed of becoming an engineer. After finishing the 12th grade in 1999, and spending one year of completely secluded life, he was able to get his name in the merit list for studying in one of the IITs. However, he decided to take up ceramic engineering at the Institute of Technology, Banaras Hindu University (IT-BHU), Varanasi. Spending four years in the holy city of Varanasi completely changed his perception about life. Living in the cultural and religious centre of India transformed him into a spiritual person. After graduation, he decided to go for advanced studies in materials science in the US, rather than going for a job directly after graduation. In summer 2004, he obtained a bachelor's degree from IT-BHU, and got admission in Materials Science and Engineering Department at the University of Florida (UF), Gainesville, Florida.

At UF, Shobit Omar joined Dr. Juan C. Nino's research group, where he spent a lonely life in the research laboratory for the first semester. He missed his family, friends, Indian food, and everything related to India. Slowly things changed, and he got some really good friends in Gainesville. As time passed, he got accustomed to US culture. After four years of his research, he is now near completion of his PhD. Throughout this period, he was exposed to numerous new things, which helped him to grow professionally and individually. Studying in University of Florida provided him the excellent environment and opportunity to build a strong career in the materials science

field. Shobit Omar has accepted a post-doctoral position in Risø National Laboratory in Roskilde, Denmark upon completion of his Ph.D. degree.